

UC San Diego

UC San Diego Electronic Theses and Dissertations

Title

Rational Design of Ligands for Transition Metal Catalysis

Permalink

<https://escholarship.org/uc/item/9qk578qb>

Author

Yazdani, Sima

Publication Date

2021

Peer reviewed|Thesis/dissertation

UNIVERSITY OF CALIFORNIA SAN DIEGO

SAN DIEGO STATE UNIVERSITY

Rational Design of Ligands for Transition Metal Catalysis

A dissertation submitted in partial satisfaction
of the requirements for the degree Doctor of Philosophy

in

Chemistry

by

Sima Yazdani

Committee in charge:

University of California San Diego

Professor Bertrand, Guy

Professor Day, James

Professor Muller, Ulrich

Professor Yang, Jerry

San Diego State University

Professor Grotjahn, Douglas B.. Chair

Professor Gustafson, Jeffrey

2021

Copyright
Sima Yazdani, 2021
All rights reserved

The Dissertation of Sima Yazdani is approved, and it is acceptable in quality and form for publication on microfilm and electronically:

Chair

University of California San Diego

San Diego State University

2021

DEDICATION

To my father and my mother

EPIGRAPH

“Human being are members of a whole, since in their creation they are of one essence. When the conditions of the time brings a member to pain, the other members will suffer from discomfort.”

Saadi Shirazzi

Golestan (chapter 1, story 10)

TABLE OF CONTENTS

Dissertation Approval Page	iii
Dedication	iv
Epigraph	v
Table of Contents	vi
List of Figures	viii
List of Tables	xi
Acknowledgements..	xii
Vita	xiv
Abstract of the Dissertation	xv
Chapter 1 The important role of molecular WOC in the future of renewable energy	1
1.1. Global warming	2
1.2. Sources of energy.....	3
1.3. Renewable energy	4
1.4. Water splitting and water oxidation	5
1.5. Artificial photosynthesis for solar liquid cell.....	6
1.6. History of molecular water oxidation catalysts (molecular WOC).....	7
1.7. Novelty in ruthenium water oxidation catalysis.....	10
Chapter 2 Coordination of tertiary phosphine axial ligands to ruthenium bda (2,2'-bipyridine-6,6'-dicarboxylato) and tda ([2,2':6',2''-terpyridine]-6,6''-dicarboxylato) scaffolds	12
2.1. X-ray crystallography and electrochemistry reveal electronic and steric effects of phosphine and phosphite ligands in complexes $Ru^{II}(\kappa^4\text{-bda})(PR_3)_2$ and $Ru^{II}(\kappa^3\text{-bda})(PR_3)_3$	13
2.2. Influence of axial phosphine ligands in six-coordinate ruthenium water oxidation catalysts.....	26
2.3. Experimental section.....	49
Chapter 3 Trans-spanning ligands with a macrocyclic cavity, capable of stabilizing a WOC.....	65
3.1. Introduction.....	66
3.2. Designing first novel ruthenium bda macrocycle	72
3.3. Novel ruthenium bda macrocycle with vinyl bridge containing a large-sized cavity	74
3.4. Novel ruthenium bda macrocycle with phenyl bridge containing a large-sized cavity	79
3.5. Conclusion and future work.....	82
3.6. Synthetic procedure	83
Chapter 4 Influence of carbene and phosphine ligands on the catalytic activity of gold complexes in the hydroamination and hydrohydrazination of alkynes.....	91
4.1. Introduction.....	92
4.2. Introduction for hydroamination and hydrazination	96

4.3. Results and discussion	98
4.4. What is the ligand effect on the catalyst performance?	109
4.5. How do ^{iPr} BiCAACAuCl compare to state-of-the-art catalysts?	115
4.6. Conclusion	117
4.7. Experimental Section	118
4.8. Synthesis of gold catalysts	119
4.9. Mechanistic studies for hydroamination and hydrazination through stoichiometric reaction	124
4.10. General method for the hydroamination	138
4.11. General method for the hydrohydrazination	166
4.12. Reaction optimization using ¹ H NMR spectroscopic studies to determine kinetics	191
References	193

LIST OF FIGURES

Figure 1.1. Global primary energy consumption by energy source.....	3
Figure 1.2. U.S. primary renewable energy consumption by source and sector in 2019.....	4
Figure 1.3. X-ray structure of the oxygen evolving complex, Mn ₄ CaO ₅	5
Figure 1.4. A photo-electrochemical cell.....	7
Figure 1.5. Molecular WOC development through the years.	10
Figure 2.1. Complexes were fully characterized by NMR spectroscopy and X-ray crystallography.....	14
Figure 2.2. General synthetic procedure for making Ru(bda)(PR ₃) ₂	16
Figure 2.3. Cyclic voltammograms of complexes 2.1 - 2.3	19
Figure 2.4. Cyclic voltammograms of complexes 2.2 , 2.3 , and 2.4	21
Figure 2.5. Selected molecular orbitals for 2.1 to 2.4	24
Figure 2.6. Selected molecular orbitals for 2.4	24
Figure 2.7. Known water oxidation catalysts 1.8 , 1.9 , the Ru-bda family 2.1 and 2.6 - 2.9 , and 2.10 with different phosphorus axial ligands (2.6 – 2.9) reported here	26
Figure 2.8. Synthesis of complexes 2.6 – 2.9	28
Figure 2.9. Solid state structures of 2.6 – 2.8 , 2.1 . Selected bond lengths and bond angles.	29
Figure 2.10. Cyclic voltammograms of 2.6	31
Figure 2.11. Cyclic voltammograms (background-subtracted) of 2.7 - 2.9	32
Figure 2.12. Reaction cell equipped with pressure transducer.	34
Figure 2.13. (a-b)Oxygen evolution catalyzed by 2.6 – 2.8 . (c) The rate of O ₂ evolution of 2.6	36
Figure 2.14. UV-vis spectra of 2.6 . Spectrophotometric redox titration of 2.6	38
Figure 2.15. (a-b) UV-vis spectrum of 2.10 and 2.9 . (c) Spectrophotometric redox titration of 2.6	39
Figure 2.16. Synthesis of [Ru(tda)(tris(2-furyl)phosphine) ₂] 2.10	40
Figure 2.17. Solid state structure of 2.10 and comparison with that of 1.9	41
Figure 2.18. (a-b) Cyclic voltammetry of 2.10 . (c) Repetitive cyclic voltammetry of 2.10	43
Figure 2.19. Plot of current for Ru ^{II/III} couple vs. square root of scan rate for 2.10	44

Figure 2.20. (a) Oxygen evolution catalyzed by 2.10 . (b) Rate of O ₂ evolution of 2.10	45
Figure 2.21. Oxygen evolution catalysed by 2.10	46
Figure 2.22. (a-b) UV-vis spectrum of 2.10 . (c) Plot of absorbance against equiv. of CAN.....	47
Figure 2.23. Two basic proposed mechanisms for water oxidation by mononuclear catalysts.	48
Figure 3.1. Known metal complexes bearing a trans-chelating dinitrogen ligand in literature.....	67
Figure 3.2. Bridged and macrocyclic Ru complexes used as a molecular water oxidation catalysts	71
Figure 3.3. Oxidation of the Ru(bda) complex and formation of the Ru ^V -oxo intermediates	72
Figure 3.4. Synthetic procedure of Ru complexes 3.10 and 3.11 and related X-ray crystals	73
Figure 3.5. Synthetic procedure of Ru complexes 3.17-3.18 and related X-ray crystal structures.....	75
Figure 3.6. CV of 3.7 in an aqueous phosphate buffer	77
Figure 3.7. μMoles of O ₂ produces over time in aqueous solution (pH 1)	78
Figure 3.8. Synthetic procedure of Ru macrocycle 3.10 and related X-ray crystal structure	79
Figure 3.9. CV of 3.21 and Sun's complex 1.6	80
Figure 3.10. (a) Concentration-dependent oxygen evolution for 3.10 (b) The plot of the initial rates.....	81
Figure 4.1. Comparison between 5 membered-ring NHC and CAAC.	93
Figure 4.2. Known families of CAAC ligands and electronic and steric properties.....	94
Figure 4.3. Comparison of known phosphines and carbenes gold catalysts.....	97
Figure 4.4. ¹ H NMR kinetic monitoring of the hydroamination to evaluate optimized condition	99
Figure 4. 5. Hydroamination substrate scope with variety amines and alkynes.	101
Figure 4. 6. Hammett correlation in (a) alkyne and (b) amine.....	102
Figure 4. 7. Rate dependence of the alkyne and amine in hydroamination	103
Figure 4. 8. Hydrohydrazination optimal conditions using ¹ H NMR kinetic monitoring.....	105
Figure 4. 9. Substrate scope with hydrazines.....	106
Figure 4. 10. Hammett equation for the hydrohydrazination.....	108
Figure 4. 11. Rate dependency for alkyne and hydrazine.....	108

Figure 4. 12. Ligand effects on the degradation of cationic gold	110
Figure 4. 13. ¹ H NMR kinetic study of the gold complex bearing 4.3.L-4.6.L	111
Figure 4. 14. Mechanistic behavior of the BiCAACAu ⁺ under stoichiometric conditions.....	112
Figure 4. 15. Energy profiles of substrate ligand exchanges as a function of 4.3.L-4.6.L	114
Figure 4. 16. Presenting the flexible sterics in ¹⁹⁹ PtBiCAACAuCl.....	115
Figure 4. 17. Comparing complexes of 4.6.L and JohnPhos.....	116
Figure 4. 18. Benchmarking the catalytic activity at 80 °C.	117
Figure 4. 18. Figure illustrating the kinetics of the hydroamination reaction.....	192

LIST OF TABLES

Table 2.1. ^1H and ^{31}P NMR spectra of compounds 2.1-2.4 in CD_3OD	14
Table 2.2. Bond lengths and angles obtained by X-ray crystallography	17
Table 2.3. Electrochemical features of 2.1-2.4	22
Table 2.4. Computed HOMO–LUMO gaps for $\text{Ru}^{\text{II}}(\text{bda})(\text{L})_2$, 2.3	22
Table 2.5. Tolman electronic parameters (TEP), Infrared data (CH_2Cl_2) for $\text{trans-}[\text{RuCl}(\text{CO})(\text{L})]$ complexes, and cone angles for 2.1 and 2.6-2.9	35
Table 2.6. Detailed concentration and yields for oxygen evolution catalyzed by 2.7-2.9	35
Table 2.7. Detailed concentration and yields for oxygen evolution catalyzed by 2.6	35
Table 2.8. Detailed concentration and yields for oxygen evolution catalyzed by 2.10	42
Table 3.1. Detailed concentration and yields for oxygen evolution catalyzed by 3.21	82

ACKNOWLEDGEMENTS

I write this acknowledgment to thank all the people who help me during my Ph.D. program.

I would like to express my deep and sincere gratitude to my advisors Prof. Douglas Grotjahn and Prof. Guy Bertrand for their continuous support, tireless guidance, and patience. I want to thank you for all the opportunities you gave me to further my research. You provided me with the knowledge and tools that I needed to choose the right direction and successfully complete my dissertation. I would like to special thank Dr. Rodolphe Jazzar. I couldn't have made it through the challenges in my research without your patient and your valuable guidance. Also, I express my thanks to Prof. Keary Engle for giving me the opportunity to collaborate with his team. I am grateful to Dr. Michele Soleihavoup and Dr. Mohand Melami. My special thanks go to all my labmates, all previous graduate students, post-docs, collaborators, and undergraduates at UCSD, SDSU, and Scripps Research Institution. All of you had an important role in my graduate studies and I am blessed to have such amazing friends during my education. I extremely thankful to all co-authors who collaborated in below papers and manuscripts.

The section 2.1 of chapter one has contents that are similar to the paper that we published in *Polyhedron*: Yazdani, S.; Silva, B. E.; Cao, T. C.; Rheingold, A. L.; Grotjahn, D. B. X-Ray Crystallography and Electrochemistry Reveal Electronic and Steric Effects of Phosphine and Phosphite Ligands in Complexes $\text{Ru}^{\text{II}}(\kappa^4\text{-bda})(\text{PR}_3)_2$ and $\text{Ru}^{\text{II}}(\kappa^3\text{-bda})(\text{PR}_3)_3$ (bda = 2,2'-bipyridine-6,6'-dicarboxylato). *Polyhedron* **2019**, *161*, 63–70.

The section 2.2 of chapter two has contents that are similar to the manuscript that we are preparing for publication in **Yazdani, S.**; Breyer, C. J.; Kumari, P.; Rheingold, A. L.; Jazzar, R.; Bertrand, G.; Grotjahn, D. B. Influence of Axial Phosphine Ligands in Six- coordinate Ruthenium Water Oxidation Catalysts.

Chapter three has contents that are similar to the manuscript that we are preparing for publication in **Yazdani, S.**; Breyer, C. J.; Kumari, P.; Rheingold, A. L.; Jazzar, R.; Bertrand, G.; Grotjahn, D. B. Trans-Spanning Ligands with a Macrocyclic Cavity, Capable for Water Oxidation.

Chapter four has contents that are similar to the paper that we published in **Yazdani, S.**; Junor, G. P.; Peltier, J. L.; Jazzar, R.; Grotjahn, D. B.; Bertrand, G. Influence of carbene and phosphine ligands on the catalytic activity of gold complexes in the hydroamination and hydrohydrazination of alkynes. *ACS Catalysis*, **2020**, *10*, 5190-5201. DOI: 10.1021/acscatal.0c01352.

I am extremely grateful to my parents, my sisters, and my brothers for their love, caring, sacrifice, and hard work that enriched and motivated me. Dad, I believe in what you told me 'You can achieve whatever you aim for'. I am very much thankful to my lovely husband for understanding, supporting, and believing in my ideas. Thanks to my friend Sara Afshar for all of her supports through my long journey.

VITA

2000 Bachelor of Geology, Azad University
2005 Master of Geology-Petrology, University of Tehran
2021 Doctor of Philosophy, Chemistry, University of California San Diego and San Diego State University

Publications

1. Yang, G.; ‡ **Yazdani, S.**; ‡ Kendrick A.; Junor, G. P.; Bertrand, G.; Jazzar, R.; Engle, K.M. Cyclic(Alkyl)(Amino)Carbene Ligands Enable Cu-Catalyzed Markovnikov Protoboration and Protosilylation of Terminal Alkynes: A Versatile Portal to Functionalized Alkenes. *Angew. Chem. Int. Ed.*, **2021**, *Accepted*. DOI: 10.1002/anie.202106107 (‡ equal contribution).
2. **Yazdani, S.**; Junor, G. P.; Peltier, J. L.; Jazzar, R.; Grotjahn, D. B.; Bertrand, G. Influence of carbene and phosphine ligands on the catalytic activity of gold complexes in the hydroamination and hydrohydrazination of alkynes. *ACS Catalysis*, **2020**, *10*, 5190-5201.
3. **Yazdani, S.**; Silva, B. E.; Cao, T. C.; Rheingold, A. L.; Grotjahn, D. B. X-ray crystallography and electrochemistry reveal electronic and steric effects of phosphine and phosphite ligands in complexes $Ru^{II}(\kappa^4\text{-bda})(PR_3)_2$ and $Ru^{II}(\kappa^3\text{-bda})(PR_3)_3$ (bda = 2,2'-bipyridine-6,6'-dicarboxylato). *Polyhedron*, **2019**, *161*, 63-70.
4. **Yazdani, S.**; Breyer, C. J.; Kumari, P.; Rheingold, A. L.; Jazzar, R.; Bertrand, G.; Grotjahn, D. B. Influence of Axial Phosphine Ligands in Six-coordinate Ruthenium Water Oxidation Catalysts, *Submitted*.
5. Vermersch, F.; **Yazdani, S.**; Junor, G. P.; Jazzar, R.; Bertrand, G. Scaling Nucleophilicity in Singlet Carbenes one Hydrogen at a Time. *In Preparation*.
6. **Yazdani, S.**; Breyer, C. J.; Kumari, P.; Rheingold, A. L.; Jazzar, R.; Bertrand, G.; Grotjahn, D. B. Trans-Spanning Ligands with a Macrocyclic Cavity, Capable for Water Oxidation. *In Preparation*.

Presentations

1. New gold catalysts in the hydrohydrazination of alkynes under ambient condition. *258th American Chemical Society National Meeting & Exposition, San Diego, August 2019*. Oral.
2. A series of novel Ru(bda) platform complexes by swapping ligands at diaxial positions as potential water oxidation catalysts. *258th American Chemical Society National Meeting & Exposition, San Diego, August 2019*. Poster.
3. A molecular tweezer: Synthesis of Ru(II) complex bearing trans-spanning ligands with olefin bridge as a water oxidation catalyst (WOC). *11th annual Student Research Symposium (SRS18), SDSU, March 2018*. Poster.

Honors and Awards

San Diego State University Graduate Fellowship (2019-2021)

Major Fields of Study

Major Field: Chemistry (Organic)
Studies in Organic Synthetic Chemistry and Organometallic Catalysis
Professor Grotjahn, Douglas B.

ABSTRACT OF THE DISSERTATION

Rational Design of Ligands for Transition Metal Catalysis

by

Sima Yazdani

Doctor of Philosophy in Chemistry

University of California San Diego, 2021

San Diego State University, 2021

Professor Grotjahn, Douglas B.. Chair

This dissertation includes exploring two scientific challenges, where both water oxidation catalysis and NH addition to alkynes will benefit greatly from the rational design of ligands. **Chapter 1:** The long-term goal for scientists is to use sunlight for the energy to split water. The main target of our research is the oxidation half reaction. Water oxidation catalysts have been reported by groups of Sun and Llobet^{1,2,3} but sustainable catalysis is still impaired by catalyst deactivation.⁴ This dissertation attempts to design robust catalysts through manipulating of the apical coordination sites. **Chapter 2** uses phosphorus in the primary coordination sphere to create stronger axial ligand-ruthenium bonds;⁵ **Chapter 3** uses a chelating macrocyclic ligand to reduce the chance of ligand loss. **Chapter 4**⁶, focuses on the hydroamination of C-C multiple bonds as the most atom-efficient method for the introducing of nitrogen atoms into organic molecules.

Chapter 1

The important role of molecular water oxidation catalysis in the future of renewable energy

1.1. Global warming

The broadly accepted definition of global warming among the scientific community is the long-term heating of Earth's climate system which has been observed since the pre-industrial period due to human activities, primarily fossil fuel burning. Besides that, we are aware of the public experience of local temperature increases, worldwide. Some of the evidence of global warming which can be perceived in our daily life is higher average temperatures, sea-level rise, and extreme weather patterns. In fact, based on research, personal experiences are the strong initial force for raising concern about global warming.⁷ Here, we will mention a few of the most important indications and causes of global warming.

Changes in temperature on surface of the earth: Based on borehole temperature-depth profiles, measurements of the national research council (2006), during the 20th century the temperature globally increased ~ 0.6 °C. Furthermore, they estimated that during the 21st century the temperature of our planet will increase roughly 2-6 °C. The evidence for this proposed increase comes from the paleoclimatology, broad geographic sedimentology studies, and instrumental records in ice cores, marine sediments, boreholes, and glaciers.⁸ More detailed studies based on data from the Advanced Very High Resolution Radiometer satellites have shown that land surface temperatures increased globally at the rate of $\sim 0.43 \pm 0.2$ °C / decade.⁹

Changes in atmospheric CO₂: The combustion of large quantities of fossil fuels has been causing a steady increase in the average global atmospheric CO₂ concentration from the pre-industrial revolution level of 280 ppm to 409.8 ± 1 ppm in 2019, a 146 % increase. Also, the projections show that shifting away from fossil fuel use will result in the rapid decrease in average global CO₂ levels by around 75%-85% by 2050.¹⁰

It is worth to noting that the 2020 COVID-19 pandemic forced restrictions in transportation due to stay-in-place orders, and caused a decrease of -17% in daily global CO₂ emissions by April 2020 in comparison with the mean for 2019. Prior to the pandemic, emission of CO₂ increased by 1% per year.¹¹ The data highlights the importance of governments' actions for facing the global warming challenge and will likely influence the global CO₂ emission path for decades.

Changes in ocean water level and acidification: The consequences of the increasing of CO₂ and methane concentrations in atmosphere are: enhancing global temperature, warming of the ocean, sea-level rise because of melting of ice sheets, in addition to dissolution of CO₂ in seawater resulting a decline in pH and increased acidification of the ocean.¹² Since pre-industrial levels, the water in the surface of the ocean has acidified ~ 0.1 pH units and is projected to decrease by another 0.3-0.4 pH units by the end of the 21st century.¹³

Based on the above-mentioned facts, it is vital that renewable and clean energies become the leading sources of energy.¹⁴ These projections inspired researchers to seek renewable sources of energy, with solar energy likely being a long-term solution.¹⁵

1.2. Sources of Energy

The majority of the energy used globally in 2018 was provided by oil (34%), followed closely by coal (27%), and natural gas (24%), making fossil fuels the greatest source of energy.^{16,17} The renewables energy share reached 4% in 2018.¹⁶ According to the Organization of the Petroleum Exporting Countries (OPEC), the world's proven oil reserves in 2018 were estimated to be 1,497.98 billion barrels.¹⁸

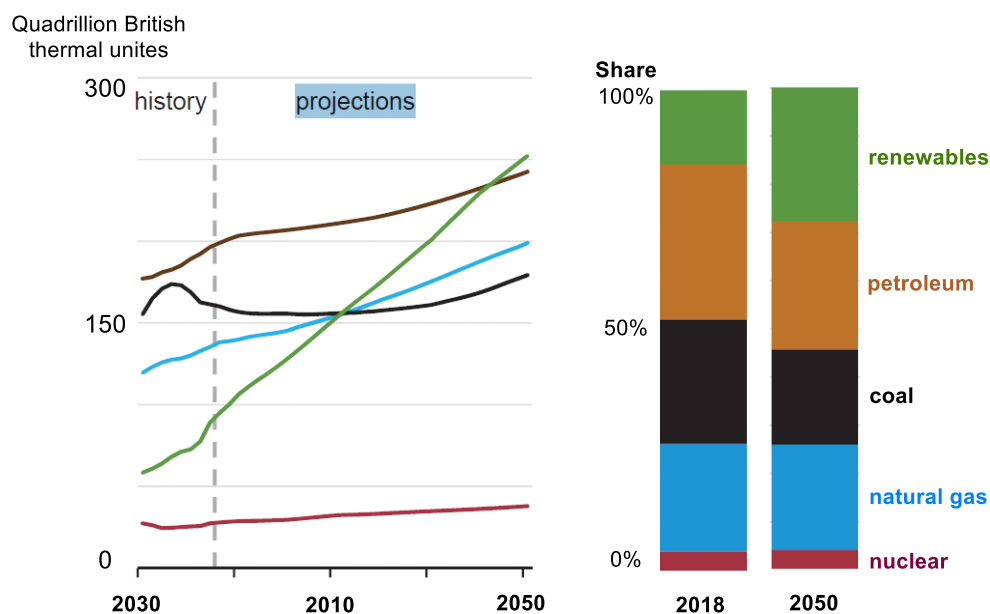


Figure 1.1. Global primary energy consumption by energy source.¹⁹

The data compiled by OPEC¹⁸ suggest that in 2018, global demand and production for oil and gas were increased compared to the previous years; oil consumption grew by 1.5% in 2018.¹⁶

Therefore, it is not surprising that the British Petroleum’s (BP) economic team reported that the rate of carbon emissions in 2018 was faster than projected by Paris climate goals.¹⁶ In the BP statistical review of world energy, it is reported that carbon emissions show 2.0% growth for seven years.

However, because of all these data, the goal of scientists is to reduce emissions of CO₂, hence renewable energy is the world’s fastest growing form of energy, and it is projected that renewable energy becomes the leading source of energy consumption by 2050 (Figure 1.1).¹⁹ The United States Energy Information Administration (EIA) projects that the global energy consumption will rise nearly 50% by 2050.¹⁰

What we know for sure, one day we will run out of oil, and we must leave the oil before oil leaves us.

1.3. Renewable energy

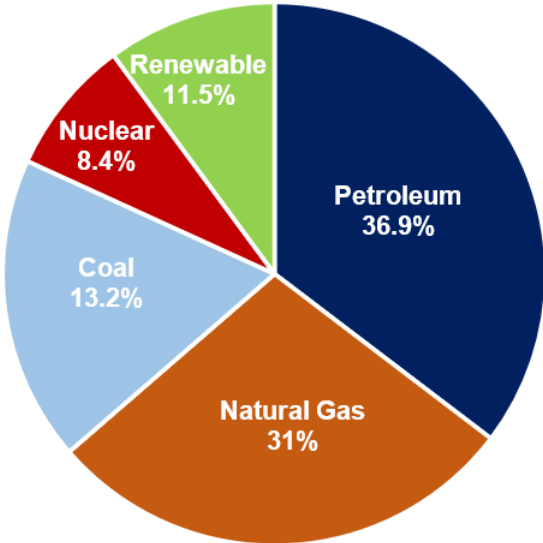
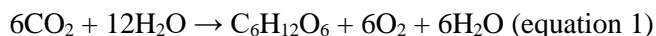


Figure 1.2. U.S. primary energy consumption by source and sector in 2019.²⁰

Production and storage of the renewable energy is one of the crucial scientific challenges in present century.²¹ The renewable energy consumption in the U.S. amplified for the fourth consecutive year in 2019, reaching 11% of total U.S. energy consumption (Figure 1.2). Although solar energy accounted for ~ 9% of total U.S renewable energy consumption in 2019, it had the largest growth rate among other renewable sources in 2019.²⁰ Using the Sun, the most powerful source of the energy, plus water assures an unlimited supply of sustainable energy.²¹ Therefore, researchers are inspired by natural photosynthesis, which utilizes the sunlight to oxidize water to O₂ in plants.²²

1.4. Water splitting and water oxidation

A long-term goal for scientists is to use solar energy to split water, and produce H₂ as fuel and O₂. In nature, the Sun's energy collected by plants being used to reduce CO₂ to carbohydrates (C₆H₁₂O₆) during the process of photosynthesis (equation 1).²¹



The chlorophylls (P₆₈₀) in leaves of plants, are excited by absorbing the solar energy and transfer electrons to the acceptors, as a result of this transformation during this step the CO₂ will be reduced. The P₆₈₀^{•+} (oxidation potential = +1.2 V vs. the normal hydrogen electrode (NHE))^{21,23} accepts the electrons from a cluster of Mn₄CaO₅ in oxygen-evolving complex or OEC (Figure 1.3). This process happens in four consecutive steps and removal of four electrons from OEC which ultimately oxidize two water molecules and generate O₂ and four protons. Natural photosynthesis is the topic of multidisciplinary research between biologists and chemists and is an inspiration for artificial photosynthesis and future development of liquid solar cells.²¹

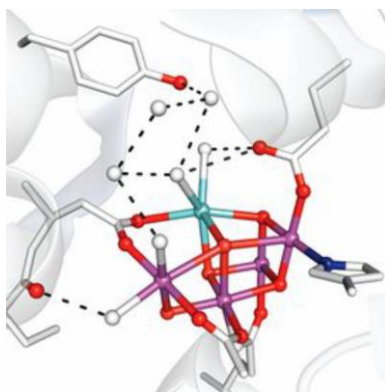
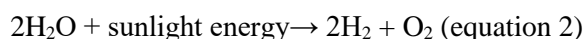
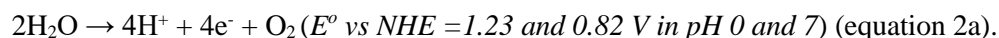


Figure 1.3. X-ray structure of the oxygen evolving complex, Mn_4CaO_5 .

In artificial photosynthesis cells, the sunlight collected by the cell is utilized to split the water according to the general equation below (2):



This overall reaction contains two, half reactions, oxidation (equation 2a) and reduction (equation 2b):



(Note: During water splitting via electrolysis, at the cathode, reduction of the H^+ to H_2 is reversible, therefore potential of equilibrium accounted 0.0 V).

Water oxidation is the more challenging of the two half reactions, yet is important as the source of electrons and protons postulated for storing solar energy in the form of chemical bonds;²⁴ eventually this half reaction will revolutionize the renewable energy field. Using the Sun's energy for artificial photosynthesis is very promising as a source of carbon-free energy. However, to achieve artificial photosynthesis, synthetic chemists need to find robust and efficient catalysts.

1.5. Artificial photosynthesis for solar liquid cells

In general equation 2, the products of the reaction ($2\text{H}_2 + \text{O}_2$) have a higher free energy (286 kJ/mol) and therefore thermodynamically are unfavored,²⁵ but sunlight will be the source of the energy required to overcome the unfavorable thermodynamics.

A scheme of photo-electrochemical cell for water splitting is demonstrated in Figure 1.4. At the anode, the water is oxidized to produce the oxygen, electrons and protons. Protons transmit to the cathode and electrons transfer through an external circuit and merge with the protons in the cathode. Reduction happens at the cathode ($4\text{H}^+ + 4\text{e}^- \rightarrow 2\text{H}_2$) resulting in H_2 gas.

The whole process requires 1.23 V of potential, plus activation energy, or in electrocatalytic terms, overpotential η to overcome the thermodynamic barrier. Therefore, the roles of an electrocatalyst to reduce overpotential at the same time enhancing the rate of the water splitting reaction.²⁵ The best heterogeneous electrocatalysts are made of precious metals for instance the platinum at the cathode as a counter electrode and IrO_2 or RuO_2 as working electrode (anode). In case of homogenous catalysis, the best catalysts are the molecular transition metal catalysts which will be discussed in the next section and specifically with regard to the water oxidation which is the focus of this dissertation.

The ultimate goal is to deposit the molecular water oxidation catalysts on the surface of the cathode, as shown in Figure 1.4.

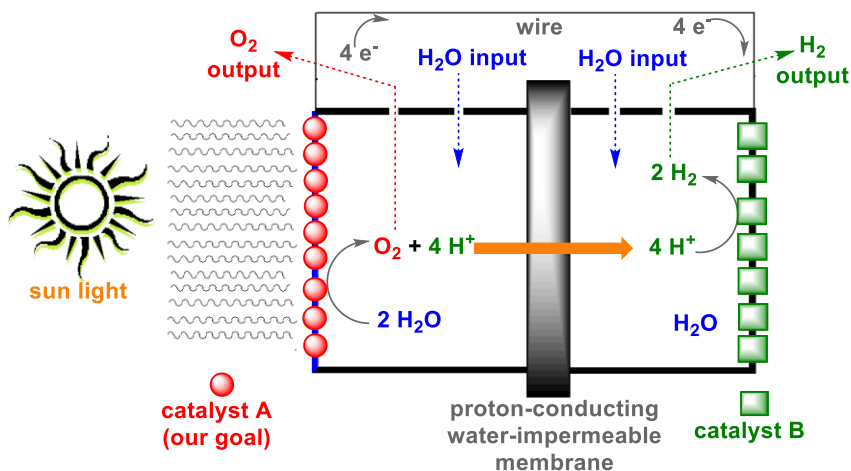


Figure 1.4. A photo-electrochemical cell.²⁶

1.6. History of molecular water oxidation catalysts (molecular WOC)

Over the past few decades, a number of both homogeneous and heterogeneous water oxidation catalysts (WOCs) have been reported.³ Molecular water oxidation catalysts (WOCs) contain organic ligands and transition metals (Ru, Ir, Cu, Co, and Ni) and have been investigated for chemical and

electrochemical water oxidation, showing reasonable to excellent reaction rates.³ Even earth-abundant first-row transition metals like Fe,²⁷ Cu,²⁸ Ni,²⁹ Mn,³⁰ and Co³¹ have been described to give viable MWOCs, attractive because of the higher abundance in the nature and lower cost and toxicity.^{10,32} However, low activity/stability and higher overpotential are still obstacles to using first-row transition metals in WOC.

On the other hand, many efforts have been made to minimize the amount of noble metals in catalysis by development of homogeneous catalysts where the metal center is surrounded by organic ligands.^{33,34} Our group decided to focus on homogeneous water oxidation catalysts, because organic ligands offer the chance to finely tune reactivity. Our target catalysts contain organic ligands which are designed to bind to a metal center and also capable of transferring protons, because four protons are lost per mole of oxygen formed. One important reason for using molecular WOC over the precious metal oxides is the lesser cost of the former. Also, it is much easier to study the mechanism and understanding of the process of water oxidation by using molecular catalysts. The characterization of the active species during WOC cycle is important for development of large scale production of solar fuels.

There are a variety of WOCs with different electronic and steric properties of the ligands.³⁵ However, the current challenge for WOCs regardless of the metal used is striking the balance between stability and reactivity. One way to measure stability of water oxidation catalyst is determining the number of turnovers (TON) by using sacrificial oxidants for instance ceric ammonium nitrate, or with persulfate ion and photosensitizers, such as Ru(bipy)₃²⁺.

The first molecular WOC, reported by Meyer in 1982, is called the ‘Blue dimer’, and is a binuclear ruthenium complex containing bipyridine ligands, [(bpy)₂(H₂O)Ru^{III}ORu^{III}(H₂O)(bpy)₂]⁴⁺ (compound **1.1**, Figure 1.4).³⁶ Since then, a vast majority of WOCs have contained rare metals for instance, ruthenium and iridium^{37,38,39,40,41,42} especially ruthenium and polypyridine ligands.⁴³ For a few years scientists tried to focus on the multimetallic catalysts and relied on multimetallic nature of the catalysts to oxidize the water (compounds **1.1-1.3**, Figure 1.4). Researchers believed that a mono-metallic catalyst would be insufficient to oxidize the water and transfer multiple electrons and protons.^{44,45} It was not until two decades later that Thummel’s group in 2005 reported mononuclear ruthenium complexes as WOC (compound **1.4**, Figure

1.5).⁴⁶ Thummel envisaged that electrophilicity of the Ru^{IV} or Ru^V is enough to facilitate the coordination of a water molecule to the metal center and forming the Ru^{IV} or Ru^V oxo intermediates after oxidation.

The investigation of monometallic catalysts continued until Sun's group synthesized a mononuclear ruthenium catalyst, bearing 2,2'-bipyridine-6,6'-dicarboxylato (bda) occupying four equatorial positions and two picoline as axial ligands ([Ru^{II}(bda)(pic)₂]) **1.5**.⁴⁷ This tetradentate ligand catalyst shows good catalyst activity up to turnover frequency (TOF) = 32 s⁻¹. In this report they identified active species during water oxidation catalysis and characterized the intermediates with crystal structure of a seven-coordinate Ru^{IV} hydroxo.⁴⁷

Later, Sun's group presented some evidence for catalyst degradation by oxidation of picoline methyl groups. Therefore, they changed the axial ligand to isoquinoline **1.6**.¹ As a result of the π -stacking interaction between the isoquinolines and ready formation of the O-O bond, catalytic activity improved to TOF of 303 s⁻¹. Another advance came in 2015 with bifunctional catalyst [Ru(tda- κ -N³O)(py)₂] (tda = [2,2':6',2''-terpyridine]-6,6''-dicarboxylato) **1.7** that was presented by Llobet's group.² The tda ligand is a hemilabile ligand by means of the carboxylate group dissociating, and at the Ru^{IV} state, the pendent anionic carboxylate is proposed to help a water molecule attack the oxygen atom of a metal oxo. The water oxidation catalytic activity of complex **1.7** by electrochemical methods at pH 7 reached to a high TOF of 8000 s⁻¹.

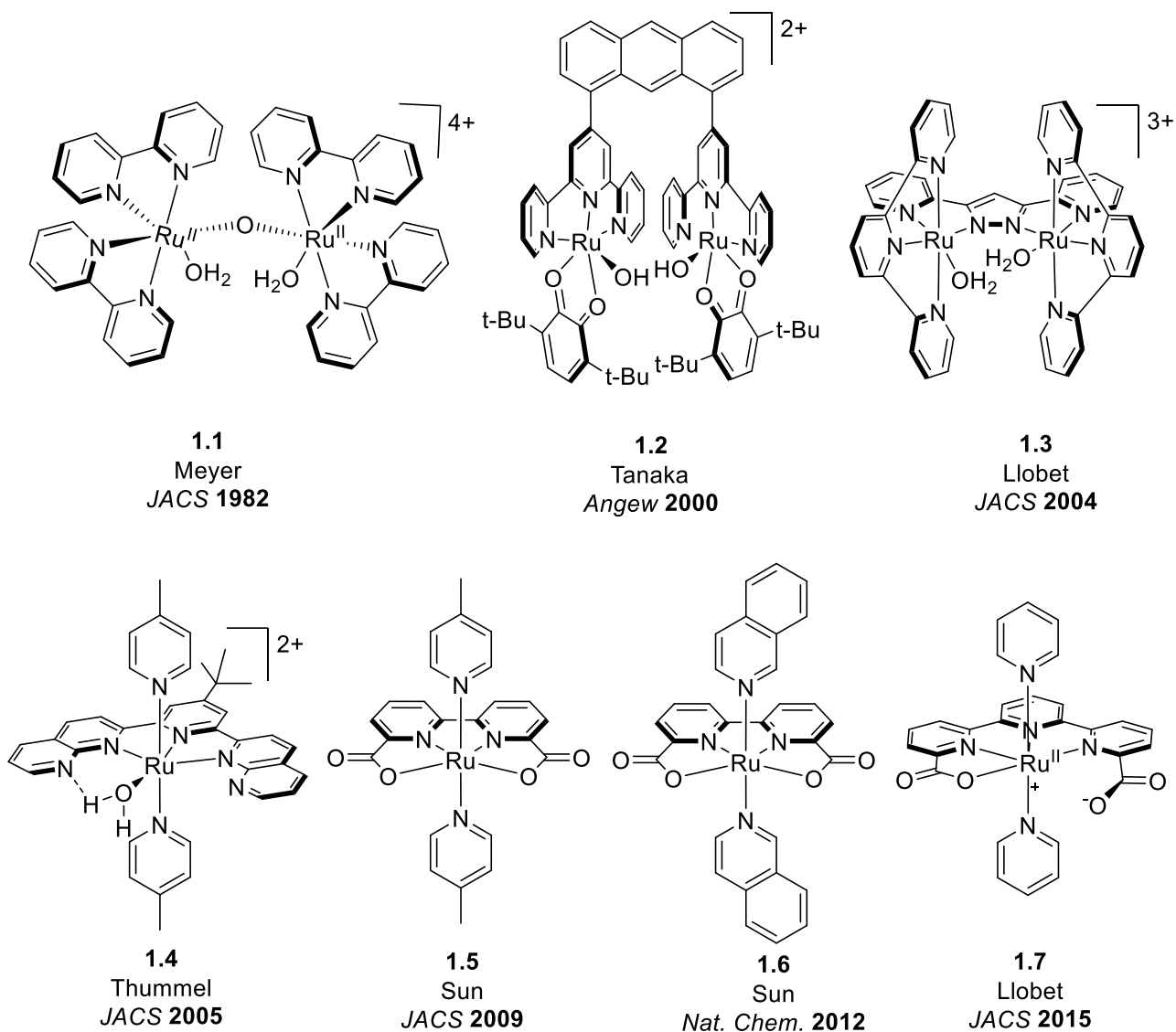


Figure 1.5. Molecular WOC development through the years.

1.7. Novelty in ruthenium water oxidation catalysis

In recent years, electrocatalytic water oxidation has appeared as a reasonable solution ultimately to produce hydrogen as a fuel, along with oxygen byproduct. In this vein, the development of novel catalysts that drive the oxidation of the water at lower overpotential is essential to the future of the artificial photosynthesis devices. To achieve faster reaction kinetics at the anode demands a lower overpotential to speed up the oxidation reaction. Therefore, the overpotential at which catalysis takes place is an important

factor for designing a molecular WOC. In addition to that, other factors are important, for instance: turnover frequency at which the catalytic cycle completes (TOF in mol O₂ mol cat.⁻¹ s⁻¹),⁴⁸ and turnover number (TON), whether the catalytically active species accommodates the oxidation of H₂O, and the robustness of the catalysts are aspects that chemist need to keep in my mind when design novel catalysts for WOC.

Despite prior accomplishments, sustainable catalysis is still impaired by catalyst deactivation in part due to harshly oxidizing reaction conditions. Sun's group detected (but did not quantify) free axial ligand by mass spectrometry in the reaction of **1.5** with Ce^{IV}, suggesting that axial ligand loss could be part of catalyst degradation.⁴

Therefore, in this dissertation one goal is to design more robust catalysts through manipulation of the apical coordination sites. Although most WOC research focuses on making faster catalysts, in our research, the first major objective is to slow the rate of catalyst degradation and synthesize a robust catalyst, using the following strategies: **Chapter 2** uses phosphorus atoms in the primary coordination sphere to create stronger axial ligand-ruthenium bonds; **Chapter 3** uses a chelating macrocyclic ligand to reduce the chance of ligand loss.

In both projects our strategy was to begin our investigations by well-known WOC ruthenium polypyridine catalysts for example Sun's Ru(bda) **1.5**, **1.6** and Llobet's Ru(tda) **1.7** and build our knowledge and modify our strategy based on the results we obtained.

Chapter 2

Coordination of tertiary phosphine axial ligands to ruthenium bda (2,2'-bipyridine-6,6'-dicarboxylato) and tda ([2,2':6',2''-terpyridine]-6,6''-dicarboxylato) scaffolds

2.1. X-ray crystallography and electrochemistry reveal electronic and steric effects of phosphine and phosphite ligands in complexes $\text{Ru}^{\text{II}}(\kappa^4\text{-bda})(\text{PR}_3)_2$ and $\text{Ru}^{\text{II}}(\kappa^3\text{-bda})(\text{PR}_3)_3$ ⁵

Tertiary alkyl and aryl phosphines and phosphites are generally employed as ancillary ligands for transition metal complexes because of their ability to stabilize low valent metal centers, as well as the amenability of their precursor compounds towards functionalization and fine-tuning of the stereoelectronic features of their transition metal complexes.^{49,50,51,52,53,54,55,56,57,58} As discussed in chapter 1, ruthenium complexes containing an anionic tetradentate bda and two axial ligands have been shown to be especially potent for WOC. The chelating nature of the bda ligand along the equatorial plane results in a distorted octahedral geometry in its d^6 metal complexes, with the remaining two coordination sites situated in a diaxial configuration.^{59,60,61} Therefore, the first strategy for modification of Ru-polypyridine family is substitution of the diaxial ligands L in $\text{Ru}(\text{bda})(\text{L})_2$. Due to outstanding catalytic properties of $\text{Ru}(\text{bda})$, a variety of these complexes containing diaxial ligands with N, S, and C atoms in first coordination sphere were reported.^{59,60,61} To our knowledge, examples of $\text{Ru}(\text{bda})(\text{L})_2$ where $\text{L} = \text{PR}_3$ have yet to be explored in the literature. In chapter 2, section 2, we describe the synthesis and characterization of five $[\text{Ru}^{\text{II}}(\text{bda})\text{PR}_3]$ complexes bearing phosphine/phosphite diaxial ligands ($\text{PR}_3 =$ triphenylphosphine **2.1**, triethylphosphine **2.2**, triisopropyl phosphite **2.3**, trimethyl phosphite **2.4**, and 1,3,5-triaza-7-phosphaadamantane (PTA) **2.5**) (Fig. **2.1**). In addition, the electronic and steric effects of phosphorus ligands on the backbone bda ligand was investigated.

One interesting feature of the work is that in case of the PTA^{51,52,53,54,55,56,57,58} **2.5** and trimethyl phosphite **2.4**, three ligands are coordinated to the metal center in axial and equatorial positions, and on the bda ligand one of the carboxylate groups is not bonded to the metal center, whereas other complexes formed with two PR_3 axial ligands and tetradentate bda ligand.

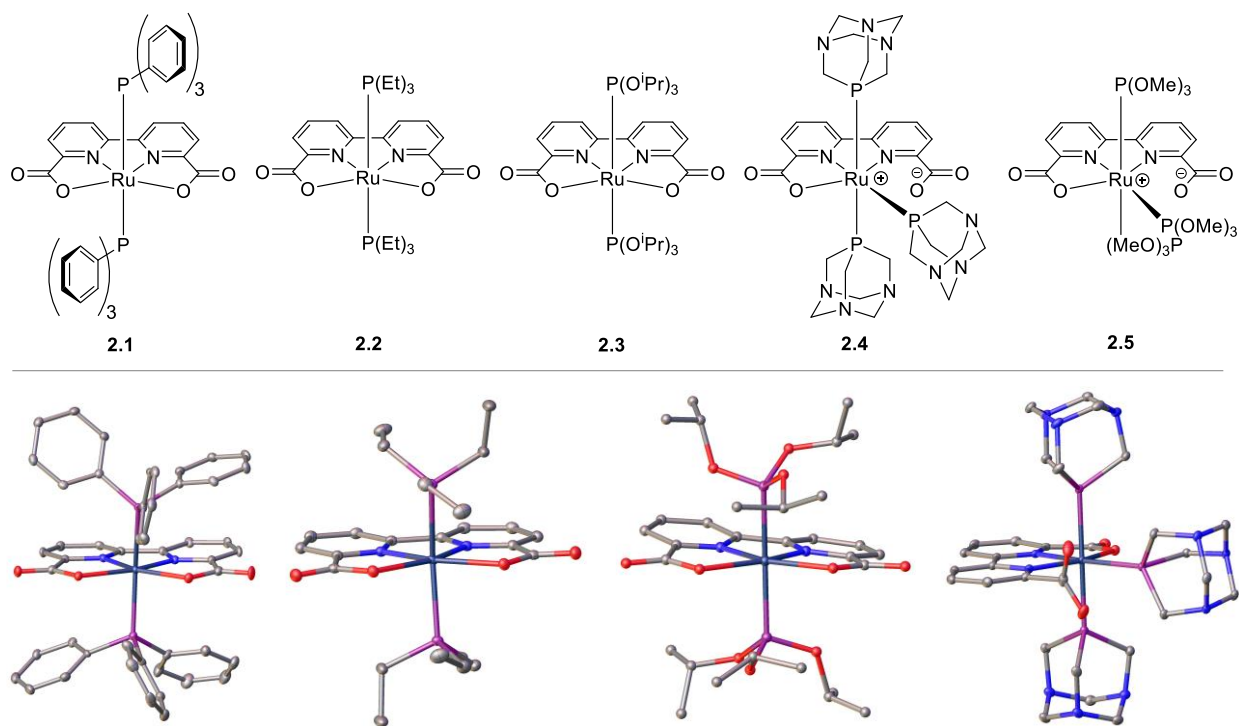


Figure 2.1. Complexes **2.1** to **2.5** and X-ray crystal structure of complexes **2.1** to **2.4**.

Table 2.1. ^1H and ^{31}P NMR spectra of compounds **2.1-2.4** in CD_3OD .^a

	^1H		^{31}P
	bda	PR_3	
2.1	8.29 (dd, $J = 8.0, 1.1, 2\text{H}$), 7.64 (t, $J = 7.8, 2\text{H}$) ^b	7.40 – 7.30 (m, 6H), 7.26 – 7.13 (m, 14H), 7.14 – 7.05 (m, 12H) ^b	30.8 (s) ^c
2.2	8.43 (dd, $J = 8.0, 1.1, 2\text{H}$), 8.15 (dd, $J = 7.7, 1.2, 2\text{H}$), 7.95 (t, $J = 7.9, 2\text{H}$)	1.27 (qt, $J = 7.5, 2.9, 12\text{H}$), 0.66 (p, $J = 7.6, 18\text{H}$)	16.4 (s)
2.3 ^d	8.38 (dd, $J = 8.0, 1.1, 2\text{H}$), 8.08 (dd, $J = 7.8, 1.1, 2\text{H}$), 8.00 (t, $J = 7.8, 2\text{H}$)	4.62 – 4.56 (m, 6H) 1.01 (d, 36H)	116.5 (s)
2.4 ^e	8.80 (d, $J = 8.2, 1\text{H}$) 8.51 (d, $J = 8.6, 1\text{H}$) 8.46 (d, $J = 8.0, 1\text{H}$) 8.30 (d, $J = 7.6, 1\text{H}$) 8.14 (t, $J = 7.8, 1\text{H}$) 7.55 (d, $J = 7.9, 1\text{H}$)	4.85, 4.67 (two d, $J = 13.1$, total 6H) 4.57 (s, 6H), 4.42, 4.32 (two d, $J = 13.1$, total 12H), 3.73, 3.60 (two d, $J = 15.3$, total 12H)	-51.6 (t) and - 55.1 (d) ($^2J_{\text{PPcis}} = 38.7$)

(a) Chemical shifts δ in ppm, coupling constants J in Hz. (b) One 2H signal for bda included under signals for PPh_3 ligands. (c) in $\text{DMSO}-d_6$. (d) in $\text{CD}_3\text{OD}-d_4$. (e) in CDCl_3 .

Comprehensive theoretical studies on diverse phosphorus ligands have been done by Suresh and co-workers^{62,63} and Bravo and co-workers,⁵⁹ to estimate the stereoelectronic properties of a variety of phosphine ligands. The two methods allow the separation of the steric effects of a PR₃ ligand from its electronic effects and allow one to select the proper ligands in the design of a catalyst system in organometallic chemistry.^{51-58,62}

The electronic and steric properties of the substituted phosphorus ligands were quantified by three parameters; 1) Molecular electrostatic potential minimum (V_{\min}), explaining electronic effects of phosphines described by Suresh and Koga;^{62,64} 2) Tolman's electronic parameter (TEP), illustrating electron-donating ability of phosphorus ligands, and is defined as the frequency of the A₁ carbonyl mode of (R₃P)Ni(CO)₃ complexes;^{49,50} 3) Cone angle (θ), introduced by Tolman to quantify the steric effects of phosphines based on the Corey-Pauling-Koltun model of ligand-metal complexes. The Tolman cone angle is very useful because the steric profile of the phosphine can impart a significant degree of control over the outcome of transition-metal-mediated reactions.^{49,50}

Therefore, in section 2.1 attempts were made by exploring various phosphine and phosphite ligands to quantify the electronic and steric effect of the ligands on Ru complexes (Fig. 2.1).

The section 2.1 of this chapter has contents that are similar to the paper that we published in *Polyhedron*: Yazdani, S.; Silva, B. E.; Cao, T. C.; Rheingold, A. L.; Grotjahn, D. B. X-Ray Crystallography and Electrochemistry Reveal Electronic and Steric Effects of Phosphine and Phosphite Ligands in Complexes Ru^{II}(κ^4 -bda)(PR₃)₂ and Ru^{II}(κ^3 -bda)(PR₃)₃ (bda = 2,2'-bipyridine-6,6'-dicarboxylato). *Polyhedron* **2019**, *161*, 63–70.⁵

2.1.1. Synthesis, isolation, and characterization of the complexes

Synthesis and isolation. Metalation of 2,2'-bipyridine-6,6'-dicarboxylic acid to synthesize complexes **2.1** to **2.5** happened at room temperature (Figure 2.2). Recrystallization was the major purification method and we achieved high yields, up to 92%. The reactions are very fast, in some cases finished in 0.5 h (complex **2.4**), however, we tried to further speed up the reaction with heating at 70 °C.

By heating, a lot of side products were obtained, possibly because in case of the PTA, the ligands suffered methanolysis and we were not able to further purify the reaction mixture.

One interesting trend observed is that the phosphorus ligands with smaller cone angle were prone to form trisubstituted complexes $\text{Ru}(\text{bda})(\text{PR}_3)_3$ (complexes **2.4** and **2.5**) while the ligands with bigger cone angles created disubstituted $\text{Ru}(\text{bda})(\text{PR}_3)_2$ species even though excess amounts of ligand were present in the reaction (complexes **2.1-2.3**). The cone angles for PPh_3 , PEt_3 , $\text{P}(\text{OiPr})_3$, and PTA are 145° , 132° , 128° , and 103° , respectively.^{57,65}

Below is presented the stepwise synthetic procedure for making $\text{Ru}(\text{bda})(\text{PR}_3)_2$ (Figure 2.2).

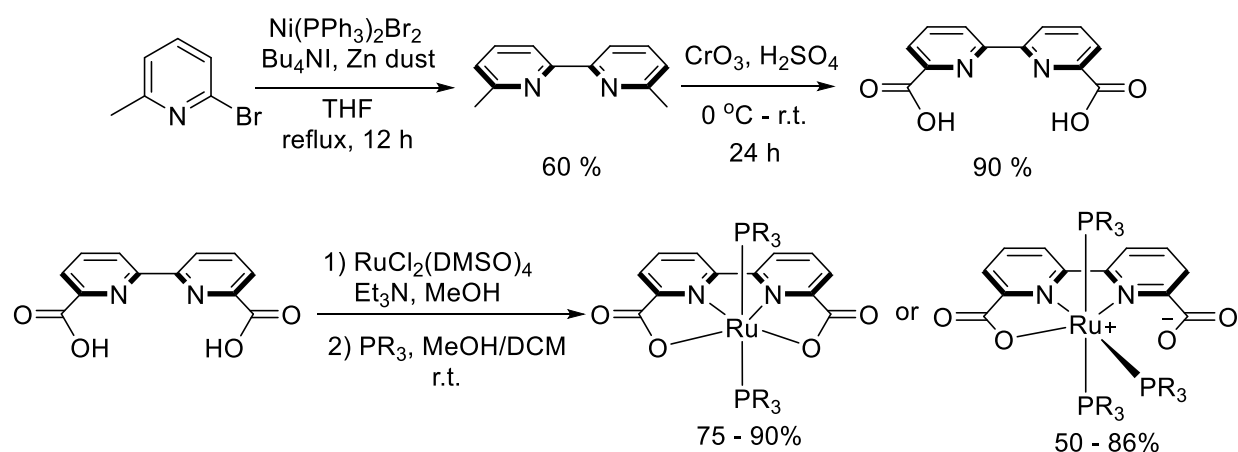


Figure 2.2. General synthetic procedure for making $\text{Ru}(\text{bda})(\text{PR}_3)_2$ and $\text{Ru}(\text{bda})(\text{PR}_3)_3$.

NMR and X-ray characterization

All compounds (**2.1-2.5**) were fully characterized by ^1H NMR and ^{31}P NMR spectroscopy (Varian 500 MHz Inova or 400 MHz VNMRS NMR spectrometers) and X-ray crystallography. The structures are presented in Figure **2.1** and all NMR characterization are in Table 2.1.

The ^1H NMR spectra of the Ru complexes show three signals, consistent with a symmetric bda and a single sharp signal for ^{31}P NMR spectra which is consistent with C_{2v} symmetry of **2.1-2.3**. In contrast, $\text{Ru}^{\text{II}}(\text{bda})(\text{PR}_3)_3$ complexes **2.4** and **2.5** demonstrate broader ^1H peaks related to bda (possibly because the

protic solvent CD₃OD interacts with the negative charge on the dangling CO₂⁻ moiety) and a doublet and triplet in ³¹P NMR spectra, consistent with one unique P coupled to two other, equivalent phosphines.

Table 2.2. Bond lengths [Å] and angles [°] obtained by X-ray crystallography.

	Complex	2.1	2.2	2.3	2.4^a	2.4^b
Bond lengths [Å]	Ru-O	2.191(3)	2.194(16)	2.208(4)	2.139(15)	-
		2.223(3)	2.194(16)	2.217(6)	-	-
	Ru-N	1.946(4)	1.944(19)	1.986(12)	2.1402(18)	-
		1.954(4)	1.944(19)	1.987(2)	2.0187(17)	-
	Ru-P	2.371(12)	2.372(6)	2.353(4)	2.349(6)	2.322(6)
		2.376(12)	2.372(6)	2.384(4)	2.334(6)	-
Angles [°]	O-Ru-O	124.58(11)	124.05(8)	125.28(15)	-	-
	P-Ru-P	167.16(4)	163.92(3)	164.55(12)	175.98(2)	90.51(2), 91.82(2)
	N-Ru-N	81.22(15)	81.40(11)	80.21(4)	77.01(3)	-
	O-Ru-P	86.03(8)	85.14(5)	86.06(4)	86.92(5)	92.56(4)
		89.31(8)	87.34(4)	89.18(5)	89.70(5)	-
	O-Ru-N	77.59(13)	77.28(7)	77.22(11)	156.35(6)	-
		157.83(14)	158.67(7)	157.48(5)	-	-

a = axial ligands; b = equatorial ligand.

Complexes were isolated by crystallization through vapor diffusion of chloroform into methanolic solutions (Figure 2.1). X-ray crystal structures were obtained with Bruker single-crystal diffractometers with CCD detectors and low-temperature cryostats with hi-flux Cu and Mo radiation sources. Crystallographic information is presented in Table 2.2. For the X-ray structures presented in Figure 2.1, complexes **2.1-2.3** have orthorhombic crystal system and Pbcn and Pbca space group. Complex **2.4** is monoclinic and has C 2/c space group.

Compounds **2.1** to **2.4** have different bond lengths and angles. In case of the **2.4**, the O-Ru-P angle (86.92 and 89.70°) is bigger than that of the compounds **2.1** to **2.3** and the O-Ru-N (156°) angle is smaller compared to the compounds **2.1** to **2.3**. Also, the Ru-N bonds are longer and Ru-P bond lengths are a bit shorter (2.349, 2.334, 2.322 Å) compared to those of the other complexes. Therefore, the P atom in **2.4** is closer to the Ru, and the N atoms of the backbone ligand are further from the metal center.

X-ray structural data clearly show that the O-Ru-P coordination site is more open, suggesting that Ru could be readily accessible for coordination of another PTA ligand in the equatorial position. This observation can explain why Ru (bda)(PTA)₃ formed and why we could not isolate the analogous complex with two PR₃ ligands.

The differences in geometry and coordination of the Ru bda complexes can be explained by the V_{min} and TEP parameters. The V_{min} for phosphine compounds PPh₃, PEt₃, and PTA are -34.07, -43.55, -33.69 kcal/mol, respectively. The more negative values of V_{min} are related to the electron-donating character and bulkiness of R groups which can shift the P character of the sp³-hybridized lone-pair orbital of the phosphorus atom.⁶²⁻⁶³ Furthermore, the P-R connection is via a single bond so the electronic effect is mainly inductive in nature. The presence of nitrogen in the PTA ligand in **2.4** creates a less-negative V_{min} (-33.69 Kcal/mol);⁶² in addition to having a small θ, both parameters document the steric interactions and an increase in π-back-bonding between Ru and the equatorial PTA ligand which ultimately are responsible for three phosphines ligands coordinated in the Ru(bda)(PR₃)₃ complex.

However because we did not see clear electronic effect based on TPE data (TEP for PEt₃ = 2061.7, PPh₃ = 2068.9, PTA = 2069, P(OⁱPr)₃ = 2075.9, and P(OMe)₃ = 2079.5 cm⁻¹)⁴⁹⁻⁵⁸ therefore, we conclude that steric effects govern whether bis- or tris(PR₃) complexes form.

2.1.2. Electrochemistry

Cyclic voltammetry (CV) measurements were carried out on CH instruments CHI760E and CHI600C potentiostats, with glassy carbon working electrode (3 mm diameter), and Pt counter-electrode, with Ag⁺/AgCl reference electrode.

We studied the redox properties of **2.1-2.4** by performing cyclic voltammetry (CV) in aqueous potassium phosphate solution (0.1 M, ionic strength I = 0.1 and pH 7) (Figures 2.3 and 2.4). Comparison of the CVs for different complexes shows an increase in the potential Ru^{II/III} redox wave as PEt₃ < PPh₃ < P(OⁱPr)₂ < PTA from 0.25 V to 0.95 V (Table 2.3).

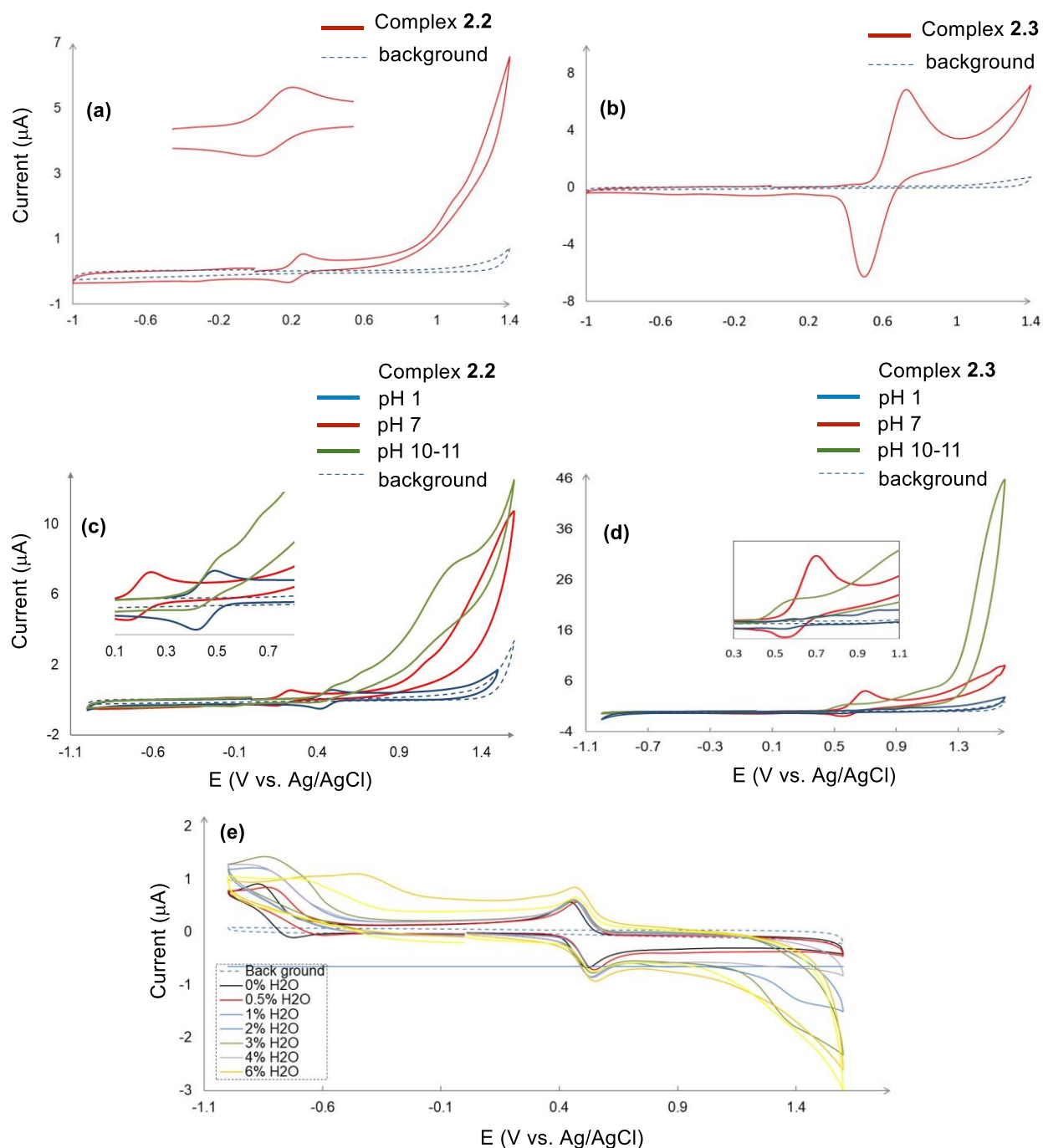


Figure 2.3. **(a,b)** Cyclic voltammograms of complexes **2.2** **(a)** and **2.3** **(b)** vs background (in blue) in 0.1 M potassium phosphate buffer/CF₃CH₂OH (4:1) solution (pH 7.0). CV of compound **2.2** shows $\Delta E_p = 0.0857$ V, forward current = $5.25e-6$ A and reverse current = $-3.48e-6$ A. Compound **2.3** shows $\Delta E_p = 0.351$ V, forward current = $6.88e-5$ A and reverse current = $-6.02e-5$ A. **(c,d)** Comparison of CVs in presence of compounds **2.2** **(c)** and **2.3** **(d)**; in mixed potassium phosphate/CF₃CH₂OH solution showing two reversible waves of Ru^{III/II} and Ru^{IV/III} redox couples. **(e)** CVs of 1 mM of **2.1** in 0.1 M nBu₄NPF₆/propylene carbonate (PC) by addition of increasing amounts of water, as illustrated in legend of the figure. The dashed line shows the background in the absence of **2.1**.

Because we did not observe a peak related to the electrocatalytic production O_2 in CV at pH 7, therefore, we performed CV at different pH from acidic to basic to see if any changes were observed in the redox behavior of these compounds. To solve the solubility problem of the complexes in acidic and basic phosphate buffer, therefore, we performed CV in mixtures of potassium phosphate buffer/ CF_3CH_2OH with three different pH values. Although we observed pH dependency for complexes **2.2** and **2.3**, the peak related to the reduction of the O_2 was not observed (Figure 2.3b).

The other observation is that at acidic and basic pH, two redox waves are observed which may be assigned to $Ru^{II/III}$ and $Ru^{III/IV}$ (Figure 2.3b).

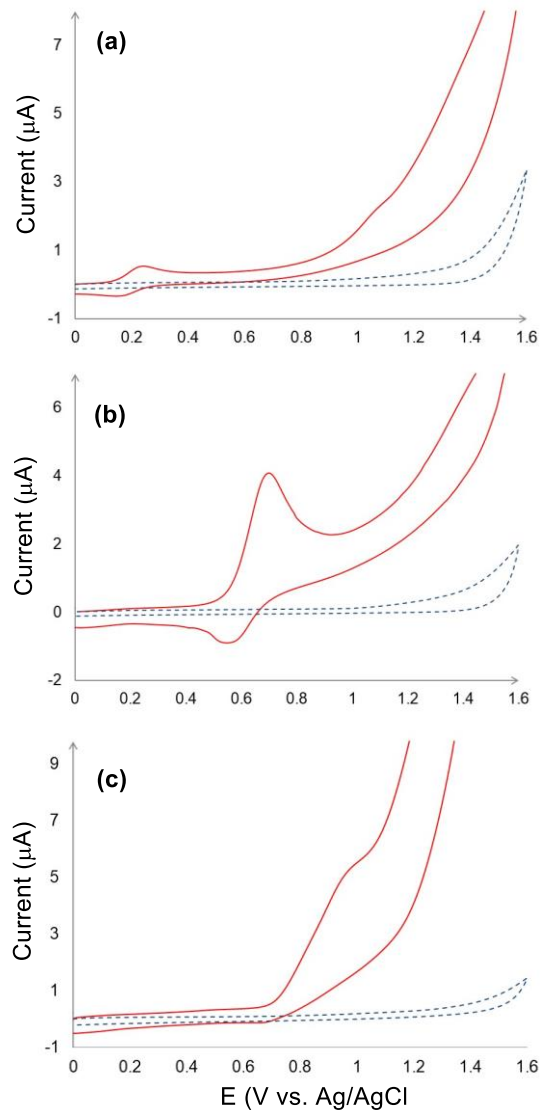


Figure 2.4. Cyclic voltammograms of complexes **2.2**, **2.3**, and **2.4** (red trace) versus background (in blue) in 0.1 M potassium phosphate buffer / $\text{CF}_3\text{CH}_2\text{OH}$ (4:1) solution ($\text{pH} = 7.0$). For preparing 500 mL of buffer ($\text{pH} = 7$), 1.36 g of KH_2PO_4 added to a 500 mL volumetric flask. Then 2.32 g of K_2HPO_4 was added to the flask. Then 500 mL deionized water added to the flask and it was shaken to dissolve solids completely.

Table 2.3. Electrochemical features of **2.1-2.4** (0.5 mM) in 0.1 potassium phosphate buffer / CF₃CH₂OH (4:1) solution (pH = 7.0).

	$E_{1/2}^{OX}$ (V vs Ag/AgCl)	
Complex	Ru(II/III)	E_{onset}
2.1 , Ru ^{II} (bda)(PPh ₃) ₂	0.45	1.4
2.2 , Ru ^{II} (bda)(PEt ₃) ₂	0.25	1.2
2.3 , Ru ^{II} (bda)(P(OiPr) ₃) ₂	0.69	1
2.4 , Ru ^{II} (bda)(PTA) ₃	0.95	1.1

In the last trial, to overcome poor solubility of the complex of the complex **2.1** we tried using propylene carbonate (PC) as a polar aprotic solvent.⁶⁶ Figure. 2.3.c illustrates the cyclic voltammograms of **2.1** mM 1 in 0.1 M 0.1 M nBu₄NPF₆/PC with water added in varying amounts. In the absence of water and in presence of water clearly a wave is observed at $E_{1/2} = 0.45$ V for redox of Ru^{III/II} but the potential of the II/III couple did not change.⁶⁶

2.1.3. DFT computations

All molecular structures were optimized in the Gaussian16 Revision D.01⁶⁷ program with the B3LYP density functional^{68,69,70} with the cc-pVDz basis set⁷⁰ for all main group atoms and the Stuttgart–Dresden (SDD)^{70,71,72} effective core potential for ruthenium. All stationary points were verified by frequency calculations and full population analysis. All calculations were carried out on isolated gas-phase species.

Table 2.4. Computed HOMO–LUMO gaps for Ru^{II}(bda)(L)₂,**2.3** species (this work) and Tolman electronic parameters for L (literature⁴⁹⁻⁵⁰).

Compound	HOMO/LUMO Gap [eV]
2.1 , Ru ^{II} (bda)(PPh ₃) ₂	2.669
2.2 , Ru ^{II} (bda)(PEt ₃) ₂	2.653
2.3 , Ru ^{II} (bda)(P(OiPr) ₃) ₂	2.760
2.4 , Ru ^{II} (bda)(PTA) ₃	2.614

Computational studies were performed for complexes **2.1** to **2.3**. We calculated two forms of complexes $[\text{Ru}^{\text{II}}(\text{bda})(\text{PTA})_3]$ and $[\text{Ru}^{\text{II}}(\text{bda})(\text{PTA})_2]$ to investigate the stability and steric effects of L_2 type versus L_3 type complexes. Our goal was to meaningfully compare complexes **2.1-2.3** with two axial ligands and compound **2.4** with three phosphine ligands. Also, a question was whether (and to what extent) equatorial phosphine/phosphite ligands can be involved in stability of each complex. The electronic structure of $[\text{Ru}^{\text{II}}(\text{bda})(\text{PTA})_3]$ shows that HOMO mixing centered on carboxyl groups from bda backbone ligand and localized over equatorial PTA ligand. However, in complexes **2.1** to **2.3**, $[\text{Ru}^{\text{II}}(\text{bda})(\text{PR})_3]$ HOMO is localized on entire bda backbone ligand. Experimental evidence supporting this observation as during synthesis of **2.4**, during which only the trisubstituted product was obtained. This point can explain our unsuccessful attempts to make the L_3 analog of complexes **2.1** to **2.3**. Electrochemical studies support our calculation result as the redox of the metal center appeared at higher potentials in case of the Ru-PTA₃ complex (Table 2.4). Furthermore, the lower energy (HOMO - 5 and HOMO -3) orbitals in **2.4** have π -bonding character between the equatorial PTA and metal center, HOMO -2 orbital shows π anti-bonding character between the axial PTA ligands and Ru and HOMO -1 orbital is π anti-bonding between the equatorial PTA and Ru.

Based on above-mentioned computational discussion we come to three conclusions: first, as we envisaged based on V_{min} parameter, the interaction between equatorial PTA and Ru is governed by a net π bonding interaction. These computational data are key to rationalize the tendency of the PTA ligand to coordinate three times. Second, computations support the electrochemistry results. For instance, delocalization of the electron density from Ru^+ onto the third equatorial phosphine through back-bonding interactions may contribute to the positive $\text{Ru}^{\text{II/III}}$ redox potential of **2.4**. Third, the results emphasize using V_{min} parameter for predicting donor/acceptor properties of a phosphine ligand when we design a complex.

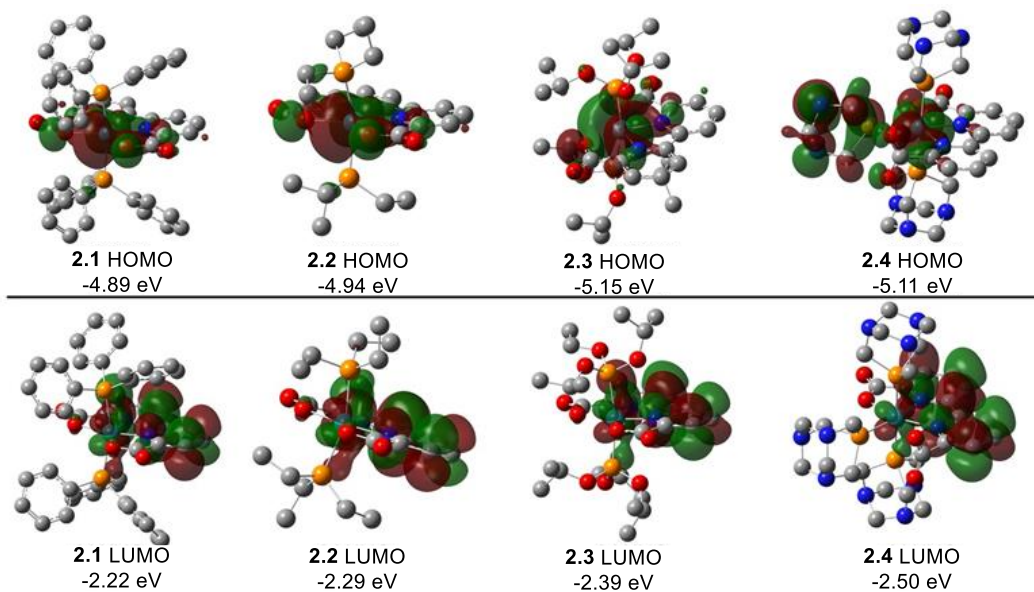


Figure 2.5. Selected molecular orbitals for **2.1** to **2.4**.

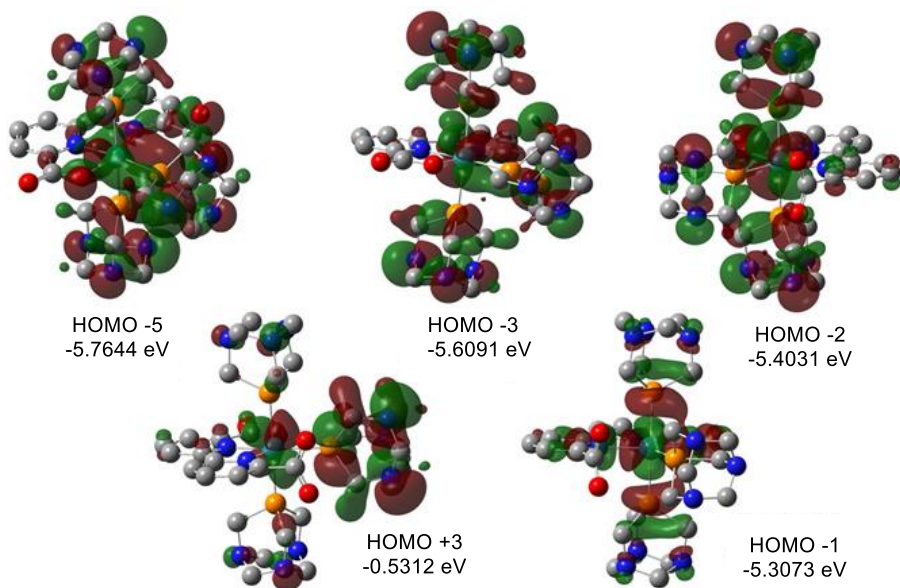


Figure 2.6. Selected molecular orbitals for **2.4**.

2.1.4. Conclusion

Chapter 2.1 reports synthesis of Ru-based complexes using the 2,2'-bipyridine-6,6'-dicarboxylic acid scaffold. For complexes **2.1** to **2.3**, phosphine and phosphite ligands occupy the two axial coordination sites of Ru(bda). In contrast, complex **2.4** possesses an additional phosphine ligand occupying the equatorial position, displacing a carboxylato of bda.

In this work we try to describe the steric and electronic effect of different PR₃. It may be noted that the steric and electronic effects are intermingled and nearly inseparable in every system, and therefore only the combined effects are always observed.

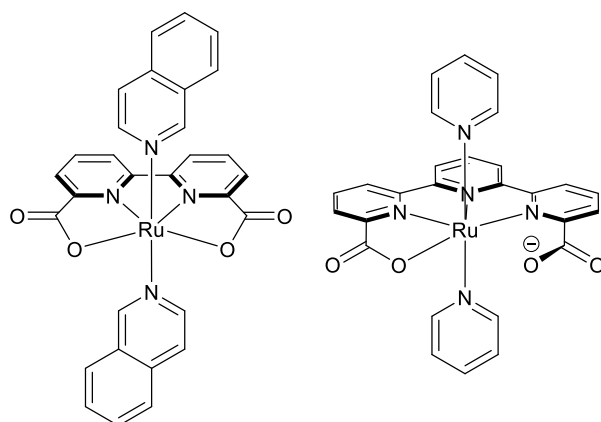
Our calculational results, X-ray structures, electrochemistry data overall are in agreement with each other (Tables 2.1-2.4). The calculated lower HOMO-LUMO gap energy of Ru(PTA)₃, overall matches with the X-ray crystal structure, that has O-Ru-O cleft-angle of 147.66° plus the smaller Ru-P bond lengths in complex **2.4**. From these data we learned that ruthenium-P bonding in complex **2.4** is favored over ruthenium-O in carboxylic acid of bda backbone ligand. As far as the coordination between the equatorial bda ligand, phosphine/phosphite axial ligands and ruthenium center is concerned, complexes **2.1-2.2** are much alike; the Ru-O bond length is close ~2.19 [Å]. Compound **2.3** is closer to **2.4** and ruthenium is more accessible for coordination with another ligand in equatorial position. In general view our conclusion is that PR₃ steric effects have the greatest role in determining whether bis-PR₃ or tris-PR₃ complex form.

This work reports the first complexes of phosphorus ligands on the Ru^{II}(bda) fragment and points to future exploration of reactivity.

Besides that, one of the goals of this project was to use these Ru-bda bearing tertiary aryl phosphine and phosphite for WOC. However, these complexes did not show impressive electrochemical oxidation of water, therefore the next strategy was to consider tertiary aryl phosphine ligands as axial ligands. We envisaged that aromaticity should help for improving the stability of the catalysts.

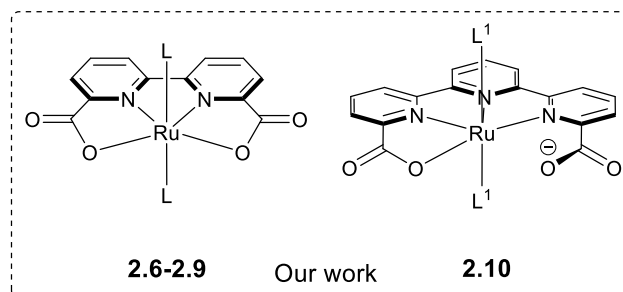
2.2. Influence of axial phosphine ligands in six-coordinate ruthenium water oxidation catalysts

Remarkable water oxidation catalysts have been reported by groups of Sun^{61,4,35,47}, Llobet,^{73,74,75,76} and Meyer.^{37,66,77} Despite these major accomplishments, sustainable catalysis is still impaired by catalyst deactivation in part due to harsh oxidizing reaction conditions. Although degradation pathways are not fully understood, Sun's group has provided some evidence suggesting that loss of axial ligands in **1.7** occurs,⁴



1.8
Sun et al.
Nature Chem. **2012**

1.9
Llobet et al.
JACS **2015**

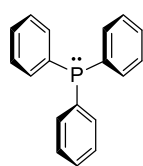


2.6-2.9

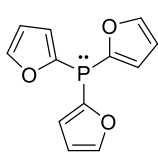
Our work

2.10

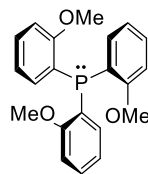
L ligands considered



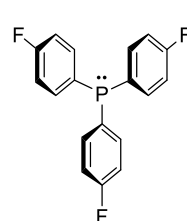
2.1



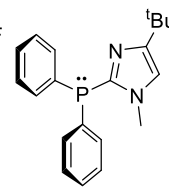
2.6



2.7



2.8



2.9

Figure 2.7. Known water oxidation catalysts **1.8**, **1.9**, the Ru-bda family **2.1** and **2.6 - 2.9**, and **2.10** with different phosphorus axial ligands (**2.6 - 2.9**) reported here.

Thus, manipulation of apical coordination sites may allow the design of more robust catalysts. In a pioneering report, Sun's group introduced π -extended isoquinolines in **1.8** as axial ligands substituting for 4-picoline,⁶¹ meanwhile, more systematic investigations of the electronic and noncovalent effects of *N*-bound axial ligands have also been carried by Murata and Concepcion groups respectively.^{78,79} Staehle *et al.* extended this study to axial *N*-heterocyclic carbene ligands,⁸⁰ demonstrating O-O bond formation via water nucleophilic attack (WNA) but a TOF of only 0.04 s⁻¹.

In line with these studies, a variety of Ru-bda complexes with different axial ligands containing N, C, S, and O in the first coordination sphere to ruthenium have been reported. Interestingly, analysis of the literature reveals no report on the effect of phosphine apical ligands on WOC catalytic activity.^{Error! Bookmark not defined.} In this section 2.2, we report the preparation of Ru-bda with aromatic tertiary phosphine (complexes **2.6-2.9**) and Ru-tda (**2.10**) and their evaluation in water oxidation processes. Compound **2.1** is also considered in this section as a base of aromatic phosphine moieties for the purpose of comparison (Figure 2.7). The complexes were prepared and fully characterized by analytical, spectroscopic (UV-vis and nuclear magnetic resonance), solid-state monocrystal X-ray diffraction analysis, and electrochemical techniques (cyclic voltammetry and differential pulse voltammetry). Catalytic activity was examined using Ce(NH₄)₂(NO₃)₆ (Ce^{IV}) as oxidant. Finally, the catalytic activity of the most efficient catalysts in this study, namely **2.6** and **2.10** bearing the tris(2-furyl)phosphine, is discussed in the light of known pyridine analogues.

Some parts of this chapter contain materials similar to the manuscript in preparation named "Yazdani, S.; Breyer, C. J.; Kumari, P.; Rheingold, A. L.; Jazzar, R.; Bertrand, G.; Grotjahn, D. B. Influence of Axial Phosphine Ligands in Six- coordinate Ruthenium Water Oxidation Catalysts".⁸¹

2.2.1. Preparation, characterization, catalytic behavior of 2.6 – 2.9

[Ru(bda)(L)₂] complexes **2.6-2.9** were readily obtained in good to excellent yield from [Ru(bda)(DMSO)₂],^{61,81} by reacting with two equivalents of the corresponding phosphorus ligand in methanol (Figure 2.8). This synthetic strategy allowed us to systematically vary the electronic and the steric properties of the phosphorus ligand.

The general method for the synthesis of complexes **2.6-2.9** is given as follows: A 20 mL scintillation vial in the glove box was charged with Ru(bda)(DMSO)₂ (0.1000 g, 0.1994 mmol, 1 equiv) then methanol (5.0 mL) was added. In another vial, the P-ligand (0.3988 mmol, 2 equiv) was dissolved in methanol (5 mL), and the resulting solution was added to the vial containing Ru(bda)(DMSO)₂. The reaction vial was sealed and the contents stirred at room temperature. The completion of the reaction was monitored with ³¹P NMR. After completion of the reaction, the mixture was filtered in the glove box, and the filtrate evaporated to dryness. The residue was crystallized either by slow evaporation over time or diffusion using methanol/dichloromethane to produce the desired product.

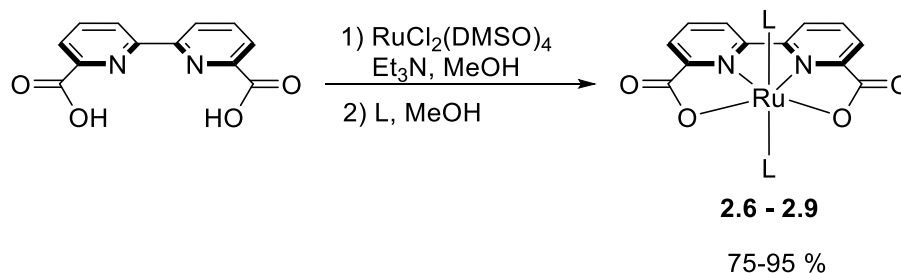


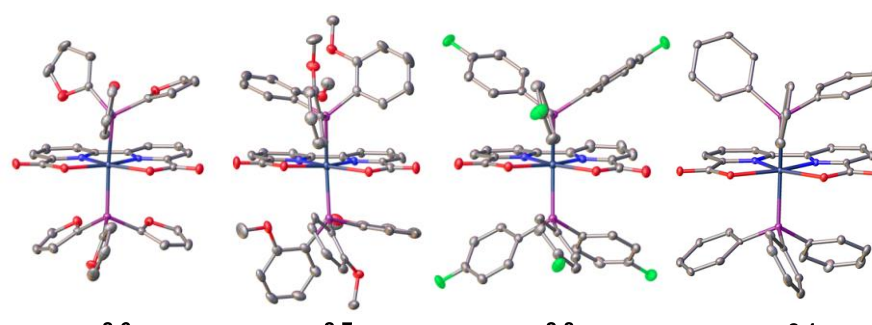
Figure 2.8. Synthesis of complexes **2.6 – 2.9**.

We were fortunate to obtain X-ray crystallographic data for **2.6 – 2.8** and **2.1** (Figure 2.9). Of interest, we found that compound **2.6** exhibits a O-Ru-O angle that is closer to the angle in **1.8**, whereas in **2.7**, **2.8**, and **2.1** the angle is slightly larger. Given the cone angles for **2.6 – 2.8** and **2.1** of 133, 136.6, 145, and 145^{o,82,83,84,85} respectively, it is likely that the increase in the steric bulk in the apical position causes more distortion in the geometry of these complexes compared to **1.8** and a wider O-Ru-O angle (see the O-Ru-O angles in Figure 2.9). In complex **2.7**, longest Ru-P distances (2.411(12) - 2.434(12) Å) observed

because of steric hindrance presented by three ortho-methoxy groups and as a result created largest O-Ru-O angle (125.50(9)°).

2.2.2. Electrochemistry

The redox properties of **2.6**–**2.9** and **2.1** in aqueous solution were assessed via cyclic voltammetry. The CV experiments were performed using glassy carbon working electrodes, a platinum wire as auxiliary, and a silver/silver chloride (Ag/AgCl) as a reference electrode. At pH 7 (phosphate buffer solution), the CV of **2.6** shows a chemically reversible peak at $E_{1/2} = +0.62$ V ($\Delta E = 80$ mV, $E_{pa} = 0.66$ V) (Figure 2.10a), assigned to metal-based one-electron oxidation process [$\text{Ru}^{\text{II}} \rightarrow \text{Ru}^{\text{III}}$]. Also clear is catalytic current at pH 7 with onset at approximately +0.9 V.



Complex	Bond Length (Å)			Bond Angle (°)		
	Ru-O	Ru-N	Ru-P	N-Ru-N	O-Ru-O	O-Ru-P
2.6	2.190(13) 2.186(13)	1.953(15) 1.954(16)	2.325(5) 2.334(5)	81.43(6)	123.45(5)	88.06(4) 90.39(4)
2.7	2.212(3) 2.207(3)	1.952(3) 1.946(3)	2.411(12) 2.434(12)			
2.8	2.196(18) 2.189(17)	1.952(2) 1.953(2)	2.321(8) 2.369(9)	81.35(9)	124.40(7)	87.19(5) 83.23(5)
2.1	2.191(3) 2.223(3)	1.954(4) 1.946(4)	2.371(12) 2.376(12)	81.22(15)	124.58(1)	89.31(8) 86.03(8)
1.6	2.172(6) 2.216(7)	1.949(7) 1.914(6)	2.070(6) ^a 2.084(6) ^a	82.10(3)	123.00(2)	87.40(2) ^b 83.89(2) ^b

Figure 2.9. Solid state structures of **2.6** – **2.8**, and **2.1**. Selected bond lengths and bond angles. Hydrogen atoms have been omitted for clarity. Data for **1.8** are from reference⁶¹. ^a Ru-picoline N distances. ^b O-Ru-N angles.

We performed differential pulse voltammetry (DPV) for **2.6** to investigate further the redox properties of this complex. In DPV, one oxidation peak is visible in the region of +0.60 V (Figure 2.10b and 10c), which corresponds to the oxidation $\text{Ru}^{\text{II}} \rightarrow \text{Ru}^{\text{III}}$.^{4,35,47,61} For **2.6**, this process occurred at +0.58 V at pH 11.18, at +0.60 at pH 7.07, and at +0.61 at pH 1.99, essentially at the same potential. The lack of change over a wide pH change is in contrast to the results on Sun's isoquinoline complex **1.6**, and may indicate that water binding occurs at a higher oxidation state.³⁷

Cyclic voltammetry for **2.1** and **2.7 – 2.9** was conducted in aqueous potassium phosphate (0.1 M, $\mu = 0.1$, pH = 7) (Figure 2.11). Clearly, reversible one-electron redox waves for $\text{Ru}^{\text{II/III}}$ were observed for PPh_3 complex **2.1** ($E_{1/2} = +0.53$ V, $E_{\text{pa}} = +0.55$ V) and $\text{P}(4\text{-FC}_6\text{H}_4)_3$ complex **2.8** ($E_{1/2} = +0.63$ V, $E_{\text{pa}} = +0.67$ V), with the more positive potential for the fluorinated analog consistent with the electron-withdrawing nature of the ligand.

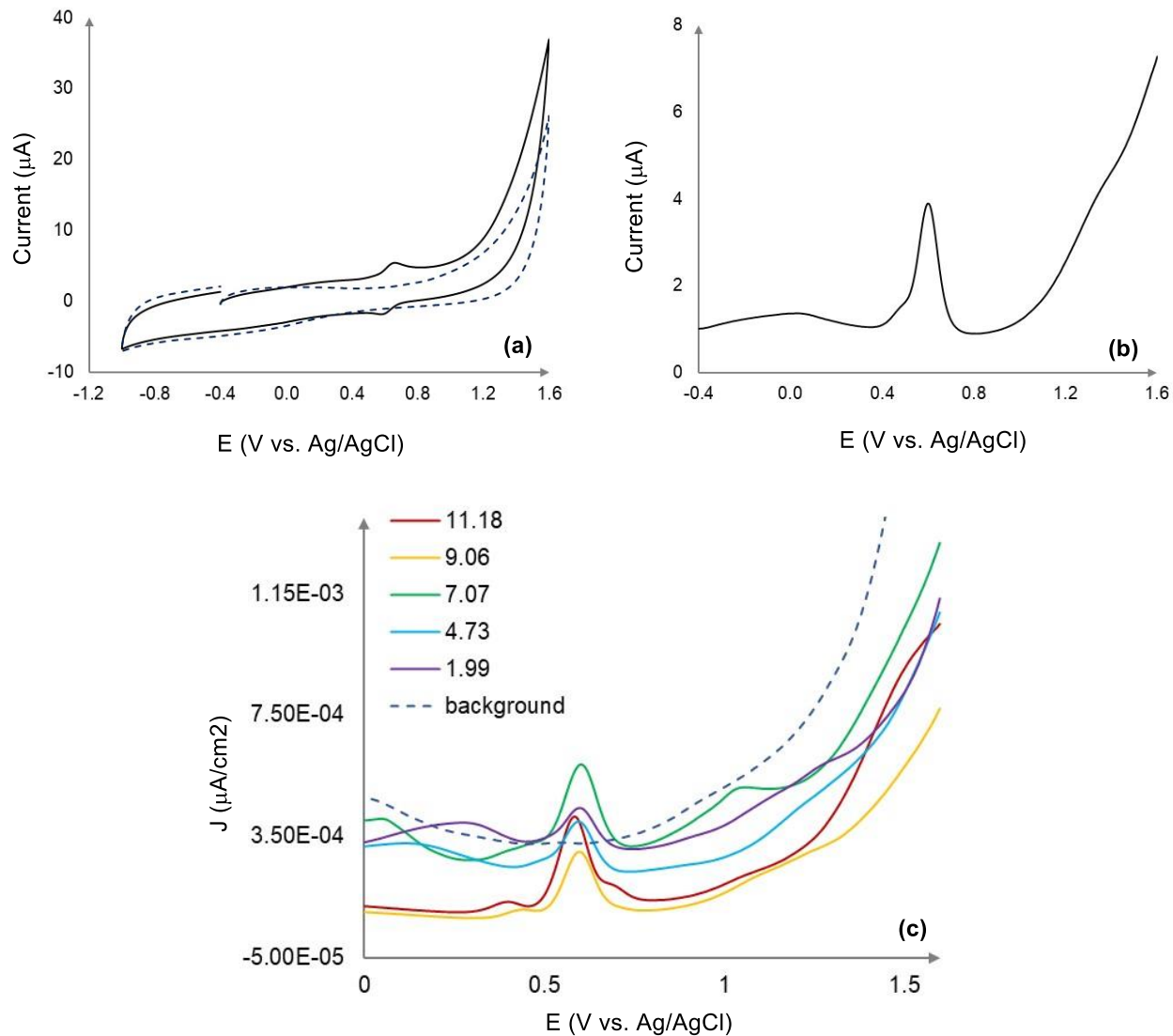


Figure 2.10. **(a)** Cyclic voltammogram of **2.6** vs. background (dashed line) in 0.1 M potassium phosphate buffer/ $\text{CF}_3\text{CH}_2\text{OH}$ (65:35) solution ($[\mathbf{2.6}] = 0.32 \text{ mM}$, 0.05 V/s , pH 7, ionic strength 0.1 M). CV demonstrates a reversible redox peak at $E_{1/2} = +0.62 \text{ V}$. **(b)** Plot of DPV of **2.6** in a phosphate buffer (pH 7). Conditions for all the electrochemistry experiments: working electrode, glassy carbon; counter electrode, Pt wire; reference electrode, Ag/AgCl. **(c)** DPV of **2.6** at pH 1.99 – 11.18 in a mixture of aqueous potassium phosphate buffer and $\text{CF}_3\text{CH}_2\text{OH}$ (65:35) and ionic strength 0.1 M ($[\mathbf{2.6}] 0.32 \text{ mM}$). Blue dashed line is the DPV background at pH 7.07. Working electrode, glassy carbon; counter electrode, Pt wire; reference electrode, Ag/AgCl.

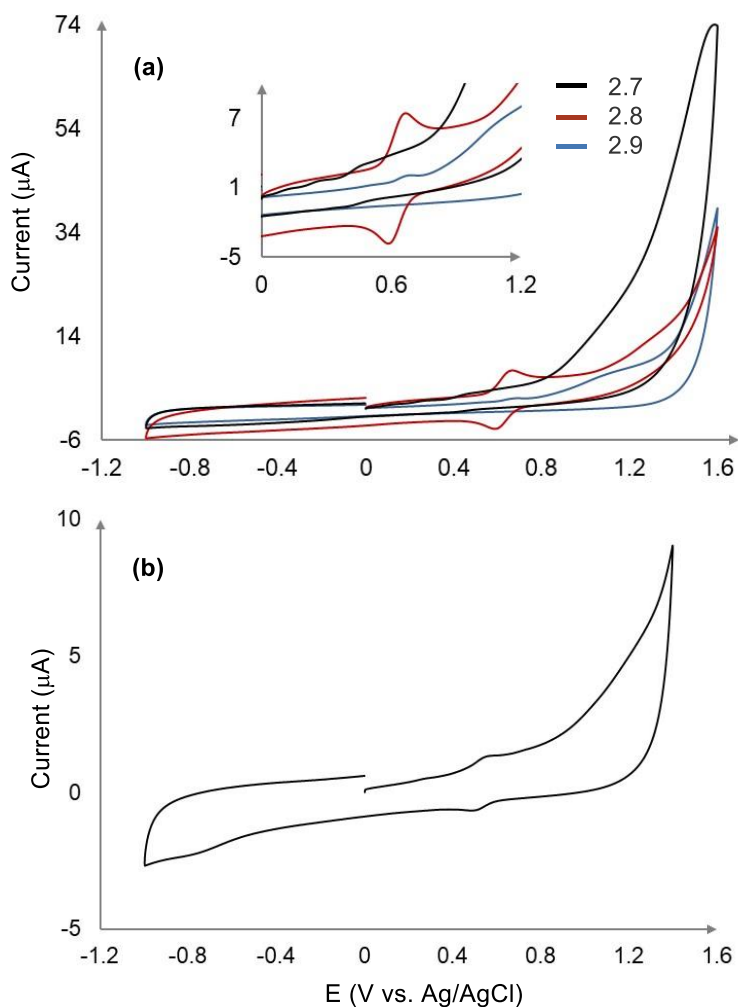


Figure 2.11. **(a)** Cyclic voltammograms (background-subtracted) of **2.7** - **2.9** in 0.1 M potassium phosphate buffer / $\text{CF}_3\text{CH}_2\text{OH}$ (4:1) solution and ionic strength 0.1 M ($[\mathbf{2.7} - \mathbf{2.9}]$ 0.79 mM, $\mu = 0.1$, pH 7). The black line is CV for **2.7** which shows $E_{p,a}$ 0.46 V and a reversible redox wave at 0.45 V. The CV of **2.8** (red line) shows a reversible redox peak for $\text{Ru}^{\text{II/III}}$. The blue line CV for **2.9** demonstrates an irreversible wave with forward current 2.04×10^{-6} A. **(b)** CV of **2.1** in 0.1 M KH_2PO_4 buffer / $\text{CF}_3\text{CH}_2\text{OH}$ (4:1) solution ($[\mathbf{2.1}]$ 0.79 mM, $\mu = 0.1$, pH 7). CV shows a reversible peak at 0.53 V and current 1.33×10^{-6} A.

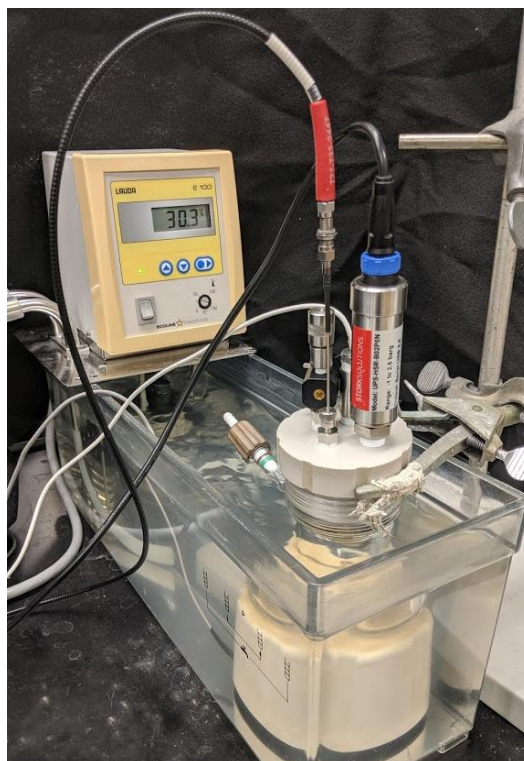
The values of $E_{1/2} = +0.62$ V, $E_{pa} = 0.66$ V for **2.6** are somewhat surprising, since by looking at both ν_{CO} in $ClRh(L_2)CO$ complexes (Table 2.5) as well as at $^1J_{PSe}$ in phosphine selenides, **2.6** is considered less electron-donating than **2.8**.^{81,85} **2.9** and **2.7** gave less clear CV data (Figure 2.11).

Therefore, in this series of Ru-bda complexes bearing tertiary phosphine axial ligands **2.6–2.8** and **2.1**, the $Ru^{III/II}$ redox potential shows an increasing trend as **2.1** < **2.6** < **2.8**.

2.2.3. Catalytic activity of bda complexes 2.6–2.9 in O₂ evolution

We studied the catalytic activity of **2.6–2.9** for generating O₂ in the presence of Ce^{IV} as an oxidant (Figure 2.13a and Table 2.6). For these experiments, aqueous ceric ammonium nitrate (CAN) at the desired concentration was used in a sealed vessel equipped with pressure transducer, and a small volume of solution containing the catalyst was injected.

Tests were run in a 110 mL custom-fabricated airtight pressure cell equipped with a pressure transducer, oxygen optode, thermocouple, injection port, shutoff valve, and purge valve. The cell is purged with N₂ gas, and 10 mL of aqueous ceric ammonium nitrate (CAN) at the desired concentration is injected into the cell. The cell is then immersed in a constant temperature bath (30 °C), allowed to reach thermal equilibrium and the pressure is relieved through the shutoff valve. An aliquot of catalyst solution in a gas tight syringe injected into the cell. A LabVIEW/PC interface is used to trigger both measurement apparatus simultaneously and record data.



Figures 2.12. Reaction cell equipped with pressure transducer.

The tris(2-furyl)phosphine complex **2.6** outperformed the other Ru catalysts (**2.7**–**2.9**) at similar concentrations, while **2.9** led to the lowest performance (Table 2.6). Our catalytic results in the order **2.6** > **2.7** > **2.8** > **2.9** correlates with a higher activity of electron-deficient apical ligands, which is in good agreement with literature precedents.^{35,74} Although complex **2.6** shows the highest TON, complex **2.8** shows the highest rate in the 30-to-60 sec time range.

Complex **2.8** had a higher onset potential and showed minimal catalytic activity compared to **2.6** (Figures 2.11 and 2.10). Under the given catalytic conditions in Figure 2.13a, complex **2.8** deactivated in about 2 minutes while complex **2.6** lasted more than 10 minutes. Possibly the loss of the bulkier phosphine ligand ($\text{P}(4\text{-FC}_6\text{H}_4)_3$, **2.8**) accelerates the degradation of the catalyst (cone angles for **2.6** and **2.8** = 133° and 145° , Table 2.5). At the lowest concentration of catalyst **2.6** examined, 5 μM , a higher catalytic activity was observed for water oxidation; the turnover number was calculated to be 258 (Figure 2.13b, Table 2.7).^{86,87}

Table 2.5. Tolman electronic parameters (TEP), Infrared data (CH_2Cl_2) for trans-[RuCl(CO)(L)] complexes, and cone angles for **2.1** and **2.6 - 2.9**. In addition to related Ru^{II/III} redox potential for **2.6**, **2.7**, **2.9**, and **2.1** in pH 1, phosphate buffer solution.^{82,84,85}

entry	TEP (cm^{-1})	$\nu(\text{CO}_{\text{Rh}})(\text{cm}^{-1})$	Cone angle($^\circ$)	$E_{1/2}$	Ru ^{II/III}
2.6	-	1998	133	0.62	0.66
2.7	2058.3(3)	-	136.6	-	0.46
2.8	2071.3(2)	1983	145(1)	0.63	0.67
2.9	-	-	-	-	-
2.1	2068.9	1979	145	0.53	0.55

Table 2.6. Detailed concentration and yields for oxygen evolution catalyzed by **2.7 - 2.9** in aqueous solution (HNO_3 , pH 1, 5.0 mL) containing Ce^{IV} .

entry	[CAN] ₀ (M)	[Cat.] ₀ (μM)	Theoretical O ₂ (μmol)	% Yield O ₂	TON*	Initial Rate ($\mu\text{mol O}_2/\text{s}$)
2.7	0.20	20.0	500	8.4	76	0.003
2.8	0.20	19.9	497	7.2	69	0.009
2.9	0.20	20.0	500	4.9	43	0.001

Table 2.7. Detailed concentration and yields for oxygen evolution catalyzed by **2.6** in aqueous solution (HNO_3 , pH 1, 5.0 mL) containing Ce^{IV} .

entry	[CAN] ₀ (M)	[Cat.] ₀ (μM)	Theoretical O ₂ (μmol)	% Yield O ₂	TON
1	0.21	5	519	2.5	258
2	0.21	10	519	3.2	163
3	0.21	20	521	4.2	54
4	0.21	40	520	3.8	97
5	0.21	80	520	6.4	41

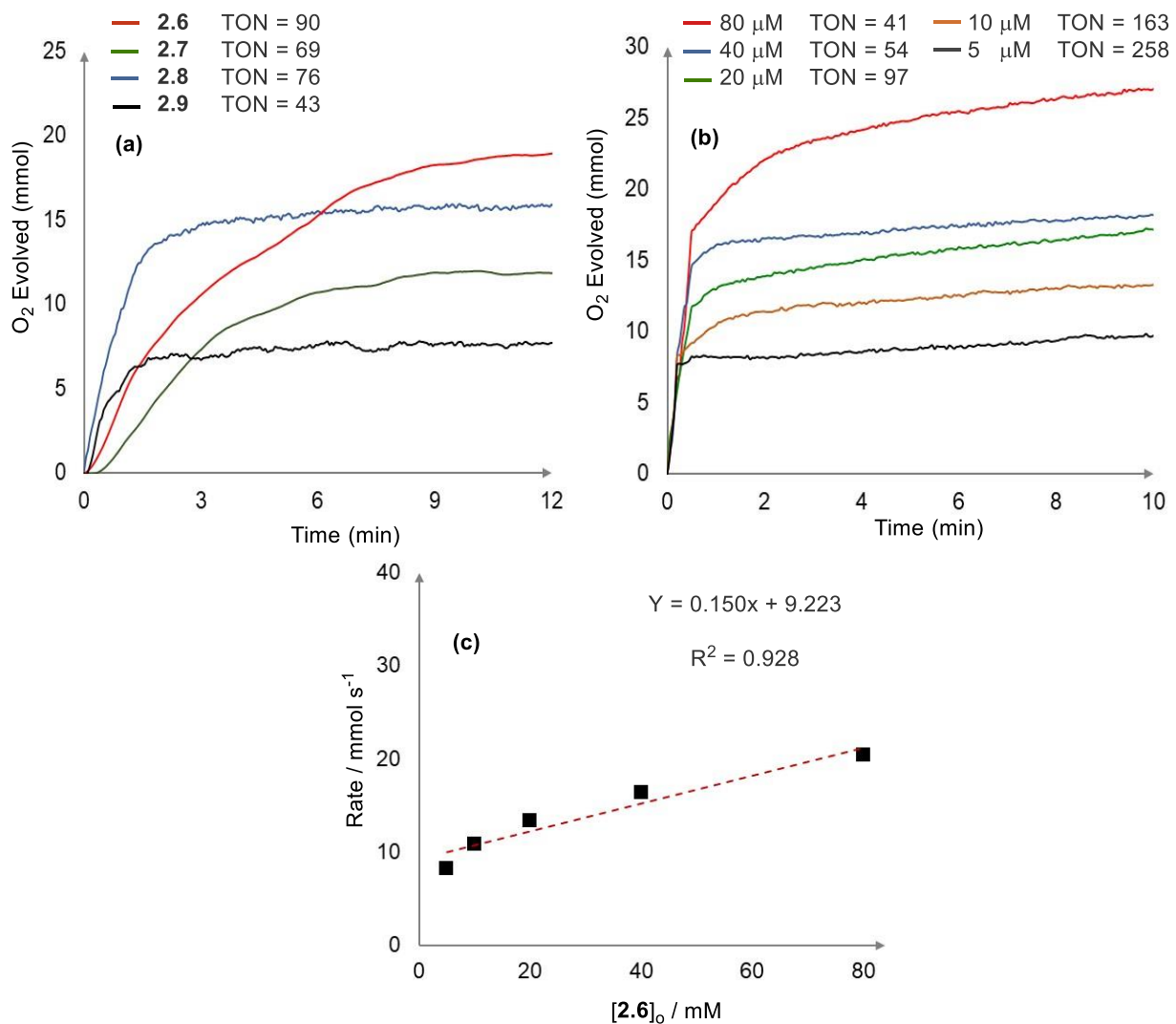


Figure 2.13. **(a)** Oxygen evolution catalyzed by **2.6 – 2.8**, [Cat.]₀ = 20 μM, in aqueous solution (HNO₃, pH 1, 10 mL) containing [Ce^{IV}]₀ = 0.20 M. More details are presented in Table 2.6; pressure buildup in a sealed cell gave the measurements shown. **(b)** Oxygen evolution catalyzed by **2.6** in aqueous solution (HNO₃, pH 1, 5.0 mL), with [Cat.]₀ ranging from 5 to 80 μM and [Ce^{IV}]₀ fixed at 0.21 M (Table 2.7). **(c)** The rate of O₂ evolution in the period 30 to 60 sec after first catalyst injection, versus initial concentration of **2.6**.

To determine the order with respect to [catalyst]_o, we measured rates at an early phase of the reaction. Two phases of the oxygen evolution were seen, a first one during the injection, from t = 0 to t = 12 to 30 sec, in which much of the O₂ was formed; to be consistent, we considered the initial phase to be 30 sec. The second phase occurred in the next 30 sec, after injection was finished, t = 30 to 60 sec. Most of the O₂ is produced during the first phase, during which also there are perturbations due to needle insertion and removal that preclude use of the data in the first phase. To estimate the order with respect to [2.6]_o, we used the second phase, but as shown in Figure 2.13c, the linear fitting from t = 30 to 60 sec is neither interpretable as first-order nor second-order reaction.^{4,35,47,61,73,74,75,76}

2.2.4. Stoichiometric oxidation of 2.6 monitored by UV-Vis spectroscopy

UV-Vis spectra were obtained on a Shimadzu UV-Vis spectrophotometer. In every experiment, Ru complex was added to a 0.1 M triflic acid solution (pH 1) and monitored during time by UV-vis. Solutions of the complexes were prepared under nitrogen in a glovebox and solution by a gas tight syringe injected into a quartz cuvette (0.3 cm x 1 cm width) with sealable cap. The absorption spectra were recorded at room temperature. An initial spectrum of Ru complexes was acquired, and then variable equivalents of CAN was added to solution. The concentration of catalysts used for UV-Vis studies were 0.1 mM.

Given the catalytic activity observed with 2.6, we added successive 0.2 equivalent portions of Ce^{IV} oxidant to 2.6 in triflic acid (pH=1) and observed the UV-vis spectra (Figures 2.14 and 2.15c). Figure 2.14c shows the [Ce^{IV}]-dependent absorbances at wavelengths 309 nm and 326 nm, that show clear dependences on amount of Ce^{IV} added. The absorption rises to a maximum at 2 equivalents, suggesting the formation of one or more higher oxidation states.

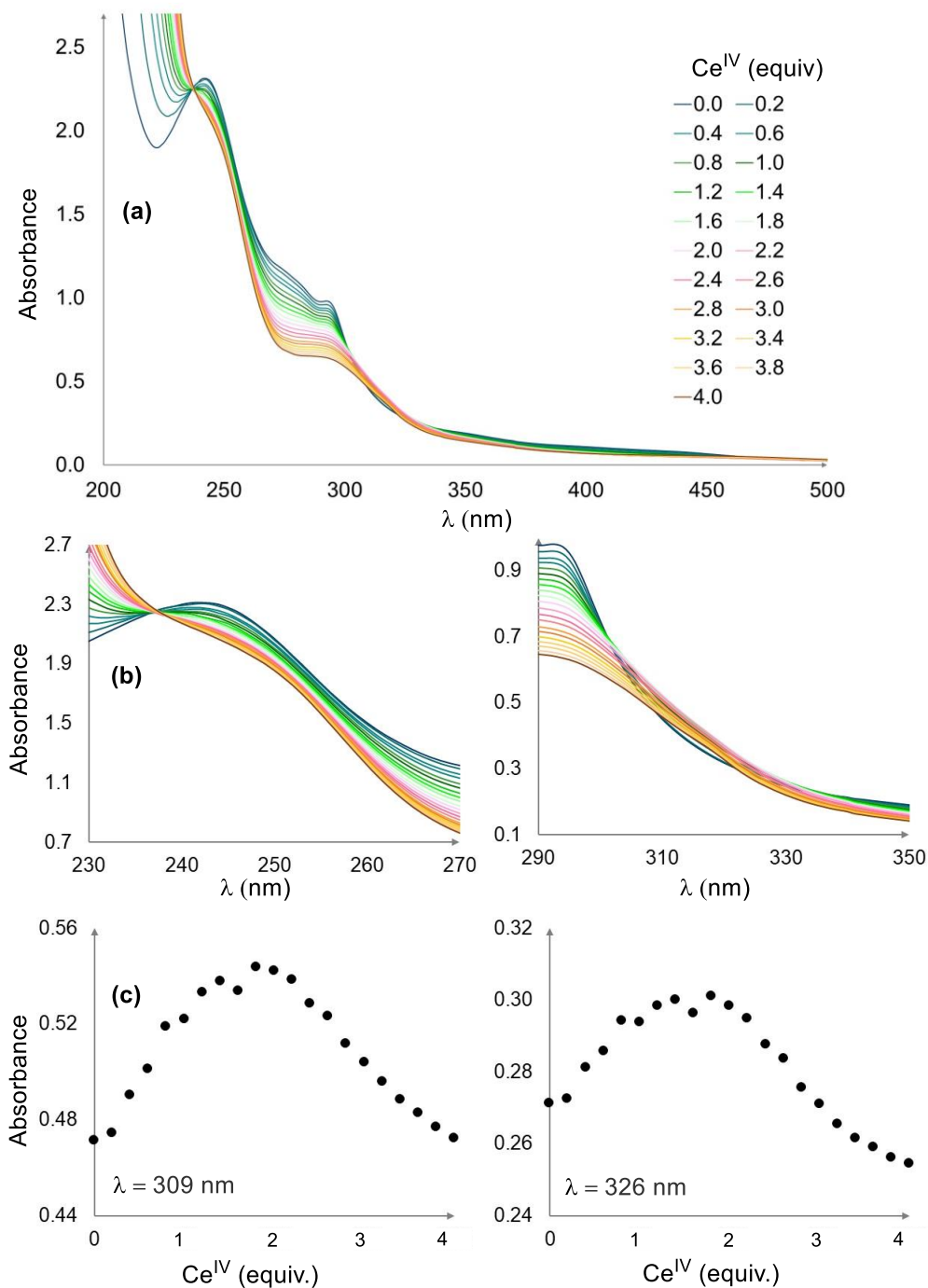


Figure 2.14. UV-vis spectra of **2.6**. **(a)** Spectrophotometric redox titration of **2.6** ($70 \mu\text{M}$) in pH 1 triflic acid (0.1 mM) by CAN (0 to 4 equivalents of CAN, and each time 0.2 equivalent CAN solution added, 1.1 mM stock solution of CAN); **(b)** Close-up of isosbestic point in the region between 230-270 nm, and second close up of the region 290-350 nm; **(c)** Plot of absorbance against equivalents of CAN at selected wavelengths (309 nm and 326 nm). Wavelengths 246 and 343 nm are presented in Figure 2.15.

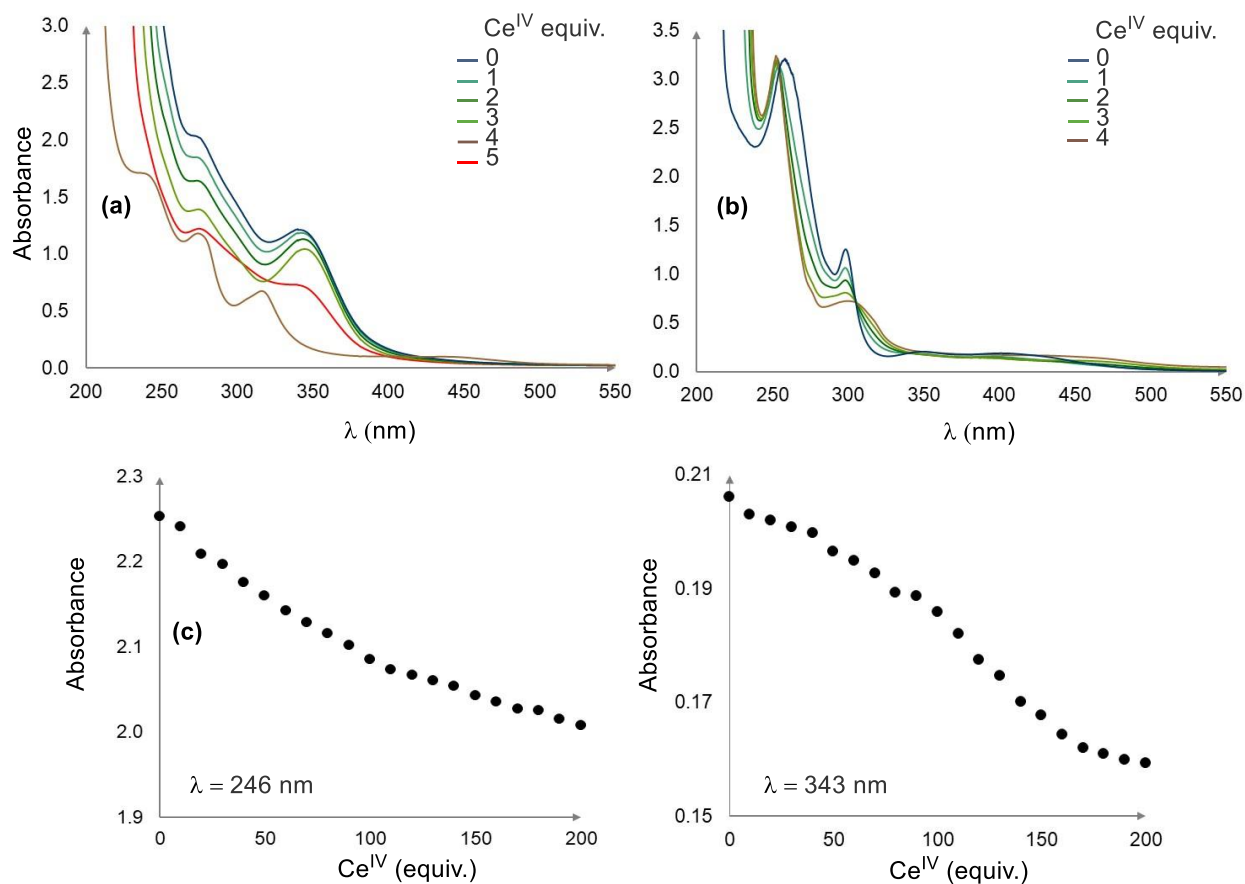


Figure 2.15. **(a)** UV-vis spectrum of **2.10** in triflic acid aqueous solution, pH 1 (dark blue line). The other traces are for mixtures after successive additions of 1 equivalent of Ce^{IV} , up to 5 equivalents total ($[\mathbf{2.10}] = 0.14$ mM). **(b)** UV-vis spectrum of **2.9** (0.1 mM) at pH 1 triflic acid (black line). Redox properties of **2.9** by successive additions of 1 to 4 equivalents of Ce^{IV} ($[\text{Cat.}]_0 = 0.15$ mM). **(c)** Spectrophotometric redox titration of **2.6** (70 μM) at pH 1 triflic acid, (0.1 mM) by CAN (0 to 4 equivalents of CAN, and each time 0.2 equivalent CAN solution added, 1.1 mM stock solution of CAN). Plot of absorbance against equivalents of CAN at selected wavelengths (246 nm and 343).

2.2.5. Preparation, characterization, catalytic behavior of **2.10**

Following upon our results with **2.6**, we expanded our investigation to a tris(2-furyl)phosphine analog of the tda ruthenium catalyst **1.9**. Consequently, Ru(tda- κ -N₃O)[tris(2-furyl)phosphine]₂ **2.10** was prepared by reaction of [2,2':6',2''-terpyridine]-6,6''-dicarboxylic acid (H₂tda) with RuCl₂(DMSO)₄,⁶¹ followed by ligand exchange with tris(2-furyl)phosphine (Figure 2.16).

Crystallographic analysis of complex **2.10** reveals a six-coordinate ruthenium center with one coordinated carboxylate, which displays the typical disordered octahedral geometry around a low-spin d⁶ Ru^{II} in center. The Ru-O distance for the bonded carboxylate is 2.347(17) Å whereas for the nonbonded carboxylate is 2.959 Å. Of note, the Ru-N bond distances (ca. 1.948(3)-2.061(2)-2.061(2)) in complex **2.10** are smaller than in the analogous Llobet complex **1.8** (2.105(2)-2.114(5)-2.118(5)).² Selected bond angles and distances are presented in Figure 2.17.

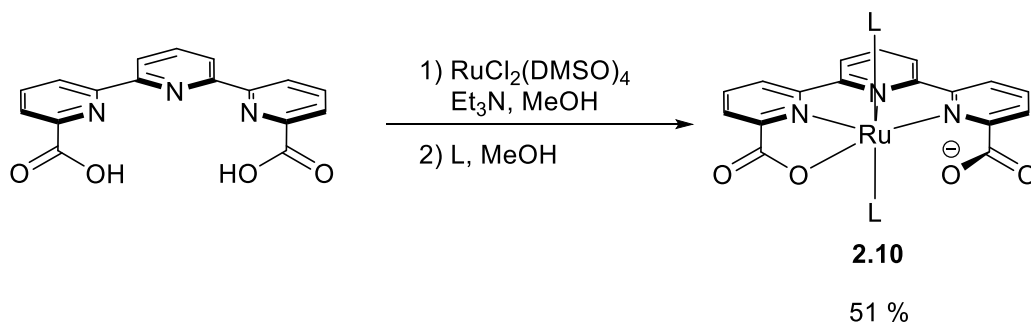
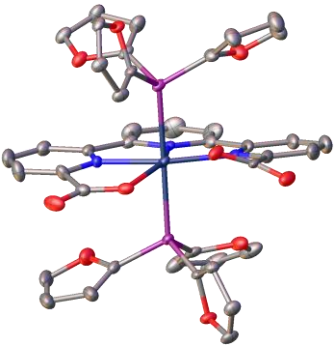


Figure 2.16. Synthesis of [Ru(tda)(tris(2-furyl)phosphine)₂] **2.10**.

2.2.6. Electrochemistry studies of complex **2.10**.

Turning to electrochemistry, complex **2.10** shows two reversible redox waves at $E_{1/2} = 0.53$ V ($\Delta E = 40$ mV) and $E_{1/2} = 0.91$ V ($\Delta E = 42$ mV) at pH 1 and 150 mV / s (Figure 2.18a). To evaluate if the potentials of these waves are pH-dependent, we also performed CV at pH 7. In this case two waves were observed at $E_{1/2} = 0.37$ V ($\Delta E = 91$ mV) and $E_{1/2} = 0.91$ V ($\Delta E = 62$ mV) (Figure 2.18b), which we assigned to two consecutive metal-based one-electron oxidation processes [Ru^{II} → Ru^{III} → Ru^{IV}]. The II/III couple potential changes with pH, unlike **2.6**, but III/IV one does not, in analog to Llobet's complex **1.9**. Using 15 CV scans between 0.05 - 1 mV/s at pH 7 allowed us to determine the scan rate dependence for this complex;

note that for this experiment, the potential was scanned up to 1.6 V. The plot of the current versus square root of the scan rates is linear which clearly demonstrates that the process is diffusion-limited (Figure 2.19). Notably, as the scan rate was reduced, we noted a progressive growth in current density in the 1.1 - 1.6 V region, which we attributed to an increasing concentration of a more active species. In line with Llobet et al., we hypothesized that a more electroactive species was formed at longer time scale.² To verify this hypothesis, up to 333 scans ($U = 20$ mV/s) were performed under similar conditions (Figure 2.18c). In our case, however, we observed a gradual deactivation of catalyst, as highlighted by a progressive loss in the intensity of the corresponding $\text{Ru}^{\text{II}} \rightarrow \text{Ru}^{\text{III}} \rightarrow \text{Ru}^{\text{IV}}$ transitions.



2.10

Complex	Bond Length (Å)			Bond Angle (°)	
	Ru-O	Ru-N	Ru-P/N	N-Ru-N	O-Ru-P/N
2.10	2.959 2.347(17)	2.061(2) 1.948(3) 2.061(2)	2.3427(6) 2.3427(6)	79.828 79.828	74.110 101.248
1.9	2.014(4) 2.026(4)	2.105(2) 2.114(5) 2.118(5)	2.108(5) 2.105(5)	72.50(3) 72.02(2)	88.15(18) 86.85(15)

Figure 2.17. Solid state structure of **2.10** and comparison with that of **1.9**. Selected bond lengths and bond angles. Hydrogen atoms have been omitted for clarity. Data for **1.9** are literature values.²

Nonetheless, our electrochemical experiments support single outer sphere electron transfer processes associated with the $\text{Ru}^{\text{II/III}}$ and $\text{Ru}^{\text{III/IV}}$ redox couples.⁸⁷ We next evaluated the catalytic activity of **2.10**, and found that this complex was reaching up to 123 TON (Table 2.8). The analysis of the O_2 evolution catalyzed by **2.10** was examined by a series of trials, in which the present concentration of **2.10** was changed, but the concentration of CAN was kept constant (large excess of Ce^{IV}) (Figure 2.20). The decay

of CAN is insignificant during the catalytic reaction because large excess of CAN was added. Therefore, the initial rate of O₂ is independent of the concentration of Ce^{IV}. However, the initial rate of O₂ evolution linearly depends on the concentration of **2.10**, following a first-order kinetics: rate = k_{O_2} [**2.10**]. The first order rate in catalyst concentration (for more information see experimental section), suggests a single-site water oxidation attack (WNA) mechanism as interpreted for analogous catalyst **1.9**.⁶¹

Table 2.8. Oxygen evolution catalyzed by **2.10** in aqueous solution (HNO₃, pH 1, 5.0 mL) containing Ce^{IV}.

entry	[CAN] ₀ (M)	[Cat.] ₀ (μM)	Theoretical O ₂ (μmol)	% Yield O ₂	TON
1	0.21	10	519	2.4	123
2	0.21	20	521	4.7	122
3	0.21	40	521	5.0	65
4	0.21	80	520	7.7	49

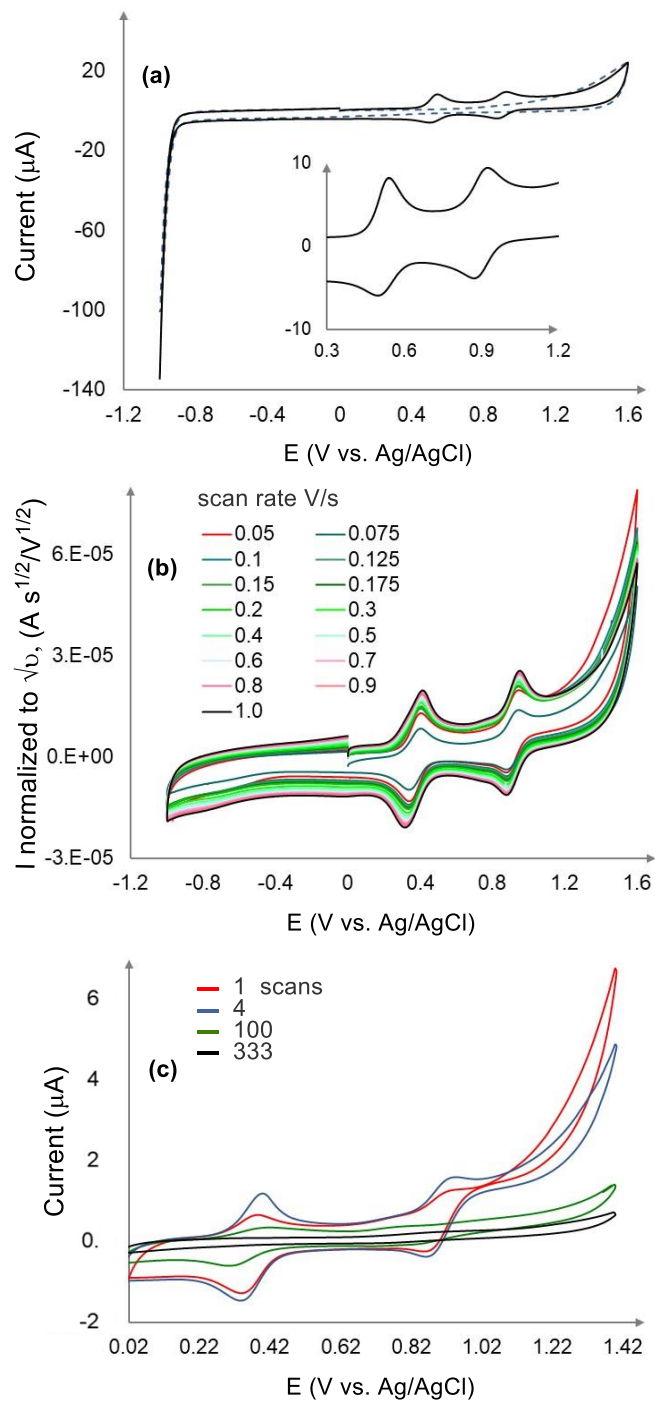


Figure 2.18. **(a)** Cyclic voltammetry of **2.10** (2.6 mM) (black line), in pH 1 aqueous triflic acid solution at a scan rate of 0.15 V/s by using a glassy carbon working electrode (background presented as a dashed line). **(b)** CV with variable scan rate (0.05 to 1 V/s) of 2.6 mM **2.10** in pH 7 in phosphate buffer. CVs with current normalized to the square root of the scan rate (ionic strength 0.1 M). **(c)** Repetitive cyclic voltammetry experiments ($U = 20$ mV/s) in pH 7 phosphate buffer of 1.7 mM of **2.10**. The red line represents the first scan, the blue line is 4 scans, and finally, the black line shows the last scan with 333 cycles in between. $[\mathbf{2.10}]_0$ 0.79 mM.

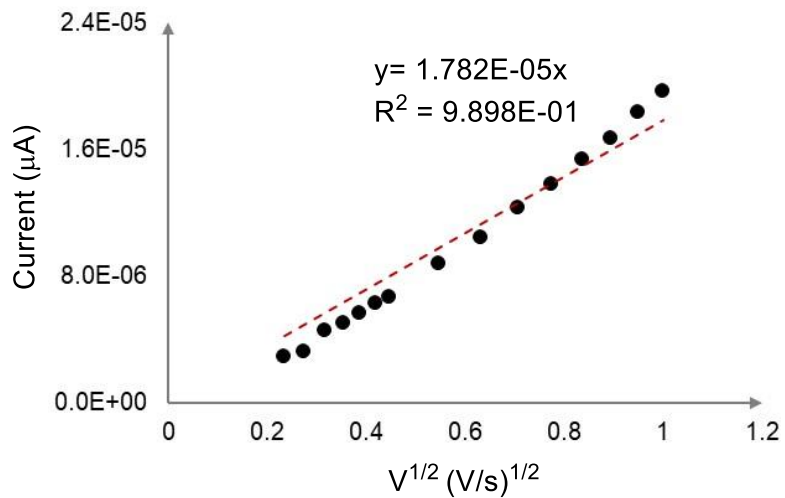


Figure 2.19. Plot of current for Ru^{II/III} couple vs. square root of scan rate for **2.10** with variable scan rate (0.05 to 1 V/s) of 2.6 mM **2.10** in pH 7 in phosphate buffer (ionic strength 0.1 M).

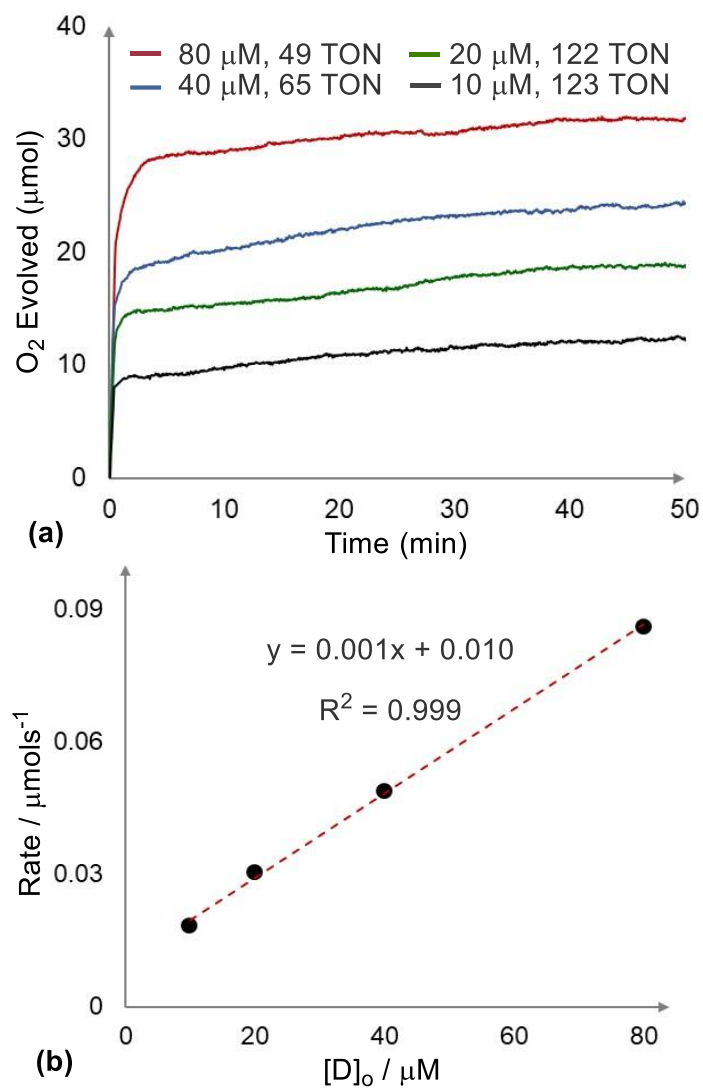


Figure 2.20. **(a)** Oxygen evolution catalyzed by **2.10** in aqueous solution (HNO₃, pH 1, 5.0 mL), [Cat.]_o variable and containing [Ce^{IV}]_o = 0.21 M. **(b)** The rate of O₂ evolution versus concentration of **2.10**. The rate is calculated by linearly fitting the post injection O₂ evolution versus time plots in 50 s time period (more information presented in Figure 2.21).

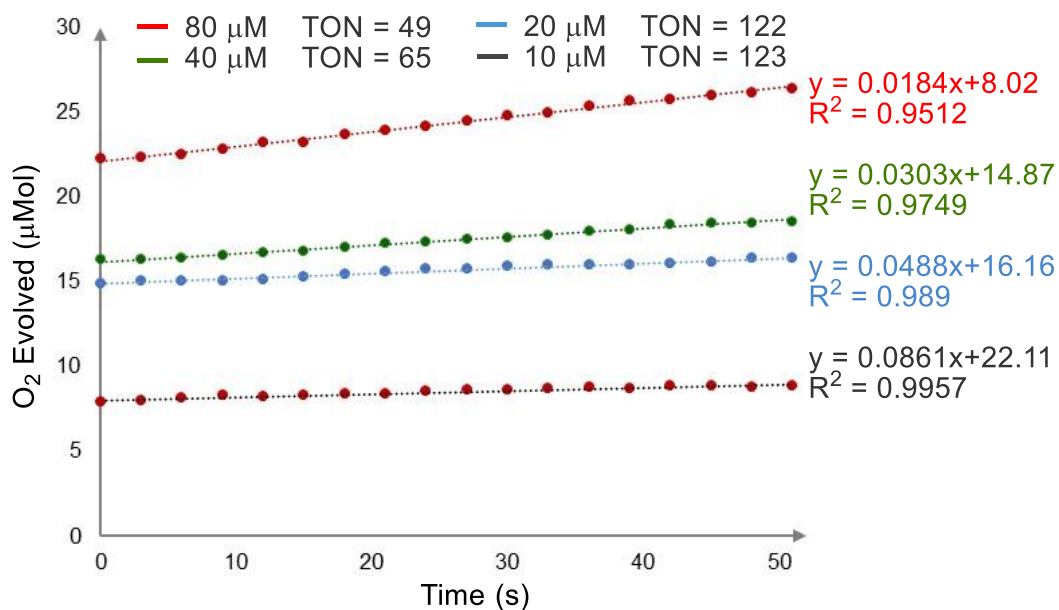


Figure 2.21. Oxygen evolution catalysed by **2.10**, [Cat.]₀ variable, in aqueous solution (HNO₃, pH 1, 5.0 mL) containing [Ce^{IV}] = 0.21 M. The rate of post injection O₂ evolution in 50 seconds at various concentration of **2.10**.

2.2.7. Stoichiometric stepwise oxidation of **2.10** monitored by UV-vis spectroscopy

To better understand these results, stepwise oxidation of **2.10** was conducted with stoichiometric quantities of Ce^{IV} followed by UV-vis and NMR spectroscopies. As previously noted for **2.6**, by adding up to 4 equivalents of Ce^{IV} (in triflic acid, pH 1; aqueous solution), a direct correlation between the absorption and the concentration of Ce^{IV} is observed. In Figure 2.22, spectrophotometric redox titration of **2.10** with Ce^{IV}, shows isosbestic points at 246, 272, 343, and 380 nm. Llobet and coworkers note that typical Ru-bda ruthenium-ligand charge transfer bands appear at wavelengths in 420-620 nm range,² which for **2.10** appear at 420-550 nm until addition of 1 equiv Ce^{IV}.

More interestingly, using 5 equivalents of Ce^{IV} resulted in a net decrease of the absorption suggesting the formation of Ru^{III} (Figure 2.15a).

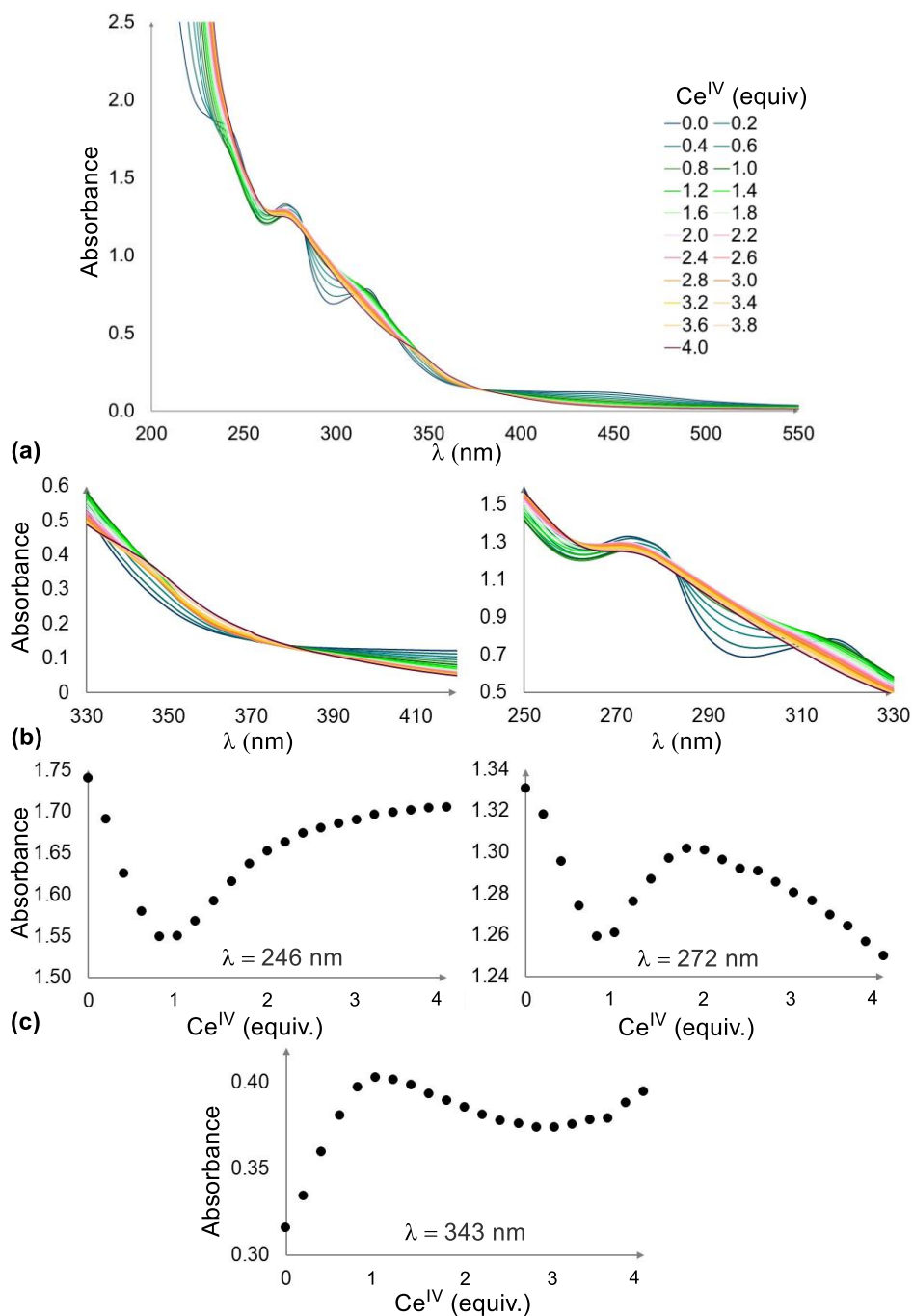


Figure 2.22. UV-vis spectrum of **2.10** at pH = 1 in triflic acid (a) Spectrophotometric redox titration of **2.10** (70 μM) at pH 1 triflic acid, (0.1 mM) by CAN (0 to 4 equivalents of CAN, and each time 0.2 equivalent CAN solution added, 1.1 mM stock solution of CAN) (b) Close-up of isosbestic point between 330-410 nm and 250-330 nm (c) Plot of absorbance against equivalents of CAN at selected wavelengths (246, 272, and 343 nm).

2.2.8. Water oxidation general mechanism

There are two proposed mechanisms for WOC forming the O-O bond during catalysis: mononuclear (one metal is involved) or binuclear (two metals are involved). In either case, first a high valent metal oxo intermediate must be formed after coordination of water to Ru, which undergo proton-coupled electron transfer or PCET to form a metal-oxo complex.

In the mononuclear cases one metal is involved in catalytic cycle, and then nucleophilic attack by another water molecule occurs. This mechanism is called water nucleophilic attack or WNA. In the whole process 4 electrons and 4 protons will be transferred (Figure 2.23). The binuclear mechanism is a radical coupling pathway, RC, in which two metal-oxo units with radical character are formed (Figure 2.23). The key step is formation of the O-O bond which either can form by water attack on a metal oxo (in mononuclear pathway), or by direct coupling of two M=O (in binuclear pathway). Changing the nature of the ligand, or reaction conditions, can result in the reaction to proceeding by either of the two mechanisms.^{88,89,90,91}

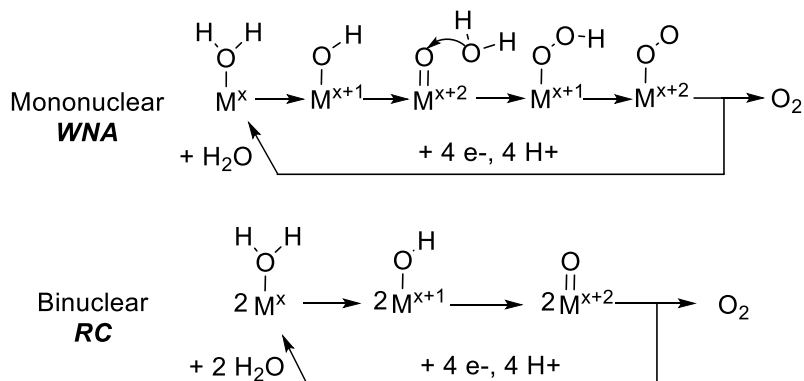


Figure 2.23. Two basic proposed mechanisms for water oxidation by mononuclear catalysts.

However, in our electrochemical and kinetic studies, we were not able to establish a WOC mechanism for complex **2.6**. In contrast, reaction of complex **2.10** is first order in catalyst concentration which suggests a single-site WNA mechanism.

2.2.9. Conclusion

In summary, we report a detailed characterization of the spectroscopic, electrochemical, and catalytic properties of related $[\text{Ru}(\text{bda})(\text{L})_2]$ and $[\text{Ru}(\text{tda}-\kappa\text{-N}^3\text{O})(\text{L})_2]$ complexes containing axial ligands L that are tertiary phosphines. Our study identified that replacing N-containing ligands with more sterically hindered and electron-donating tertiary phosphorus ligands did not significantly affect the geometry of the equatorial plane despite the bulk of the PR_3 ligands. Despite the electrochemistry and kinetic studies, a WOC mechanism could not be established for complex **2.6**. In the case of **2.10**, however, first order rate in catalyst concentration suggests a single-site water oxidation attack (WNA) mechanism, also proposed for analogous catalyst **1.7**. Furthermore, for **2.10** the $\text{Ru}^{\text{II/III}}$ couple occurs at 0.37 V followed by the $\text{Ru}^{\text{III/IV}}$ couple at 0.91 V, and the onset of catalysis begins at ~ 1.3 V.

Complexes **2.6** (TON = 258) and **2.10** (TON = 123) feature axial ligands that are very different than the normal pyridinic type. **2.6** - **2.9**, **2.1** and **2.10** are not nearly as robust as benchmark catalysts such as **1.8** or **1.9**, but they compare favorably with other attempts to drastically change the axial ligand, such as using a with N-heterocyclic carbene in the axial position ($[\text{Cat.}]_0 = 0.3 \mu\text{mol}$, $[\text{Ce}^{\text{IV}}]_0 = 0.40 \text{ M}$, TON = 32).⁸⁰

Chapter 2 manifests how steric and electronic changes in the axial ligand can exert significant effects on the activity of the complex.

2.3. Experimental section

All synthetic reactions were performed using standard glovebox and Schlenk techniques. Glassware was dried in an oven or flame-dried, and solvent were dried and degassed before use. Methanol, dichloromethane, chloroform and triethylamine were freshly distilled over CaH_2 .

NMR: Deuterium-labeled solvents were purchased from Cambridge Isotope Laboratories. **NMR:** Multinuclear NMR data were recorded on a Varian INOVA 500 MHz, a Bruker Avance 300 MHz at UCSD or a Bruker 400 MHz and Bruker 600 MHz at SDSU. Chemical shifts (δ) are reported in parts per million (ppm) and are referenced to residual solvent signals (^1H , ^{13}C). Coupling constants J are given in hertz (Hz).

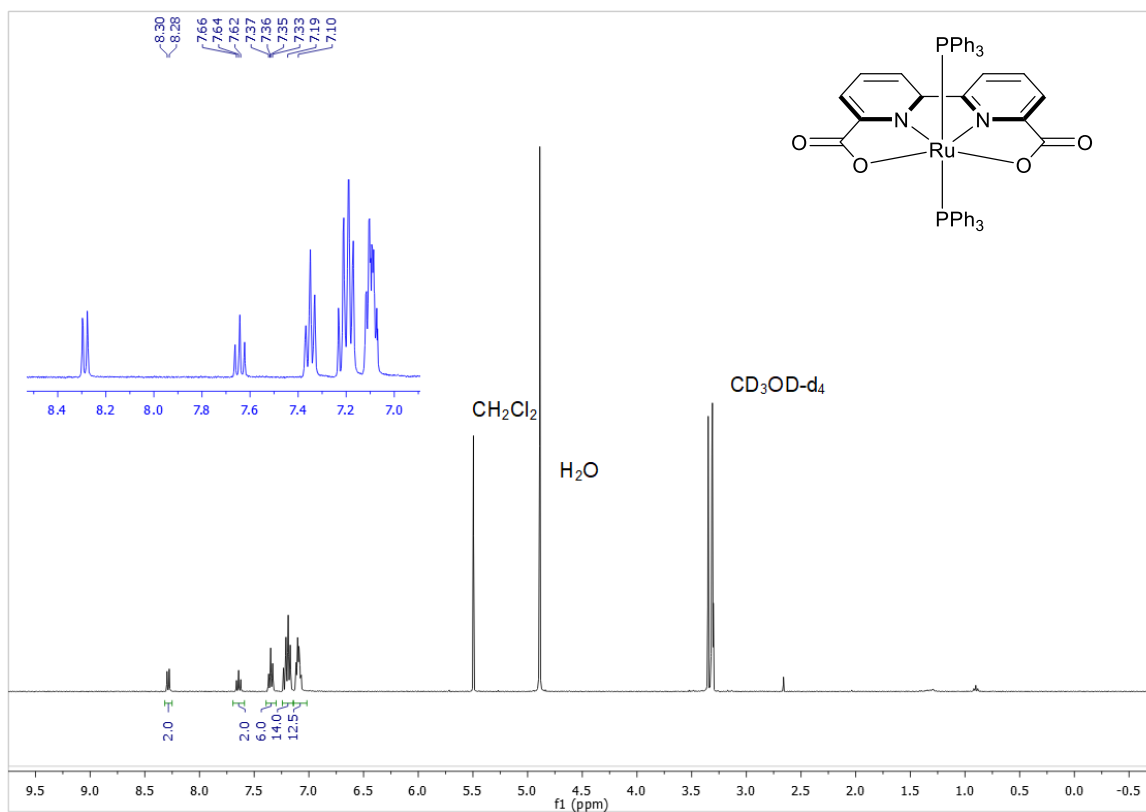
NMR multiplicities are abbreviated as follows: s = singlet, d = doublet, t = triplet, q = quartet, sext = sextet, sept = septet, m = multiplet, br = broad. All spectra were recorded at 298 K unless otherwise noted.

Synthesis of 6,6'-dimethyl-2,2'-bipyridine.⁹² A mixture of Ni(PPh₃)₂Br₂ (12.95 g, 0.01743 mol), Bu₄NI (21.46 g, 0.05811 mL) and Zn dust (3.81 g, 0.0583 mol) in this order was added to a flask which was then charged with THF (210 mL) and mixture was stirred under N₂ atmosphere at room temperature, after which 2-bromo-6-methylpyridine (10.0 g, 0.0581 mol) was added, and the mixture was refluxed overnight. The solvents were removed by rotary evaporation, and the crude product checked by ¹HNMR. Diethyl ether (200 mL) and 10% NH₄OH (50 mL) were added to the crude reaction and the mixture was stirred for 1 h, after which solids were removed by filtration and purified by column chromatography on silica gel using ethyl acetate and hexane yielding 6,6'-dimethyl-2,2'-bipyridine as a white solid (4.20 g, 60%).

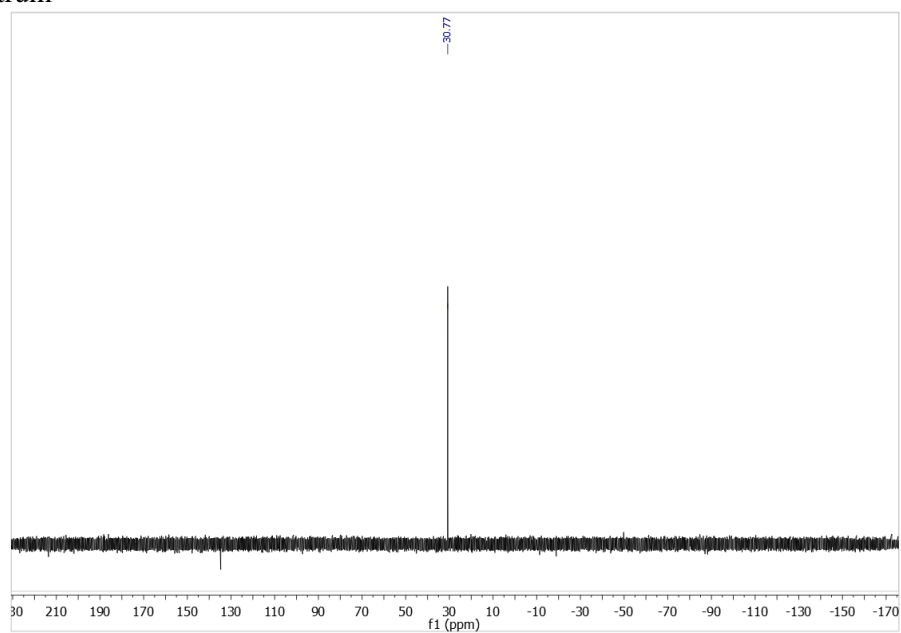
Synthesis of 2,2'-bipyridine-6,6'-dicarboxylic acid.⁶¹ The white solid 6,6'-dimethyl-2,2'-bipyridine (4.00 g, 0.0217 mol) was added to concentrated sulfuric acid (80 mL) cooled by an ice bath. Chromium trioxide (13.02 g, 0.1302 mol) was slowly added over 1 h, and the reaction mixture stirred at room temperature for 24 h. Ice was added and the mixture was filtered and the solid washed with water and dry in oven under vacuum (4.76 g, 90 %).

Synthesis of Ru (bda)(dmsO)₂.⁶² Under nitrogen atmosphere a mixture of 2,2'-bipyridine-6,6'-dicarboxylic acid (H₂bda) (1.001 g, 4.099 mmol) and Ru(dmsO)₄Cl₂ (1.984 g, 4.095 mmol) was added to a 20 mL vial and methanol (5 mL) was added to the vial, followed by Et₃N (0.3 mL), and the mixture refluxed for 24 h. The reaction mixture was allowed to cool, filtered and the solid washed with methanol (20 mL). The product dried under vacuum and the compound was obtained as red-brown solid (1.23 g, 60 %).

Synthesis of Ru (bda)(PPh₃)₂ 2.1: A 20 mL vial in the glove box was charged with Ru(bda)(dmsO)₂ (0.1000 g, 0.1994 mmol) and methanol (2.5 mL) was added. Another vial was charged with triphenylphosphine (0.1046 g, 0.3988 mmol) and methanol (2.5 mL) was added. The two suspensions were mixed together. The resulting mixture sonicated for 1 h, then was stirred overnight. The completion of reaction was verified by ³¹P NMR and filtered to give product (0.156 g, 92 %).



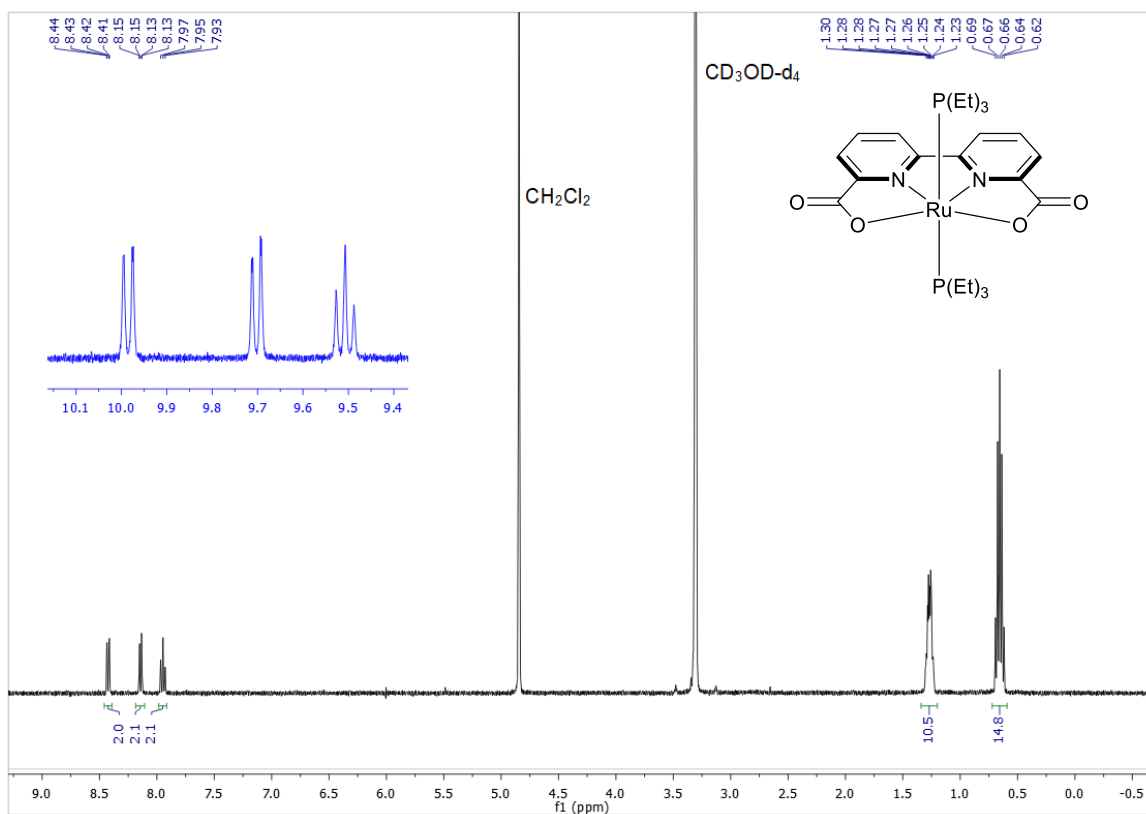
¹H NMR spectrum



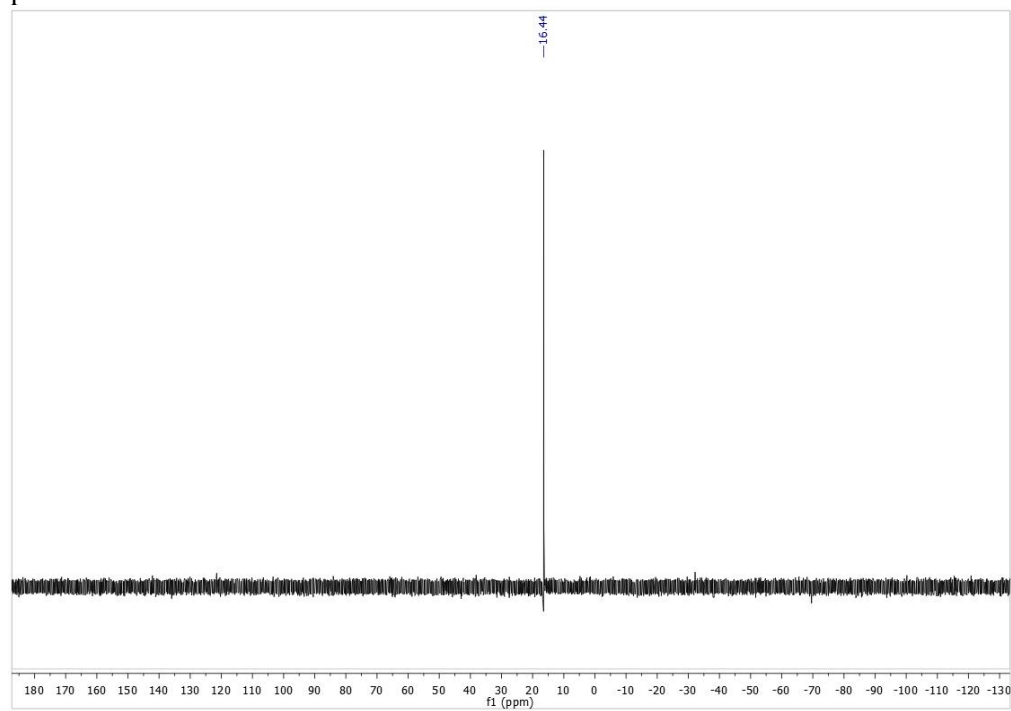
³¹P NMR spectrum

Synthesis of Ru(bda)(PEt₃)₂ 2.2: The Ru^{II} (bda)(dmsO)₂ complex (0.0500 g, 0.0997 mmol) were dissolved in methanol (10 mL) then triethylphosphine (0.0271 mL, 0.2004 mmol) was added. The reaction

mixture was stirred 12 h at room temperature. The suspension was filtered, and the brown filtrate solution was concentrated under vacuum. The residue was recrystallized from methanol (0.0348 g, 60%).

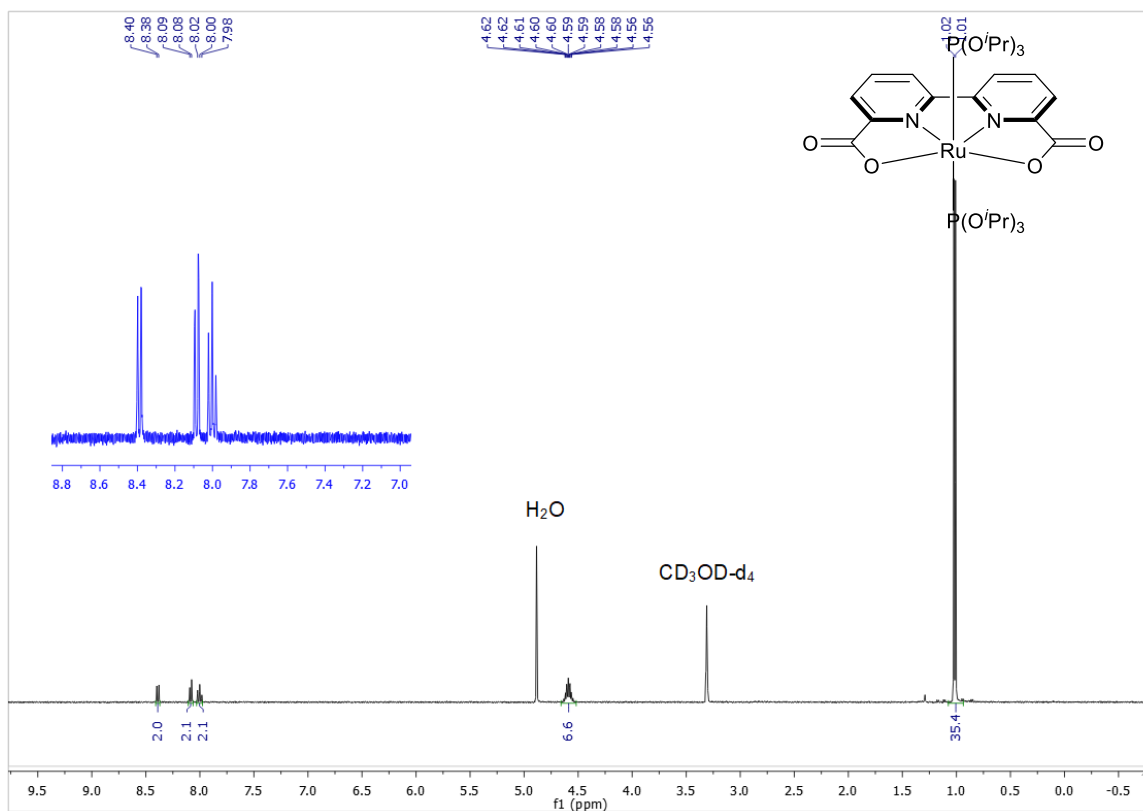


^1H NMR spectrum

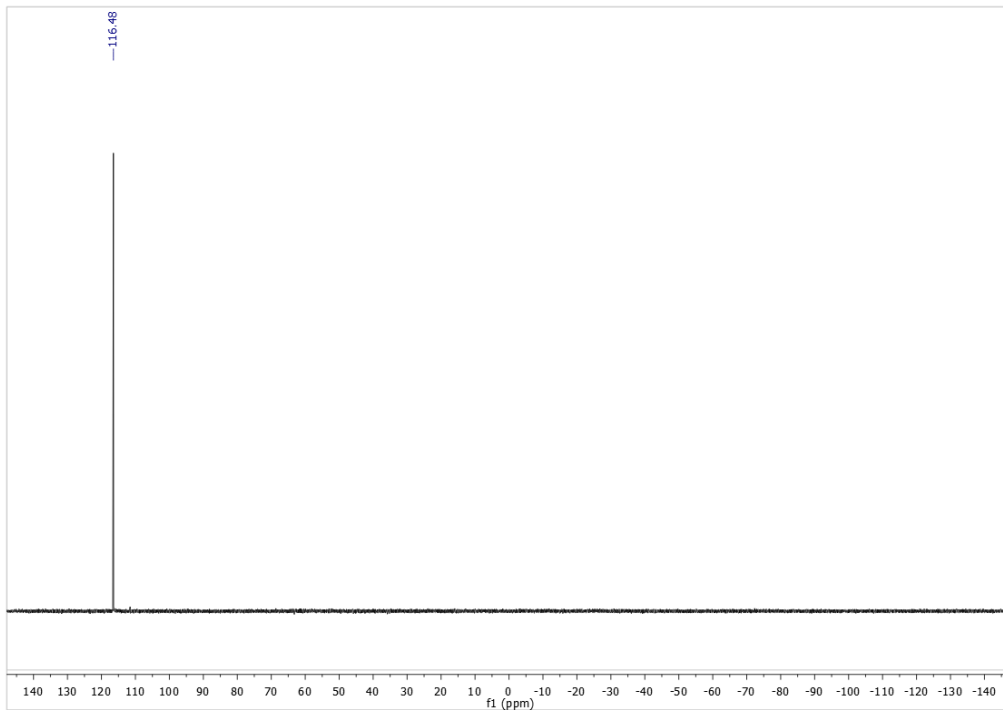


^{31}P NMR spectrum

Synthesis of Ru(bda)(P(OⁱPr)₂)₂ 2.3: Under N₂ atmosphere in a 20 mL vial Ru^{II}(bda)(dmsO)₂ (0.050 g, 0.0996 mmol) was added and CH₂Cl₂ (3.5 mL) was added. In a separate vial, triisopropyl phosphite (0.049 mL, 3.988 mmol) was added to CH₂Cl₂ (3.5 mL) and then the solution was added to the content of the other vial. The reaction mixture was stirred for 12 h. The reaction was filtered, and the filtrate was concentrated to dryness and product checked by ¹H and ³¹P NMR (0.0547 g, 72%).

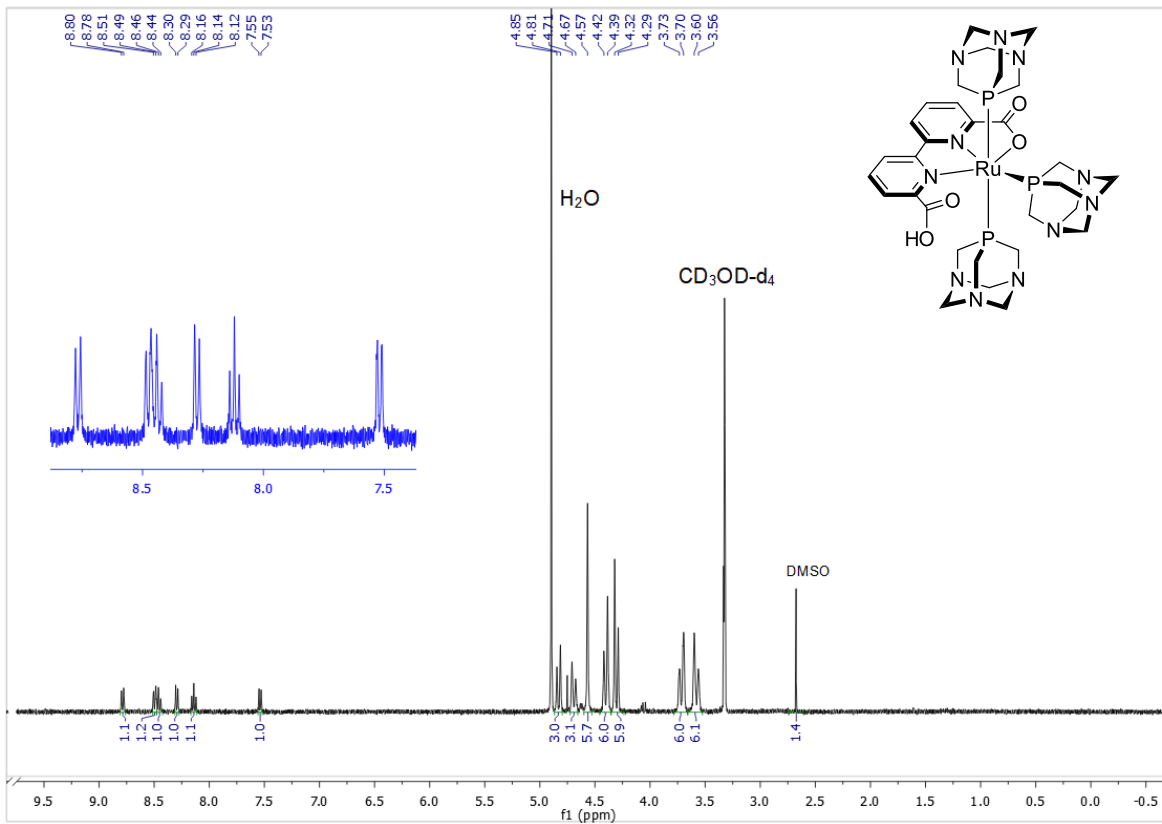


¹H NMR spectrum

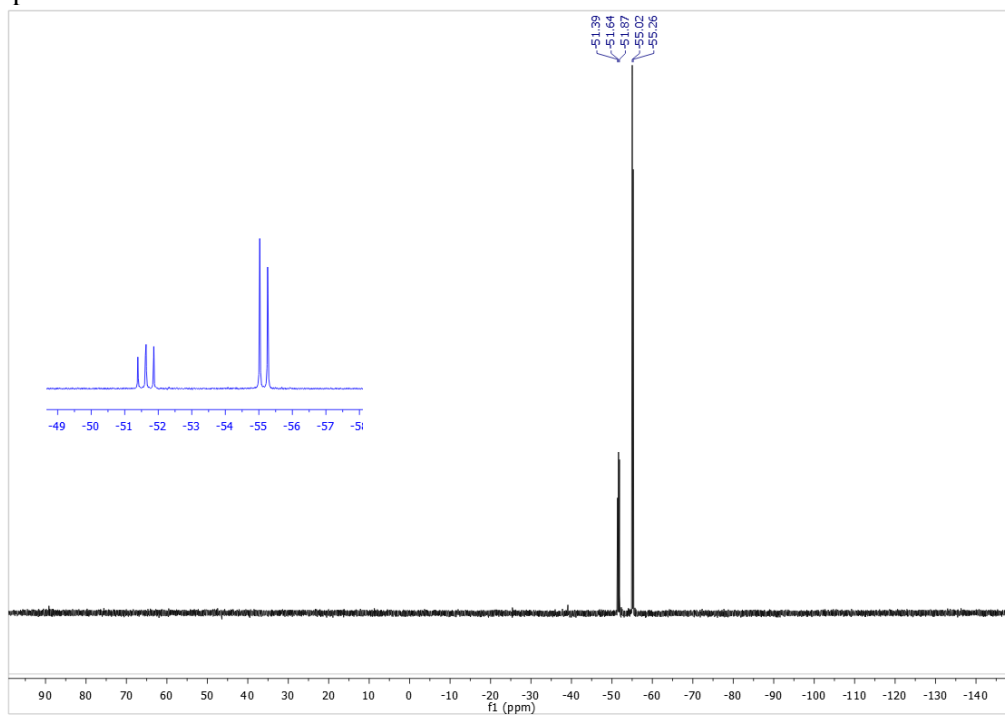


^{31}P NMR spectrum

Synthesis of Ru^{II} (bda)(PTA) $_3$ 2.4: Under N_2 atmosphere to Ru^{II} (bda)(dmsO) $_2$ (0.0311 g, 0.06200 mmol) was added methanol (1 mL). In a separate vial the 1,3,5-triaza-7-phosphaadamantane (0.0342 g, 0.1550 mmol) dissolved in methanol (1.5 mL total amount of methanol) and two precursor solutions were combined and the resulting mixture stirred at room temperature for 0.5 h. The mixture was filtered, and filtered solid was dried under vacuum. The obtained orange solid was washed with methanol (0.5 mL) (0.0475 g, 86%).

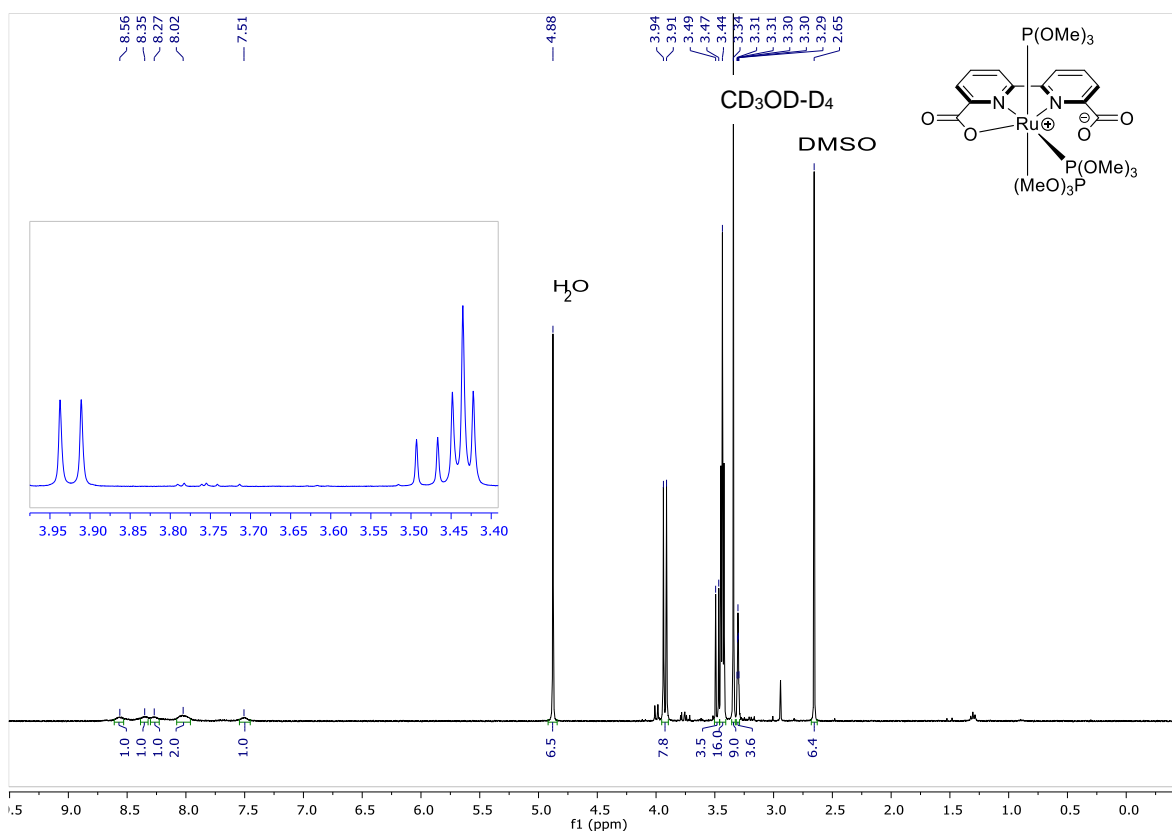


¹H NMR spectrum

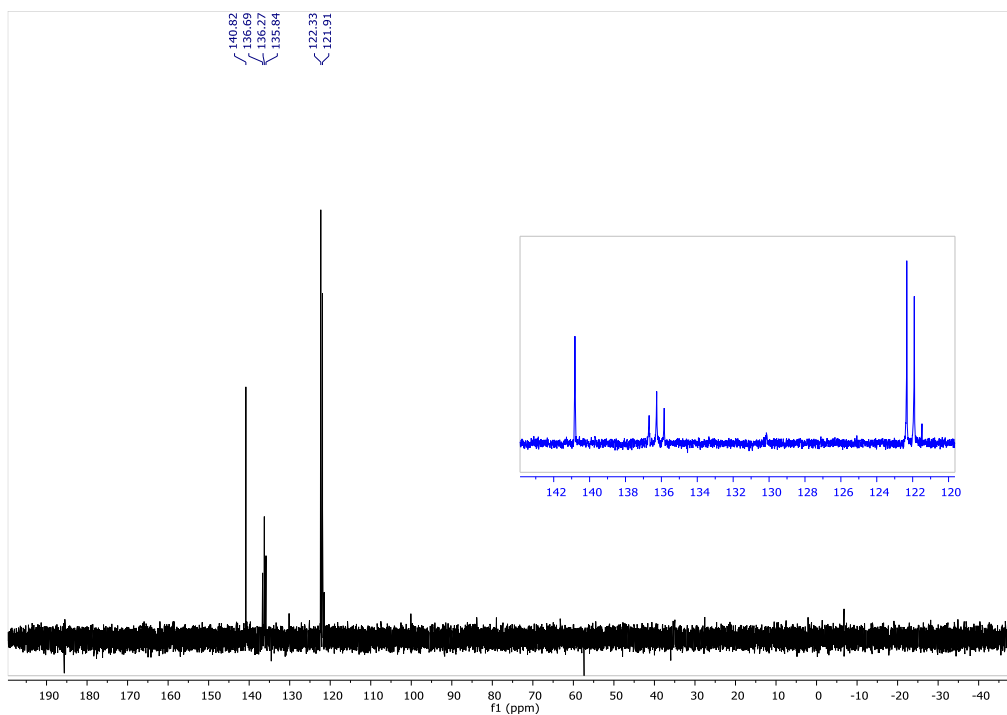


³¹P NMR spectrum

Synthesis of Ru^{II} (bda)(POMe)₃ 2.5: Under N₂ atmosphere to Ru^{II} (bda)(dmsO)₂ (0.0311 g, 0.06200 mmol) was added methanol (1 mL). Then trimethylphosphine (0.007 g, 0.0933 mmol) was added and the resulting mixture stirred at room temperature for few hours till the yellow solid appear. The mixture was filtered and filtered solid was dried under vacuum. The obtained orange solid was washed with small amount of methanol (0.5 mL) (0.0184 g, 50%).



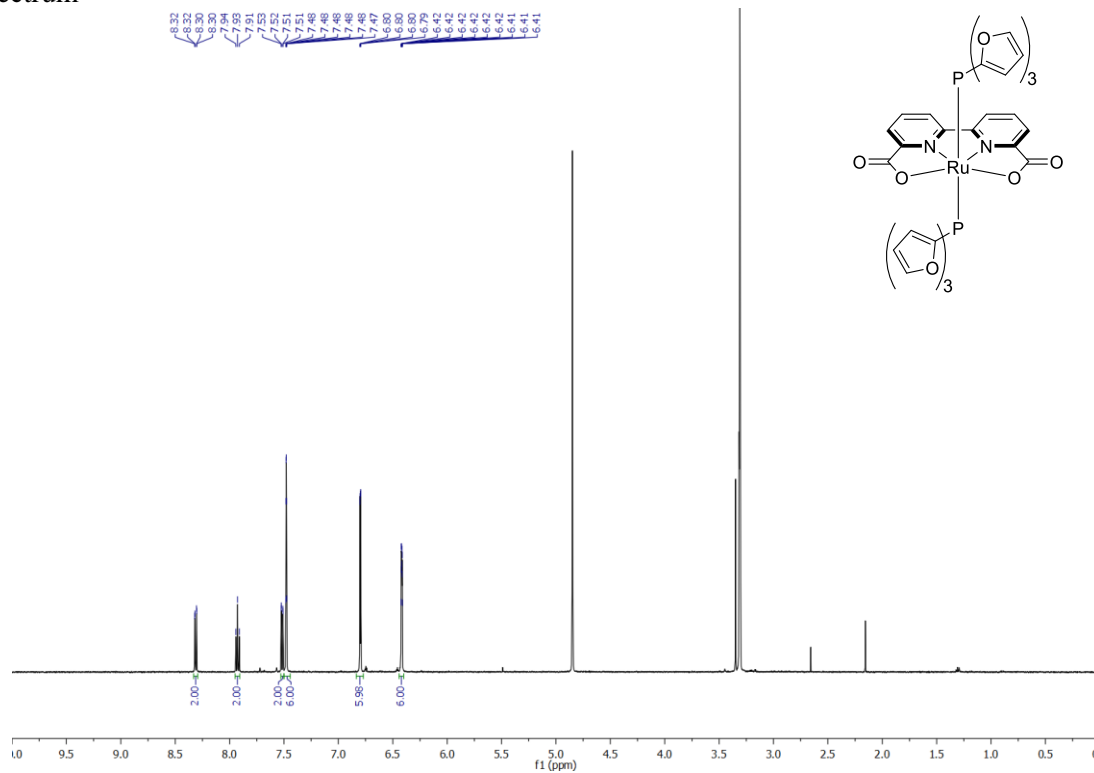
¹H NMR spectrum



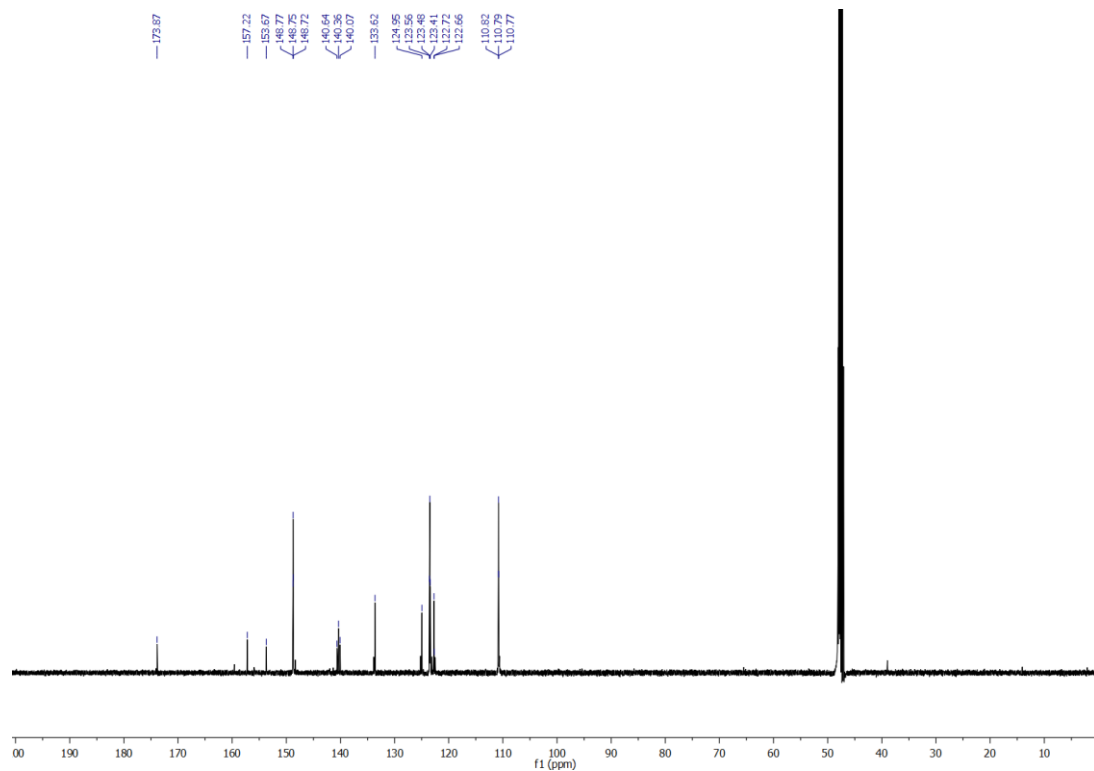
^{31}P NMR spectrum

Ru(bda)[tris(2-furyl)phosphine]₂ 2.6 was isolated in 90% yield (0.145 g) and as a yellow fine solid. ^1H NMR (500 MHz, Methanol-*d*₄) δ 8.31 (dd, $J = 8.1, 1.0$ Hz, 2H), 7.93 (t, $J = 7.9$ Hz, 2H), 7.52 (dd, $J = 7.8, 1.0$ Hz, 2H), 7.48 (dt, $J = 1.6, 0.8$ Hz, 6H), 6.80 (dd, $J = 3.5, 0.7$ Hz, 6H), 6.42 (ddd, $J = 3.4, 1.6, 0.8$ Hz, 6H). $^{13}\text{C}\{^1\text{H}\}$ NMR (126 MHz, Methanol-*d*₄) δ 173.9 (s), 157.2 (s), 153.7 (s), 148.8 (vt, $N = 5.4$ Hz), 140.4 (vt, $N = 71.2$ Hz), 133.6 (s), 124.9 (s), 123.5 (vt, $N = 18.6$ Hz), 122.7, 110.8 (t, $J = 3.3$ Hz). ^{31}P NMR (202 MHz, Methanol-*d*₄) δ -4.62 ppm.

^1H spectrum

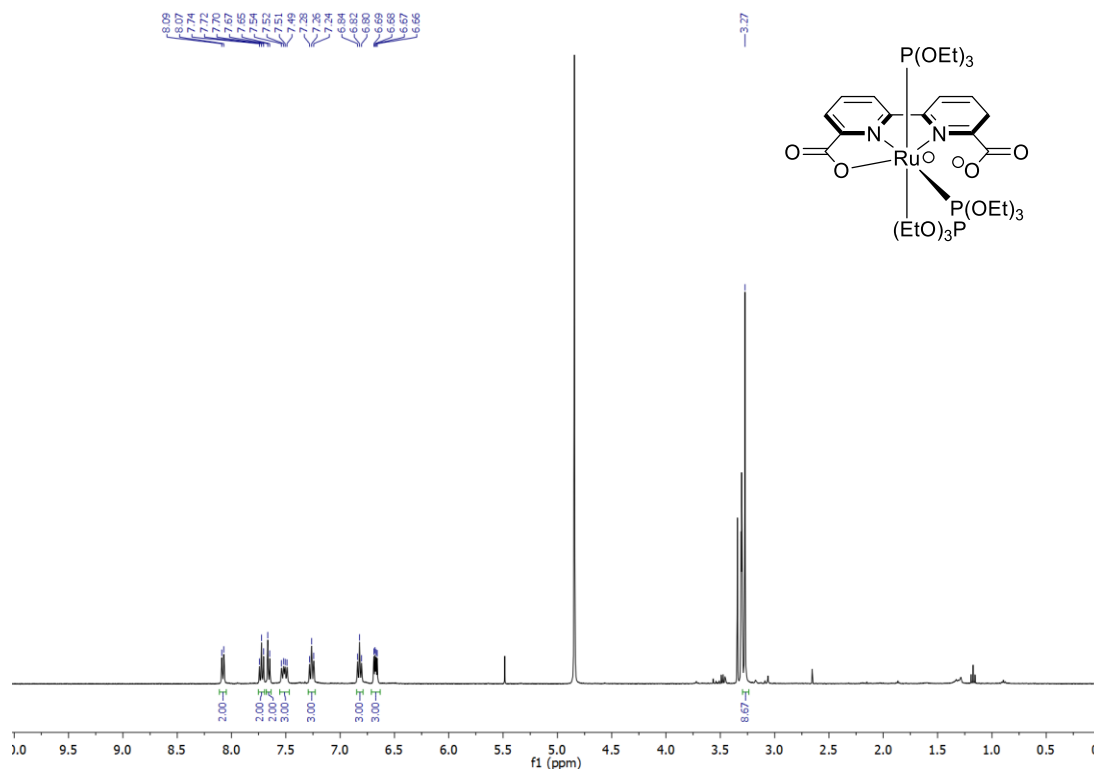


$^{13}\text{C}\{^1\text{H}\}$ spectrum



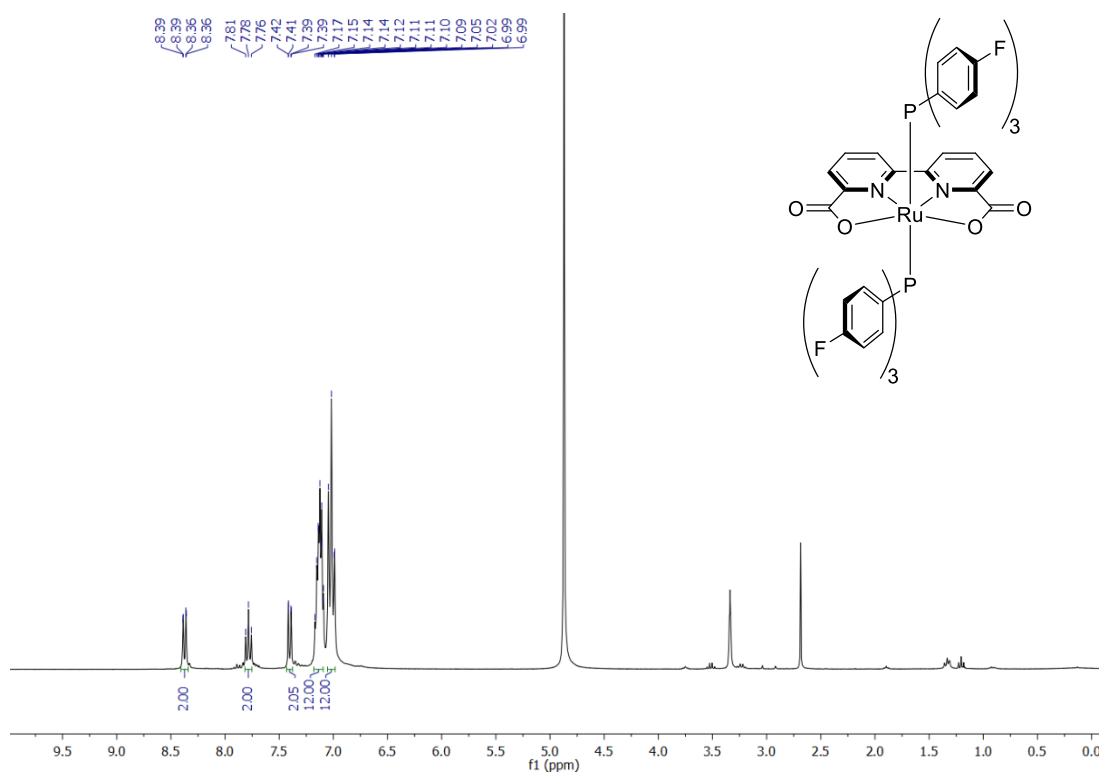
Ru(bda)[tris(2-methoxyphenyl)phosphine]₂ 2.7 was isolated in 75% yield (0.156 g) as a red brownish solid. ¹H NMR (400 MHz, Methanol-*d*₄) δ 8.08 (d, *J* = 7.2 Hz, 2H), 7.72 (t, *J* = 7.8 Hz, 2H), 7.66 (d, *J* = 7.1 Hz, 2H), 7.51 (dd, *J* = 12.9, 7.3 Hz, 3H), 7.26 (t, *J* = 7.8 Hz, 3H), 6.82 (t, *J* = 7.5 Hz, 3H), 6.67 (dd, *J* = 8.1, 4.4 Hz, 3H), 3.27 (s, 9H). ³¹P NMR (162 MHz, Methanol-*d*₄) δ 23.74 ppm.

¹H spectrum

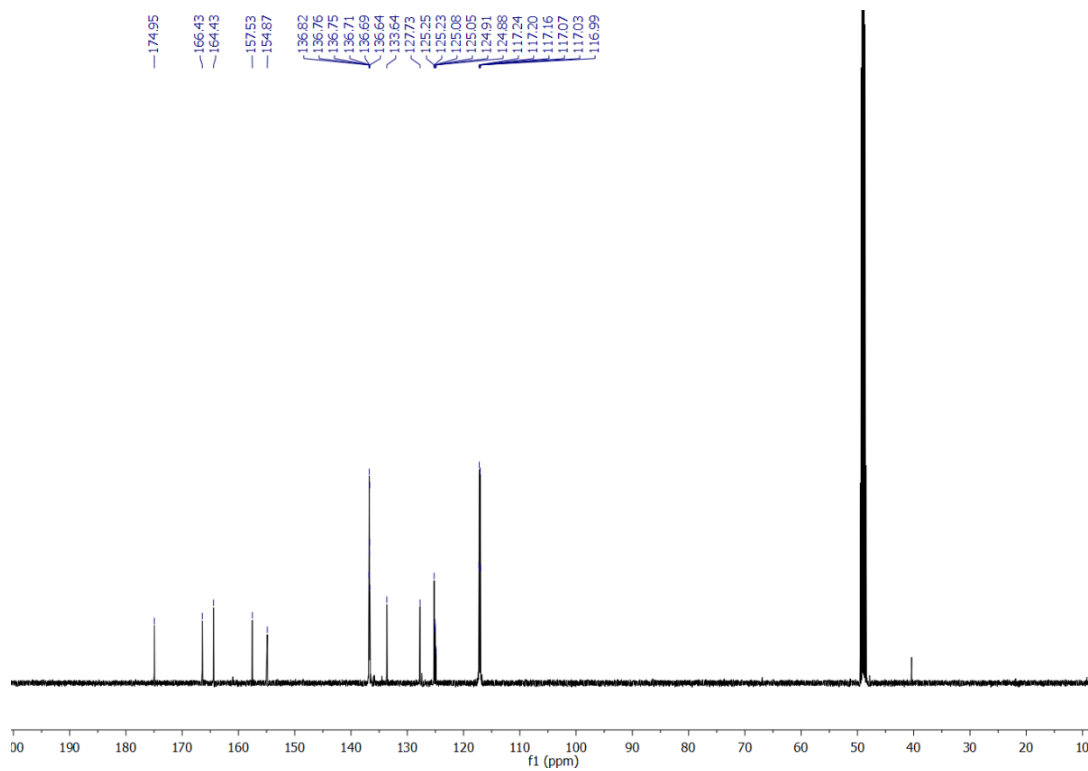


Ru(bda)[tris(4-fluorophenyl)phosphine]₂ 2.8 was isolated in 81% yield (0.157 g) as a greenish solid. ¹H NMR (300 MHz, Methanol-*d*₄) δ 8.37 (dd, *J* = 8.1, 1.1 Hz, 2H), 7.78 (t, *J* = 7.9 Hz, 2H), 7.40 (dd, *J* = 7.8, 1.0 Hz, 2H), 7.13 (dq, *J* = 6.5, 5.0 Hz, 12H), 7.02 (t, *J* = 8.3 Hz, 12H). ¹³C{¹H} NMR (126 MHz, Methanol-*d*₄) δ 174.9, 166.4, 164.4, 157.5, 154.9, 136.7 (dvt, *N* = 13.8, *J*_{C-F} = 8.4 Hz), 133.6, 127.7, 125.7 (dvt, *N* = 36.8, *J*_{C-F} = 21.9 Hz), 117.1 (dvt, *N* = 10.4, *J*_{C-F} = 21.6 Hz). ³¹P{¹H} NMR (121 MHz, Methanol-*d*₄) δ 30.54 ppm.

^1H spectrum

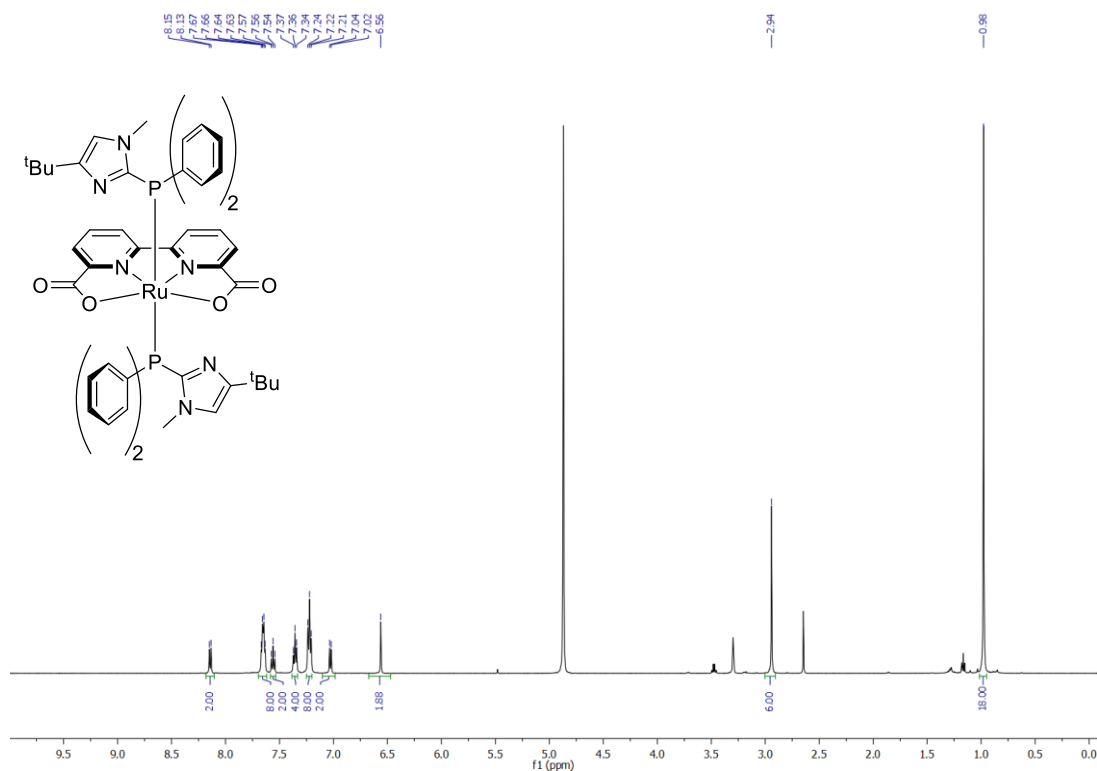


$^{13}\text{C}\{^1\text{H}\}$ spectrum of $\text{Ru}(\text{bda})[\text{tris}(4\text{-fluorophenyl)phosphine}]_2$ 2.8

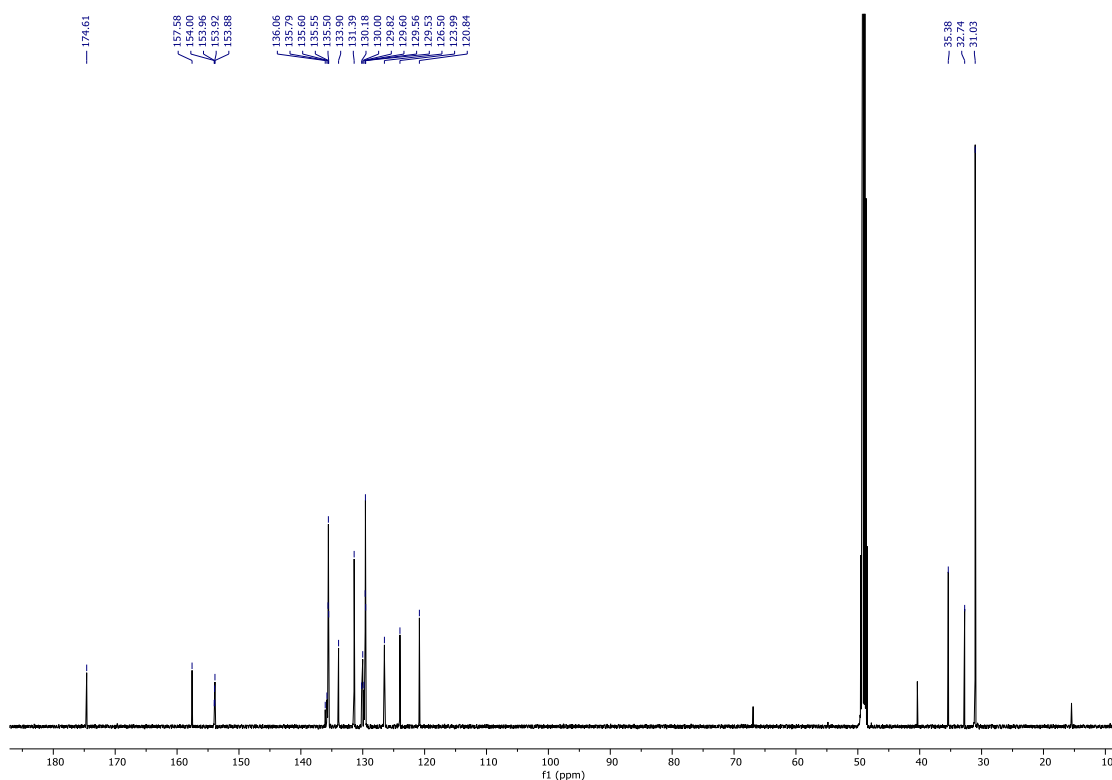


Ru(bda)[(4-(tert-butyl)-2-(diphenylphosphino)-1-methyl-1H-imidazole)]₂ 2.9 was isolated in 90% yield (0.177 g) as a greenish solid. ¹H NMR (500 MHz, Methanol-*d*₄) δ 8.14 (d, *J* = 7.9 Hz, 2H), 7.65 (dd, *J* = 12.2, 5.4 Hz, 8H), 7.56 (t, *J* = 7.9 Hz, 2H), 7.36 (t, *J* = 7.4 Hz, 4H), 7.22 (t, *J* = 7.6 Hz, 8H), 7.03 (d, *J* = 7.6 Hz, 2H), 6.56 (s, 2H), 2.94 (s, 6H), 0.98 (s, 18H). ¹³C{¹H} NMR (126 MHz, Methanol-*d*₄) δ 174.6, 157.6, 153.9 (vt, *N* = 19.6 Hz), 136.06, 135.79, 135.5 (vt, *N* = 12.4 Hz), 133.9, 131.4, 130.0 (vt, *N* = 46.7 Hz), 129.6 (vt, *N* = 9.8 Hz), 126.5, 124.0, 120.8, 35.4, 32.7, 31.0. ³¹P{¹H} NMR (202 MHz, Methanol-*d*₄) δ 25.22 ppm.

¹H spectrum



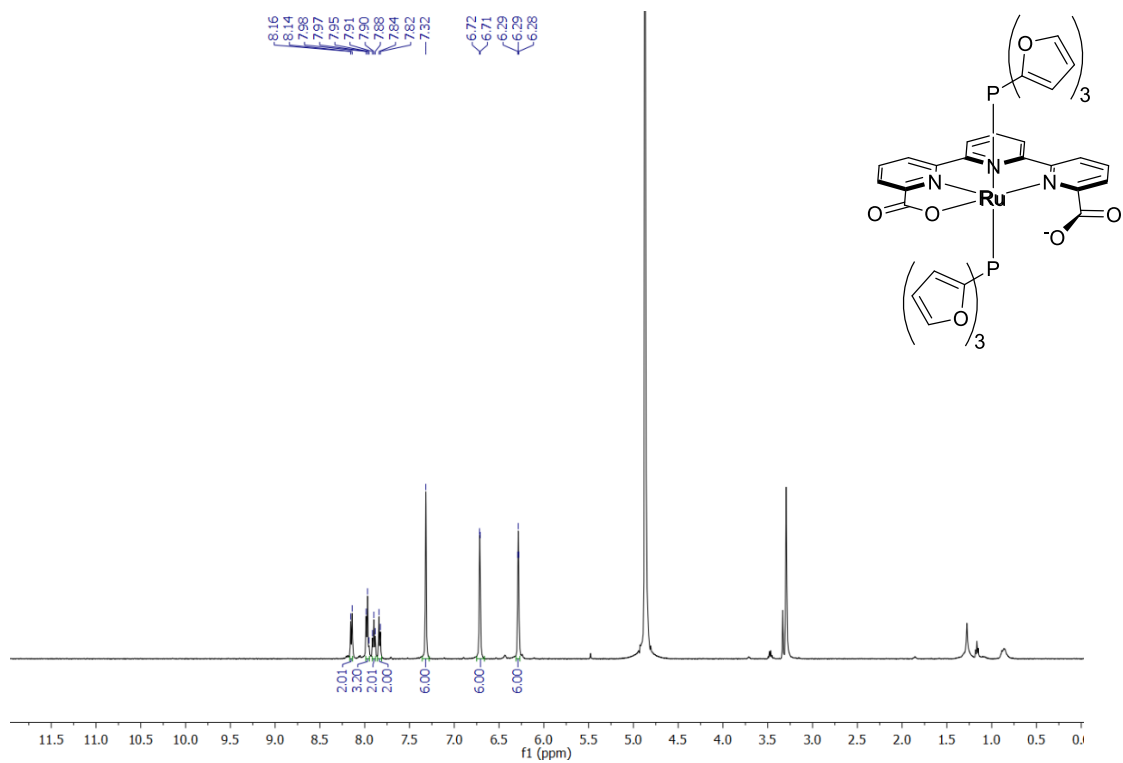
$^{13}\text{C}\{^1\text{H}\}$ spectrum



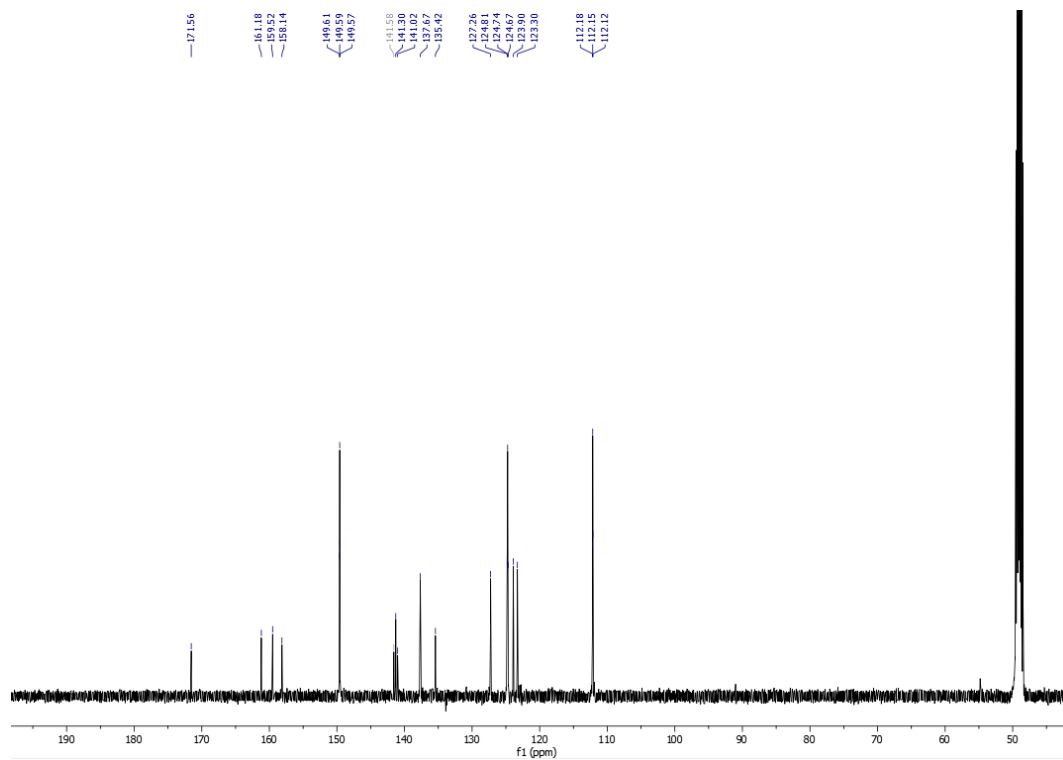
Procedure for synthesizing complex 2.10

The procedure of Llobet *et al.*² was used for the first step: a 1:1 molar ratio of $\text{RuCl}_2\text{DMSO}_4$ and H_2tda in Et_3N and dry MeOH was refluxed for 6 hours and cooled to room temperature. A brown solid appeared in the reaction mixture, which was filtered, and washed with methanol and ether.² The resulting solid (which is highly insoluble) was used for the next step without further purification and was assumed to have the formula $\text{Ru}(\text{tda})(\text{DMSO})_2$. In the glove box, a 20 mL scintillation vial was charged with the assumed $\text{Ru}(\text{tda})(\text{DMSO})_2$ (0.050 g, 0.0996 mmol, 1 equiv), followed by dry methanol (10 mL), resulting in a suspension. Then tris(2-furyl)phosphine) (0.0463 g, 0.1992 mmol, 2 equiv) was added to the suspension, and the mixture was stirred at 70 °C for 3 days. The solvents were removed by high vacuum, and the residue was crystallized from methanol (yield 51%, 0.045 g).

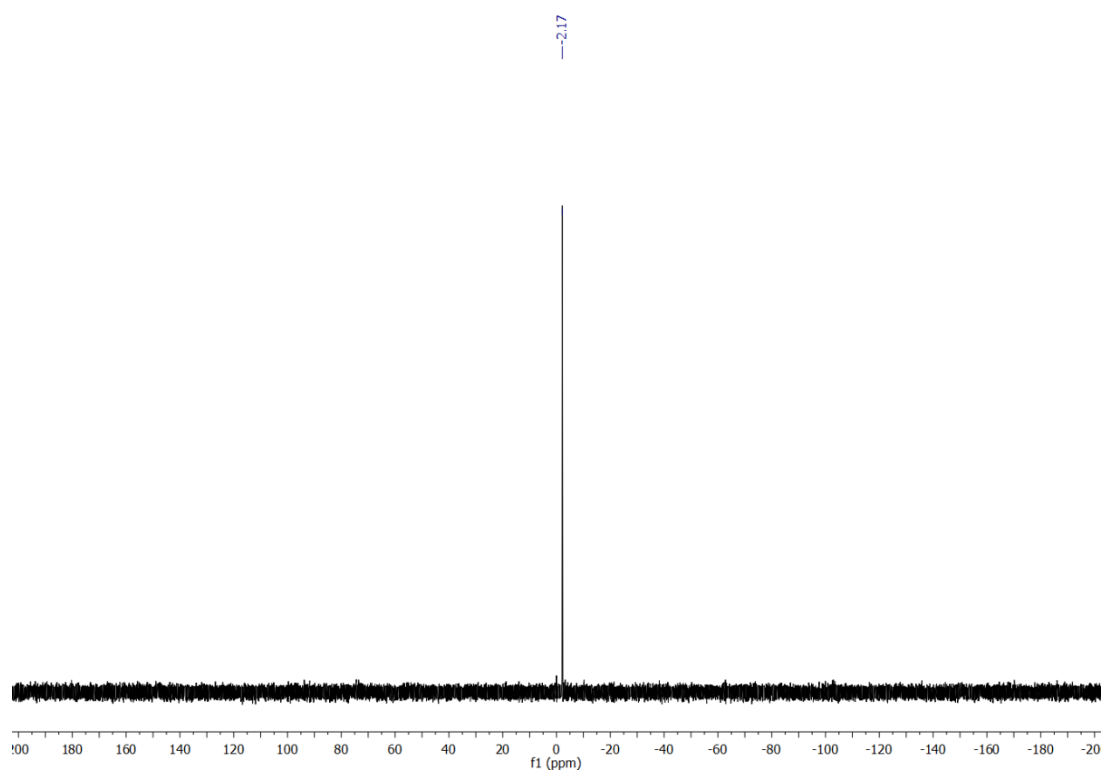
^1H spectrum



$^{13}\text{C}\{^1\text{H}\}$ spectrum



$^{31}\text{P}\{^1\text{H}\}$ spectrum



Chapter 3

Trans-spanning ligands with a macrocyclic cavity, capable of stabilizing a water oxidation catalyst

3.1. Introduction

As mentioned before, most of WOC research focuses on making faster catalysts for oxidation of the water. In this chapter not only we did aim to synthesize fast catalysts, but also we attempted to slow the rate of catalyst degradation to create long-lived catalysts. According to the literature, one of the challenges with the best WOCs is proposed to be separation of at least one axial ligand during harsh testing conditions.¹

Our strategy in this chapter is to use chelating ligands to reduce the chance of ligand loss. We proposed designing a trans-spanning macrocyclic ligand, which holds two pyridine-derived ligands in proper distance from both sides of the ruthenium center. With this design, we use the chelate effect to stabilize the complex; if one pyridine dissociates, the linker will keep it close to re-coordinate.

Macrocyclic ligands are known in literature, but they have small cavities **3.1**. For instance, Hu and coworkers in 2002⁹³ and recently Erdelye group,^{94,95,96} proposed a trans-bis(pyridine)ligand **3.1** containing linear fragments like Au⁺ or I⁺, or small square-planar fragments like PdCl₂ (**3.1b-3.1d**) for different catalytic reactions. In a study of Suzuki et al., the trans-chelating dinitrogen ligand coordinated to the arylpalladium(II) (**3.1e**) improved the coupling reaction of arylboronic acids with aromatic halides.⁹⁷ More interestingly, a novel mononuclear iron(II) Schiff base-like pincer complex (**3.1f**) remains in the high spin state (HS) at different temperatures due to the steric hindrance between the triple bond of the pincer ligand and the Schiff base-like ligand.⁹⁸

In addition, trans-spanning metal complexes are capable of self-assembly formation of the two- and three-membered ring complexes (**3.1g**) in solution.⁹⁹

However, the ligand **3.1** is not proper for our purpose because the cavity between nitrogens is too small for fitting Ru(κ^4 -bda) or other metal fragments of significant size in the right orientation, as will be discussed below.

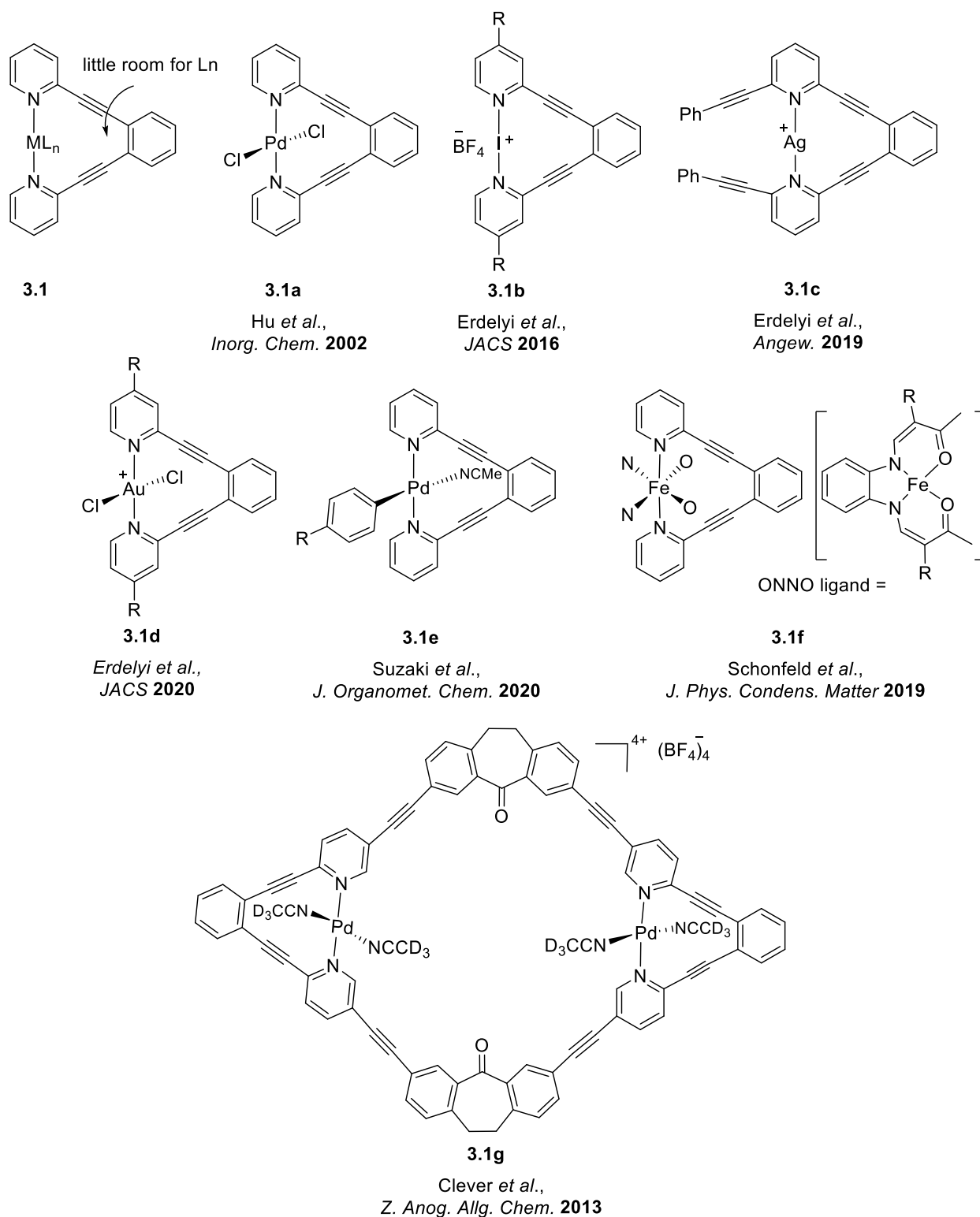


Figure 3.1. Selected known metal complexes bearing a trans-chelating dinitrogen ligand in literature.

Sun's group reported a binuclear catalyst containing two Ru(bda) units, which are linked using a linker bearing an imidazole at each end and $-(\text{CH}_2)_4$ **3.2** and $-\text{CH}_2\text{C}_6\text{H}_4\text{CH}_2-$ **3.3** spacers (Figure 3.2).¹⁰⁰ They designed this structure to minimally perturb the original structure of the Ru(bda)(pyridine-derived)₂ complexes, while also holding two Ru(bda) units in a non-rigid structure. In complexes **3.2** and **3.3** they used imidazole as the axial ligands because modification of the imidazole is much easier than that of pyridine. During water oxidation catalysis with Ce^{IV} , dimer **3.3** showed a better activity, reaching a TON of 42,840 ($[\text{Cat.}]_0$ 0.25 μM , $[\text{Ce}^{\text{IV}}]_0$ 10 mM, pH 1.0 in aqueous $\text{CF}_3\text{SO}_3\text{H}$ solution). The kinetics of oxygen evolution for dimer **3.3** was found to be first order reaction with respect to catalyst concentration. Authors suggested that using a large excess of Ce^{IV} decomposed the catalyst.¹⁰⁰ Sun et al. concluded that contrary to the conventional beliefs in the literature, a rigid connecting ligand is not necessary for improving bimetallic WOC.

In support of the Sun group's statement and as an example of the binuclear ruthenium complex with a rigid linker, we can mention the report of Gao et al.,¹⁰¹ in which a dinuclear ruthenium catalyst with a rigid xanthene **3.4** bridge for WOC was synthesized. It was not surprising that they reported a low catalytic water oxidation activity for **3.4** with a first-order reaction in catalyst kinetic mechanism. They rationalized low activity of **3.4** by the steric hindrance effects of the rigid linker and bda ligand which could disfavor forming the face-to-face configuration of the two active sites in one dimer molecule.¹⁰¹

Sun and coworkers expanded the field of multinuclear Ru framework for WOC. They believe that presence of more Ru metal centers in a single molecular catalyst is advantageous because the probability of O-O bond formation through intramolecular radical coupling would increase and ultimately the catalytic activity would be enhanced.¹⁰² Based on this hypothesis, they designed a trinuclear ruthenium bearing bda ligands **3.5** which displayed a better catalytic activity compared to the mononuclear catalyst **1.5** and achieved a high TON 86,498 ($[\text{Cat.}]_0 = 0.5 \mu\text{M}$, $[\text{Ce}^{\text{IV}}]_0 = 0.5 \text{ mM}$, in $\text{CF}_3\text{SO}_3\text{H}$ solution and pH 1.0). Water oxidation reactions of catalyst **3.5** confirm a first-order reaction in both $[\text{Ce}]_0$ and $[\text{Cat.}]_0$.¹⁰²

Würthner's group also actively are working on creating active WOCs by incorporation of several catalytically active Ru(bda) fragments into macrocycles. They reported a series of trinuclear complexes

connecting three Ru(bda) fragments with ditopic axial bridging ligands to form macrocycles **3.6**.¹⁰³ The activity of this trinuclear metallosupramolecular macrocycle increased in comparison to the mononuclear analogs as seen by TON = 7,400 ([Cat.]₀ = 24.3 μM, [Ce^{IV}]₀ = 536 mM, pH 1, using CF₃SO₃H). However, due to the large molecular size of this macrocycle, the solubility in water is very low, therefore, they performed reactions in the presence of an unusually high amount of the organic solvents (> 50% in some cases) (CH₃CN/H₂O (pH 1) 6: 4).^{104,105,106} Minor fragmentation during testing was observed by the loss of one bridging ligand, which is known to be main degradation pathway in the mononuclear case as well.¹⁰⁶

Metallosupramolecular WOCs are not limited to the Ru(bda) frameworks; the Ru(bpp) (bpp = 3,5-bis(2-pyridyl)pyrazolate) catalysts have been of interest because of their I2M mechanism.^{1001,107,108,109} However, a challenge with using Ru(bpp) complexes is the consumption of the bpp ligands during water oxidation testing causing degradation of the catalyst. Therefore, Llobet and others envisaged that by encapsulating or heterogenising the molecular catalyst in MOFs they might overcome this limitation.^{110,111,112}

Llobet and coworkers designed a metal organic framework (MOF) incorporating a Ru(bpp) water oxidation catalyst in a hexametalllic [Fe₂Ru₄] macrocycle **3.7**, which has two catalyst units linked by two [Fe(R-trpy)₂] (trpy = terpyridine) bridges. Unfortunately, similar catalytic activity was seen when compared to the non-cyclic catalyst precursors.¹¹³

Based on the aforementioned discussion, we can say that the incorporation of the Ru sub-units into macrocyclic frameworks could be beneficial to enhance the stability of the catalyst, but there is also a chance that they are not beneficial.

Therefore, we designed a monometallic macrocycle which benefits from the Ru(bda) structure and has a large cavity inside of the bridging ligand. We assumed a few parameters for designing our macrocycle: 1) the new bridging ligand should hold the two pyridine-derived ligands in the right position, placing the nitrogens 4 to 4.5 Å apart, on opposite sides of the ruthenium (trans). 2) We assumed that stability can be improved by the chelate effect of the bridging ligand, reducing the amount of self-oxidation because steric constraints allow only small molecules to reach the catalytic center. 3) We envisaged that the rigid cyclic

structure may hinder dimerization of two catalytic subunits, therefore, possibly favoring the unimolecular WNA mechanism, but this will need to be investigated. 4) Another advantage is that the large cavity presents no hindrance to the metal to interact with H₂O and water nucleophilic attack and absorption of protons. For the purpose of the water oxidation, a large cavity is needed to allow water molecules to access the catalytic site.

In this chapter we present the synthesis of a series of Ru(bda) macrocycles by manipulating the length and structure of the bridging ligand.

Some parts of this chapter contain materials similar to the manuscript in preparation: Yazdani, S.; Breyer, C. J.; Kumari, P.; Rheingold, A. L.; Jazzar, R.; Bertrand, G.; Grotjahn, D. B. Trans-Spanning Ligands with a Macrocyclic Cavity, Capable for Water Oxidation. *In Preparation*.

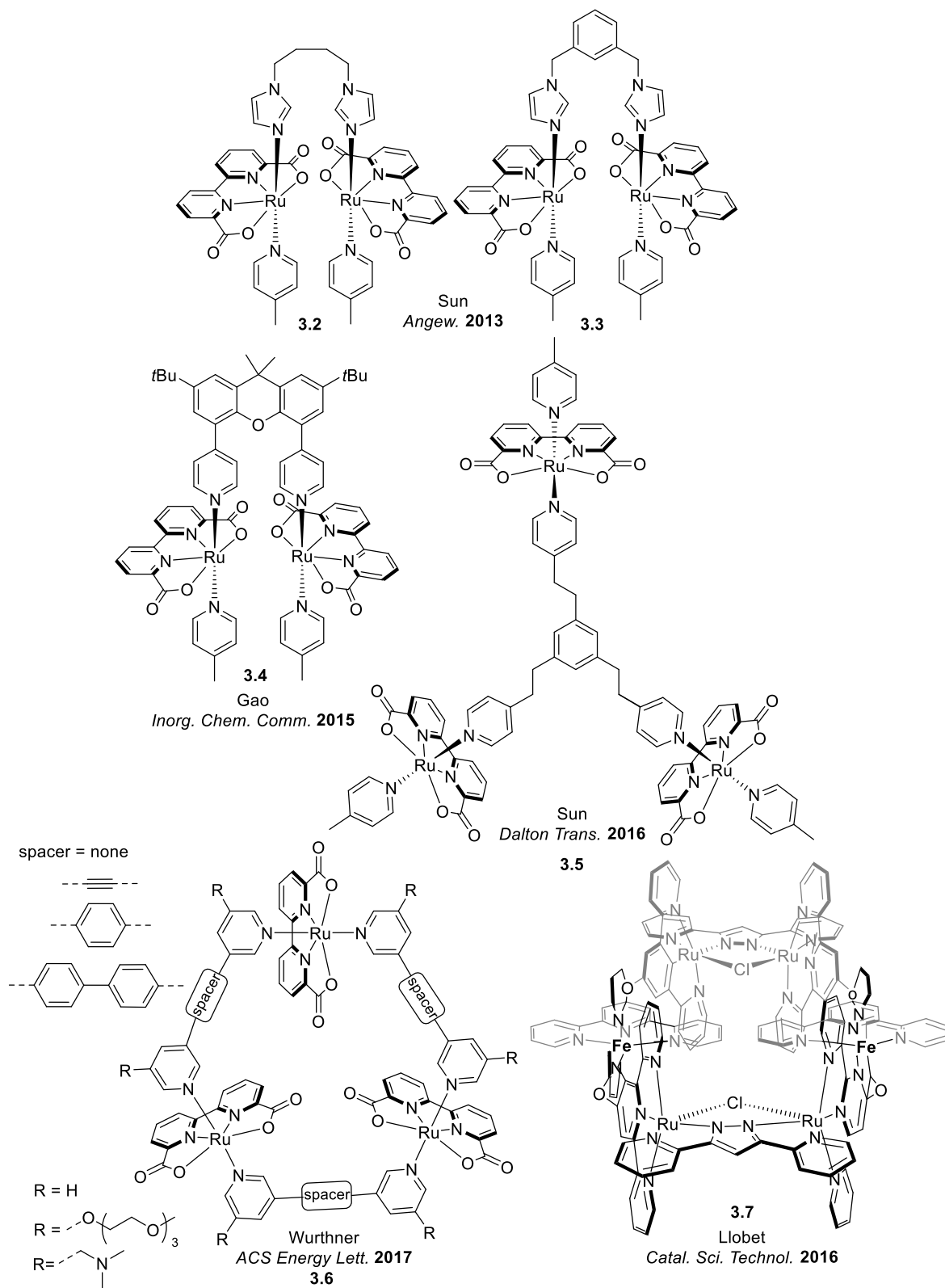


Figure 3.2. Bridged and macrocyclic ruthenium complexes used as a molecular water oxidation catalysts.

3.2 Designing first novel ruthenium bda macrocycle

We designed novel trans-spanning ligand **3.11** because we wanted to examine the hypothesis that loss of an axial pyridine derived ligand degraded WOCs based on the Ru^{II}(bda) scaffold. Above, we explained the need to bridge the two axial ligands to prevent their coordination; here we will explain why we need a large cavity.

There is reasonable evidence from Sun's group that Ru(bda) complexes of type **3.8** undergo oxidation and activation of water to form Ru^V=O intermediates which in many cases create dioxygen by coupling of two oxo ligands **3.9** (Figure 3.3) on two molecules of Ru^V=O.^{1,114}

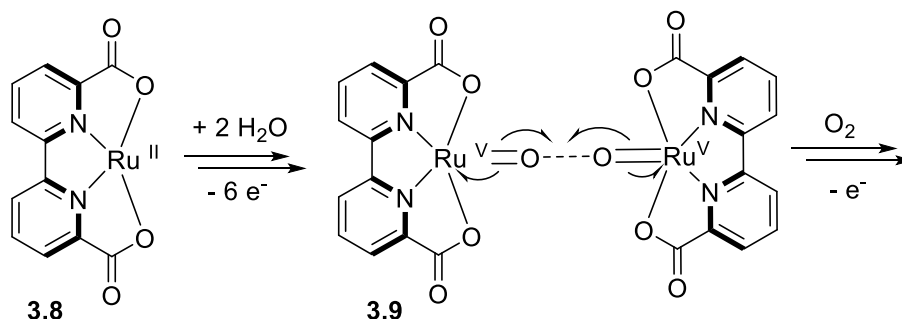


Figure 3.3. Oxidation of the Ru(bda) complex and formation of the Ru^V-oxo intermediates.

Therefore, Dr. Grotjahn designed a novel macrocycle which has enough room through bridging two pyridine-containing heterocycles by an alkyne **3.11** and performed a preliminary study.¹¹⁵ The synthesis of this complex was straightforward. For the metalation step, we first attempted to use the standard methods we used for a previous project (see the synthesis of Ru(bda)(PPh₃)₂; experimental section 2.3). However, when we tried reaction of the ligand and Cl₂Ru(DMSO)₄ in presence of excess amine base, a lot of side reactions happened, including apparent reduction of the alkyne to an alkene. After some experimentation, we were able to make **3.10** with Cl₂Ru(CH₃CN)₂ possibly because less steric restrictions. Ultimately, our group successfully made the target **3.11** by using **3.10** and bda, plus di-isopropylethylamine and heating at 70 °C for 2 days (Figure 3.4).

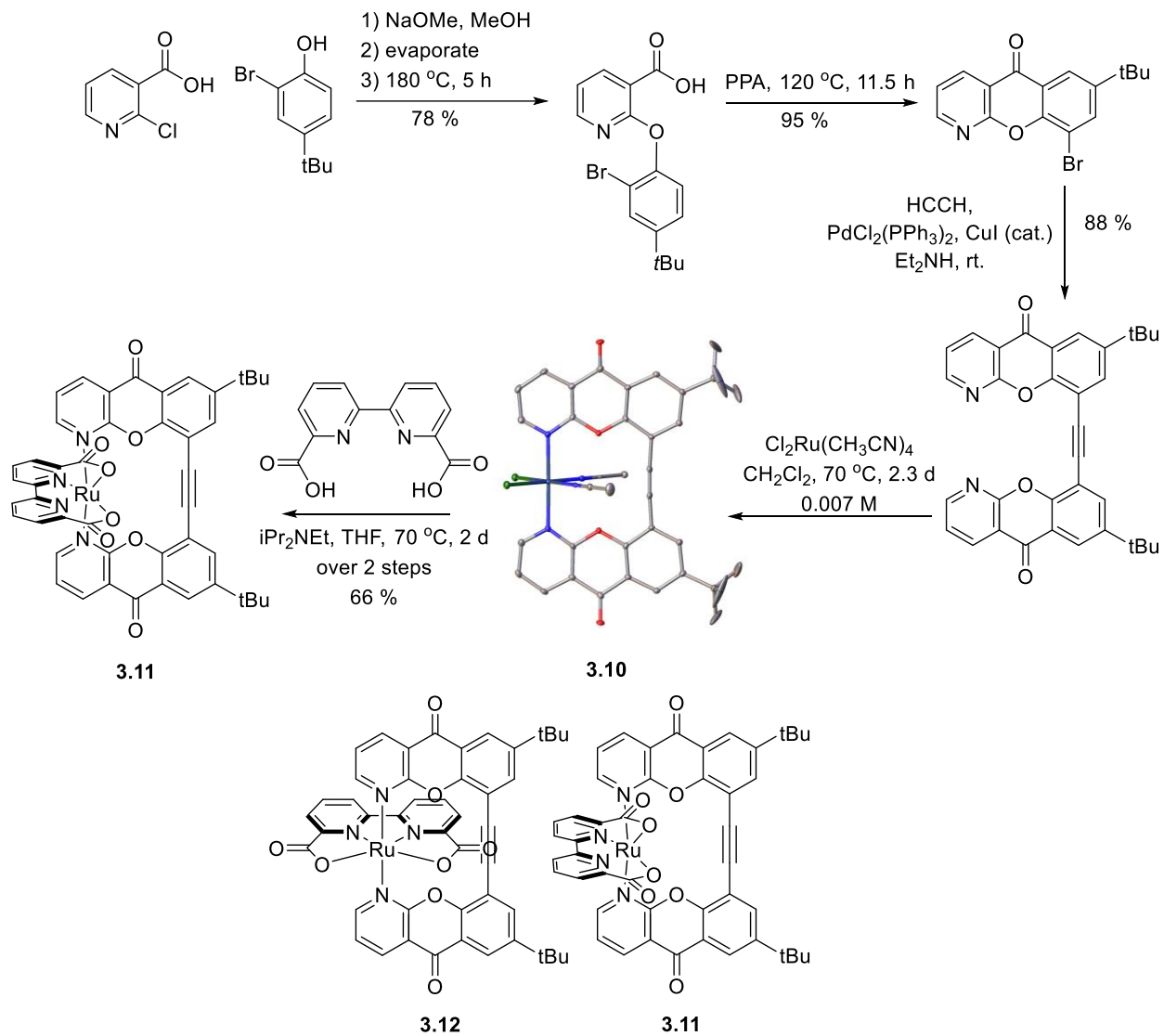


Figure 3.4. Synthetic procedure for making **3.11**. X-ray crystal structure of the trans-spanning ligand complex shows a moderate sized cavity. **3.12** shows the geometry needed for effective catalysis.

The x-ray structure of the **3.10** in Figure 3.4 shows N-N = 4.196 Å and N-Ru-N = 180.0° (for comparison, Sun's compound **1.5** analog; N-N = 4.146 Å and N-Ru-N = 173.0°)³. By seeing this X-ray structure we envisaged that there is likely not enough space to favor coordination of the bda ligand. We need two molecules of Ru^V-oxo to come within O-O bonding distance (Figure 2.23), unless the WNA mechanism operates and possibly in case of the **3.11** one carboxylate group would be repelled by the alkyne connector as illustrated by **3.12** in Figure 3.4. In **3.11**, placing the oxo inside the cavity makes the oxo neither accessible to a second oxo unit, nor to WNA.

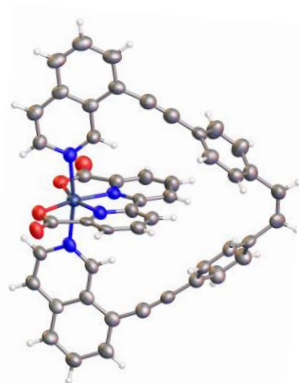
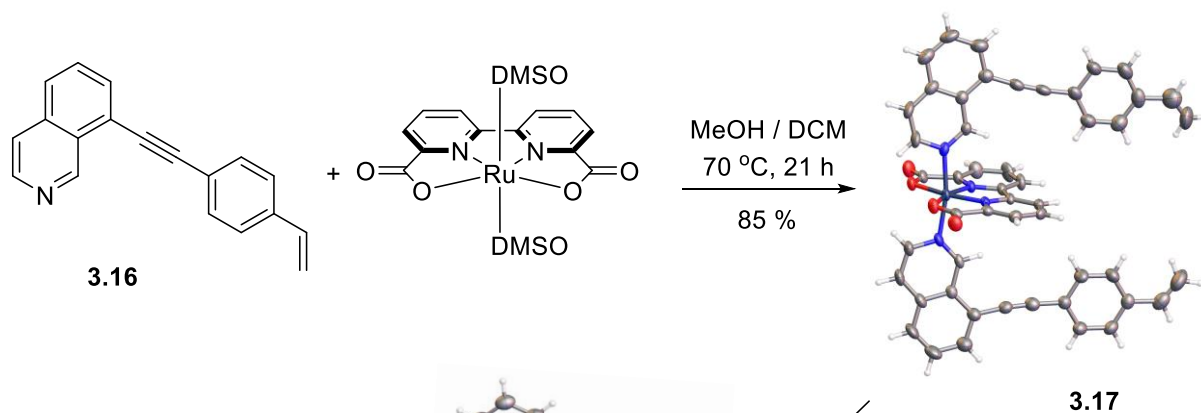
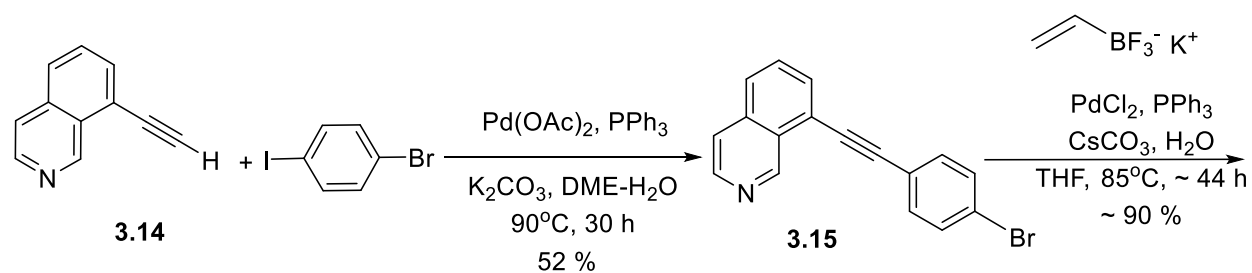
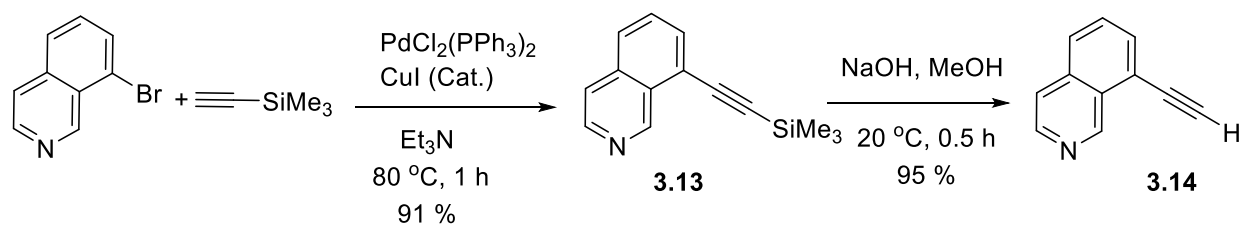
Our preliminary electrochemistry data showed no O₂ reduction peak in CV in case the of the **3.11** which is consistent with our analysis that the bda unit needs to rotate.¹¹⁵

Thus, we thought about another design to construct a larger macrocycle, which is complex **3.18**.

3.3. Novel ruthenium bda macrocycle with vinyl bridge containing a large-sized cavity

Novel macrocycle **3.18** attempts to overcome the above-mentioned challenges (the moderate cavity size for the compound **3.11**) as the olefin plus aryl rings bridge the two isoquinolines and can be expected to stabilize and prevent degradation of the catalyst, yet the large cavity should allow bda to rotate. Another advantage is that the large cavity presents no hindrance to the metal to interact with H₂O.

Here we discuss the challenges faced during synthesis, especially getting high yields in a ring-closing metathesis step. Using a new procedure, we achieved clean conversion in this challenging ring closing step.



Grubbs II Cat.
 7 mol%
 DCM, 50° C
 0.0026 M
 < 20 %

Figure 3.5. Synthetic procedure of Ru complexes **3.17** and **3.18** and related X-ray crystal structures.

3.3.1. Materials and Methods

The Ru complexes were synthesized, isolated, and characterized by NMR and solid-state monocrystal X-ray diffraction analysis. A Varian 500-MHz INOVA (500 MHz for ^1H = 499.940 MHz) spectrometer was used. Single crystal X-Ray diffraction data were collected on a Bruker Apex II diffractometer equipped with hi-flux Cu-K α (λ = 1.54178 Å) or Mo-K α (λ = 0.71073 Å) radiation source. The structure was solved using SHELXTL and Olex2 software. Suitable crystals of complexes **3.18** and **3.21** were grown in methanol by slow evaporation of methanol over time. Electrochemistry was performed using a Model # CHI760E (CH Instruments, Inc) potentiostat for cyclic voltammetry and differential pulse voltammetry (DPV). Aqueous cyclic voltammetry experiments were performed with a glassy carbon working electrode, a silver/silver chloride (Ag/AgCl) reference electrodes, and a platinum wire counter electrode.

3.3.2. Results and Discussion

The complex Ru(bda)(DMSO) $_2$ was prepared based on literature.⁸⁰ The displacement of two axial DMSO ligands led to **3.17** in high yield (Figure 3.5). The ring closing metathesis step was very challenging, possibly because the two axial ligands spin and favor to polymerize. We tried several catalysts and conditions, but Grubbs second-generation catalyst was best for ring closing metathesis. In addition, in some samples of compound **3.17** broad peaks in the ^1H NMR spectrum were observed which could be because of competing polymerization. The best way to prevent polymerization of the compound **3.17**, and optimize fragmentation of **3.18** was to perform reactions at low concentration. Our optimal conditions were using 7 mol % Grubbs II catalyst, 0.0026 M concentration of reactant and DCM as solvent.

3.3.3. X-ray crystallography data

Our design required the two isoquinoline nitrogens held at just the right distance, on opposite sides of the ruthenium center. Based on the X-ray crystal structure, the cavity dimension is 10.705 \times 11.141 Å, N-Ru-N distance 4.134 Å, O-Ru-O open angle is 120.59°, and N-Ru-N 168.52°, therefore giving an optimized

cavity size for exposing the Ru center to water molecules in complex **3.18**. However, compared to complex **1.6**, the O-Ru-O angle (catalyst active site) of the macrocycle **3.18** is smaller (120.59° in **3.18**, 123.00° in **1.6**). The X-ray crystal structure of the **3.17** in Figure 3.5 perfectly shows the huge distance between two vinyl groups, even though by chance in the crystal, the two axial ligand side chains are on the same side. Also, as demonstrated in the X-ray structure of **3.18** (Figure 3.5), the cavity of the macrocycle is large enough to surround the ruthenium with bda equatorial ligand and have enough space for rotation of the bda inside the cavity. Examining the structure using space-filling representation shows that the bda π system nicely fits in the cavity.

3.3.4. Cyclic voltammetry for complex **3.18**

We analyzed the redox properties of the complex **3.18** in aqueous solution at pH 7 by electrochemical measurements based on CV experiments.

In neutral pH phosphate buffer, complex **3.18** at 0.5 mM shows two reversible redox peaks which are assigned to $\text{Ru}^{\text{II/III}}$ at +0.65 V and $\text{Ru}^{\text{III/IV}}$ at +1.05 V, after exposure to 1.6 V vs Ag/AgCl. Also, a catalytic current at more positive potentials, and an O_2 reduction wave beginning at -0.4 V were observed.

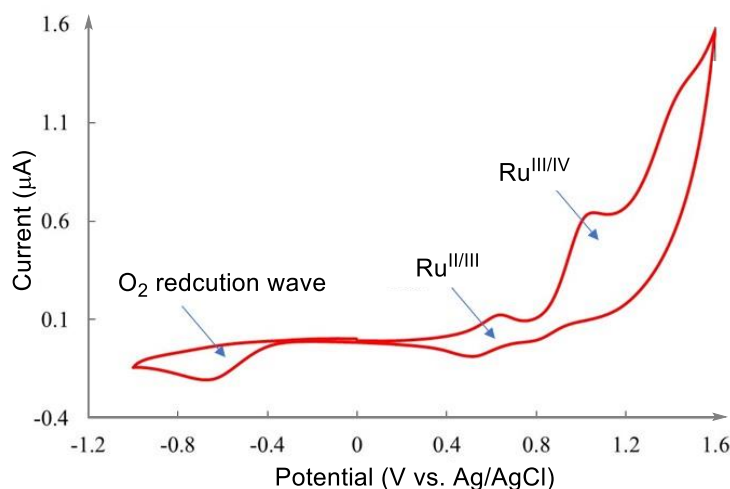


Figure 3.6. CV of **3.18** in an aqueous phosphate buffer at pH 7, [Cat.] 0.5 mM. Catalyst was dissolved in 200 μL of $\text{CF}_3\text{CH}_2\text{OH}$, then added to 5 mL of buffer. Scan rate, 0.1 V/s; working electrode, glassy carbon, counter electrode, Pt wire; reference electrode, Ag/AgCl. CV shows two reversible redox peaks for $\text{Ru}^{\text{II/III}}$ and $\text{Ru}^{\text{III/IV}}$.

3.3.5. Water oxidation testing of catalyst 3.18

The testing of complex **3.18** was performed in presence of the ceric ammonium nitrate and pH 1 of nitric acid. As a comparison, we tested the Ru^{II}(bda)(picoline)₂ reference catalyst **1.5** under the same conditions. The oxygen evolution catalyzed by **3.18** ([Cat.]₀ = 250 μM), in aqueous solution (HNO₃, pH 1) containing [Ce^{IV}]₀ = 250 mM reached TON 100, whereas the maximum possible number of turnovers was 250. However, water oxidation testing of catalyst **1.5** under the same condition reached TON = 250, the maximum possible. Less O₂ was formed using complex **3.18**. We think degradation of the vinyl moiety on the ligand could be a reason for lower catalytic performance of **3.18**.

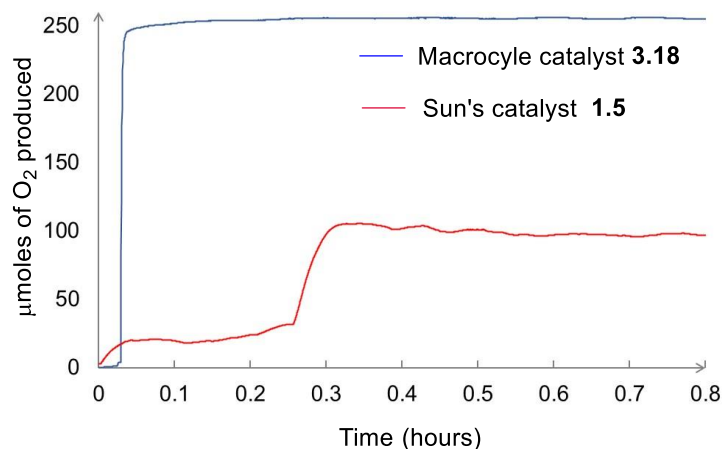


Figure 3.7. μMoles of O₂ produces over time in aqueous solution (pH 1). [Ce^{IV}]₀ = 250 mM, [Cat.]₀ = 250 μM, T = 30°C.

3.3.6. Significance

Our aim in this section was to design a novel trans-spanning ligand and a complex with big macrocycle cavity to have a more robust and longer-lived water oxidation catalyst. Synthetic procedures for making these trans-spanning ligands can be helpful in literature for other purposes beside water oxidation. We characterized the target catalyst by NMR and X-ray crystallography. However, the WOC testing of macrocycle bearing alkyne-containing bridge with CAN obtained low 100 TON, which is less than TON for the standard catalyst **1.5** (TON = 250). Degradation of the olefin bridge due to very oxidizing condition could be a possible reason for low performance of the complex.

3.4. Ruthenium bda macrocycle with phenyl bridge containing a large-sized cavity

Based on the low performance of the Ru bda macrocycle with a vinyl bridge in sacrificial oxidant testing, we replaced the vinyl with a phenyl. We envisaged that the aromatic ring would be more stable under oxidizing conditions of the testing compared to the vinyl bridge.

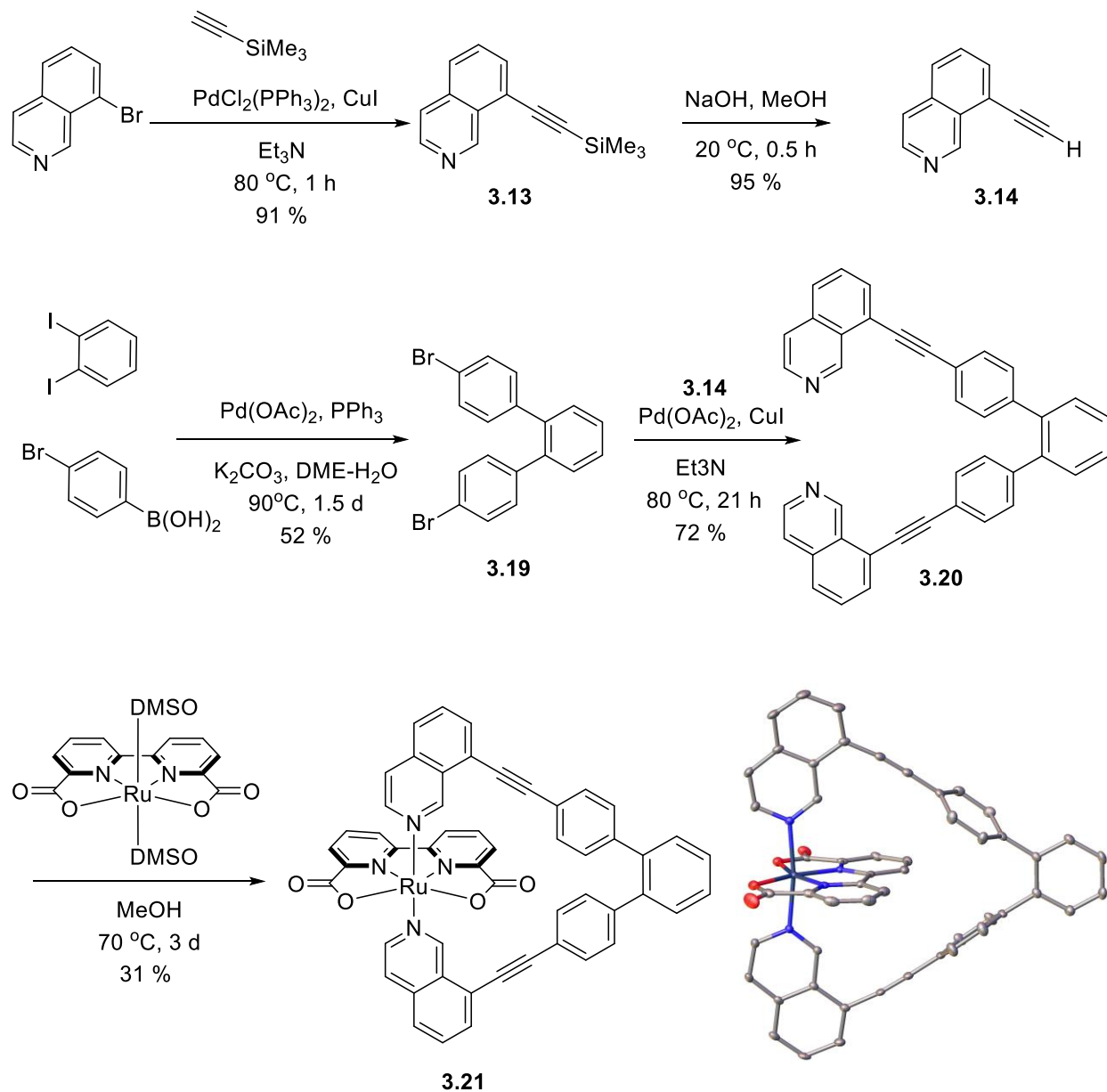


Figure 3.8. Synthetic procedure of Ru macrocycle **3.21** and related X-ray crystal structure.

3.4.1. X-ray structure

The geometric parameters for instance bond length and angle are important to understand the performance of a catalyst. As demonstrated in the X-ray structure of **3.21** (Figure 3.8), the N-N distance is 4.136 Å, Ru-N_{isoquinoline} = 1.923 Å, and Ru-O = 2.169 Å. The N-Ru-N angle involving the two isoquinolines is 171.3° and the angle of the coordinating side O-Ru-O is 121.713°. However, compared to complex **1.6**, the N-Ru-N distance of the macrocycle **3.21** is shorter (4.146 Å) and the N-Ru-N angle is (173.0°) bigger. We hypothesize that the shorter N-Ru-N distance in **3.21**, maybe one of the reasons for better performance of the **3.21**, but the difference is close to the experimental uncertainty, so other reasons will be explored as well.

3.4.2. Cyclic voltammetry for complex 3.21

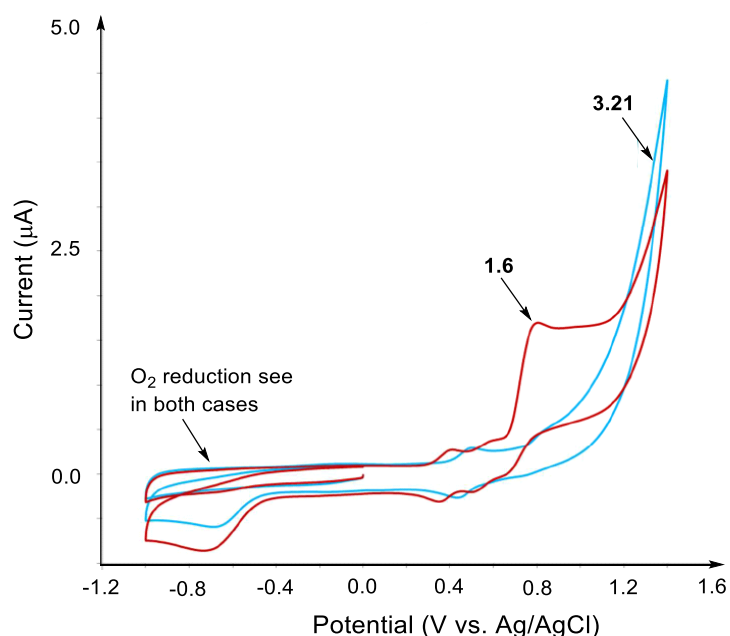


Figure 3.9. CV of **3.21** (blue) and Sun's complex **1.6** (red), an aqueous phosphate buffer at pH 7 at 0.25 mM concentration. Scan rate, 0.1 V/s; working electrode, glassy carbon, counter electrode, Pt wire; reference electrode, Ag/AgCl.

CV of **3.21** shows two reversible redox peaks assigned to Ru^{II/III} and Ru^{III/IV}. For the purpose of the comparison Sun's complex (red) with isoquinoline axial ligands (**1.6**) are presented under the same

conditions (Figure 3.9). The result suggests that if we keep the potential at +1.4 V we can finally determine the longevity of the catalyst, by performing bulk electrolysis.

3.4.3. Water oxidation testing for catalyst **3.21**

Evaluation of complex **3.21** in the water oxidation test with Ce^{IV} in acidic aqueous solution afforded 1518 TON under our optimized condition (Figure 3.10 and Table 3.1) (for comparison Sun's bis(picoline) catalyst **1.5** reaches 519 TON under the same conditions). We use acetonitrile as co-solvent to dissolve the complex. The condition was used for the testing was based on known conditions that were used in the report from Würthner's group.¹⁰³

As we expected, our new designed macrocycle **3.21** with phenyl bridging two isoquinolines, finally enhanced the catalytic longevity up to TON = 1518. We investigated the rate order of WOC which is first order in relation to concentration of catalyst **3.21** (Figure 3.10b).

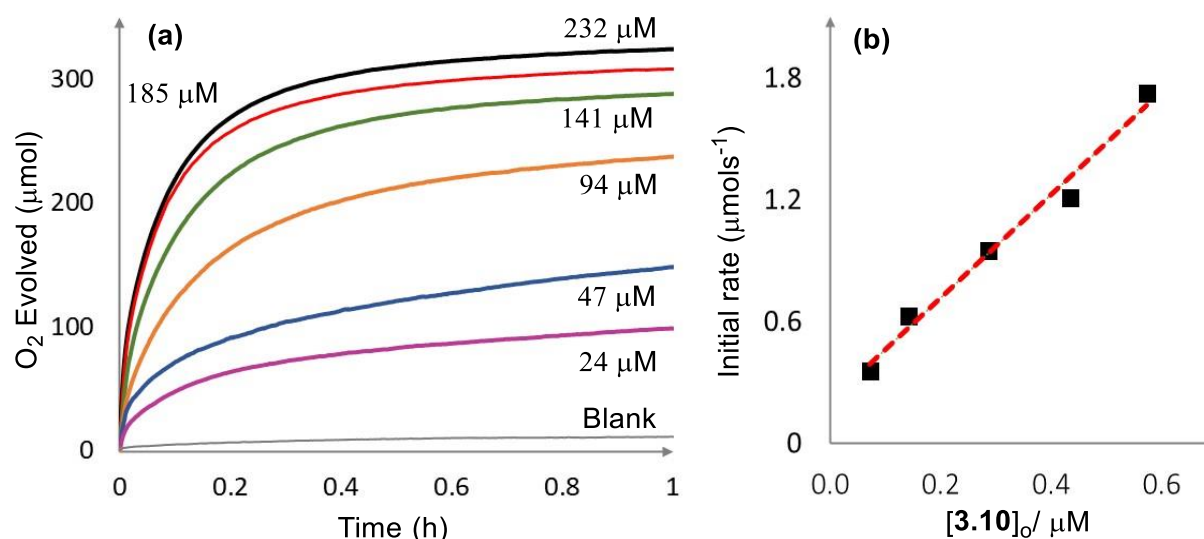


Figure 3.10. (a) Concentration-dependent oxygen evolution over time for **3.21** with 75% (v/v) acetonitrile as a co-solvent at 30 °C, pH 1 and $[\text{Cat.}]_0 = 24$ to 232 μM . (b) The plot of the initial rates (O_2 evolved μMol per sec) vs. the catalyst concentration. 1.0 g Ce^{IV} was dissolved in 3.0 mL organic solvents/ H_2O (pH 1, acid HNO_3) 4 : 1 and 400 μL of catalyst solution in organic solvents / H_2O (pH 1) 4:1 was injected). Organic solvent stock solution consisted of 80% (v/v) of acetonitrile + 20% (v/v) of $\text{CF}_3\text{CH}_2\text{OH}$. The initial rate of O_2 evolution vs. $[\mathbf{3.21}]_0$ shows the reaction is first order with respect to catalyst.

Table 3.1. Detailed concentration and yields for oxygen evolution catalyzed by **3.21** and standard catalyst **1.5** for comparison. Catalyzed oxygen evolution from ceric ammonium nitrate solutions with using aqueous buffer solution plus MeCN for macrocycle with phenyl bridge (more details is presented in Figure 3.6).

Catalyst	TON	Theoretical			Ce ^{IV} , mmol	[Ce ^{IV}] ₀ M	% Theoretical Yield
		O ₂ μmol	Cat. μmol	[Cat.] μM			
3.21	446	456	0.722	232	1.824	0.59	73.7 (5 h)
3.21	581	456	0.573	185	1.824	0.59	74.1 (5 h)
3.21	721	456	0.434	141	1.824	0.59	70.7 (5 h)
3.21	945	456	0.287	94	1.824	0.60	59.4 (5 h)
3.21	1321	456	0.142	47	1.824	0.60	42.2 (3 h)
3.21	1518	456	0.072	24	1.824	0.61	26.6 (1.9 h)
1.5	370	456	0.715	232	1.824	0.59	60.5 (2 h)
1.5	508	456	0.430	141	1.824	0.60	49.6 (1.8 h)
1.5	519	456	0.725	24	1.824	0.60	8.7 (1.4 h)

3.5. Conclusion and future work

In this chapter our goal was to have a robust and sustainable catalyst for water oxidation which is fast with high turnover frequency. Most research is focused on creating fast catalysts, but our emphasis is slowing down the rate of undesired catalyst degradation by exploring new trans-spanning ligand complexes with large cavities. Catalytic activity was enhanced by using a macrocyclic ruthenium complex with phenyl bridge. As we expected, we obtained 1518 TON in our optimized conditions compared to Sun's catalyst with 519 TON.

In future work, we will try to evaluate the mechanism water oxidation reaction by using ruthenium macrocycle complexes and isolating intermediates during catalytic cycle. In this vein we will elaborate our knowledge about the mechanism of reaction by kinetic study, computational studies, and bulk electrolysis. One potential advantage of bulk electrolysis is that the potential and pH of the catalyzed reaction can be varied. The redox potential of Ce^{IV} in acid has been reported for ruthenium water oxidation catalysts,¹¹⁶ and is in the order of 1.61 V for aqueous nitric acid solutions, whereas onset potential for **3.21** is only 0.78 V, so it is clear that Ce^{IV} is far too strong oxidant.

Macrocyclic ligands such as the one here are expected to show benefits not only in water oxidation, but in any field where catalyst stability and ligand loss are a concern.

3.6. Synthetic procedure

Compounds **3.13** to **3.16** were prepared based on modified procedures in the literature.^{117,118,119,120}

Synthesis of compound **3.17**, [Ru^{II}(bda)(8-((4-vinylphenyl)ethynyl)isoquinoline)₂]

A 20 mL scintillation vial in the glove box was charged with Ru(bda)(DMSO)₂ (0.1256 g, 0.2504 mmol, 1 equiv) then methanol/DCM (1:3 ratio, 5.0 mL) was added. In another vial, compound **3.16** (0.008 mmol, 2 equiv) was dissolved in methanol/DCM (1:3 ratio, 5 mL), and the resulting solution was added to the vial containing Ru(bda)(DMSO)₂. The reaction vial was sealed and the contents stirred in a pre-heated oil bath at 70 °C. The completion of the reaction was monitored by TLC. After completion of the reaction in almost 21 h, the mixture was filtered in the glove box, and the filtrate evaporated to dryness. The residue was further purified by chromatography with silica gel as a stationary phase and mobile phase was a combination of methanol/DCM (1:9). The product is red-brown fine solid, yield 85% (0.187 g). The product **3.17** was characterized by ¹H, ¹³C NMR and X-ray crystallography Figure 3.2.

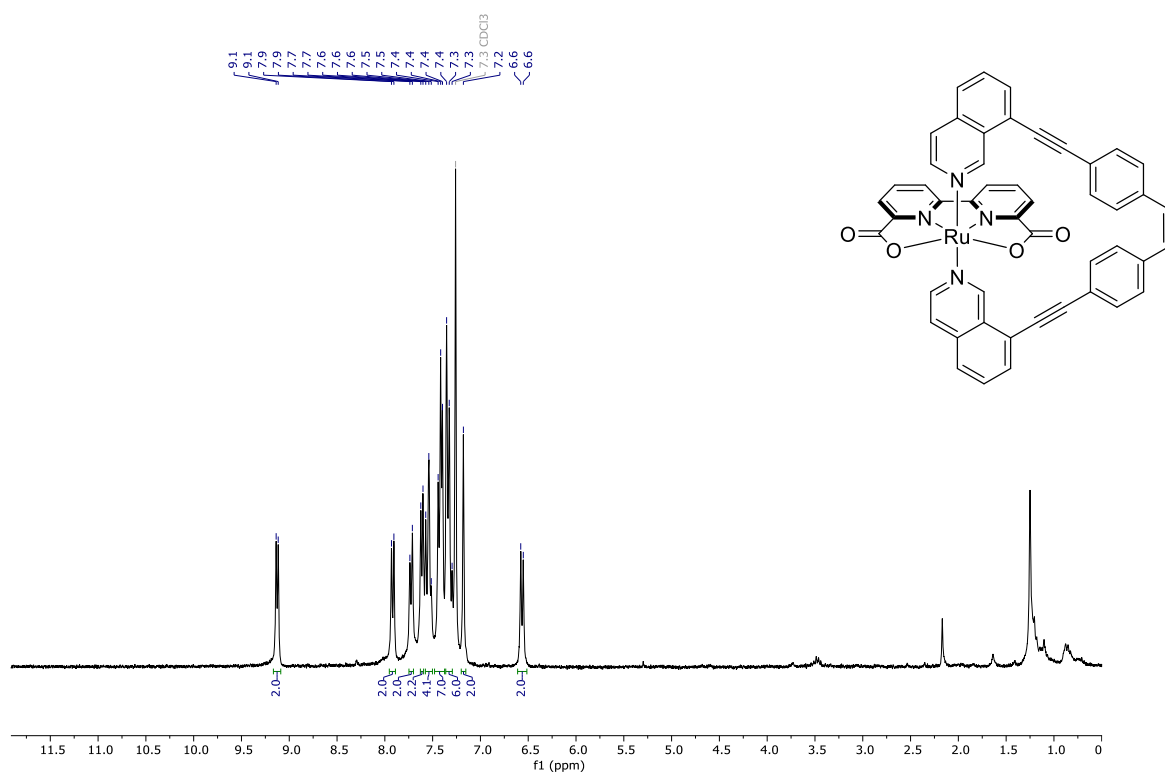
¹H NMR (300 MHz, Chloroform-*d*) δ 8.88 (d, *J* = 6.4 Hz, 2H), 7.98 (d, *J* = 7.5 Hz, 2H), 7.83 (s, 2H), 7.73 – 7.63 (m, 2H), 7.62 – 7.51 (m, 11H), 7.43 (d, *J* = 8.4 Hz, 6H), 6.87 (dd, *J* = 17.6, 10.9 Hz, 2H), 5.96 (d, *J* = 17.6 Hz, 2H), 5.49 (d, *J* = 10.9 Hz, 2H). ¹³C NMR (126 MHz, Chloroform-*d*) δ 173.0, 159.1, 157.9, 151.6, 147.1, 138.6, 136.1, 134.9, 132.2, 132.0, 131.2, 130.3, 127.8, 127.1, 126.3, 125.8, 121.7, 120.2, 116.0, 95.5, 85.0, 41.1 ppm.

Synthesis of compound **3.18**, [Ru^{II}(bda)(*Z*-1,2-bis(4-(isoquinolin-8-ylethynyl)phenyl)ethene)]

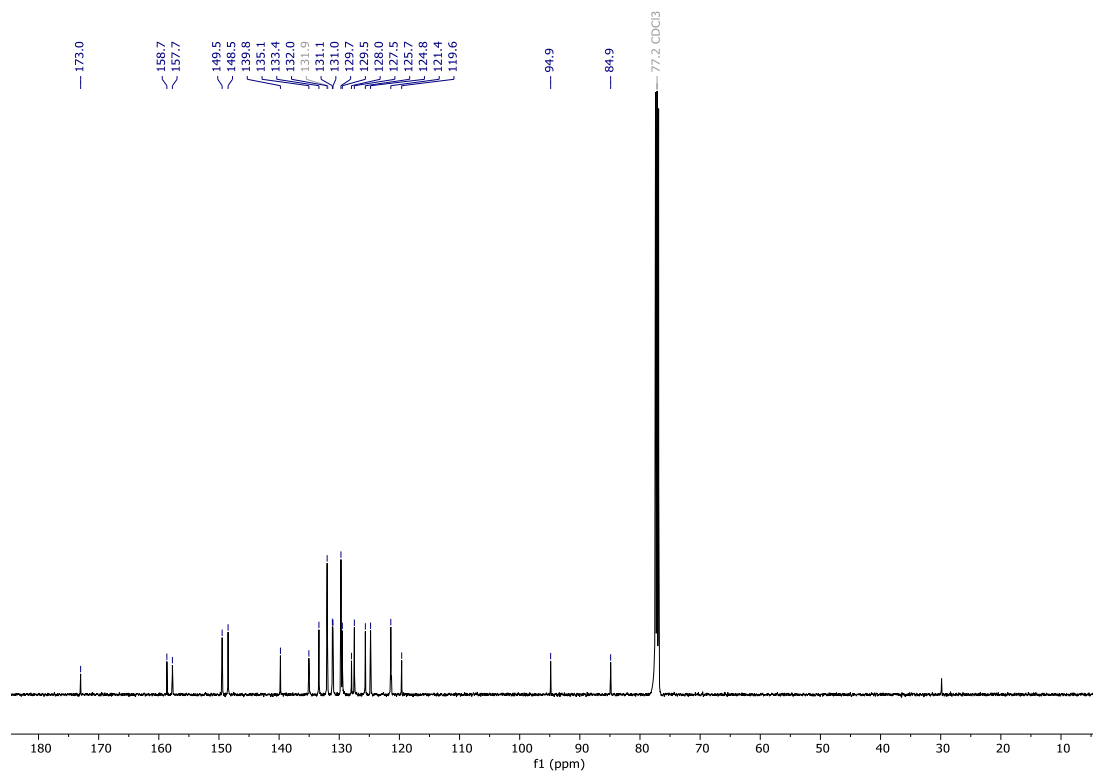
A 50 mL Schlenk in the glove box was charged with Ru complex **3.17** (0.200 g, 0.2340 mmol, 1.00 equiv) then DCM (45.0 mL) was added. In another vial, Grubbs second generation catalyst (0.0167 mmol, 0.0104 g, 7 mol%) was dissolved in DCM (45 mL), and the resulting solution was added to the Schlenk containing **3.17**. The reaction Schlenk was sealed and the contents stirred at a pre-heated oil bath at 50 °C for 30 hours. The completion of the reaction was monitored by TLC. After completion of the reaction, the mixture was filtered in the glove box, and the filtrate evaporated to dryness. The residue was washed with ether and further purified by chromatography with silica gel as a stationary phase and mobile phase was a combination of methanol/DCM (0.6:7). The product is red-brown fine solid, yield 20% (0.040 g). The product **3.18** was characterized with ¹H, ¹³C NMR and X-ray crystallography (Figure 3.5).

¹H NMR (300 MHz, Chloroform-*d*) δ 9.13 (d, *J* = 6.5 Hz, 2H), 7.92 (d, *J* = 7.6 Hz, 2H), 7.73 (d, *J* = 7.8 Hz, 2H), 7.61 (d, *J* = 6.8 Hz, 2H), 7.54 (t, *J* = 8.7 Hz, 4H), 7.42 (t, *J* = 6.9 Hz, 6H), 7.34 (d, *J* = 8.3 Hz, 6H), 7.18 (s, 2H), 6.56 (d, *J* = 8.1 Hz, 2H). ¹³C NMR (126 MHz, Chloroform-*d*) δ 173.0, 158.7, 157.7, 149.5, 148.5, 139.8, 135.1, 133.4, 132.0, 131.1, 131.0, 129.7, 129.5, 128.0, 127.5, 125.7, 124.8, 121.4, 119.6, 94.9, 84.9 ppm.

^1H NMR spectrum of **3.17** in chloroform-*d*, 300 MHz.



$^{13}\text{C}\{^1\text{H}\}$ NMR spectrum, chloroform-*d*, 126 MHz.



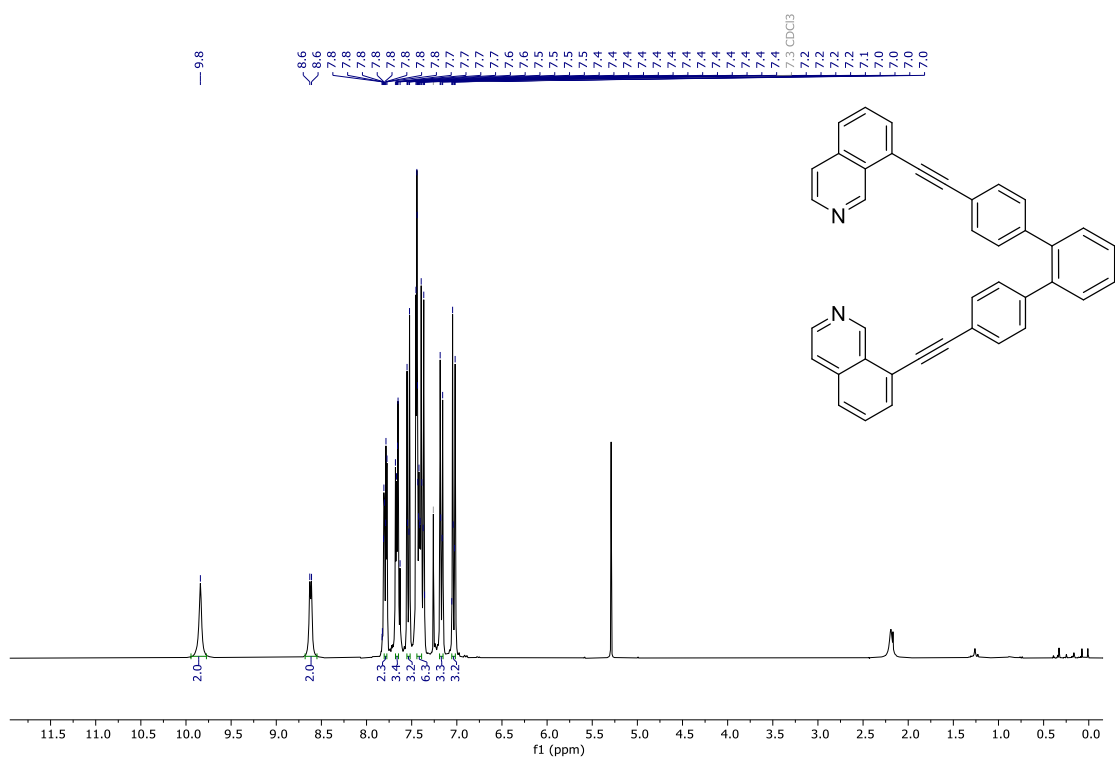
Compound **3.19** was prepared based on literature.¹²¹

Synthesis of compound 3.20 (8-((4''-(naphthalen-1-ylethynyl)-[1,1':2',1''-terphenyl]-4-yl)ethynyl)isoquinoline)

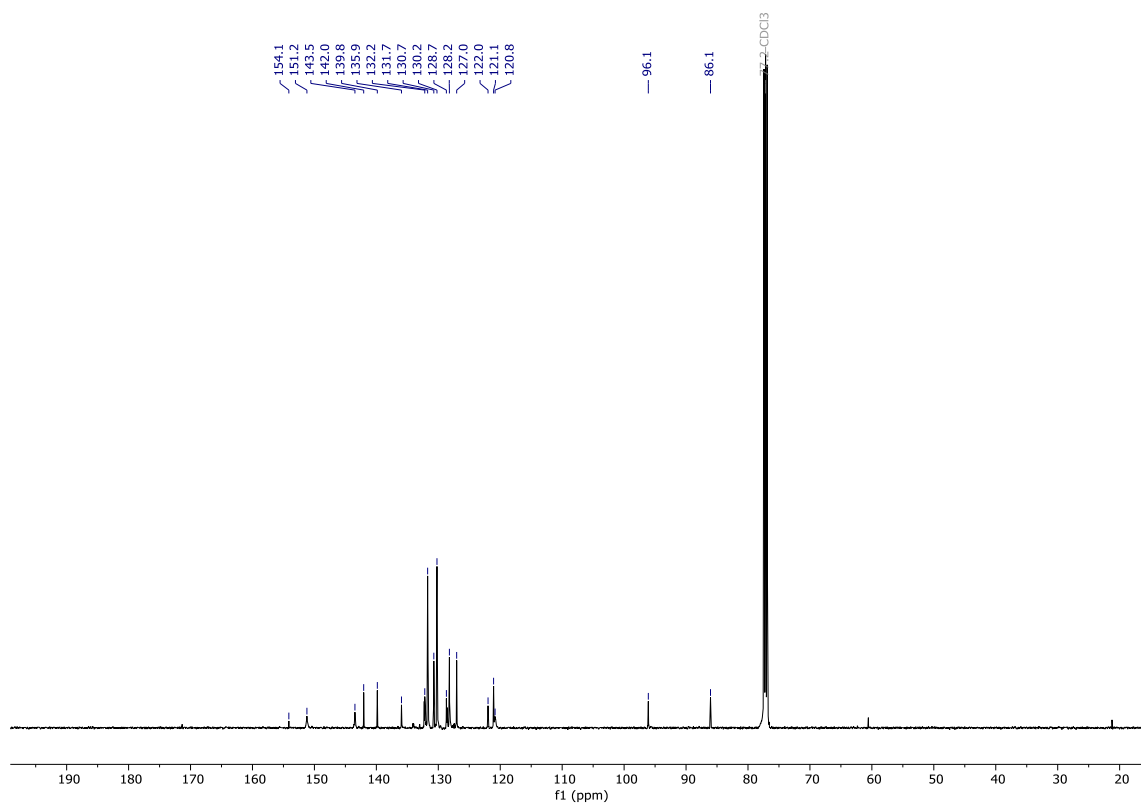
A 100 mL bomb Schlenk in the glove box was charged with compound **3.19** (0.3304 g, 0.850 mmol, 1 equiv) then compound **3.14** (0.3975 g, 2.590 mmol, 3 equiv), Pd(PPh₃)₂Cl₂ (0.043 g, 7.2 mol%) and CuI (0.0254 g, 30.4 mol%) were added, respectively. To the resulting mixture NEt₃ (12 mL) was added. The Schlenk was sealed, and the brown suspension stirred in a pre-heated oil bath at 85 °C. The completion of the reaction was monitored by TLC. After completion of the reaction (almost 1 d), the mixture was evaporated to dryness. The residue was further purified by chromatography with Florisil gel as a stationary phase and mobile phase was a combination of DCM/EtOAc (9:1). The product is foamy yellowish solid, yield 72% (0.326 g). The product **3.20** was characterized by ¹H and ¹³C NMR.

¹H NMR (300 MHz, Chloroform-*d*) δ 9.84 (s, 2H), 8.62 (d, *J* = 5.7 Hz, 2H), 7.79 (dt, *J* = 8.2, 2.3 Hz, 2H), 7.70 – 7.61 (m, 3H), 7.58 – 7.51 (m, 3H), 7.48 – 7.33 (m, 6H), 7.21 – 7.12 (m, 3H), 7.08 – 6.99 (m, 2H). ¹³C NMR (126 MHz, Chloroform-*d*) δ 154.1, 151.2, 143.5, 142.0, 139.8, 135.9, 132.2, 131.7, 130.7, 130.2, 128.7, 128.2, 127.0, 122.0, 121.1, 120.8, 96.1, 86.1 ppm.

^1H NMR spectrum of **3.20** in chloroform-*d*, 300 MHz.



$^{13}\text{C}\{^1\text{H}\}$ NMR spectrum, chloroform-*d*, 126 MHz.

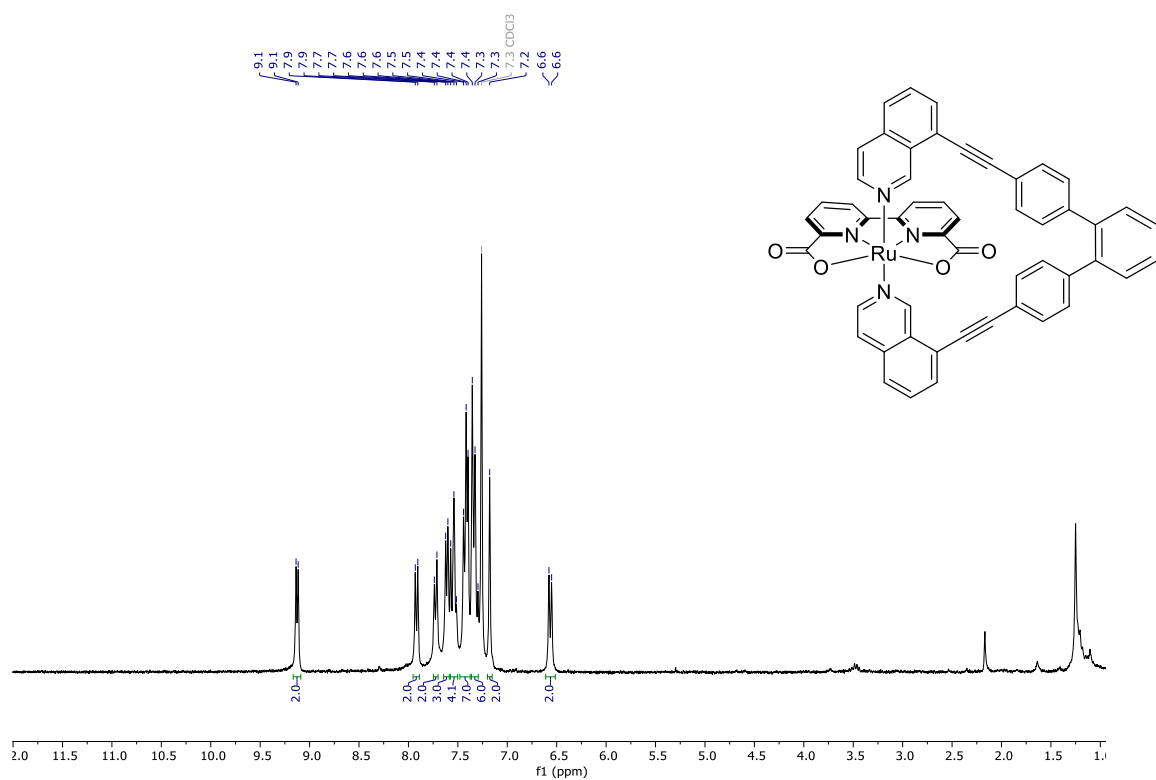


Synthesis of compound 3.21, [Ru^{II}(bda)(8-((4''-(naphthalen-1-ylethynyl)-[1,1':2',1''-terphenyl]-4-yl)ethynyl)isoquinoline)

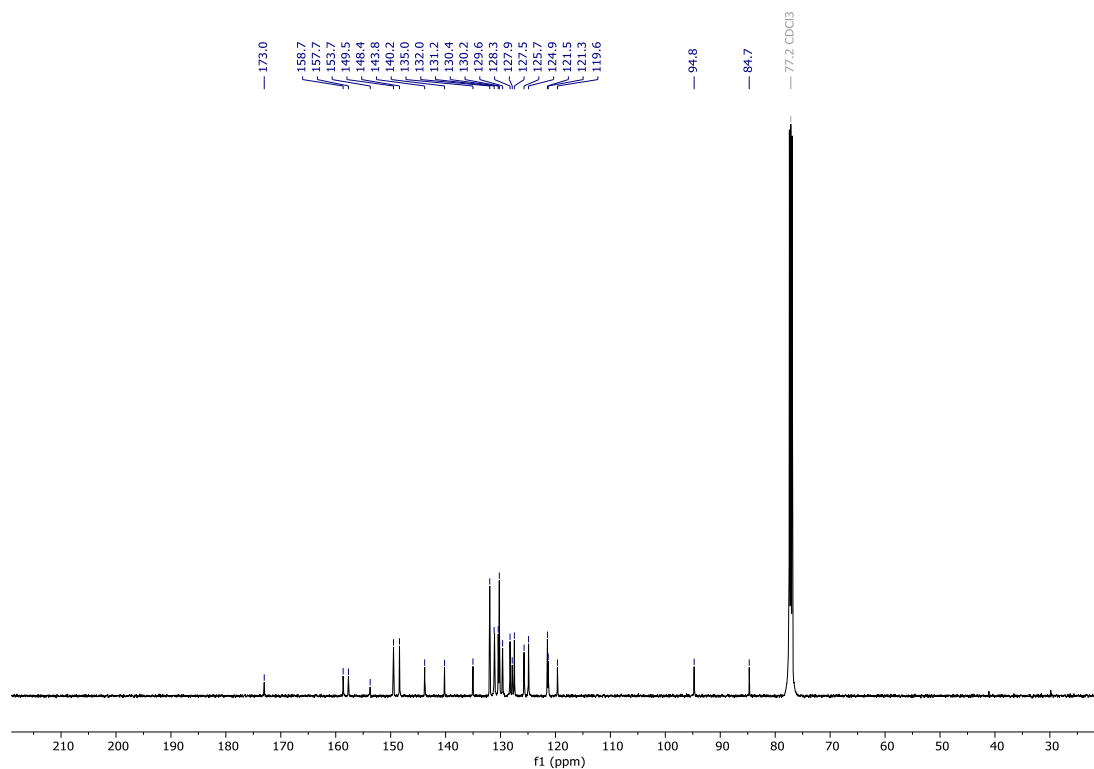
A 20 mL scintillation vial in the glove box was charged with Ru(bda)(DMSO)₂ (0.0470 g, 0.0939 mmol, 1 equiv) then methanol (5 mL) was added. In another vial, compound **3.20** (0.050 g, 0.0939 mmol, 1 equiv) was dissolved in methanol (5 mL), and the resulting solution was added to the vial containing Ru(bda)(DMSO)₂. The molarity of the solution was 9.4×10^{-3} M. The reaction vial was sealed and the contents stirred in a pre-heated oil bath at 70 °C. The completion of the reaction was monitored by TLC. After completion of the reaction (3 d), the mixture was filtered in the glove box, and the filtrate evaporated to dryness. The residue was further purified by chromatography with silica gel and mobile phase was a combination of methanol/DCM (1:9). The product is red-brown fine solid, yield 31% (0.026 g). The product **3.21** was characterized by ¹H, ¹³C NMR and X-ray crystallography (Figure 3.8).

¹H NMR (300 MHz, Chloroform-d) δ 9.13 (d, *J* = 6.5 Hz, 2H), 7.92 (d, *J* = 7.6 Hz, 2H), 7.73 (d, *J* = 7.8 Hz, 2H), 7.61 (m, 3H), 7.54 (t, *J* = 8.7 Hz, 4H), 7.37-7.49 (m, 7H), 7.25-7.35 (d, *J* = 8.3 Hz, 6H), 7.18 (s, 2H), 6.56 (d, *J* = 8.1 Hz, 2H). ¹³C NMR (126 MHz, Chloroform-d) δ 173.0, 158.7, 157.7, 153.7, 149.5, 148.4, 143.8, 140.2, 135.0, 132.0, 131.2, 130.4, 130.2, 129.6, 128.3, 127.9, 127.5, 125.7, 124.9, 121.5, 121.3, 119.6, 94.8, 84.7. ppm.

^1H NMR spectrum of **3.21** in chloroform-*d*, 300 MHz.



$^{13}\text{C}\{^1\text{H}\}$ NMR spectrum, chloroform-*d*, 126 MHz.



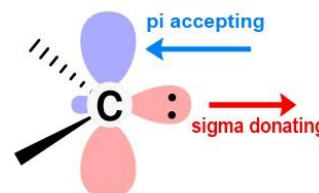
Chapter 4

Influence of carbene and phosphine ligands on the catalytic activity of gold complexes in the hydroamination and hydrohydrazination of alkynes

4.1. Introduction

The following chapter discusses the ability of gold carbene complexes and to catalyze NH additions to alkynes, and discusses the important role of ligand choice. Carbene ligands are the focus, so an introduction is warranted.

What is a singlet carbene? A singlet carbene is a divalent carbon which has both a lone pair and a vacant p orbital. Therefore, a carbene can both donate and accept electrons, making it a good σ -donor and π -acceptor. These properties have allowed carbenes to become a powerful tool in chemistry.



Carbene background: Following pioneering work by the group of Bertrand in 1988,¹²² and the isolation of the first *N*-heterocyclic carbene (NHC) by the group of Arduengo in 1991,¹²³ the field of stable carbenes has witnessed exceptional breakthroughs and outstanding developments.¹²⁴ Today, a large panel of carbenes with different sterics and electronics properties are available across many fields of chemical science including in organic, inorganic and organometallic chemistry.

In past decade, Bertrand's group has developed numerous singlet carbenes,¹²⁵ including the Cyclic Alkyl Amino Carbene (CAAC) first isolated in 2005, which has gained in popularity across both academia and industry. To understand the advantages of CAACs, one can look at the difference between NHCs and CAACs. While NHCs have two nitrogen substituents in alpha position to the carbene center which pull electron density away from the carbon and lone pairs on the nitrogens donating into the empty π -orbital of the carbene,¹²⁶ CAACs have only one nitrogen and one σ -donating quaternary carbon atom. This specificity makes CAACs more nucleophilic and electrophilic than NHCs. (Figure 4.1).¹²⁷ Recently, Bertrand's group extended this family of very electrophilic carbenes to the bicyclic CAAC (BiCAAC)¹²⁸ and the 6-membered CAAC (CAAC-6)¹²⁹ analogs with unique electronic and steric properties (Figure 4.2).

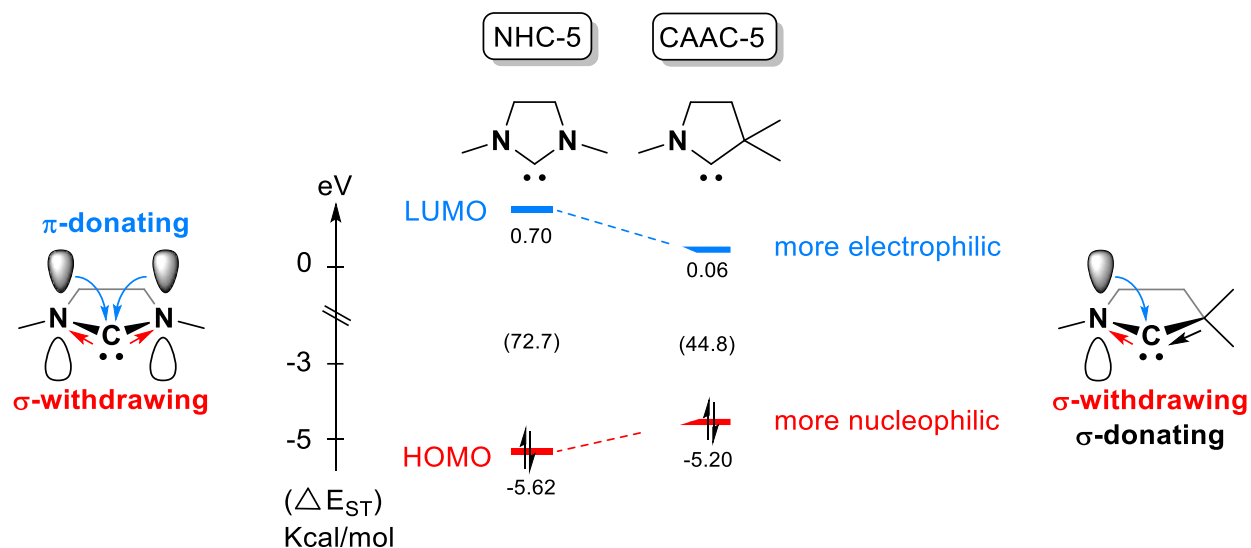


Figure 4.1. Comparison between 5 membered-ring CAAC and NHC.

Applications of the CAACs: Efficient and selective preparation of organic molecules through homogenous transition-metal catalysis is a key to the discovery of new materials for both industry and academia. Because of the finite number of transition metals, success heavily depends on the development of ligand frameworks capable of tuning the behavior of metal centers toward specific transformations. CAACs are suitable ligands for transition metal complexes thanks to their strong σ -donating and π -accepting abilities of carbenes forms a strong bond to the metal center and as a result a more robust complex for different transformation.

The Bertrand group has demonstrated that CAACs peculiar electronic and unique steric properties allowed for the improvement of known processes with Au¹³⁰ (hydroamination and hydrozination)⁶, Pd (α -arylation), Cu (hydroborylation and hydrosilylation), Ru (methathesis),¹³¹ Rh (hydrogenation),¹³² and Ir (hydrogenation),¹³³ as well as promoting new reactions with coinage metals.

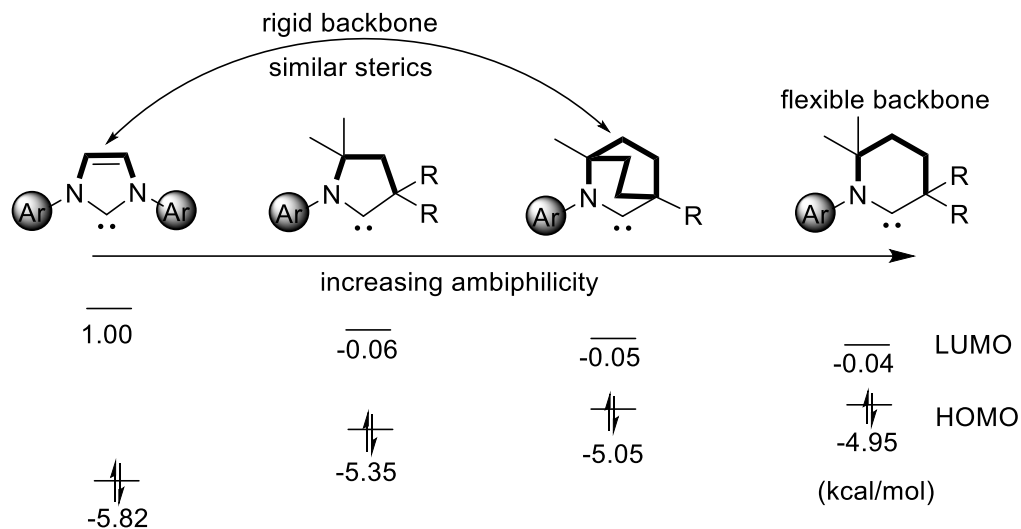


Figure 4.2. Comparison of steric and electronic properties across known families of CAAC ligands with respect to NHCs.

In this chapter, we applied state-of-the-art carbene metal catalysts to the hydroamination and hydrohydrazination of alkynes as a convenient and powerful means of accessing imine products. Although imines can be obtained by condensation of amines with aldehydes and ketones, this type of the reaction is usually slow and often limited in scope. To circumvent such limitations, efficient and selective transition metal catalysts are highly desirable.

In recent years a large variety of gold catalysts bearing carbene or phosphine ligands have been designed to promote the hydroamination of alkynes and alkenes.¹³⁴ Previous work from the Bertrand group had shown that CAAC-5 gold complexes could be suitable for this transformation,¹³⁵ specifically in the *inter-* and *intra-* molecular electrophilic activation of alkynes, alkenes, and allenes for the nucleophilic addition of amines and hydrazines.^{136,137,138} The robustness of gold CAACs proved advantageous in the activation of ammonia.¹³⁹ However, in this chapter we wished to investigate reactivity of (CAAC)Au catalysts in the hydroamination and hydrozination of the alkynes with a particular emphasis towards mechanistic considerations. Note that Chapter 4 has contents that are similar to the paper that we published: Yazdani, S.; Junor, G. P.; Peltier, J. L.; Jazzar, R.; Grotjahn, D. B.; Bertrand, G. Influence of carbene and

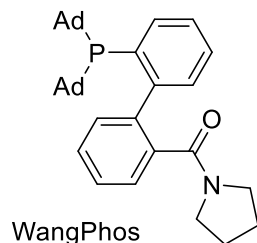
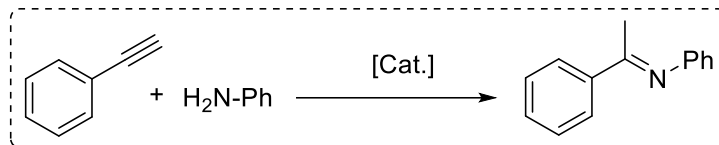
phosphine ligands on the catalytic activity of gold complexes in the hydroamination and hydrohydrazination of alkynes. *ACS Catalysis*, **2020**, *10*, 5190-5201.

4.2. Introduction to hydroamination and hydrazination

The hydroamination of C-C multiple bonds is the most efficient synthetic pathway for the introduction of nitrogen moieties in organic molecules.¹⁴⁰ The first report of gold-catalyzed hydroamination of alkynes was reported in 1989. Tanaka's group used (PPh₃)AuNTf₂ for hydroamination of the alkyne.¹⁴¹ After seeing acceptable activity of a readily available gold complex, the field of gold chemistry for hydroamination catalysts has witnessed an outstanding evolution.¹⁴² This field expanded even more thanks to Buchwald-type phosphines and singlet carbenes which proved to be privileged ligands for these transformations.¹⁴³

Interestingly despite most current research focusing on the design of an all-inclusive ligand (high TON/TOF, large substrate scope, broad scope of transformations), there is still no consensus on which ligands, phosphines or carbenes will afford the most efficient catalysts. We reasoned that a lack of comparative studies could be at the source of this predicament. This is well illustrated in a very detailed report by Xu and coworkers who observed a remarkable ligand effect in the intermolecular hydroamination of phenyl acetylene with aniline,¹⁴⁴ yet did not consider carbene ligands. It is thus not surprising that Xu's group only envisaged potential development in this field through P-centered ligand modifications.

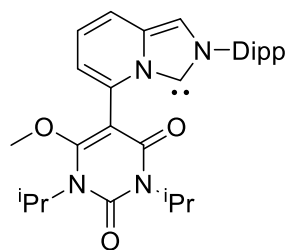
Another point which attracted our attention was that most ligand design strategies available in the literature relied on highly functionalized motifs.^{145,146} This is well exemplified by Zhang and co-workers who have designed very sophisticated ligand sets in recent years. For examples WangPhos phosphine bears an amido functional group **4.1.L**,¹⁴⁷ and was used to achieve up to 8500 TON in the hydroamination of phenyl acetylene with aniline. Similar strategies are also available for NHCs as seen in example **4.2.L** bearing a barbituric heterocycle on the NHC,¹⁴⁸ and reaching up to 7500 TON in the same transformation (Figure 4.3). It worth mentioning that Hashmi and co-workers have performed a comprehensive study of the catalytic activities of select phosphines and carbenes in gold catalyzed reactions emphasizing some differences between both of the ligand families.¹⁴⁹



4.1.L

[LAuNTf₂]
8500 TON

Zhang
Nat. Comm. **2014**



4.2.L

[LAuCl]
7600 TON

César, Michelet
Angew. **2019**

Figure 4.3. State of the art phosphine and carbene gold catalysts for the hydroamination of phenyl acetylene with aniline.

Rationalizing that protodeauration in gold-catalyzed hydroamination and hydrazination of alkynes is the rate-determining step and that catalyst deactivation is significant,^{144,150} we hypothesized that more strongly σ -donating carbenes (such as CAAC ligands) should yield more stable and more reactive catalysts. To demonstrate this idea, we performed a detailed investigation of the catalytic activities of CAAC ligands versus more traditional ligands such as NHCs and phosphines. To complement our study, we also performed numerous *in-situ* kinetic measurements which allowed us to optimize the reaction conditions but also more classically to determine the order of reaction for each reagent. Finally, we also conducted mechanistic studies to rationalize the stability imparted by CAAC ligands.

4.3. Results and discussion

4.3.1. Hydroamination reaction

Optimizing reaction conditions by kinetic studies: Conventional ligand optimization has been done in the literature by obtaining the overall yield of the reaction at the end. In our view, the final yield of the reaction might not provide enough information on the overall effectiveness of the ligand. Therefore, we decided to conduct *in-situ* kinetic measurements via ^1H NMR spectroscopy, as a direct probe into our catalytic system similar to the work has been done by Blackmond group.¹⁵¹ The process includes taking ^1H NMR spectra in 60-second intervals during the reaction of the aniline with *para*-methoxy-phenyl acetylene at room temperature. Practically, we monitored the formation of **4.8a** in the reaction mixture under varying conditions such as different gold catalysts (Figure 4.4a-b), solvents (Figure 4.4c), and different concentration and the catalyst loading to evaluate the optimized conditions.

To begin, we confirmed the accuracy of our kinetic methodology with using $(\text{Ph}_3\text{P})\text{AuCl}$ plus KBAr^{F} as an ionizing reagent, and achieved comparable results to those reported by Xu's group.¹⁴⁴ We performed the same reactions catalyzed with $(\text{THT})\text{AuCl}$. As illustrated in Figure 4.4b, spectator ligands like $(\text{Ph}_3\text{P})\text{AuCl}$ and $(\text{THT})\text{AuCl}$ are not supreme choices for this transformation.

Based on kinetic studies and as illustrated in Figure 4.4b, we observed an electronic effect on the rate of the catalysts, with faster catalysts bearing more donating ligands, $^{\text{Et}}\text{CAAC-5}$ (**4.3.L**) and $^{\text{Et}}\text{CAAC-6}$ (**4.4.L**). To investigate the steric effects of the ligands, we calculated the percent buried volume or $\%V_{\text{bur}}$. The buried volume quantifies the space occupied by the ligand in first coordination sphere of the gold center.^{152,153} The $\%V_{\text{bur}}$ values of the ligands are presented in Figure 4.4a, and we did not observe a clear effect for enhancing efficiency of catalyst bearing a sterically hindered ligand.

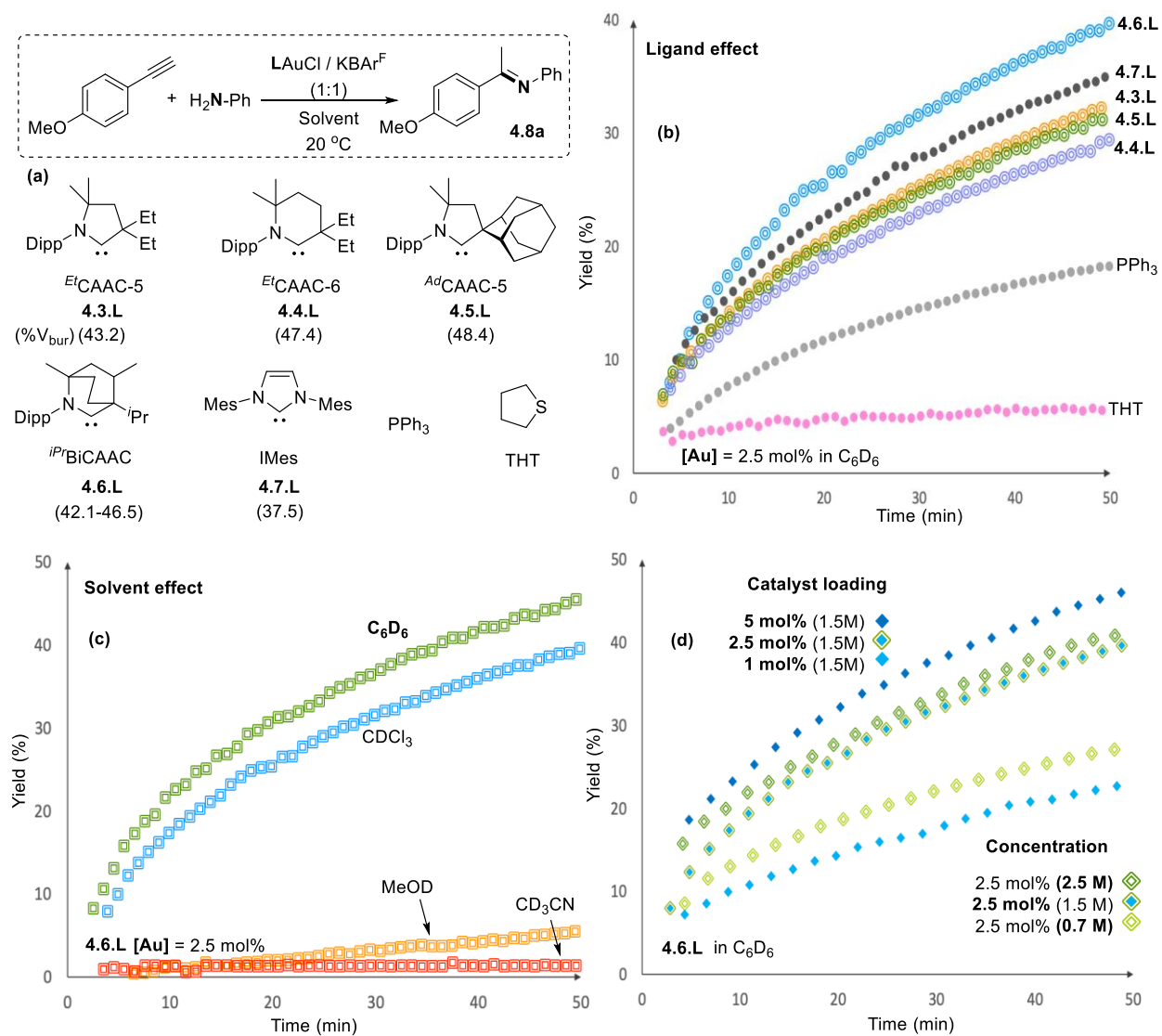


Figure 4.4. ^1H NMR kinetic monitoring of the hydroamination to evaluate optimized conditions.

From these kinetic studies we could conclude that: 1) In the absence of secondary ligand-metal interactions, enhancing the steric bulk around the gold center did not improve the reactivity of the catalyst; 2) *IPr*BiCAAC (**4.6.L**) is the most efficient catalyst for our target transformation, likely because of strong σ -donating properties and a rigid steric profile.

Using the same rationale, we also investigated different solvents and narrowed the best solvent to benzene (Figure 4.4c). In contrast, solvents such as CH₃CN were found to reduce the catalytic activity probably due to a binding competition at the gold between the solvent and the amine and alkynes.¹⁵⁴ To conclude, we selected our optimal conditions to be: 2.5 mol% *IPr*BiCAACAuCl/KBAr^F catalyst loading, 1.5 M (Figure 4.4d), and performing the reaction in benzene.

Reaction scope: With optimal conditions in hand, we performed a substrate scope using a range of alkynes and anilines (Figure 4.5). We found *IPr*BiCAACAuCl to be very efficient with aryl-substituted terminal alkynes and *p*-toluidine, with all reactions proceeding within a few hours in very high yields and at 20 °C (**4.8a-4.8e**). However, in case of the alkyl-substituted terminal alkynes, high conversions were only achieved upon longer reaction time (**4.8f-4.8g**). As expected, faster reaction could be obtained by increasing the reaction temperature (**4.8h**). Internal alkynes required longer reaction times and higher temperatures but could be efficiently transformed nonetheless (**4.8i-4.8k**).

We also examined the nature of the aniline and as illustrated in Figure 4.5 found few limitations in this case (**4.8l-4.8p**), even with sterically demanding 2,6-diisopropylaniline (**4.8m**) or electron deficient perfluorinated aniline (**4.8o**). Also, alkyl amines showed less reactivity and demanded higher temperature up to 80 °C.

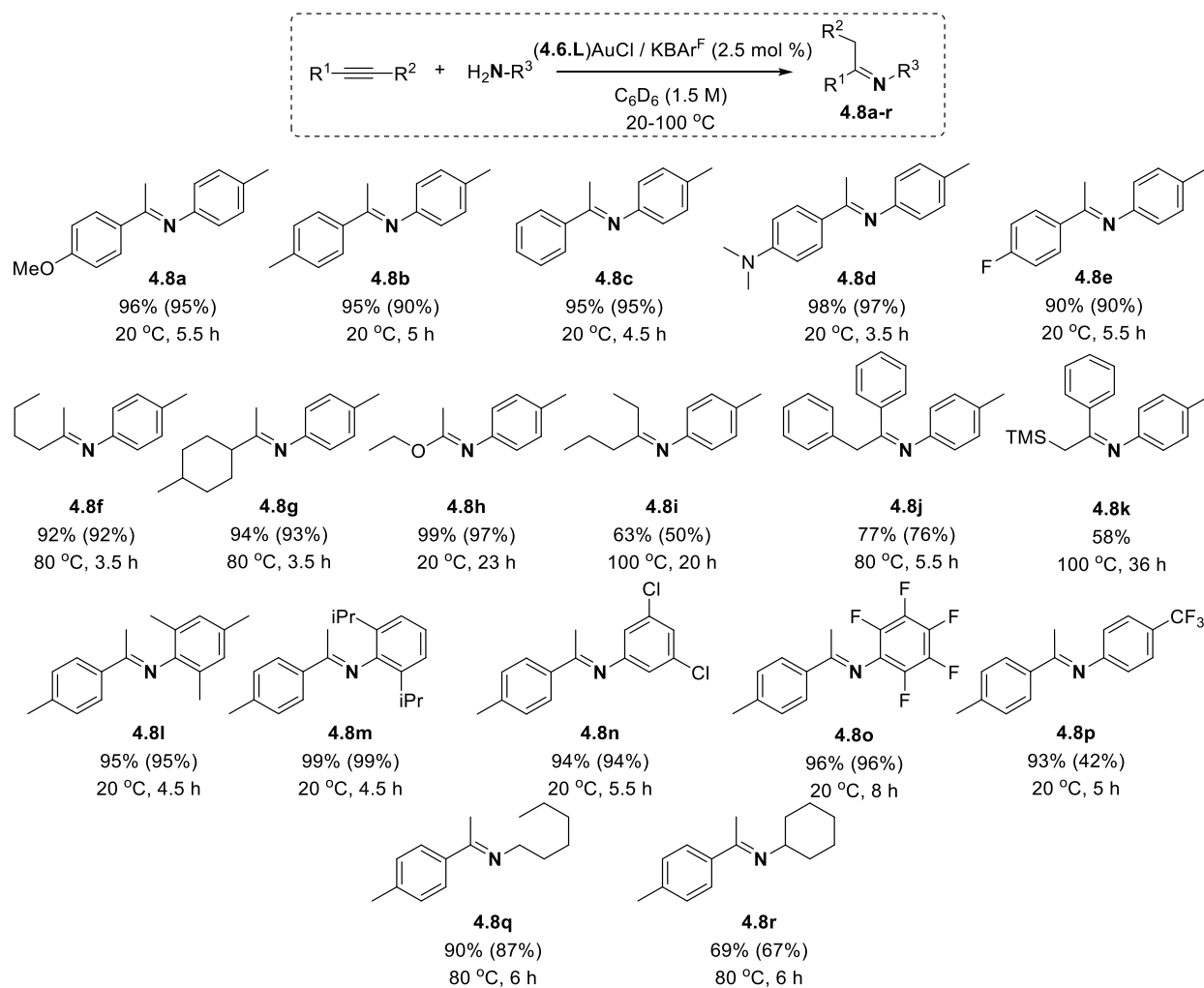


Figure 4.5. Hydroamination substrate scope with variety amines and alkynes. NMR yields (isolated yields).

Hammett plot: To understand the influence of electronics contributions at the substrate we conducted a Hammett correlation study. As illustrated in Figure 4.6, both anilines and alkynes showed slower reaction kinetics with electron-withdrawing *para*-substituents (ρ value < 0) which supports for a positive charge being built on the reaction center. The exception was the *p*-NMe₂-substituted alkyne, which may interfere with alkyne coordination by binding to the NMe₂ group.

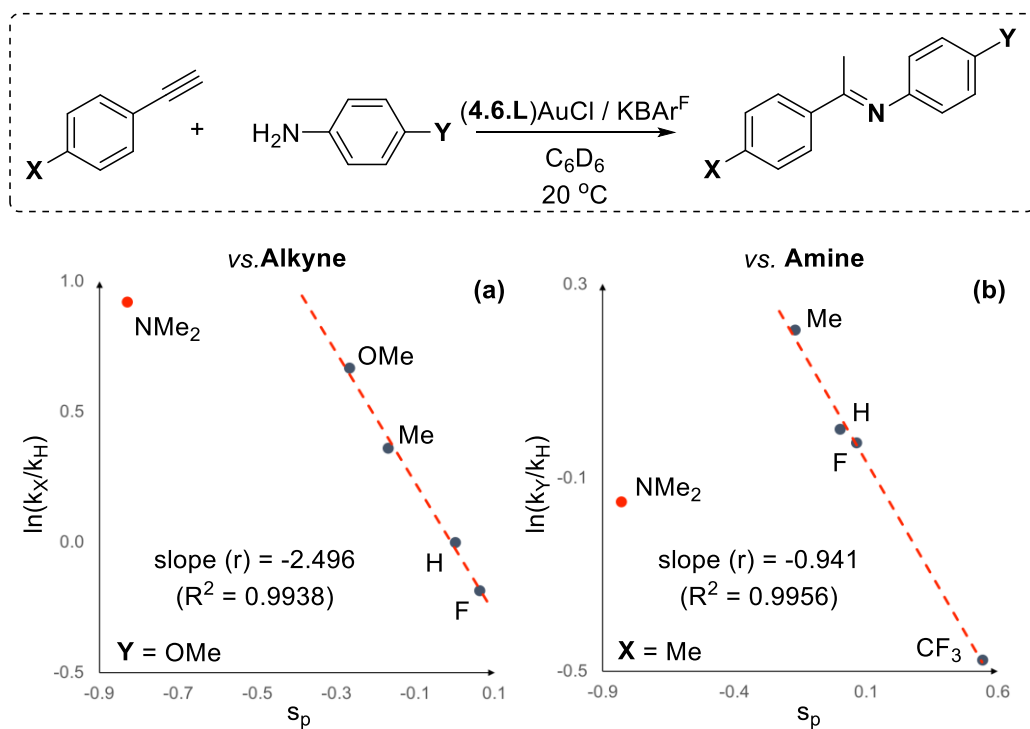


Figure 4.6. Hammett correlation in (a) alkyne and (b) amine; to quantify the electronic influence of the substrates in alkynes and amines.

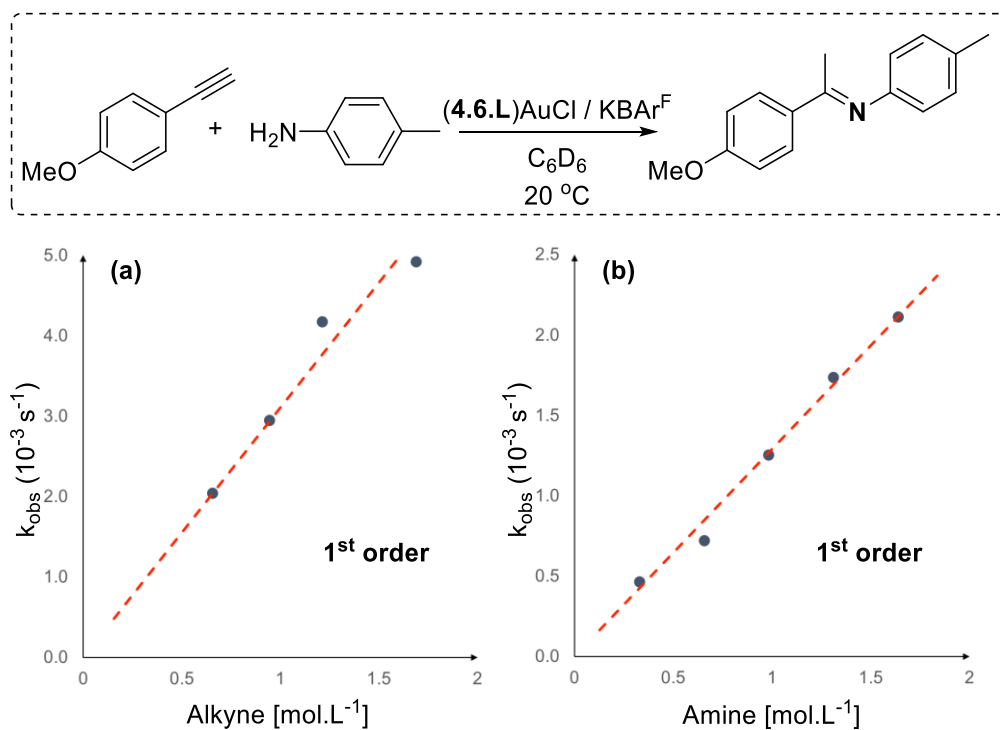


Figure 4.7. Rate dependence of the alkyne and amine in hydroamination.

Rate order: To determine the rate order of the reaction, we also investigated the rate behavior of both reagents, alkyne and amine, under pseudo first-order conditions (Figure 4.7). In both cases, a first order dependency was observed suggesting that both reagents are involved in the rate-limiting step.

4.3.2. Hydrohydrazination reaction

Having obtained good result for the hydroamination reaction, so we decided to extend our study investigate to the hydrazination of alkynes. Compared to amines, hydrazines are more challenging mostly due to their propensity of promote the formation of inert gold(0) nanoparticles,¹⁵⁵ or unreactive Werner complexes.^{156,157} In 2011, our group reported that (CAAC-5)Au complex **4.3.L** was able to catalyze the hydrohydrazination of variety of alkynes, however under very demanding reaction temperatures (90-100 °C).¹³⁶ It should be noted that the same transformation was also achieved by Hashmi et al. (2014) using a

saturated NHC (*sa*NHC)¹⁵⁸ and our group (2012-2013) using an *anti-Bredt*-NHC,^{159,160} albeit in limited substrate scope.

Reaction conditions: Having found a convenient way to evaluate amines we proceeded to investigate hydrazines. Starting with the reaction of phenyl hydrazine with *para*-methoxy-phenyl acetylene at room temperature we monitored the formation of **4.9a**, meanwhile changing reaction condition parameters such as catalysts, solvent, the concentration, and the catalyst loading (Figure 4.8). Note that here also KBar^F was used as an ionizing reagent. The accuracy of our kinetic methodology was confirmed by performing the same reaction with (Ph₃P)AuCl.¹⁴⁴

During optimizing reaction condition, we realized that less sterically hindered ^{*Et*}CAAC-5 (**4.3.L**, %V_{bur} : 43.2) did perform as well as bulkier ^{*Et*}CAAC-6 (**4.4.L**, %V_{bur} : 47.4) and ^{*Ad*}CAAC-5 (**4.5.L**, %V_{bur} : 48.4). This result and the importance of the ligand other the stability of the catalyst towards disproportionation,¹⁶¹ is discussed in detail in section 4.3.

¹H NMR kinetic studies showed that the optimal conditions for the hydrohydrazination reaction involve performing the reaction in chloroform, with 0.5 mol% catalyst loading and 1.8 M concentration as a compromise between conversion and reaction time (Figure 4.8). Based on the increasing trend of the catalytic activity **4.5.L** < **4.4.L** < **4.7.L** < **4.6.L**, we believe that the same previously-mentioned rationale of an electronic and steric effects in amine additions with the ^{*IPr*}BiCAAC **4.6.L** applies for hydrazine addition reactions.

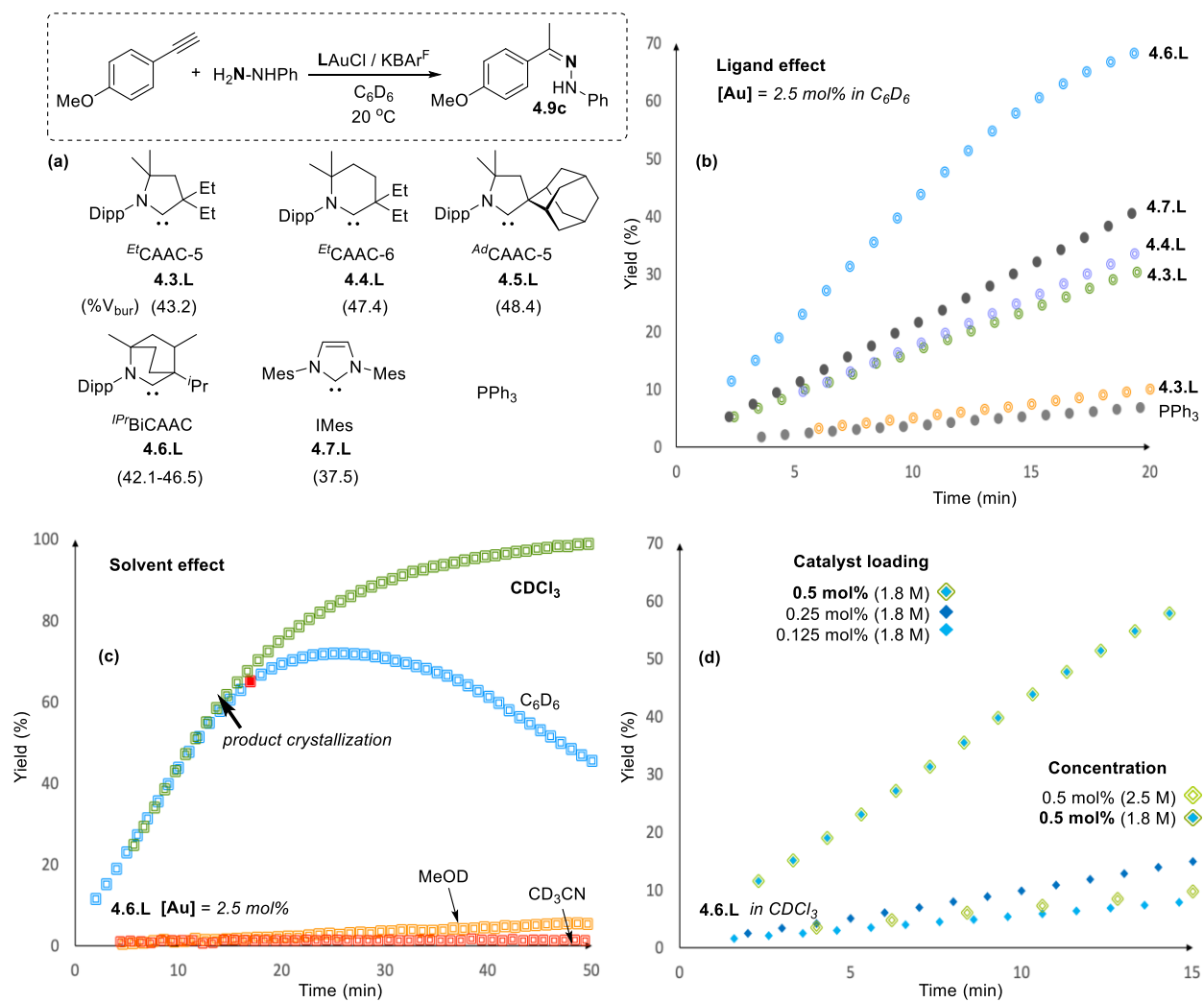


Figure 4.8. Optimization of hydrohydrazination conditions using ^1H NMR kinetic monitoring.

Reaction scope: To expand the substrate scope we evaluated other hydrazines and alkynes using 0.5-2.5 mol% of **4.6.L-AuCl**/KBAr^F in benzene - 1.8M (Figure 4.9).

Using phenylhydrazine, we found this catalyst to be very efficient with aryl substituted terminal alkynes (**4.9a-4.9e**). The reaction is much slower with 3-ethynylpyridine (**4.9f**), demanding higher reaction conditions and 2.5 mol% catalyst loading (80 °C, 10 h). The same observation obtained by using alkyl substituted terminal alkynes, as well as internal alkynes: **4.9g-4.9k** required higher reaction temperatures to reach high conversion within a reasonable time. Mono-substituted and parent hydrazines were easily converted under mild conditions (**4.9l-4.9m**), as well as disubstituted hydrazines **4.9o** and **4.9p**, albeit they were much less reactive.

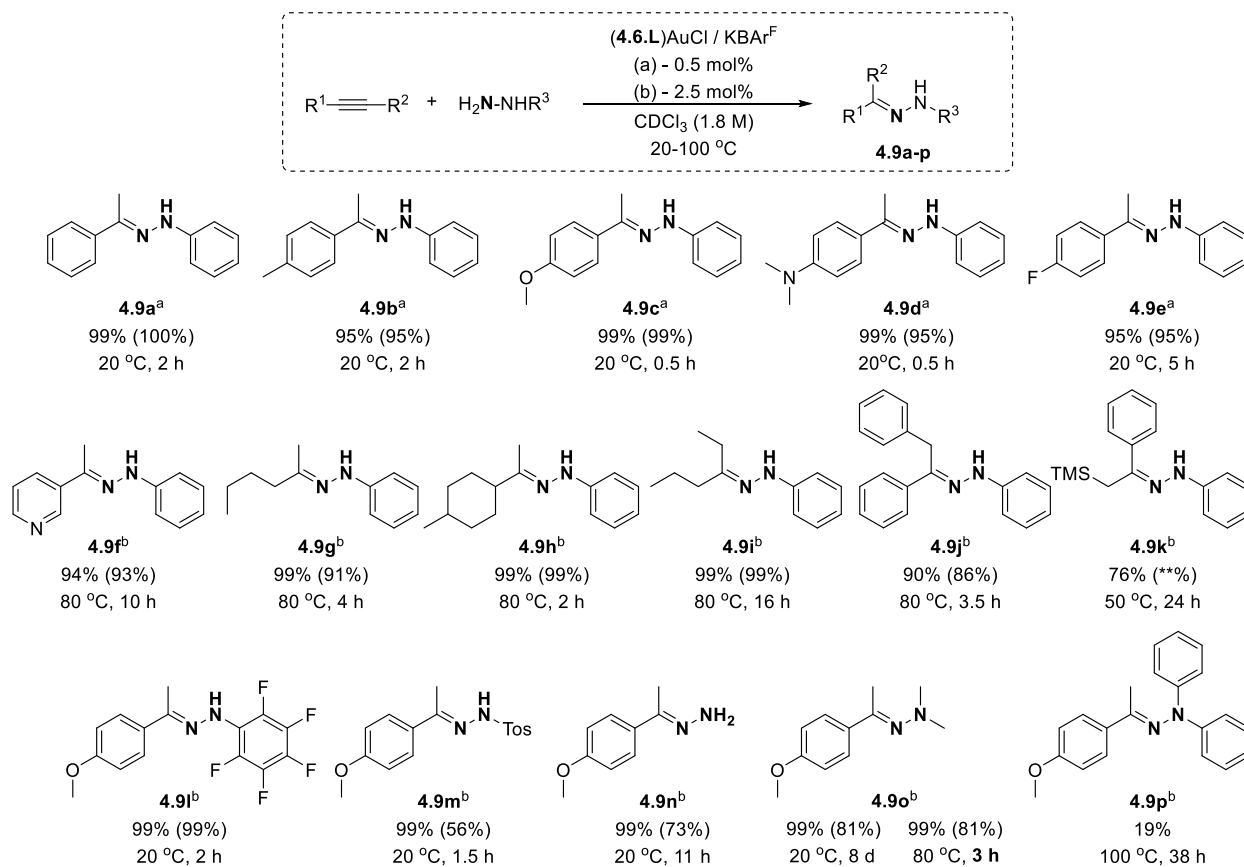


Figure 4.9. Substrate scope with hydrazines. NMR yields (isolated yields).

Hammett plot: To understand the influence of electronics contributions at the substrate we conducted a Hammett correlation study (Figure 4.10). Slower reaction kinetics were obtained with electron withdrawing *para*-substituents on alkynes (ρ value < 0) consistent with a positive charge being built on the gold center. In contrast and as illustrated in Figure 4.10, with phenylhydrazine, faster kinetics were obtained with electron withdrawing substituents (ρ value > 0). This observation is in good agreement with the experimental results (4.9.1-o) and could be due to the higher affinity of the most basic hydrazines to the gold center.

Rate order: To determine the rate order of the reaction, we also investigated the rate behavior of both reagents, alkyne and hydrazine, under pseudo first-order conditions (Figure 4.11). For both reagents, we observed first order dependency, here also meaning that both reagents are involved in the rate-limiting step.

Based on the upper mentioned results for hydroamination, we can conclude that both reactions likely involve a nucleophilic attack of an amine or hydrazine nucleophile onto a gold π adduct (activated C-C triple bond), followed by nucleophile-assisted nitrogen-to-carbon atom proton transfer.^{144, 162}

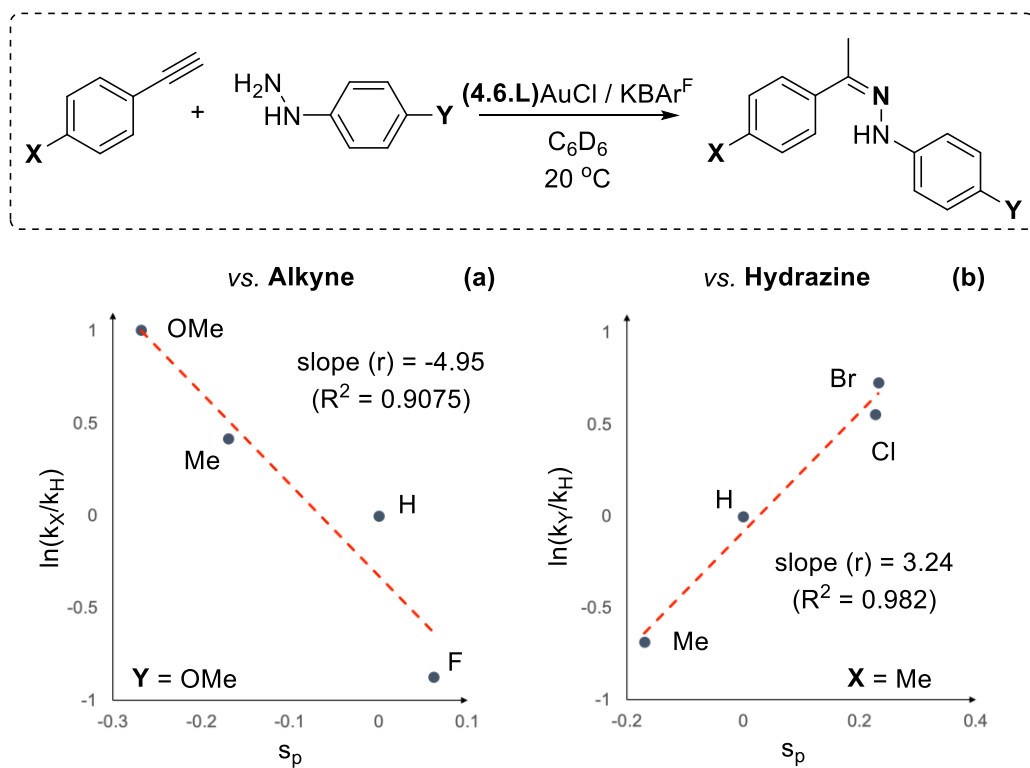


Figure 4.10. Hammett equation for the hydrohydrazination

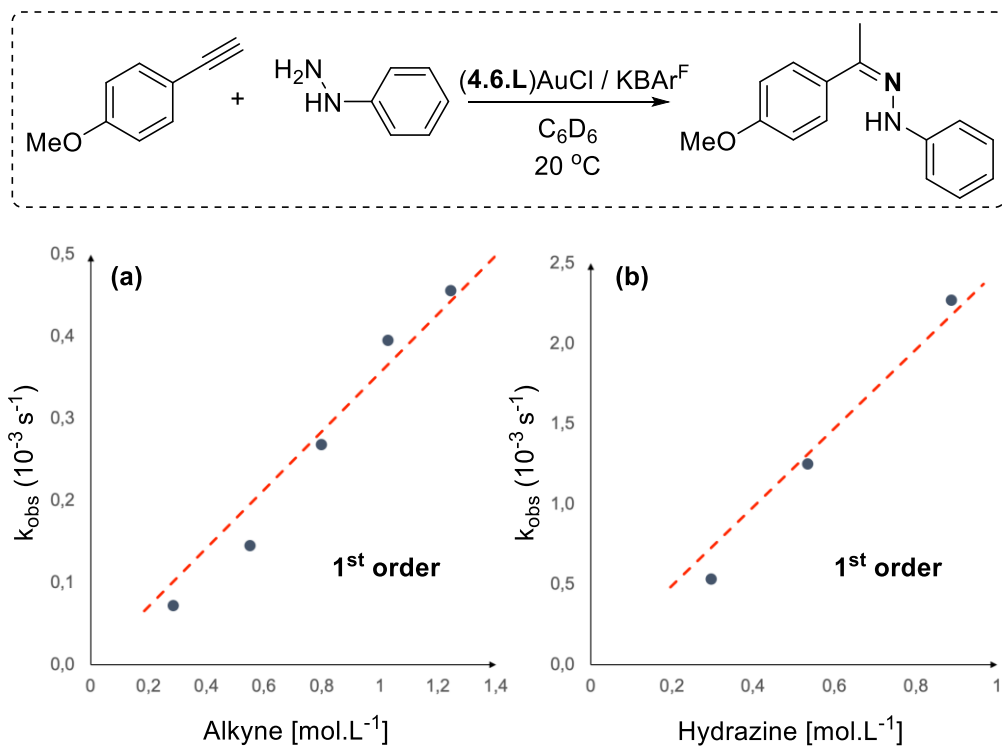


Figure 4.11. Rate dependency for alkyne and hydrazine.

4.4. What is the ligand effect on the catalyst performance?

Effect of the ligand on gold catalyst stability: Based on literature precedents we are aware of two facts:

1) the main reason for catalyst degradation and ultimately low turnovers is related to the formation of unreactive Au⁰ nanoparticles or unreactive cationic gold species (L)₂Au⁺. For instance, Xu and coworkers reported that the decay of cationic gold [(R₃P)Au⁺(η²-π-alkyne)][OTf⁻] is phosphine dependent.¹⁴⁴ On the other hand, Buchwald-type biphenyl phosphine ligands were shown to afford very stable cationic gold complexes,¹⁴⁴ thanks to secondary η²-C_{ipso} stabilizing interactions.¹⁶³

2) A key intermediate of the gold catalyzed hydroamination and hydrohydrazination reactions involves a transient gold π-adduct (L)Au⁺(η²-π-alkyne).

To understand the effect of the ligands on the stability of the cationic gold (L)Au⁺(η²-π-alkyne) under pseudo-catalytic conditions, we performed a series of decomposition experiments. For that, cationic gold species bearing **4.3.L-4.6.L** were mixed with 1-hexyne at room temperature and the NMR spectrum was monitored over time (Figure 4.12). During these systematic studies we discovered that **4.3.L**, **4.5.L**, and **4.6.L** yielded cationic gold species which are stable up to 4 days under these conditions. In marked contrast, gold species from **4.4.L**, **4.10.L** and PPh₃ degraded rapidly. In case of the gold complexes from **4.4.L** and PPh₃, we also observed the formation of insoluble black deposits in the NMR sample indicative of the decomposition of the catalyst by formation of gold(0) nanoparticles. To better understand the stability for the complex derived from ^{lpr}BiCAAC **4.6.L**, we also considered the smaller ^{Me}BiCAAC **4.10.L**. In the case of gold complex from ^{Me}BiCAAC **4.10.L**, rapid decomposition was observed suggesting that the steric profile of the BiCAAC ligand is an important component of the catalyst.

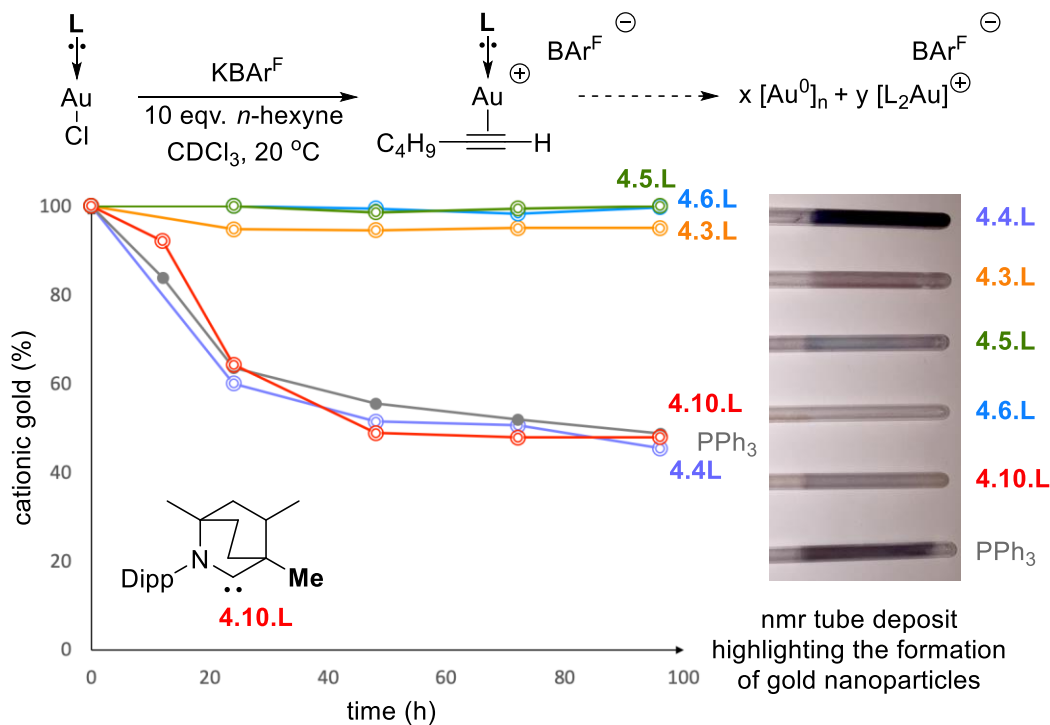


Figure 4.12. Ligand effects on the degradation of cationic gold $[\text{LAu}^+][\text{BAR}^{\text{F}-}]$.

Effect of the ligand on gold catalyst reactivity: The further demonstrate the importance of sterics in ligands $^{i\text{Pr}}\text{BiCAAC}$ **4.6.L** and $^{\text{Me}}\text{BiCAAC}$ **4.10.L**, we looked closely at the reactivity under catalytic conditions. As illustrated in Figure 4.13, in both hydroamination and hydrohydrazination reactions, we found that the gold complex of **4.6.L** outperforms that of **4.10.L**. To confirm these results we also performed the same reaction under stoichiometric conditions (Figure 4.14). With **4.10.L**, we observed the formation of the bis-ligated $(^{\text{Me}}\text{BiCAAC})_2\text{Au}^+$ **4.10** which we were able to isolate and characterize by X-ray crystallography. A similar phenomenon has been observed with a copper catalyst.¹²⁸ Comparatively, when performing the same reaction with **4.6.L**, the $(^{i\text{Pr}}\text{BiCAAC})\text{Au}^+(\text{alkyne})$ adduct **4.12** bearing either BF_4 or BAR^{F} anion was isolated and the structure of the $[(^{i\text{Pr}}\text{BiCAAC})\text{Au}^+(\text{PhCCPh})(\text{BAR}^{\text{F}})]$ was confirmed by X-ray crystallography. We went further and reacted this complex with an excess of tolylamine or tosylhydrazine. As we expected the formation of the corresponding imine **4.8b** and hydrazone **4.9q** were observed. More importantly, these experiments also showed the concomitant formation of the Werner

adducts **4.13** and **4.14** (Figure 4.14) which illustrates that **4.6.L** is able to stabilize the gold center at every step of the catalytic cycle.

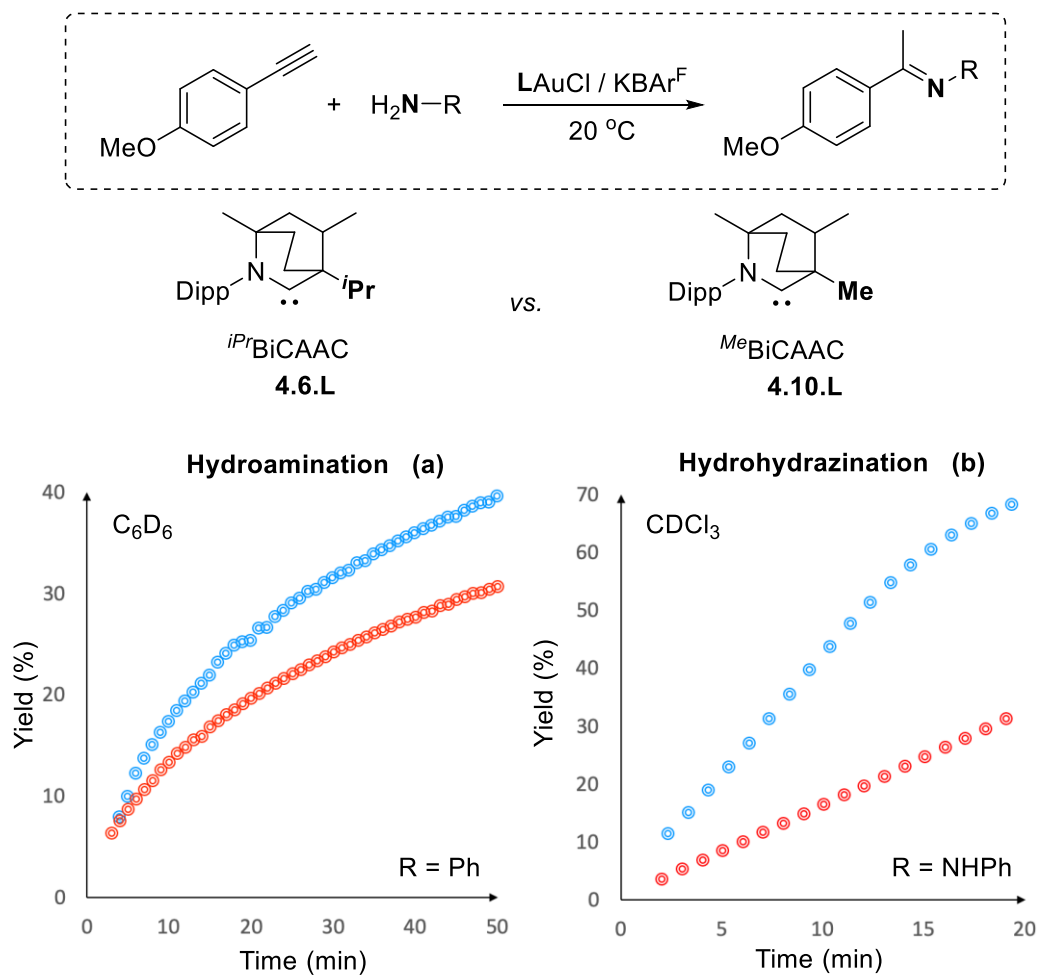


Figure 4.13. ^1H NMR spectroscopic study of the kinetics of reactions of gold complexes bearing **4.6.L**-**4.10.L**.

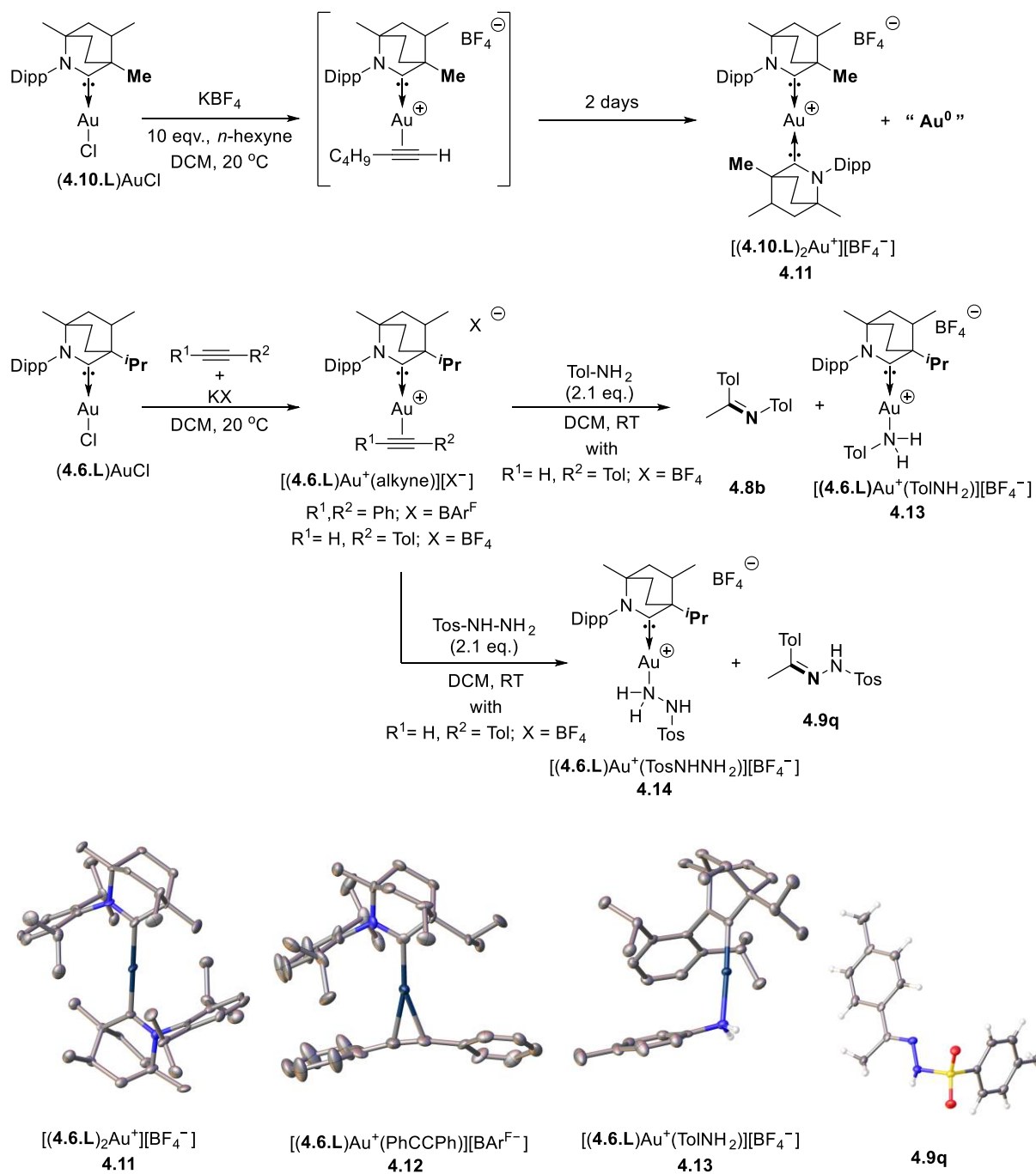


Figure 4.14. Mechanistic behavior of BiCAACAu⁺ under stoichiometric conditions.

Computational studies to investigate the effect of the ligand on catalyst activity: All DFT calculations were performed with the Gaussian09 program suite¹⁶⁴ using ultrafine (99,590) integration grids.¹⁶⁵ All structures were optimized with the ω B97X-D¹⁶⁶ functional basis set for all atoms except Au, which was treated with the SDD basis set and ECP. Solvent was treated as a polarizable continuum of benzene.¹⁶⁷ This work was done by my co-author, former Ph.D. students Glen P. Junor.

Using DFT, Ujaque and coworkers showed that the transition state barrier for substrate exchange between the Werner complex (catalyst resting state) and the active gold species (η^2 - π complex) follows the order of stability of the π -complex,¹⁵¹ meaning that the more stable the π -complex, the lower the barrier for a given ligand. With the help of computational studies, we compared the energy differences between the Werner complexes of phenyl hydrazine and the η^2 - π complex of phenylacetylene for (L)Au⁺ complexes bearing ligands **4.3.L** to **4.6.L** (Figure 4.15). Our DFT study explains that in both hydroamination and hydrohydrazination the ^{IPr}BiCAAC **4.6.L** forms the most accessible η^2 - π adducts, which could explain the relative efficiency of (4.6.L)Au⁺ complexes in catalysis. There is a trend for increasing barrier height for proton transfer with increasing donor-strength of the ligand (barrier height CAAC > saNHC). This principle provides a conundrum for chemists designing catalysts, where there is a trade-off between the strength of the ligand to metal (L-M) bonds allowing for more durable catalysts and lower barriers to promote proton transfer.¹⁶⁸

Therefore, the strongest L-M bonds may be produced by using the most ambiphilic ligands (for instance **4.3.L**, **4.4.L**, **4.5.L**, and **4.6.L**), but at the expense of increased barriers for proton transfer in the order **4.4.L** > **4.6.L** > **4.3.L** = **4.5.L**. Based on these results, we can rationalize why ^{Et}CAAC-6 (**4.4.L**) performs much worse than other carbenes despite its strongest M-L bond and a sterically flexible backbone. This scenario is applicable for the NHC **4.7.L** as well, which performs well compared to the more ambiphilic carbenes because of its relatively weak donor-ability resulting in a low proton transfer barrier.

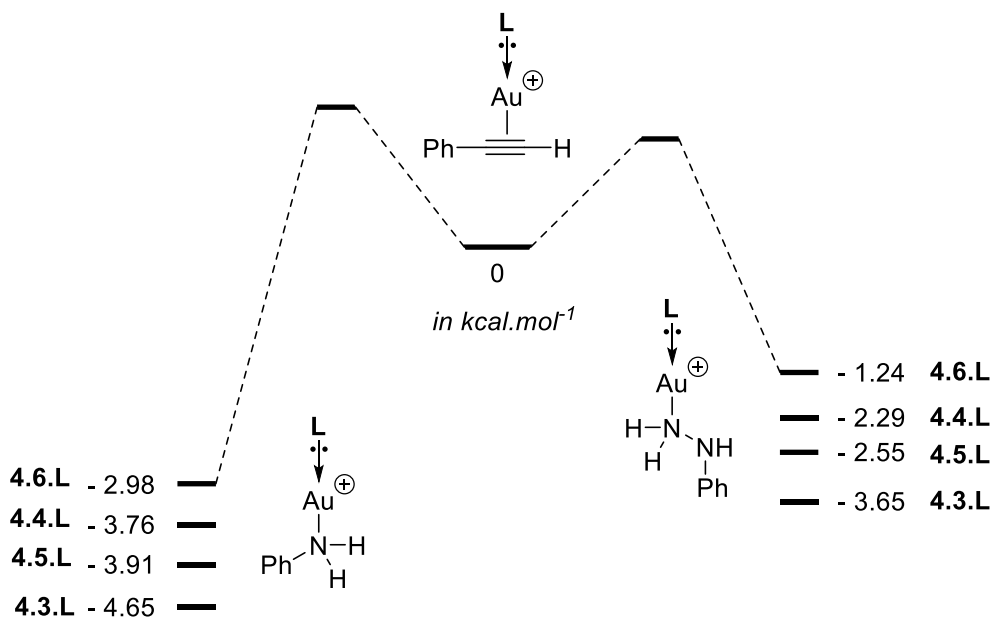


Figure 4.15. Energy profiles of substrate ligand exchanges as a function of **4.3.L-4.6.L**.

We also used DFT combined with %V_{bur} (percent buried volume)^{152,153} to further establish our experimental observations related to the stabilizing character of ^{IPr}BiCAAC **4.6.L** and ^{Me}BiCAAC **4.10.L**. As shown in Figure 4.16, rotation of the isopropyl substituent on the tertiary carbon of the ^{IPr}BiCAAC rotate changes the %V_{bur} value. Consequently, the steric bulk of ^{IPr}BiCAAC is more amenable to variations at the metal during the catalytic cycle. Combined with the high ambiphilicity of the ^{IPr}BiCAAC, it yields a more robust catalyst compared to the other ligands we have used.

To conclude, our data indicate that ^{IPr}BiCAAC **4.6.L** benefits from both a strong M-L bond, which maybe associated also with a relatively low barrier to proton transfer, both of which explain remarkable catalytic activity in both hydroamination and hydrohydrazination processes.

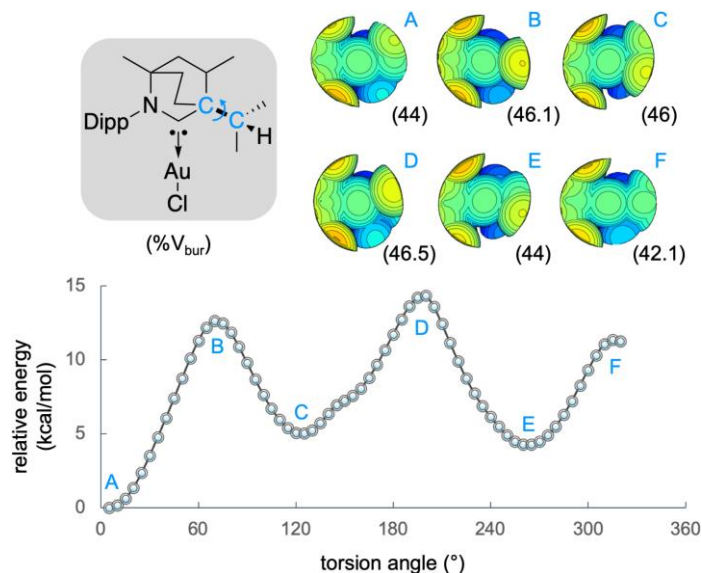


Figure 4.16. Presenting the flexible sterics in $IPrBiCAACAuCl$.

4.5. How do $IPrBiCAACAuCl$ compare to state-of-the-art catalysts?

The challenge and limitation for most of the gold catalytic reactions is the robustness of gold complexes to perform under long reaction time and high temperatures. However, sophisticated complexes derived from ligands such as WangPhos **4.1.L**,¹⁴⁷ NHC bearing barbituric heterocycle **4.2.L**,¹⁴⁸ and Lavallo anionic phosphine ligands **4.15.L**¹⁶⁹ relying on second-coordination sphere interactions have been shown to some extent to overcome these limitations. To compare catalytic activity of the $IPrBiCAACAuCl$ to known gold complexes bearing sophisticated ligands, we performed a series of benchmark reactions.

To begin, we compared the gold complex of $IPrBiCAAC$ **4.6.L** to that of JohnPhos ligand **4.15.L** (Figure 4.17), which has been shown to be very efficient in the hydroamination reaction.¹⁴⁴ As presented in Figure 4.17, we found gold complex from JohnPhos **4.15.L** to outcompete the complex from **4.6.L** in the hydroamination, whereas the complex from **4.6.L** gave a complex significantly more active in hydrohydrazination.

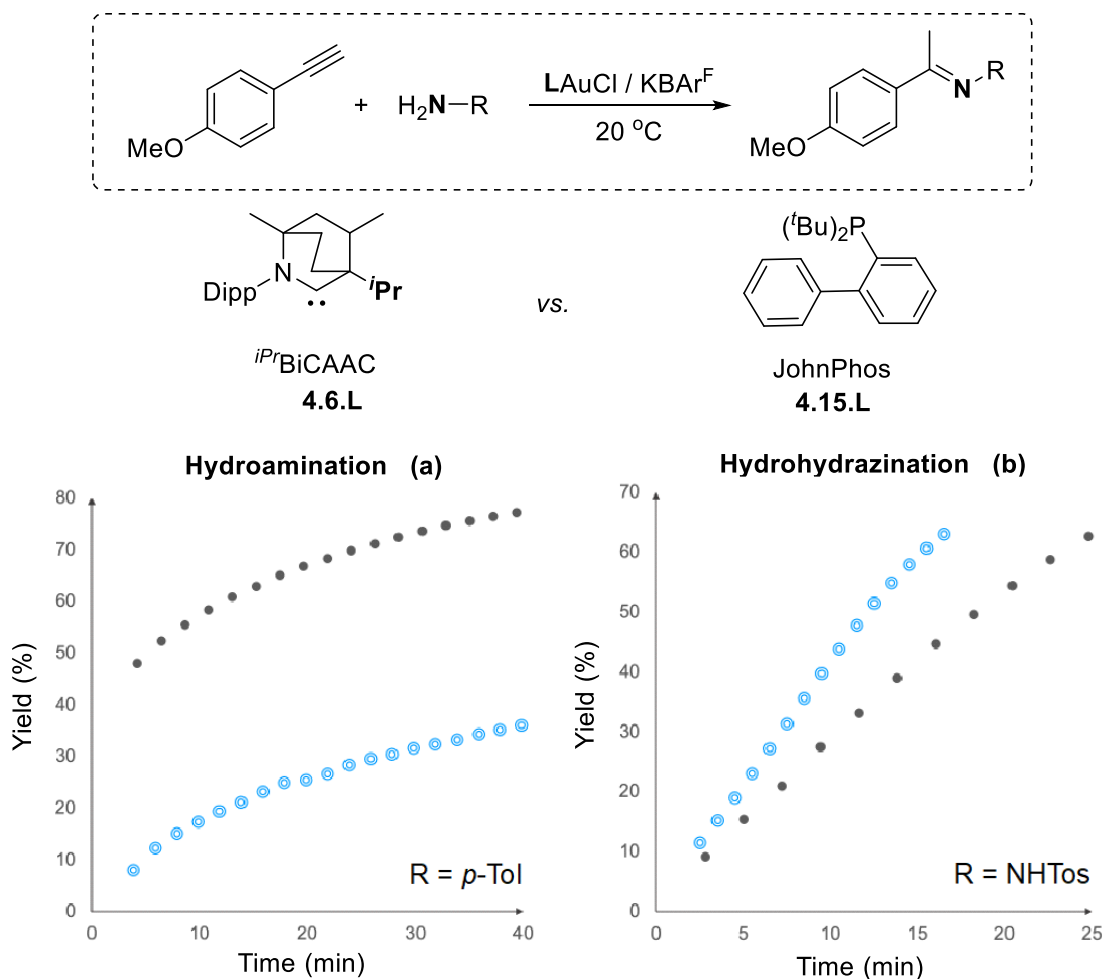


Figure 4.17. Comparing complexes of **4.6.L** and JohnPhos.

Capitalizing on the strength of the L-M bond in the AuCl complex of **4.6.L**, we hypothesized that this catalyst should remain stable at higher temperature, thus contrasting with catalyst made using JohnPhos. Hence, we evaluated the catalytic activity of **4.6.L** at 80 °C.^{147,148} Under these conditions we obtained 18,700 TON in 19 h for hydroamination of phenylacetylene and aniline. We also evaluated the hydrohydrazination under the same conditions which reached up to 36,700 TON (Figure 4.18). This is to the best of our knowledge the highest catalytic activity reported for hydrohydrazination of phenylacetylene. It is worth noting that catalyst made with the *i*PrBiCAAC compares well with catalysts made from complex and tailored state-of-the-art phosphine **4.1.L** and NHC **4.2.L** and anionic phosphine **4.15.L** ligands.

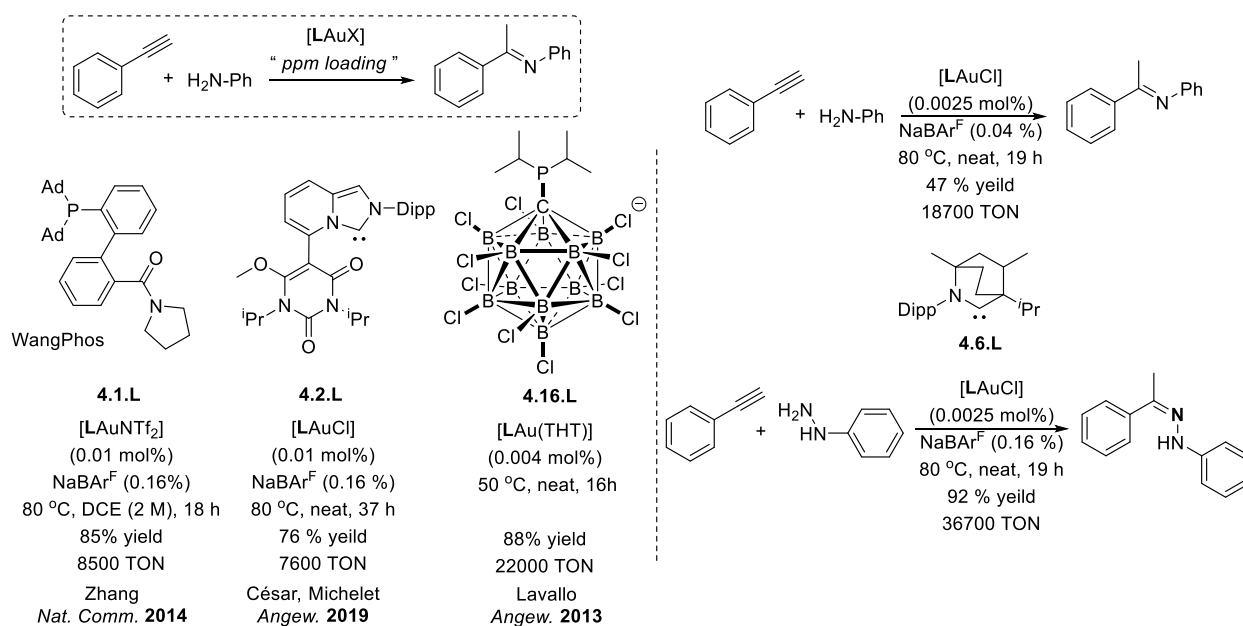


Figure 4.18. Benchmarking the catalytic activity at 80 °C.

4.6. Conclusion

In summary, we have reported a comprehensive study of the reactivity of CAAC gold complexes in the hydroamination and hydrohydrazination of alkynes. Our kinetic measurements demonstrate that the ⁱPrBiCAAC **4.6.L** provides a very active catalyst for this transformation, which we rationalized through our mechanistic and DFT studies.

We concluded that the unique steric and electronic environment provided by ⁱPrBiCAAC **4.6.L** moiety shields the gold from degradation and also stabilizes the η^2 - π complex which is the active gold intermediate during catalytic cycle. As a result of unique character of the **4.6.L**, we obtained high TON for hydroamination and hydrohydrazination of alkynes, thus competing with the best phosphine and NHC ligands in the field.

Highlight of my research: There is a general opinion among researchers in this field that improvement of gold catalysts can only be achieved through the design of complex and tailored secondary interactions. However, I have provided comprehensive evidence that there is still much to be gained in controlling the core of the ligands. In fact, if anything, the remarkable progress made in the past 30 years

in the design and tuning of stable carbenes have taught us that these species provide an exceptional handle for the tuning of the electronic and steric environment around a metal center.

4.7. Experimental Section

All the catalytic experiments were performed in air unless using commercial grade solvents and reagents unless otherwise noted. All the kinetic experiments were performed three times to verify the reproducibility of the results. All other manipulations were performed using standard glovebox and Schlenk techniques. Glassware was dried in an oven overnight at 150 °C or flame-dried before use. Benzene, diethyl ether, and n-pentane were freshly distilled over Na metal. Hexanes, dichloromethane, and chloroform were freshly distilled over CaH₂. Deuterium-labeled solvents were purchased from Cambridge Isotope Laboratories.

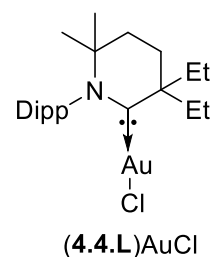
NMR: Multinuclear NMR data were recorded on a Varian INOVA 500 MHz or a Bruker Avance 300 MHz. Chemical shifts (δ) are reported in parts per million (ppm) and are referenced to residual solvent signals (¹H, ¹³C). Coupling constants *J* are given in hertz (Hz). NMR multiplicities are abbreviated as follows: s = singlet, d = doublet, t = triplet, q = quartet, p = pentet, sext = sextet, sept = septet, m = multiplet, br = broad. All spectra were recorded at 298 K unless otherwise noted.

Crystallographic structure determinations: Single-crystal X-ray structure determinations were carried out at low temperature on a Bruker P4, Platform, or Kappa diffractometer equipped with a Mo ($\lambda = 0.71073 \text{ \AA}$) or Cu ($\lambda = 1.54178 \text{ \AA}$) radiation source and a Bruker APEX detector. Crystals were selected under oil, mounted on nylon loops, then immediately placed in a cold stream of nitrogen. All structures were solved by direct methods with SIR 2004 or SHELXS and refined by full-matrix least-squares procedures utilizing SHELXL within the Olex 2 small-molecule solution,¹⁷⁰ refinement, and analysis software package.

4.8. Synthesis of gold catalysts

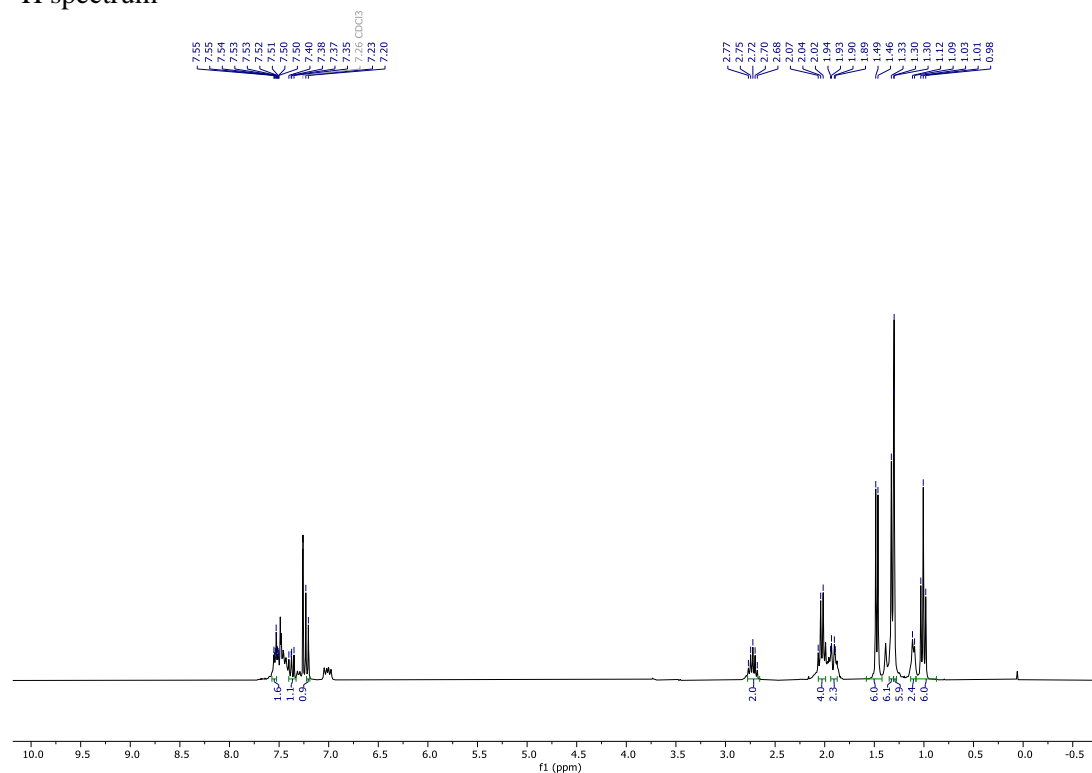
Synthesis of (4.4.L)AuCl:

Under an argon atmosphere, a 50 mL Schlenk flask was charged with [(4.4.L)AuPh] (1.000 g, 1.702 mmol, 1.0 eq.) and 15 mL of anhydrous THF. The solution was then cooled to -78 °C and stirred for 15 min, before adding a 2 M HCl solution in Et₂O (1.28 mL, 1.5 eq.) dropwise. Warming up to room temperature slowly over the course of 5 h, and evaporation of the volatiles in vacuo afforded (4.4.L)AuCl

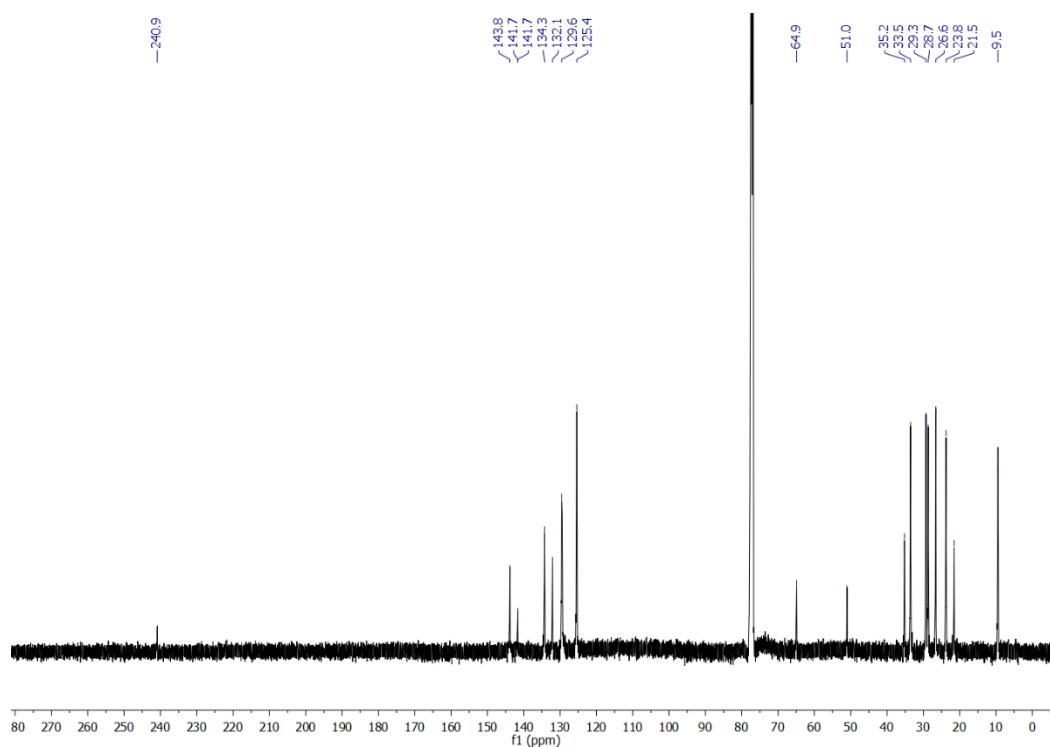


as a white powder (0.919 g, 99% yield). ¹H NMR (300 MHz, CDCl₃) δ 7.58 – 7.49 (m, 1H), 7.38 (dd, *J* = 8.3, 7.1 Hz, 1H), 7.22 (d, *J* = 7.7 Hz, 1H), 2.72 (p, *J* = 6.7 Hz, 2H), 2.08 – 1.99 (m, 4H), 1.96 – 1.88 (m, 2H), 1.47 (d, *J* = 6.7 Hz, 6H), 1.33 (d, 6H), 1.30 (d, 6H), 1.30 (s, 3H), 1.10 (d, *J* = 6.2 Hz, 2H), 1.01 (t, *J* = 7.4 Hz, 6H). ¹³C{¹H} NMR (126 MHz, CDCl₃) δ 240.9, 143.8, 141.7, 141.7, 134.3, 132.1, 129.6, 125.4, 64.9, 51.0, 35.2, 33.5, 29.3, 28.7, 26.6, 23.8, 21.5, 9.5.

¹H spectrum

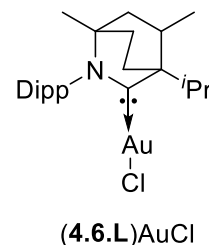


$^{13}\text{C}\{^1\text{H}\}$ spectrum

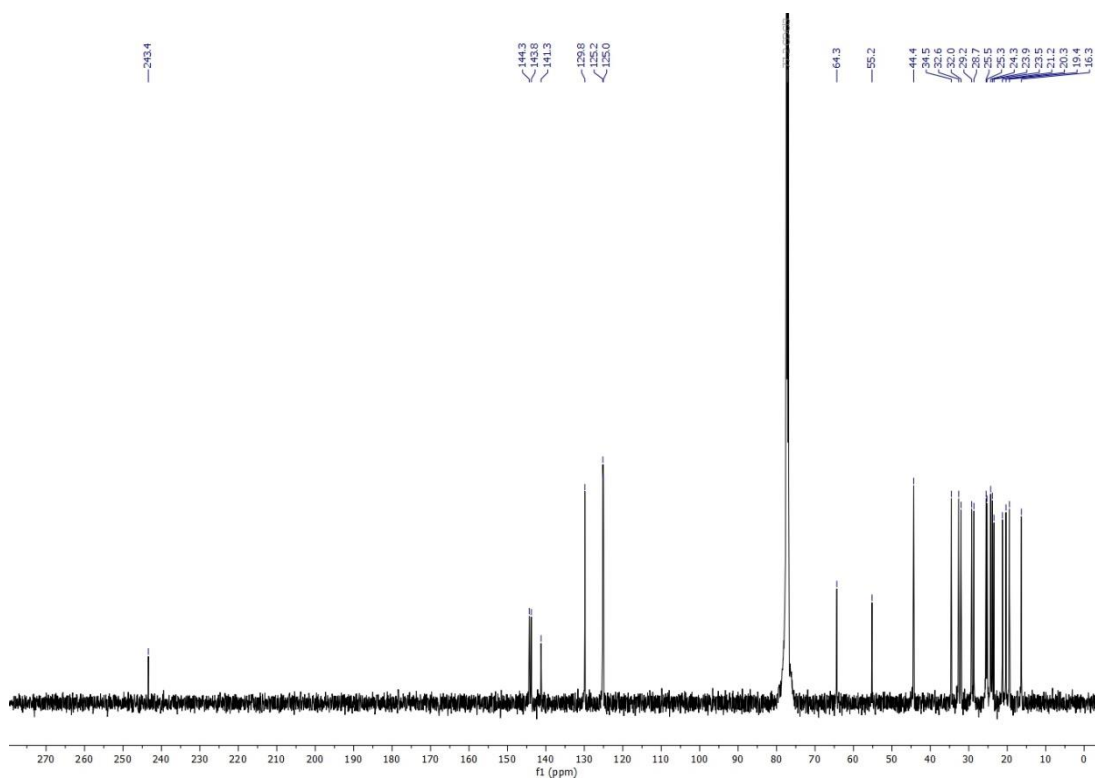


Synthesis of (4.6.L)AuCl

(4.4.L)AuCl was prepared in a two-step procedure from the free carbene.⁸ Step 1 - (4.6.L)AuPh: Under an argon atmosphere, a 50 mL Schlenk flask was charged with 20 mL of THF, the free carbene **4.6.L** (1.000 g, 2.945 mmol, 1.01 eq.) and [(PPh₃)AuPh] (1.563 g, 2.916 mmol, 1.0 eq.). After stirring the solution at room temperature for 2 hours, the volatiles were removed in vacuo and the oily crude residue was triturated with pentane to enforce precipitation of the titled compound. After filtration and further drying under vacuum (4.6.L)AuPh was obtained as a white solid (1.396 g, 80% yield). ¹H NMR (300 MHz, CDCl₃) δ 7.38 (t, *J* = 7.7 Hz, 1H), 7.27 – 7.16 (m, 2H), 7.11 – 7.00 (m, 4H), 6.90 – 6.81 (m, 1H), 3.29 (p, *J* = 6.8 Hz, 1H), 3.05 (p, *J* = 6.8 Hz, 1H), 2.63 (p, *J* = 6.8 Hz, 1H), 2.26 – 2.13 (m, 1H), 1.75 – 1.85 (m, 1H), 2.11 – 2.00 (m, 1H), 1.70 (d, *J* = 1.4 Hz, 2H), 1.56 (d, *J* = 6.8 Hz, 4H), 1.51 (d, *J* = 6.7 Hz, 4H), 1.38 (d, *J* = 6.8 Hz, 3H), 1.33 (d, *J* = 6.9 Hz, 3H), 1.25 (d, *J* = 6.9 Hz, 3H), 1.09 – 0.98 (m, 9H). ¹³C{¹H} NMR (126 MHz, CDCl₃) δ 269.0, 169.5, 144.8,

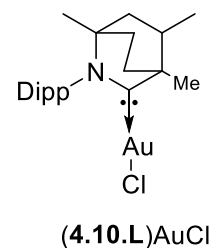


$^{13}\text{C}\{^1\text{H}\}$ spectrum

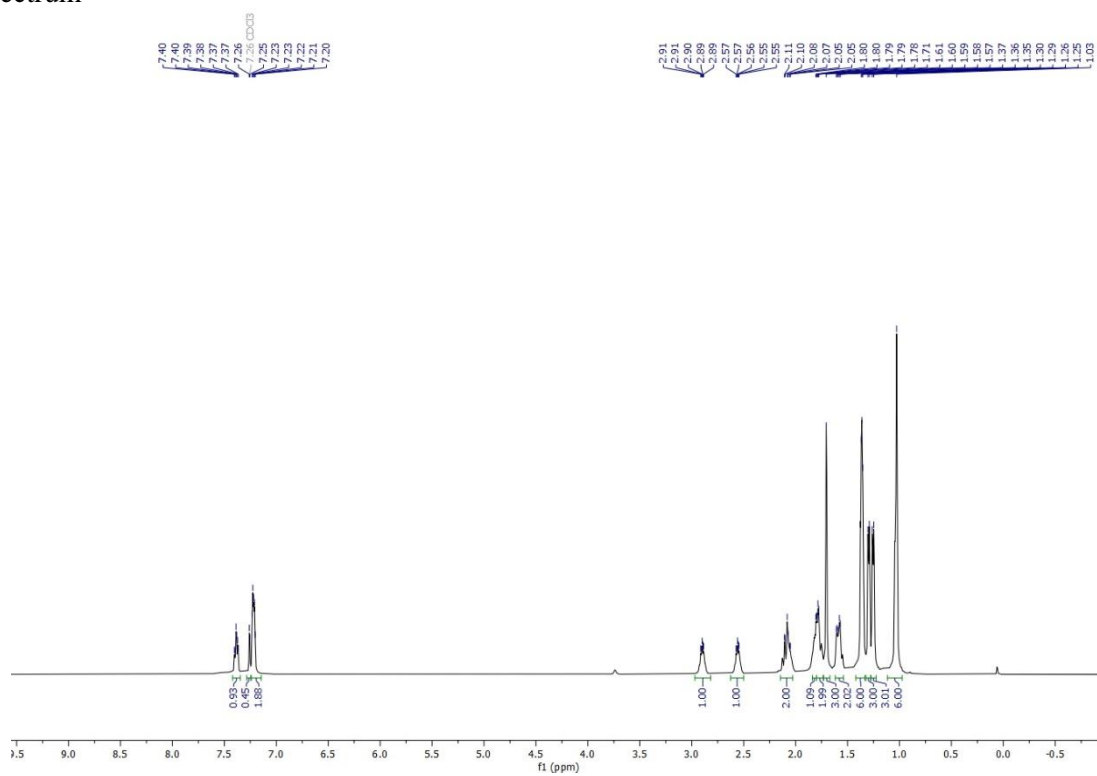


Synthesis of (4.10.L)AuCl

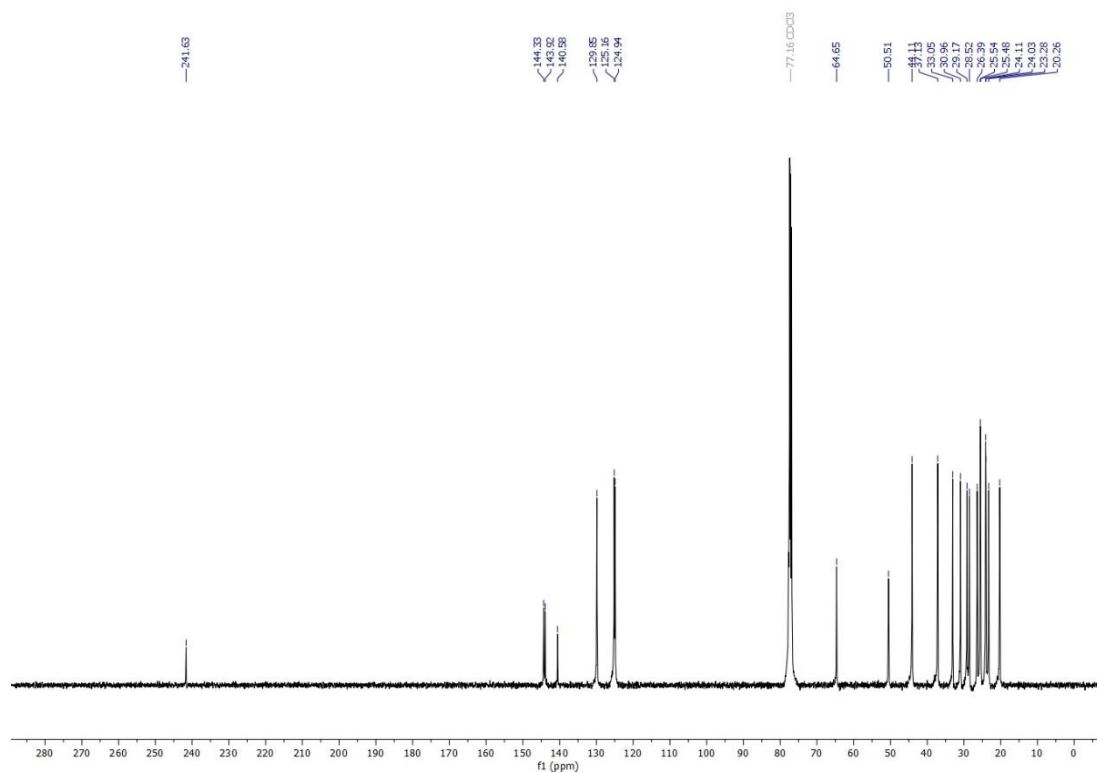
Following the same general procedure described for (4.6.L)AuCl, (4.10.L)AuCl was prepared in a two-step procedure from the free carbene (0.840 g, 95% yield). ^8H NMR (500 MHz, CDCl_3) δ 7.39 (td, $J = 7.7, 3.1$ Hz, 1H), 7.26 (d, $J = 3.2$ Hz, 1H), 7.22 (dt, $J = 7.5, 3.3$ Hz, 2H), 2.90 (dd, $J = 8.5, 5.3$ Hz, 1H), 2.56 (dd, $J = 8.5, 5.3$ Hz, 1H), 2.14 – 2.04 (m, 2H), 1.79 (dd, $J = 10.4, 3.7$ Hz, 3H), 1.71 (s, 3H), 1.61 – 1.56 (m, 2H), 1.39 – 1.33 (m, 6H), 1.30 (d, $J = 7.2$ Hz, 3H), 1.25 (d, $J = 7.1$ Hz, 3H), 1.03 (s, 6H). $^{13}\text{C}\{^1\text{H}\}$ NMR (126 MHz, CDCl_3) δ 241.6, 144.3, 143.9, 140.6, 129.9, 125.2, 124.9, 64.7, 50.5, 44.1, 37.1, 33.0, 31.0, 29.2, 28.5, 26.4, 25.5, 25.5, 24.1, 24.0, 23.3, 20.3.



^1H spectrum



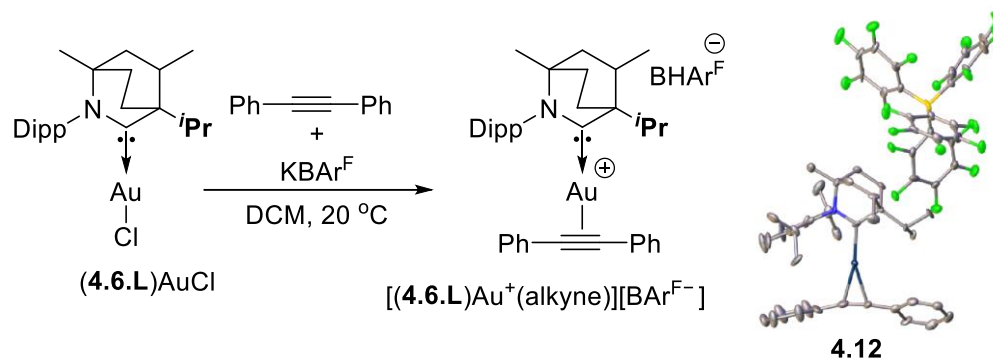
$^{13}\text{C}\{^1\text{H}\}$ spectrum



4.9. Mechanistic studies for hydroamination and hydrazination through stoichiometric reactions

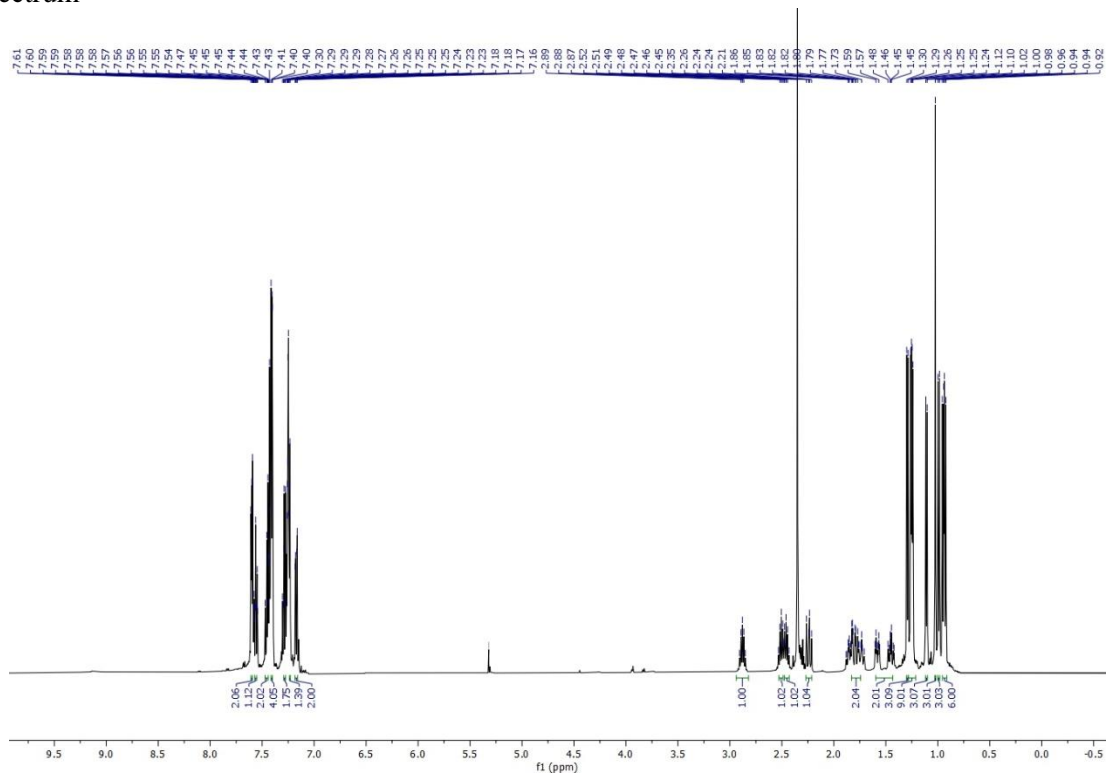
4.9.1. Isolating intermediates and active gold species during the catalytic cycle

Complex [(4.6.L)Au⁺(PhCCPh)(X)] 4.12

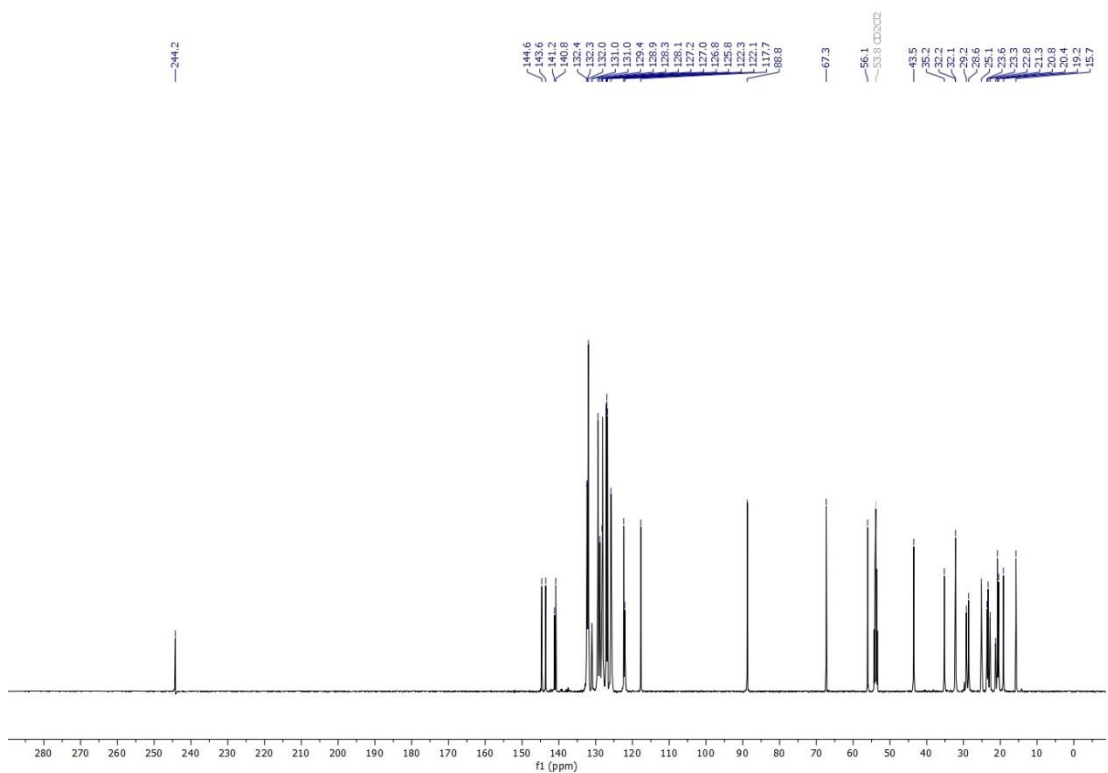


Under an argon atmosphere, a 25 mL Schlenk flask was charged with 2 mL of toluene/DCM mixture (50:50), KBar^F (0.250 g, 0.349 mmol, 1.0 eq.) and [(4.6.L)Au(Cl)] (0.200 g, 0.349 mmol, 1.0 eq.). The reaction was stirred for 1 h at room temperature and then filtered through celite into a separate reaction flask to remove KCl. The volatiles were removed under vacuum to afford an off-white residue. Following the addition of 2 mL of CH₂Cl₂ and diphenylacetylene (0.0622 g, 0.349 mmol, 1.0 eq.), the reaction mixture was stirred overnight at 50 °C. Removal of the volatiles under vacuum, trituration in pentane, filtration, and drying of precipitate afforded the titled compound as a greenish solid. X-ray quality crystals were obtained from a CH₂Cl₂/pentane mixture.

^1H spectrum



$^{13}\text{C}\{^1\text{H}\}$ spectrum

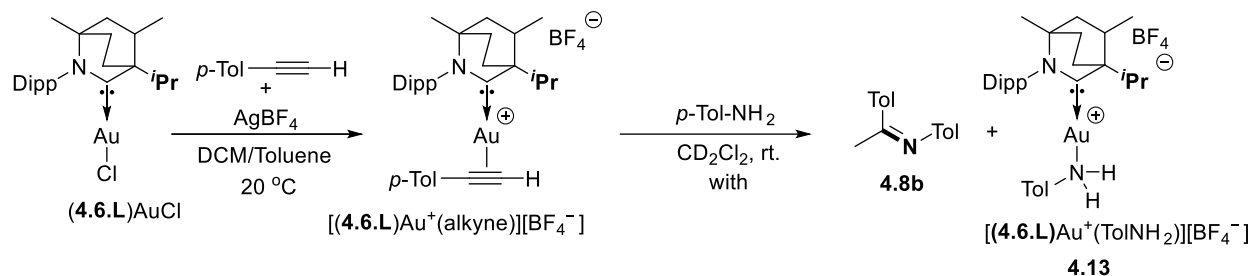


[(4.6.L)Au⁺(PhCCPh)(BF₄)⁻].

Under an argon atmosphere, a 25 mL Schlenk flask was charged with 2 mL of toluene, AgBF₄ (0.068 g, 0.349 mmol, 1.0 eq.) and [(4.6.L)Au(Cl)] (0.200 g, 0.349 mmol, 1.0 eq.). The reaction was stirred for 1 h at room temperature and then filtered into a separate reaction flask to remove AgCl. The volatiles were removed under vacuum to afford a brown residue. Following the addition of 2 mL of CH₂Cl₂ and diphenylacetylene (0.0622 g, 0.349 mmol, 1.0 eq.), the reaction mixture was stirred overnight at 50 °C. Removal of volatiles under vacuum, trituration in pentane, filtration, and drying of precipitate afforded the titled compound as a greenish solid (0.288 g, 95% yield). ¹H NMR (500 MHz, CD₂Cl₂) δ 7.61 – 7.58 (m, 2H), 7.58 – 7.54 (m, 1H), 7.49 – 7.42 (m, 2H), 7.42 – 7.39 (m, 4H), 7.29 (dd, *J* = 7.9, 6.8 Hz, 1H), 7.27 – 7.22 (m, 1H), 7.17 (dd, *J* = 7.8, 1.6 Hz, 2H), 2.88 (p, *J* = 6.8 Hz, 1H), 2.52 (dp, *J* = 23.1, 6.8 Hz, 1H), 2.48 (dp, *J* = 23.1, 6.8 Hz, 1H), 2.24 (dd, *J* = 13.8, 10.4 Hz, 1H), 1.90 – 1.81 (m, 2H), 1.80 – 1.58 (m, 2H), 1.29 (d, *J* = 6.9 Hz, 3H), 1.25 (dd, *J* = 6.9, 3.4 Hz, 9H), 1.11 (d, *J* = 6.8 Hz, 3H), 1.02 (s, 3H), 0.99 (d, *J* = 7.2 Hz, 3H), 0.94 (dd, *J* = 9.9, 6.7 Hz, 6H). ¹³C{¹H} NMR (126 MHz, CD₂Cl₂) δ 244.2, 144.6, 143.6, 141.2, 140.8, 132.4, 132.3, 132.0, 131.0, 131.0, 129.4, 128.9, 128.3, 128.1, 127.2, 127.0, 126.8, 125.8, 122.3, 122.1, 117.7, 88.8, 67.3, 56.1, 43.5, 35.2, 32.2, 32.1, 29.2, 28.6, 25.1, 23.6, 23.3, 22.8, 21.3, 20.8, 20.4, 19.2, 15.7. ¹⁹F{¹H} NMR (282 MHz, CDCl₃) δ -153.68. ¹¹B{¹H} NMR (96 MHz, CDCl₃) δ -1.01.

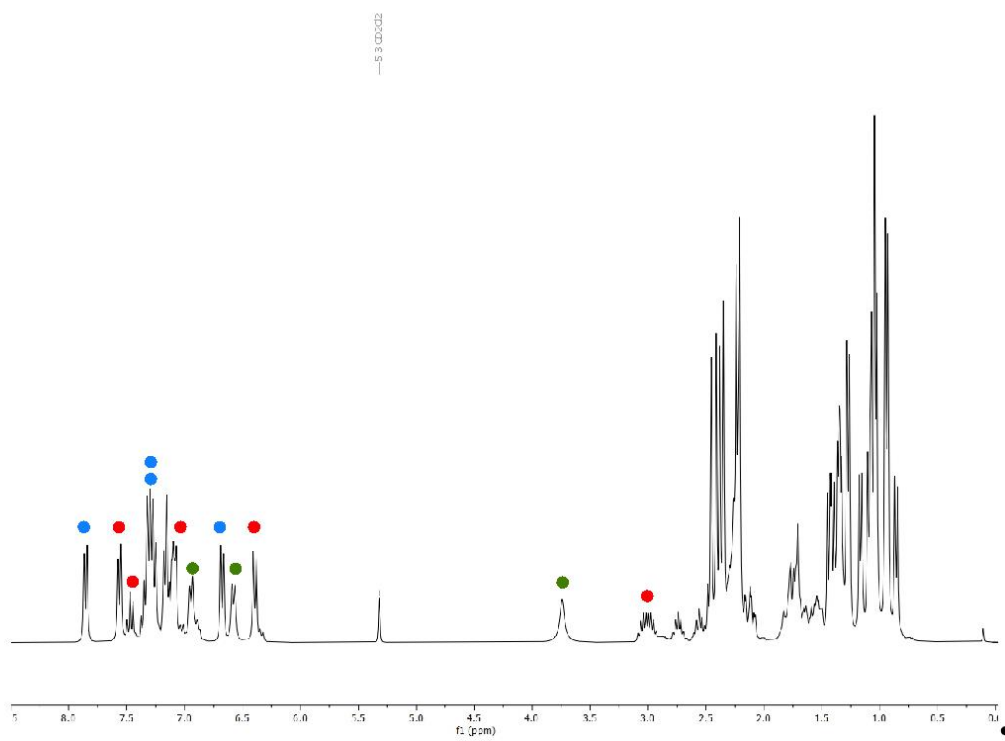
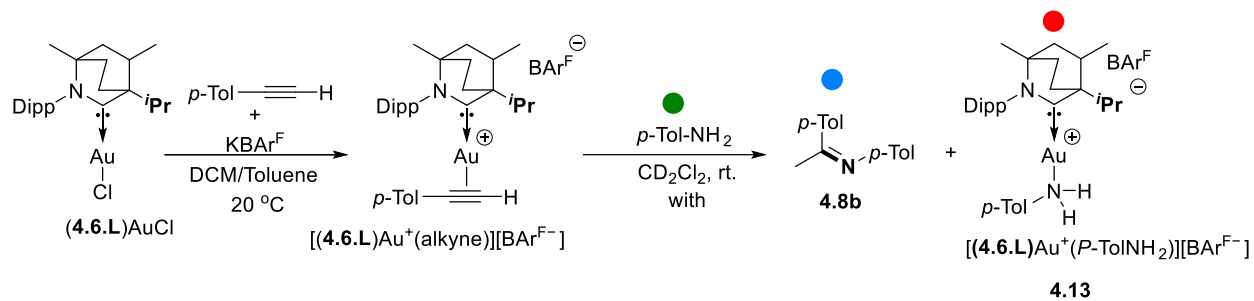
4.9.2. Examining the reactivity of the gold intermediates

Reaction of [(4.6.L)Au⁺(TolCCH)(BF₄⁻)] with Tol-NH₂

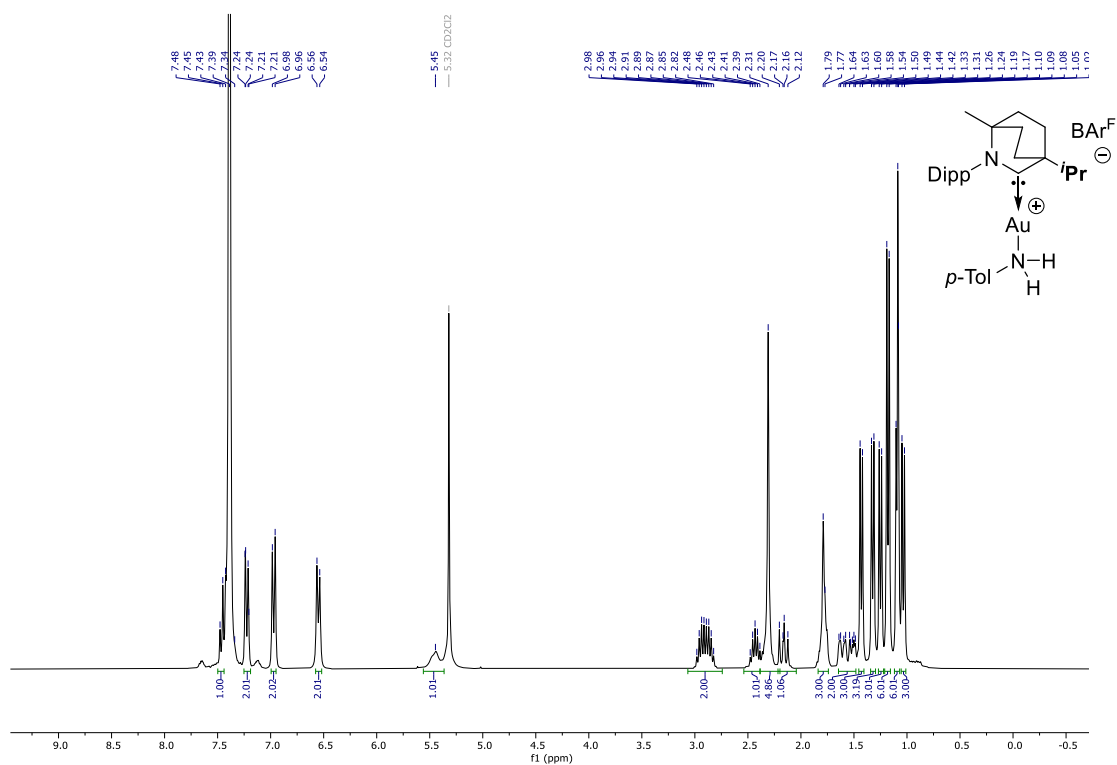


Under an argon atmosphere, a 5 mL Schlenk flask was charged with 1 mL of toluene/DCM mixture (50:50), AgBF₄ (0.017 g, 0.087 mmol, 1.0 eq.) and [(4.6.L)AuCl] (0.050 g, 0.087 mmol, 1.0 eq.). The reaction was stirred for 1 h at room temperature and then filtered through celite into a separate reaction flask to remove AgCl. The volatiles were removed under vacuum to afford an off-white residue. The residue was transferred to a J.Young NMR tube using 0.5 mL of CD₂Cl₂, followed by the addition of *p*-tolyl-acetylene (0.011 g, 0.087 mmol, 1.0 eq.). After confirming the formation of [(4.6.L)Au⁺(TolCCH)(BF₄⁻)] by NMR (δ 237.4 ppm characteristic signal by ¹³C{¹H} NMR), tolyl-amine was added to the NMR tube (0.093 g, 0.087 mmol, 1.0 eq.). The reaction mixture was monitored after 1 h at room temperature showing the formation of 4.8b and [(4.6.L)Au⁺(*p*-tol-NH₂)(BF₄⁻)]. Removal of volatiles under vacuum, trituration in pentane, filtration, and drying of precipitate afforded the latter as a white solid. This compound was successfully recrystallized by layering a DCM solution with pentane. ¹H NMR (300 MHz, CD₂Cl₂) δ 7.48 – 7.14 (m, 1H), 7.26 – 7.14 (d, 1H), 6.97 (d, *J* = 7.9 Hz, 1H), 6.55 (d, *J* = 7.8 Hz, 1H), 5.45 (s, 1H), 2.90 (dp, *J* = 20.5, 6.8 Hz, 2H), 2.43 (p, *J* = 6.8 Hz, 1H), 2.31 (s, 5H), 2.16 (dd, *J* = 13.7, 10.4 Hz, 1H), 1.78 (d, *J* = 5.1 Hz, 3H), 1.68 – 1.47 (m, 2H), 1.43 (d, *J* = 6.7 Hz, 3H), 1.32 (d, *J* = 6.8 Hz, 3H), 1.25 (d, *J* = 6.9 Hz, 3H), 1.18 (d, *J* = 6.7 Hz, 6H), 1.09 (t, *J* = 3.5 Hz, 6H), 1.04 (d, *J* = 7.1 Hz, 3H). ¹³C{¹H} NMR (126 MHz, CD₂Cl₂) δ 240.5, 144.8, 143.9, 142.1, 136.9, 135.7, 130.3, 130.1, 128.7, 125.6, 121.5, 65.8, 55.7, 44.3, 35.1, 32.8, 32.1, 29.4, 28.8, 25.1, 24.8, 24.0 (d, *J* = 3.0 Hz), 23.3, 21.2, 20.6, 19.6, 16.2. ¹⁹F{¹H} NMR (282 MHz, CD₂Cl₂) δ -153.7. ¹¹B{¹H} NMR (96 MHz, CD₂Cl₂) δ 0.82. NB: Reagents and solvents were stored over molecular sieves before use.

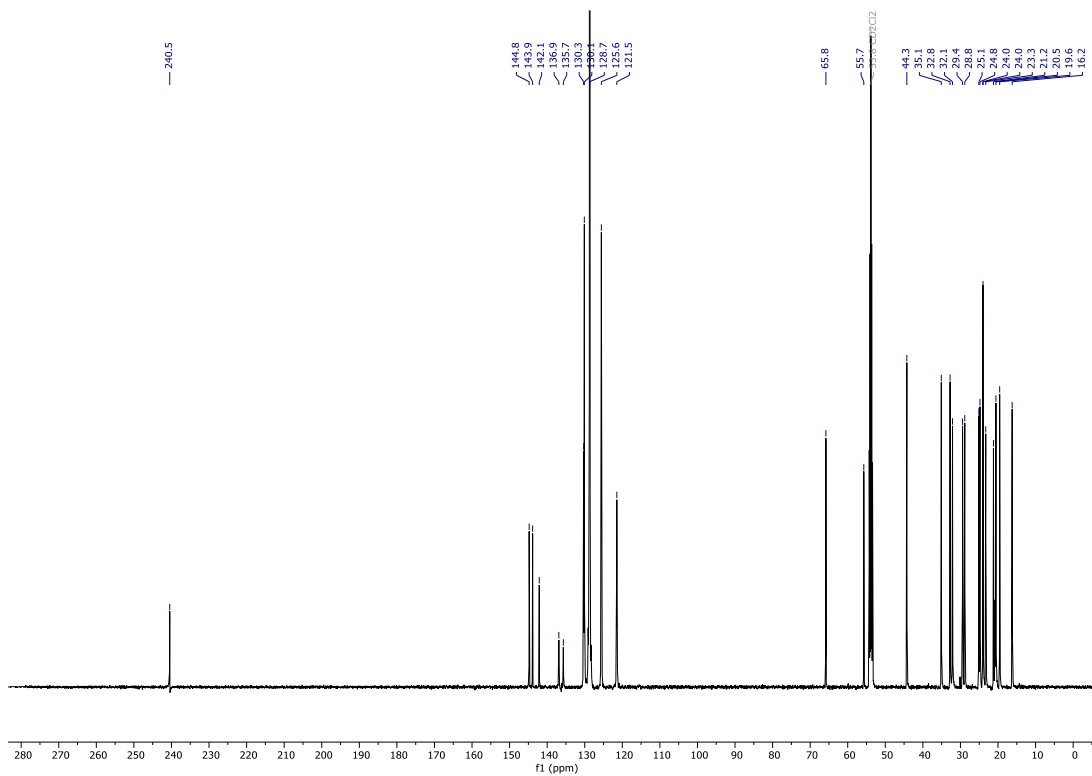
4.9.3. Evidence for the formation of $[(4.6.L)Au^+(p\text{-TolNH}_2)(\text{BAR}^F)]^-$ and 4.8b.



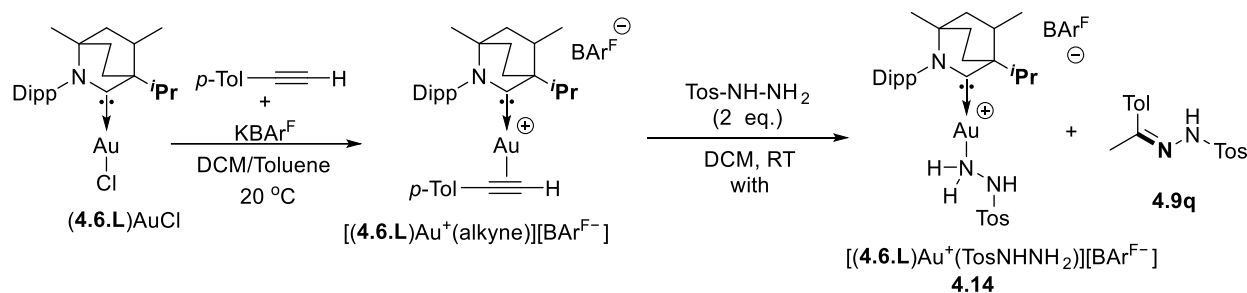
^1H spectrum



$^{13}\text{C}\{^1\text{H}\}$ spectrum



Reaction of the [(4.6.L)Au⁺(TolCCH)(BAR^F)⁻] with Tos-NHNH₂:

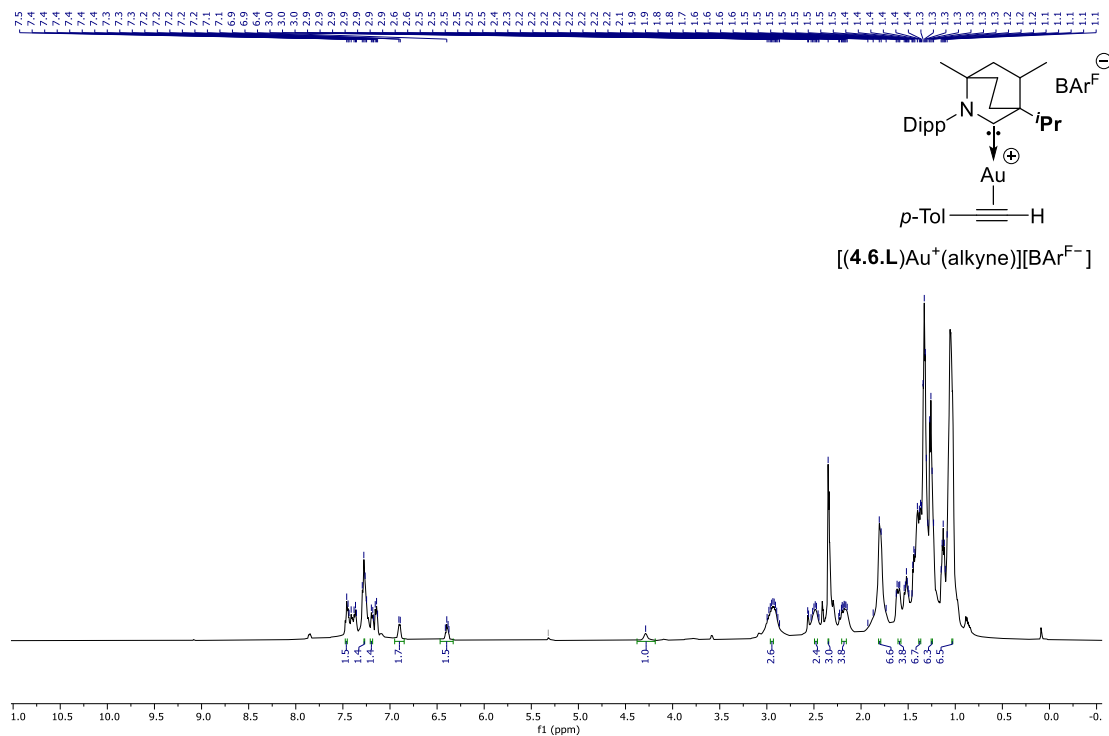


Under an argon atmosphere, a 5 mL Schlenk flask was charged with 1 mL of toluene/DCM mixture (50:50), KBAR^F (0.062 g, 0.087 mmol, 1.0 eq.) and [(4.6.L)AuCl] (0.050 g, 0.087 mmol, 1.0 eq.). The reaction was stirred for 1 h at room temperature and then filtered through celite into a separate reaction flask to remove KCl. The volatiles were removed under vacuum to afford an off-white residue. The residue was transferred to a J.Young NMR tube using 0.5 mL of CD₂Cl₂, followed by the addition of *p*-tolyl-acetylene (0.010 g, 0.087 mmol, 1.0 eq.). After confirming the formation of [(4.6.L)Au⁺(TolCCH)(BAR^F)⁻] by NMR (δ 237.4 ppm characteristic signal by ¹³C{¹H} NMR), Tosyl-hydrazine was added to the NMR tube (0.016 g, 0.087 mmol, 1.0 eq.). The reaction mixture was monitored after 1h at room temperature showing the formation of 4.9q and [(4.6.L)Au⁺(TosNH-NH₂)(BAR^F)⁻]. Evaporation of the volatiles and addition of C₆H₆ (0.5 mL) resulted in the slow crystallization of 4.9q overnight in the NMR tube which was confirmed by X-ray crystallography. Subsequent transfer of the mother liquor to a 5 mL schlenk flask, removal of volatiles under vacuum, trituration in pentane and filtration, afforded [(4.6.L)Au⁺(TosNH-NH₂)(BAR^F)⁻] as a white solid. [(4.6.L)Au⁺(TolCCH)(BAR^F)⁻]: ¹H NMR (300 MHz, CD₂Cl₂) δ 7.48 – 7.34 (m, 1H), 7.27 (q, *J* = 7.9 Hz, 1H), 7.21 – 7.10 (m, 1H), 6.90 (d, *J* = 7.3 Hz, 2H), 6.39 (q, *J* = 6.2, 4.8 Hz, 2H), 4.29 (s, 1H), 3.00 – 2.87 (m, 2H), 2.60 – 2.44 (m, 2H), 2.35 (s, 3H), 2.25 – 2.04 (m, 3H), 1.80 (d, *J* = 10.0 Hz, 6H), 1.64 – 1.46 (m, 3H), 1.45 – 1.21 (m, 6H), 1.13 (p, *J* = 5.5 Hz, 6H), 1.09 (m, 6H). ¹³C{¹H} NMR (126 MHz, CD₂Cl₂) δ 237.4, 149.4, 147.5, 144.8, 143.8, 141.6, 139.6, 137.6, 135.7, 130.5, 130.4, 129.3, 125.5, 124.7, 76.7, 66.4, 55.7, 44.2, 35.2, 34.5, 32.6, 29.5, 28.9, 25.5, 25.2, 23.8, 23.1, 22.7, 21.1, 20.7, 19.4, 16.3, 14.2. ¹⁹F{¹H} NMR (282 MHz, CD₂Cl₂) δ -133.85 (d, *J* = 14.2 Hz), -164.44 (t, *J* = 20.3

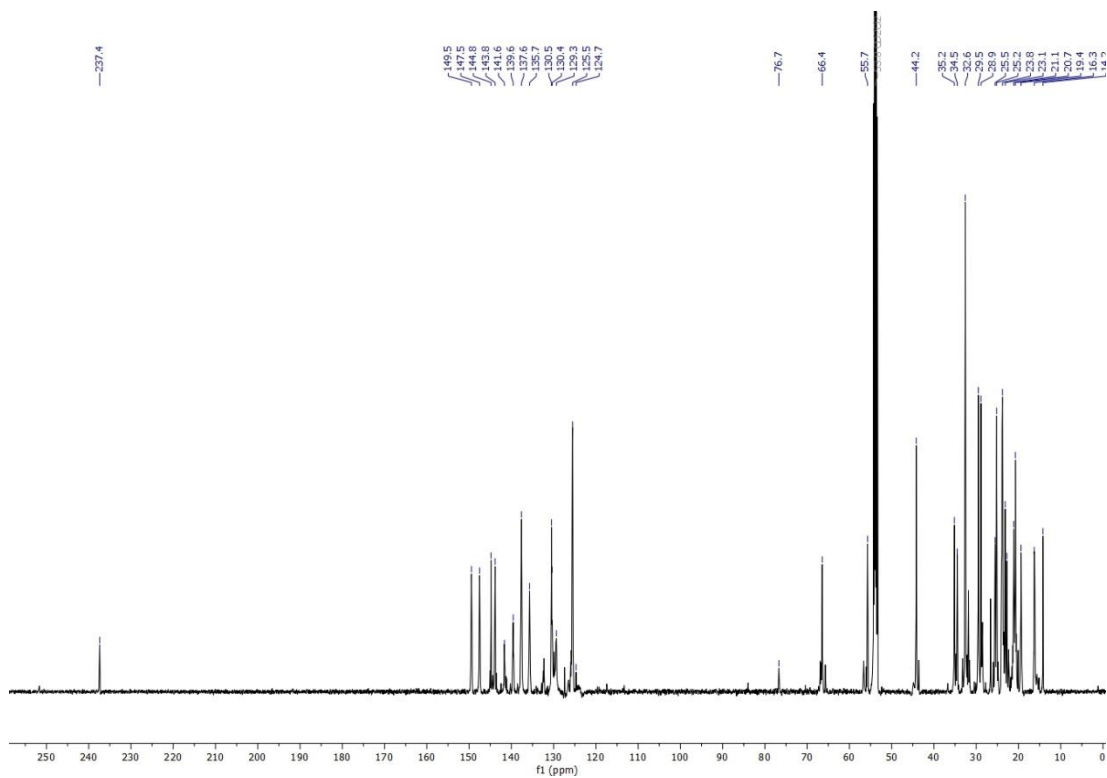
Hz), -168.28 (t, $J = 19.9$ Hz). $^{11}\text{B}\{^1\text{H}\}$ NMR (96 MHz, CD_2Cl_2) δ -16.62. [(**4.6.L**) $\text{Au}^+(\text{TosNH-NH}_2)(\text{BAr}^{\text{F}})^-$]: ^1H NMR (300 MHz, CD_2Cl_2) δ 7.69 (d, $J = 7.9$ Hz, 2H), 7.43 (t, $J = 7.8$ Hz, 1H), 7.33 (d, $J = 8.0$ Hz, 2H), 7.25 (t, $J = 6.4$ Hz, 2H), 5.92 (s, 1H), 3.83 (s, 2H), 2.84 (dp, $J = 19.6, 6.8$ Hz, 2H), 2.42 (s, 3H), 2.31 (m, 1H), 2.17 (dd, $J = 13.7, 10.3$ Hz, 1H), 1.80 (s, 3H), 1.55 (ddt, $J = 22.9, 10.8, 5.8$ Hz, 3H), 1.38 – 1.33 (m, 4H), 1.30 (m, 3H), 1.29 – 1.22 (m, 8H), 1.05 (m, 6H), 1.00 (m, 3H). $^{13}\text{C}\{^1\text{H}\}$ NMR (126 MHz, CD_2Cl_2) δ 149.4 (broad), 147.5, 144.9, 143.9, 141.7, 139.6, 137.6, 135.7, 130.5, 130.4, 128.4, 125.5, 66.3, 55.7, 44.2, 35.1, 32.6, 32.5, 29.5, 28.9, 25.55, 25.2, 24.0, 23.7, 23.1, 21.7, 21.1, 20.7, 19.4, 16.2. $^{19}\text{F}\{^1\text{H}\}$ NMR (282 MHz, CD_2Cl_2) δ -133.14 – -135.72 (m), -164.37 (t, $J = 20.3$ Hz), -168.23 (t, $J = 19.4$ Hz). $^{11}\text{B}\{^1\text{H}\}$ NMR (96 MHz, CD_2Cl_2) δ -16.62. NB: Reagents and solvents were stored over molecular sieves before use.

Complex [(4.6.L)Au⁺(TolCCH)(BAr^F-)]

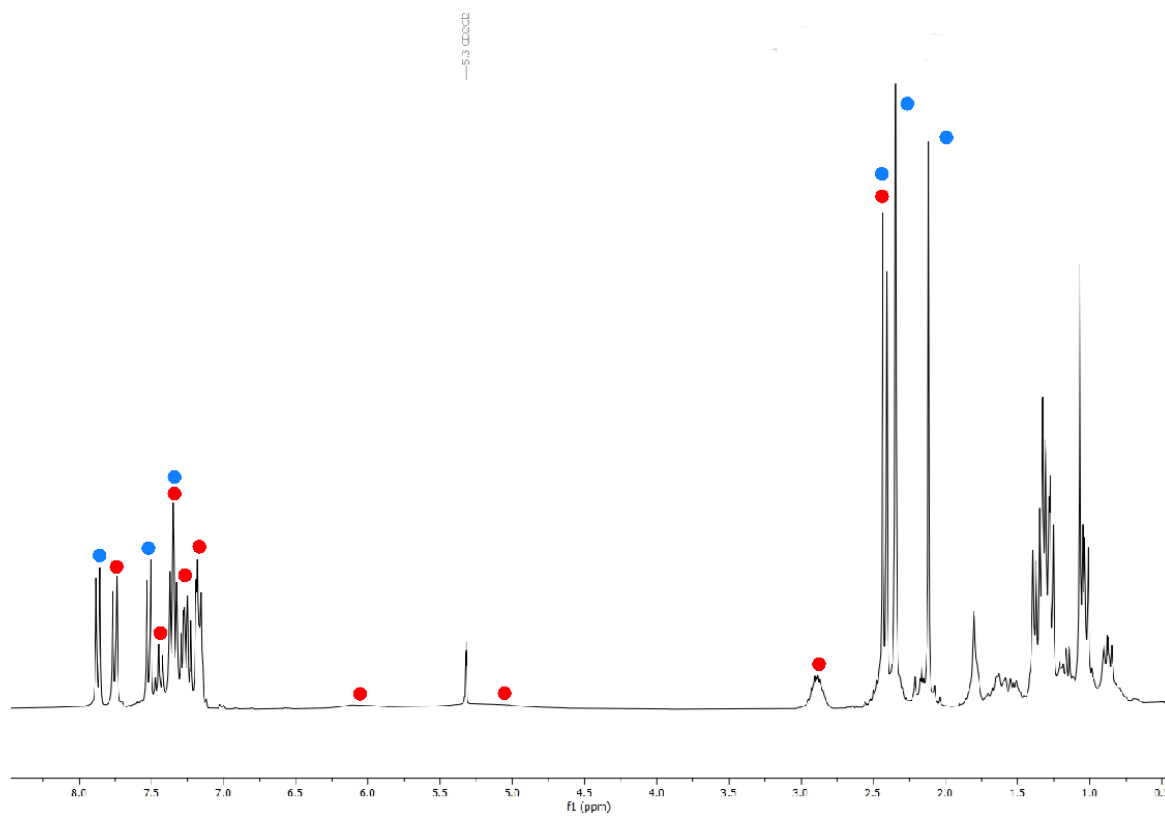
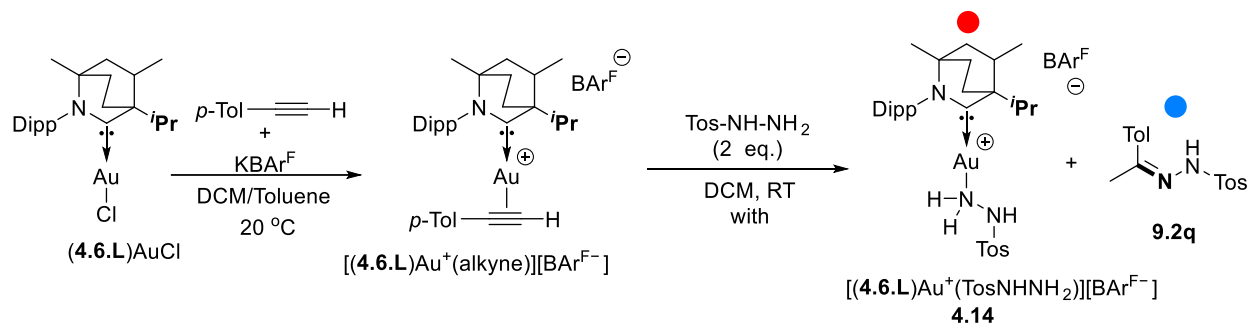
¹H spectrum



¹³C{¹H} spectrum

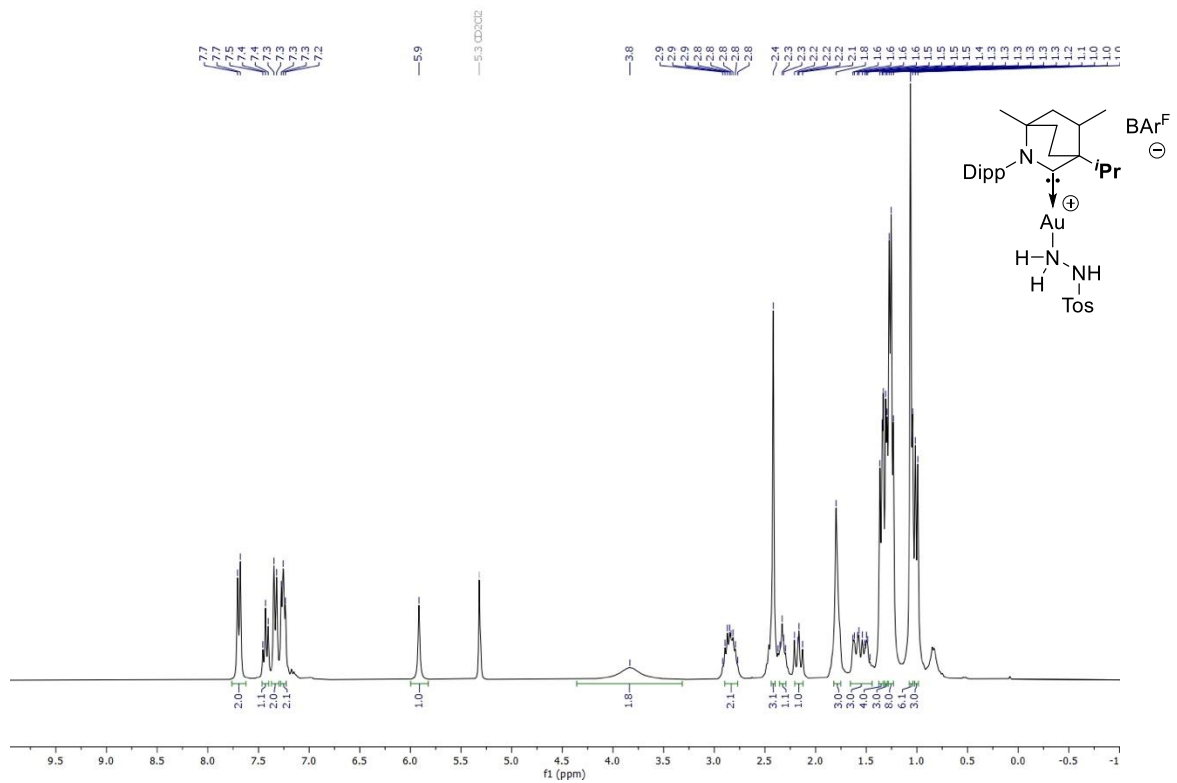


Evidence for the formation of $[(4.6.L)Au^+(p\text{-TosNH-NH}_2)(BAR^F)]$ and 4.9q.

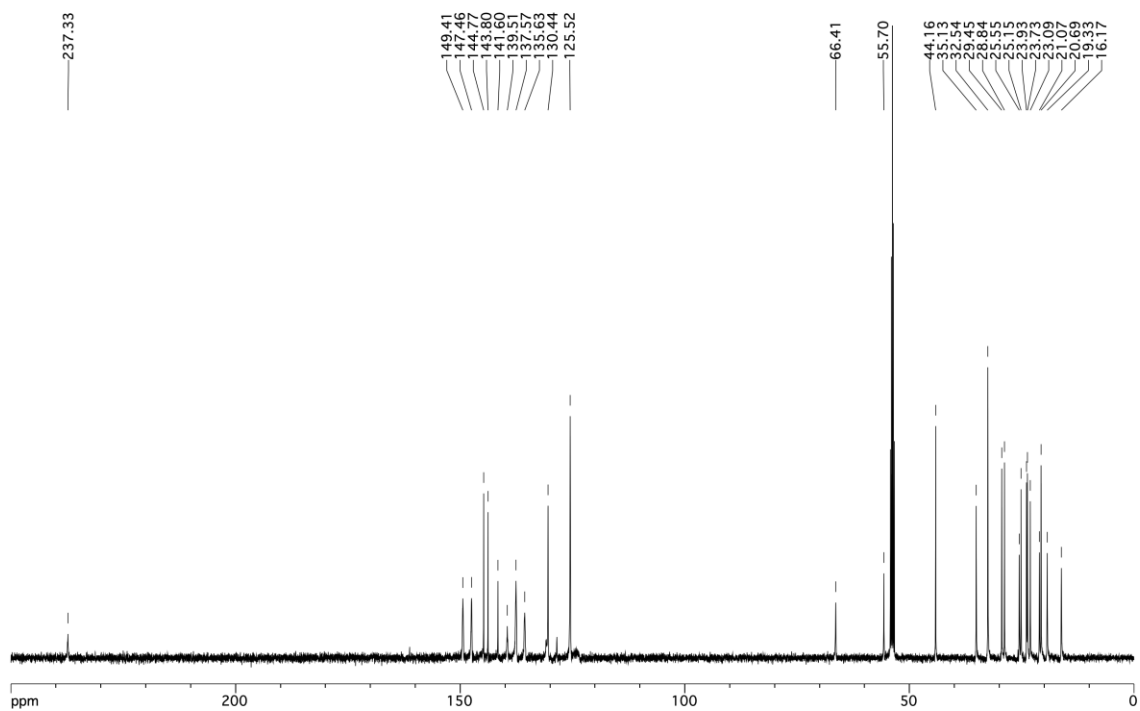


Complex [(4.6.L)Au⁺(*p*-TosNH-NH₂)(BAR^F-)]

¹H spectrum

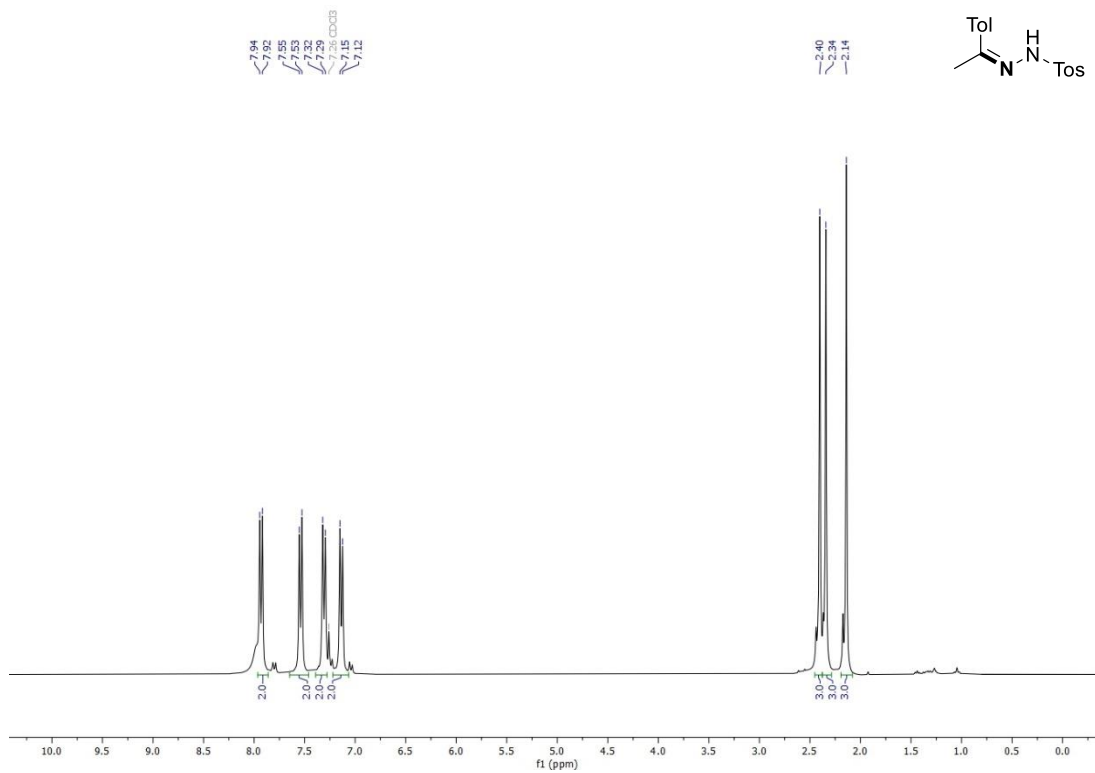


¹³C{¹H} spectrum

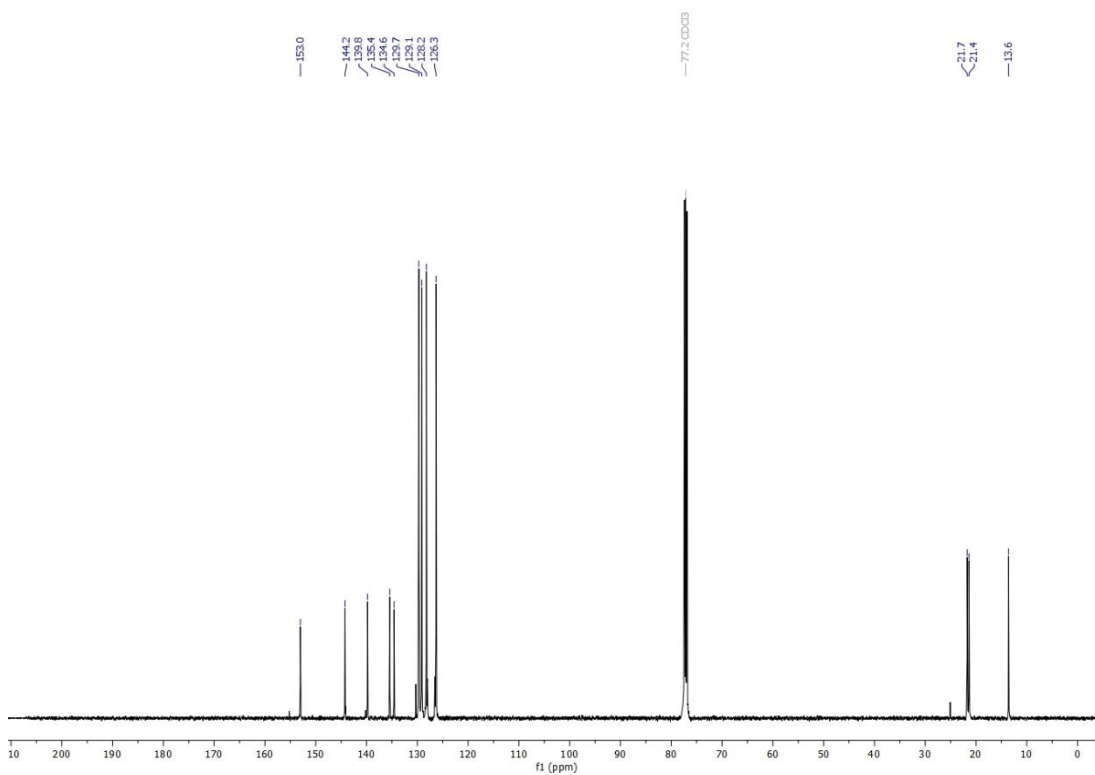


Compound 4.9q

^1H spectrum

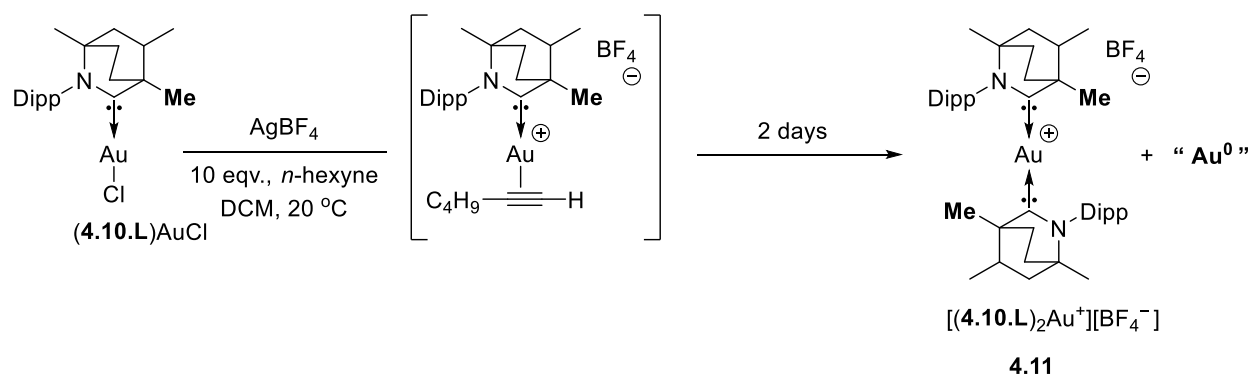


$^{13}\text{C}\{^1\text{H}\}$ spectrum



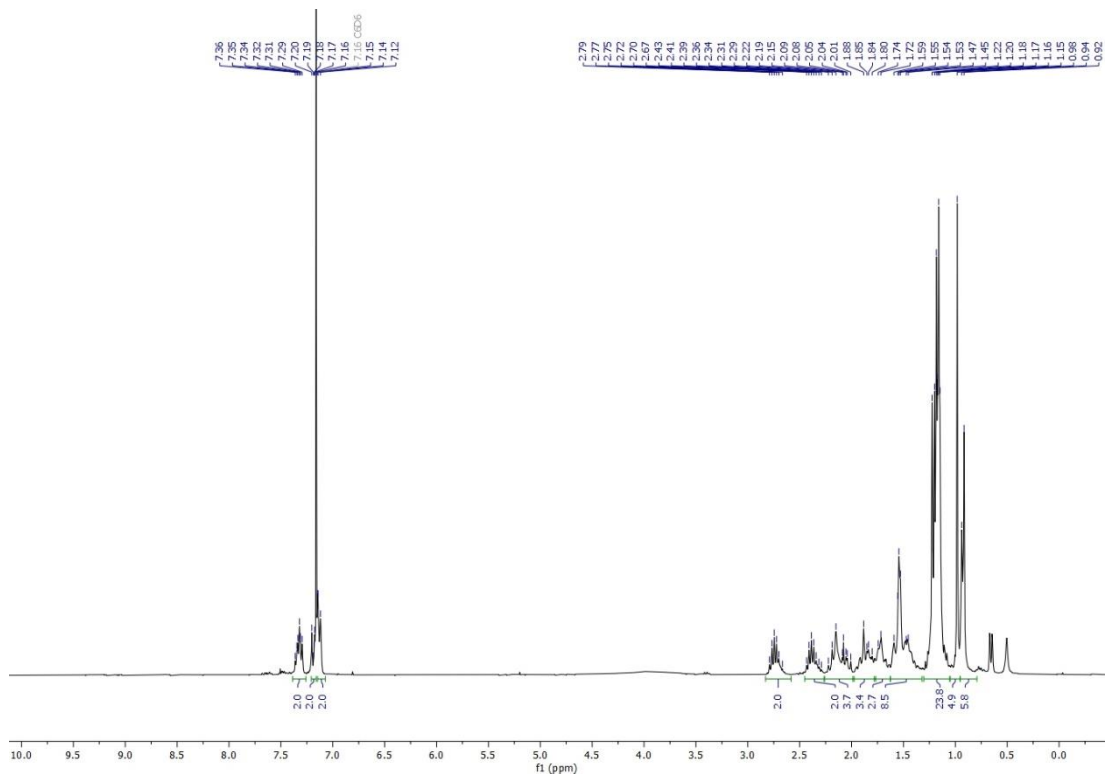
4.9.4. Deactivated gold species during catalytic cycle

Complex [(4.10.L)₂Au⁺(BF₄)⁻]

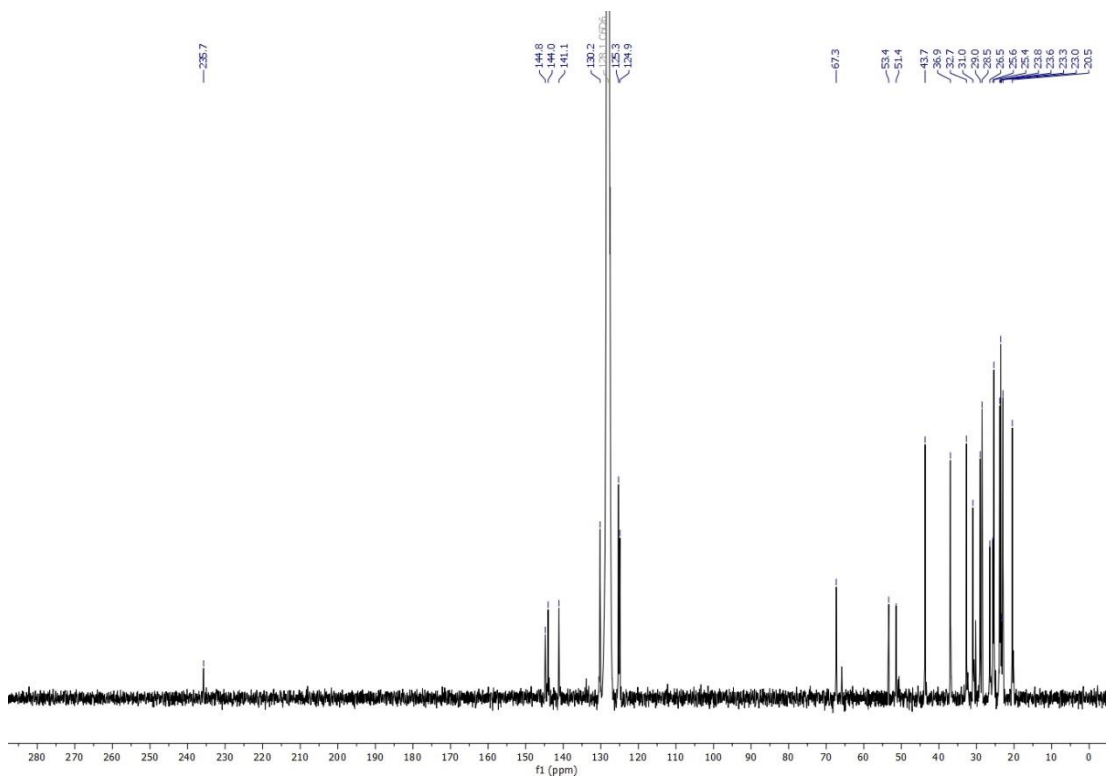


Following the same general procedure described for [(4.6.L)Au⁺(PhCCPh)(BF₄)⁻], but instead using [(4.10.L)Au(Cl)] (0.150 g, 0.261 mmol, 1.0 eq.) and *n*-hexyne (0.214 g, 2.610 mmol, 10.0 eq.), we monitored the reaction by NMR. The slow formation of [(4.10.L)₂Au⁺(BF₄)⁻] was observed upon stirring the reaction mixture at room temperature over 2 days. The title compound was isolated as a white powder by evaporation of the volatiles in vacuo, and trituration with pentane. This compound was successfully recrystallized by layering a DCM solution with pentane. ¹H NMR (300 MHz, C₆D₆) δ 7.33 (td, *J* = 7.8, 4.9 Hz, 2H), 7.20-7.16 (m, 2H), 7.15-7.12 (m, 2H), 2.75 (p, *J* = 6.9 Hz, 2H), 2.36 (dp, *J* = 15.0, 6.9 Hz, 2H), 2.23 – 1.99 (m, 4H), 1.95 – 1.67 (m, 4H), 1.61 – 1.40 (m, 9H), 1.18 (dt, *J* = 10.4, 5.2 Hz, 24H), 0.98 (s, 6H), 0.93 (d, *J* = 6.7 Hz, 6H). ¹³C{¹H} NMR (126 MHz, C₆D₆) δ 235.7, 144.8, 144.0, 141.1, 130.2, 125.3, 124.9, 67.3, 53.4, 51.4, 50.9, 43.7, 36.9, 36.8, 32.7, 31.0, 30.6, 29.0, 28.5, 26.5, 25.6, 25.4, 23.8, 23.6, 23.0, 20.5. ¹⁹F{¹H} NMR (282 MHz, CD₂Cl₂) δ -151.0. ¹¹B{¹H} NMR (96 MHz, CD₂Cl₂) δ 0.25.

^1H spectrum



$^{13}\text{C}\{^1\text{H}\}$ spectrum

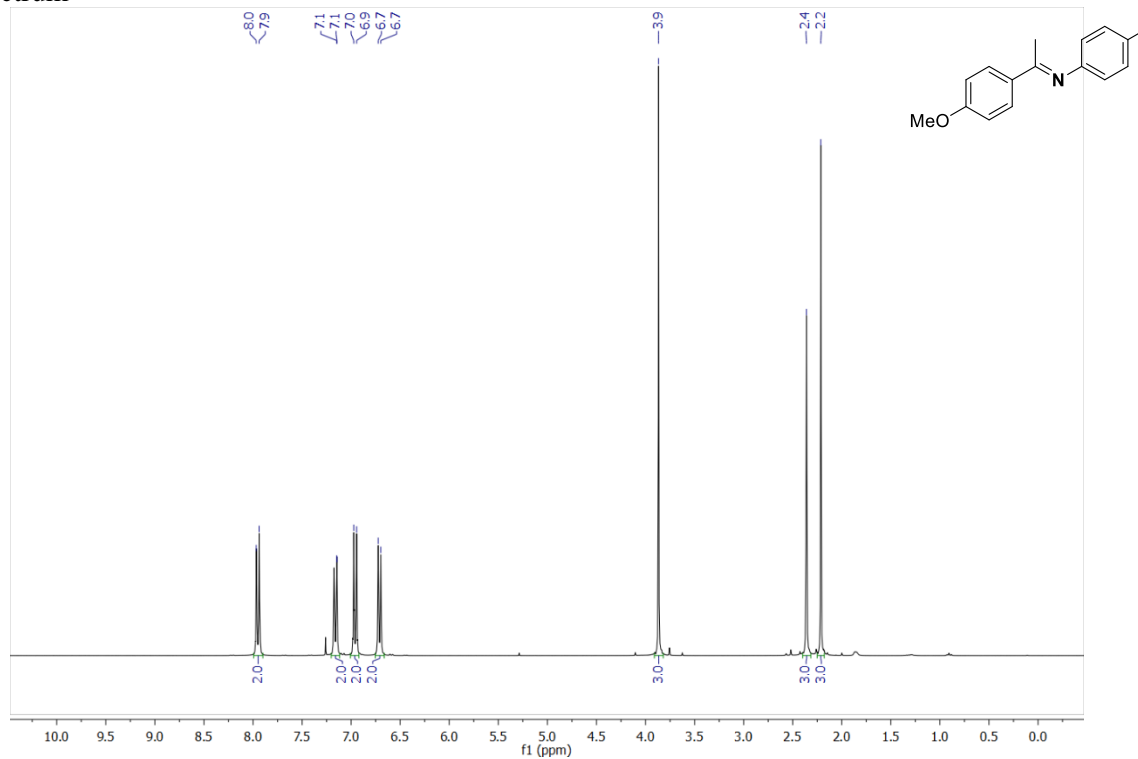


4.10. General method for the hydroamination

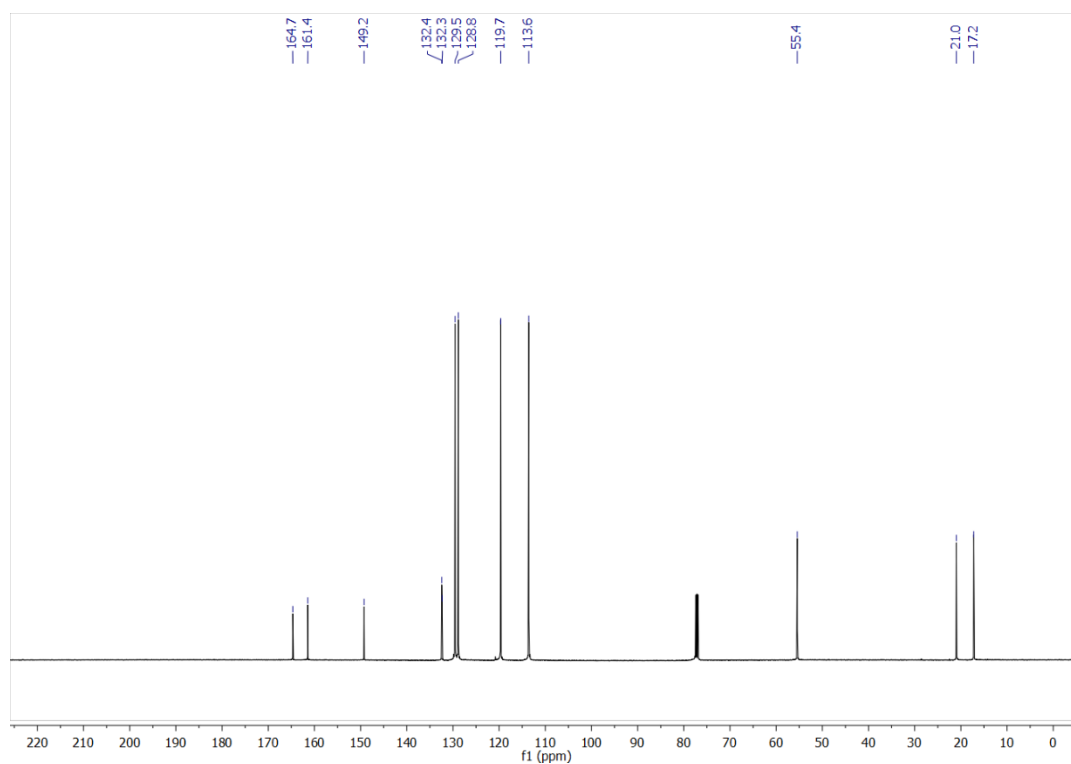
In air, a scintillation vial (3 mL) was charged with (**4.6.L**)AuCl (2.5 mol%, 0.029 mmol), $\text{KB}(\text{C}_6\text{F}_5)_4$ (2.5 mol%, 0.029 mmol), C_6H_6 (1 mL) and the alkyne (1.163 mmol, 1.0 eq.). After stirring for two minutes, the amine (1.163 mmol, 1.0 eq.) was added as a solution in C_6H_6 (0.5 mL). The mixture was then set stirring according to reaction time and temperature listed in Figure 4.5. The products were purified by column chromatography using Florisil eluting with a gradient mixture of DCM/hexane.

Compound **4.8a** was isolated in 95% yield (0.264 g) and agrees with a previous literature report.¹⁷¹ ^1H NMR (300 MHz, CDCl_3) δ 7.95 (d, $J = 9.0$ Hz, 2H), 7.18 – 7.13 (m, 2H), 6.96 (d, $J = 8.9$ Hz, 2H), 6.71 (d, $J = 8.2$ Hz, 2H), 3.87 (s, 3H), 2.36 (s, 3H), 2.21 (s, 3H). $^{13}\text{C}\{^1\text{H}\}$ NMR (126 MHz, CDCl_3) δ 164.7, 161.4, 149.2, 132.4, 132.3, 129.5, 128.8, 119.65, 113.6, 55.4, 20.97, 17.2 ppm.

^1H spectrum

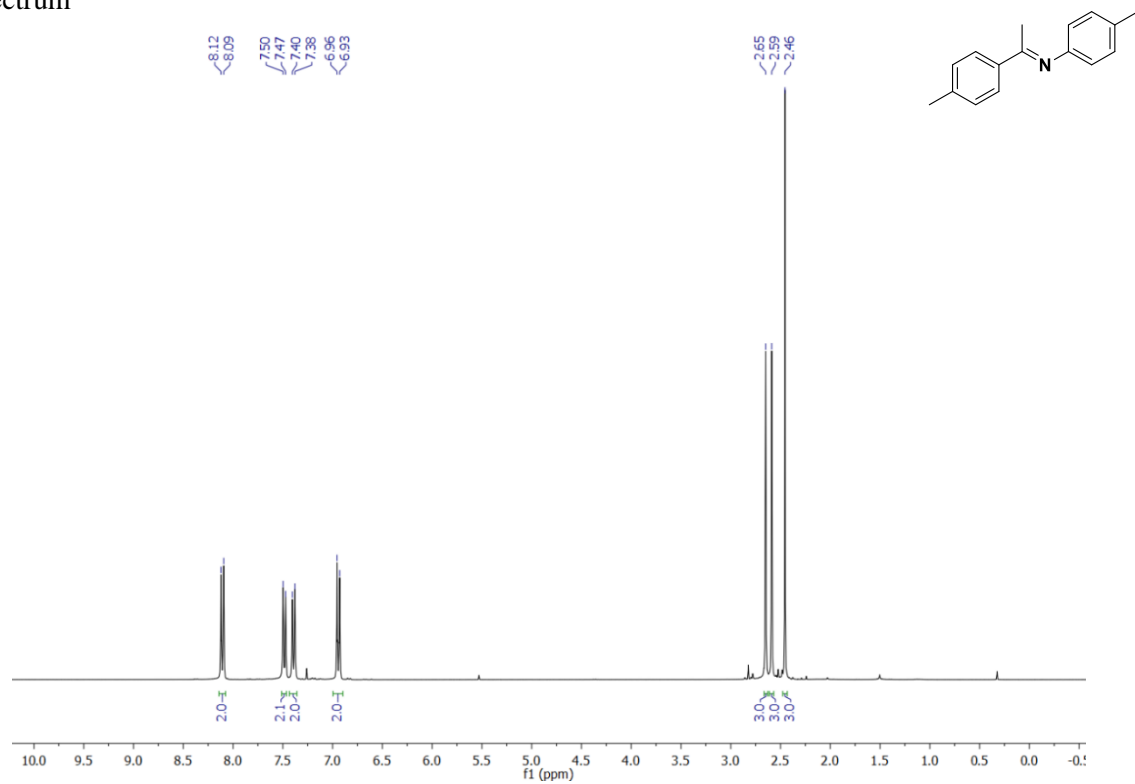


$^{13}\text{C}\{^1\text{H}\}$ spectrum

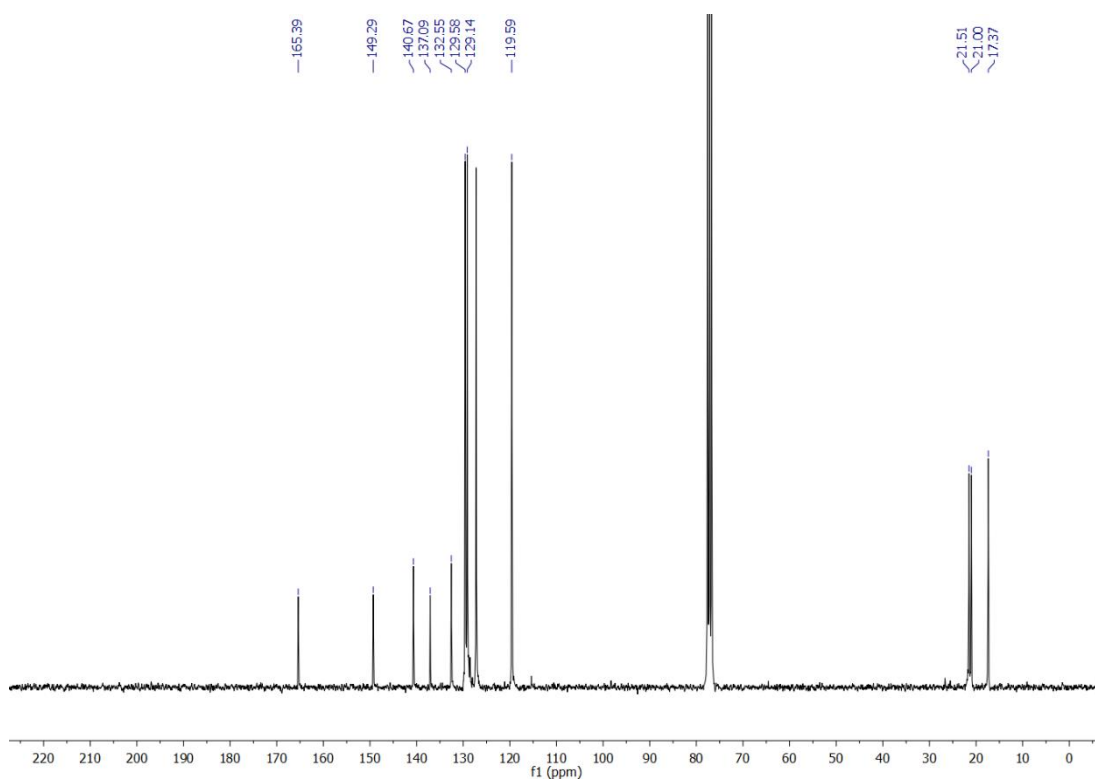


Compound **4.8b** was isolated in 90% yield (0.234 g) and agrees with a previous literature report.¹⁷¹ ^1H NMR (300 MHz, CDCl_3) δ 8.11 (d, $J = 8.2$ Hz, 2H), 7.48 (d, $J = 7.7$ Hz, 2H), 7.39 (d, $J = 7.7$ Hz, 2H), 6.94 (d, $J = 8.2$ Hz, 2H), 2.65 (s, 3H), 2.59 (s, 3H), 2.46 (s, 3H). $^{13}\text{C}\{^1\text{H}\}$ NMR (75 MHz, CDCl_3) δ 165.4, 149.3, 140.7, 137.1, 132.6, 129.6, 129.1, 119.6, 21.5, 21.0, 17.4 ppm.

^1H spectrum



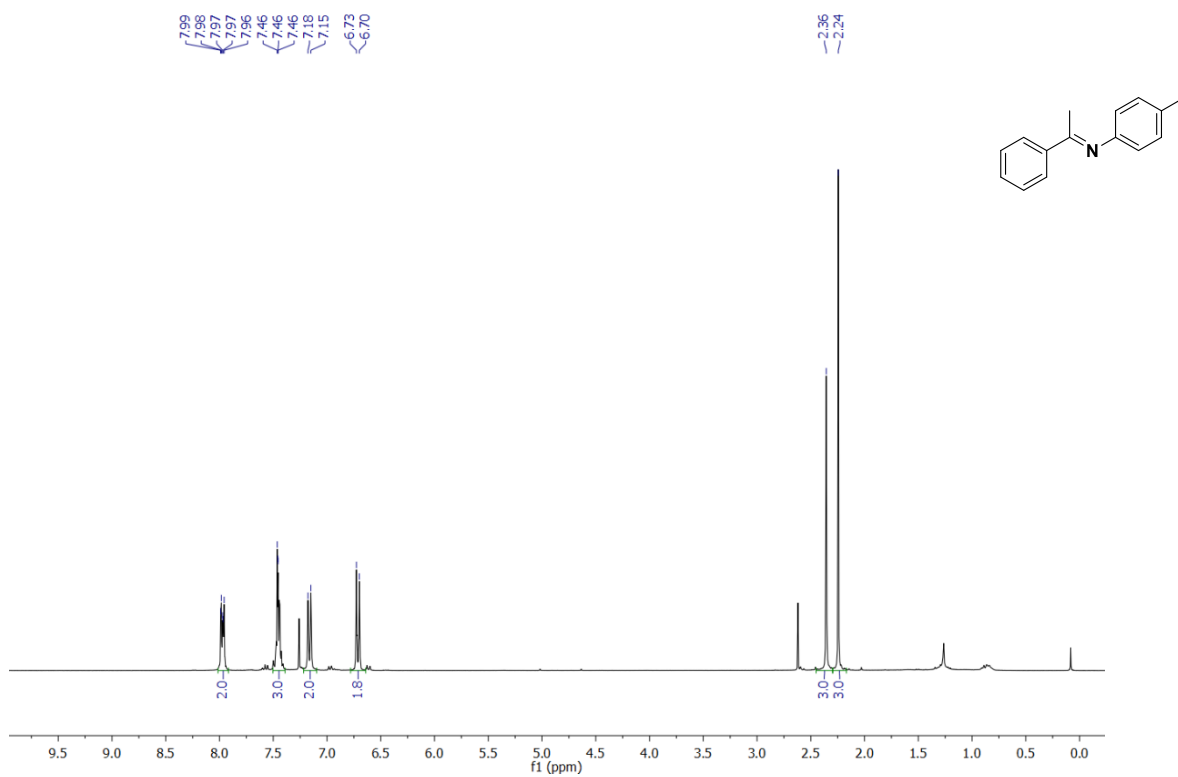
$^{13}\text{C}\{^1\text{H}\}$ spectrum



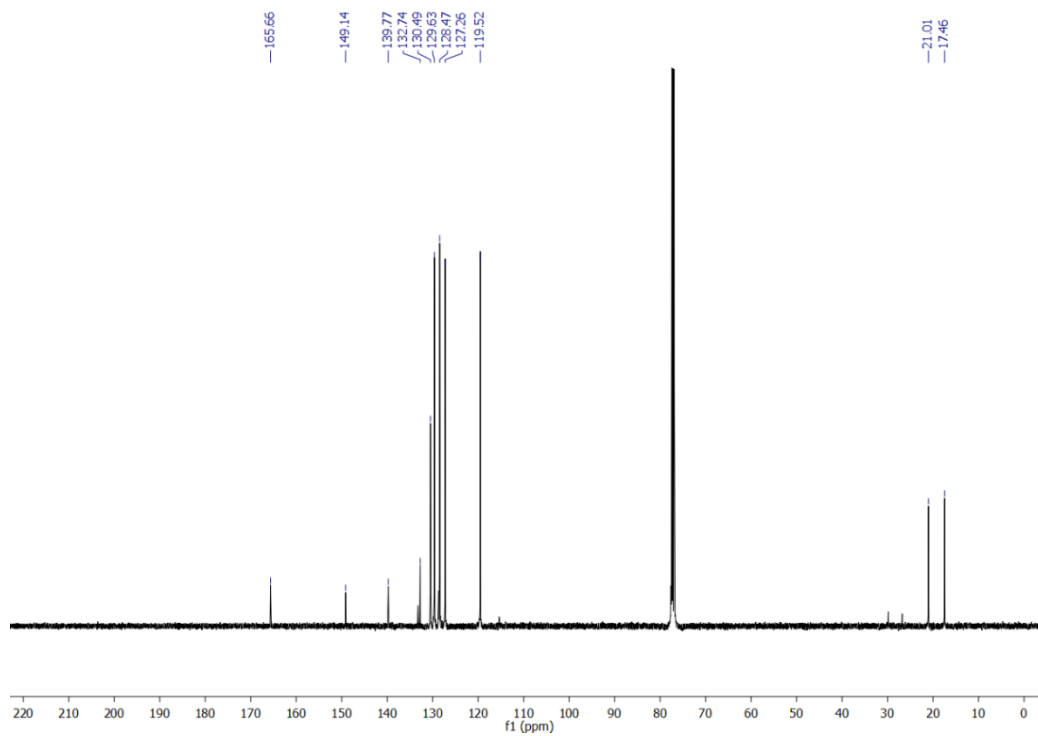
Compound **4.8c** was isolated in 95% yield (0.231 g) and agrees with a previous literature report.¹⁷¹

¹H NMR (300 MHz, CDCl₃) δ 8.00 – 7.95 (m, 2H), 7.47 – 7.43 (m, 3H), 7.16 (d, *J* = 8.0 Hz, 2H), 6.71 (d, *J* = 8.2 Hz, 2H), 2.36 (s, 3H), 2.24 (s, 3H). ¹³C{¹H} NMR (126 MHz, CDCl₃) δ 165.7, 149.1, 139.8, 132.7, 130.5, 129.6, 128.5, 127.3, 119.5, 21.0, 17.5.

¹H spectrum



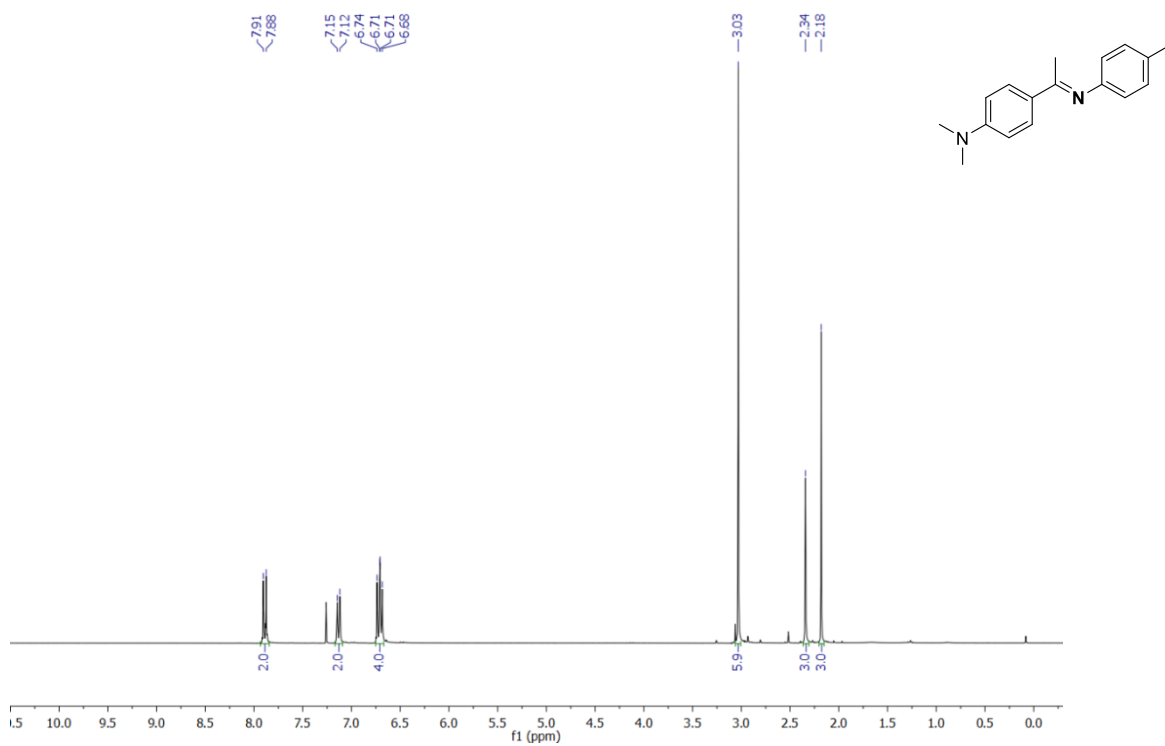
$^{13}\text{C}\{^1\text{H}\}$ spectrum



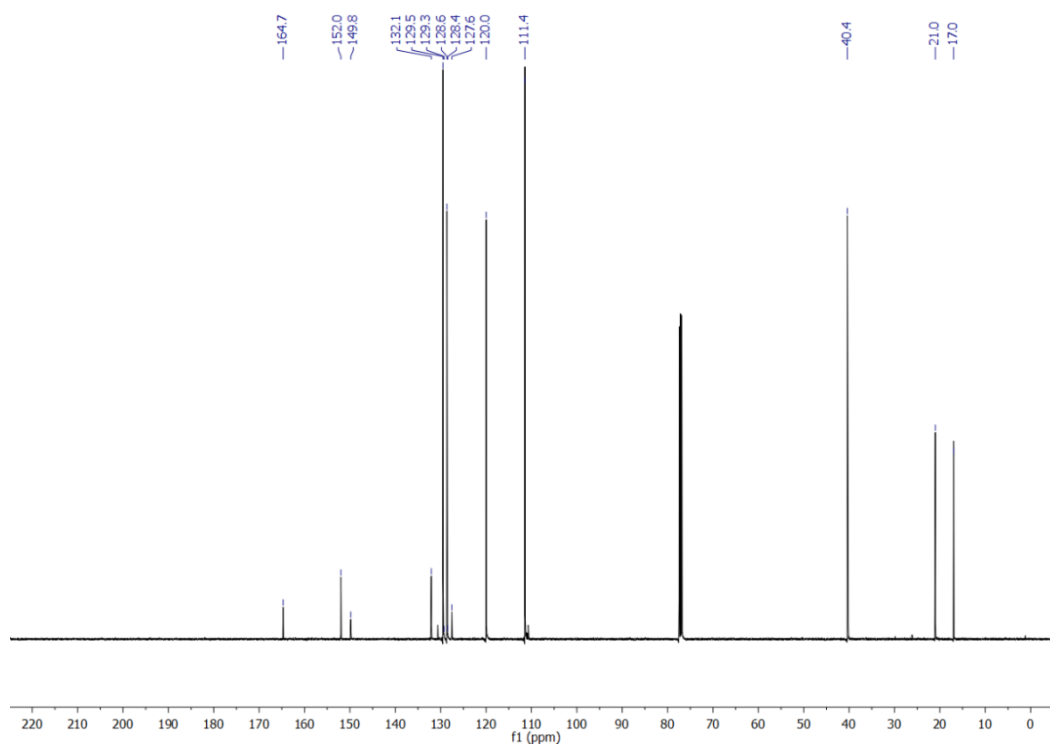
Compound **4.8d** was isolated in 97% yield (0.284 g) and agrees with a previous literature report.¹⁷²

¹H NMR (300 MHz, CDCl₃) δ 7.89 (d, *J* = 9.0 Hz, 2H), 7.13 (d, *J* = 7.9 Hz, 2H), 6.71 (dd, *J* = 8.7, 7.4 Hz, 4H), 3.03 (s, 6H), 2.34 (s, 3H), 2.18 (s, 3H). ¹³C{¹H} NMR (126 MHz, CDCl₃) δ 164.7, 152.0, 149.8, 132.1, 129.5, 128.6, 127.5, 120.0, 111.4, 40.4, 21.0, 17.0 ppm.

¹H spectrum

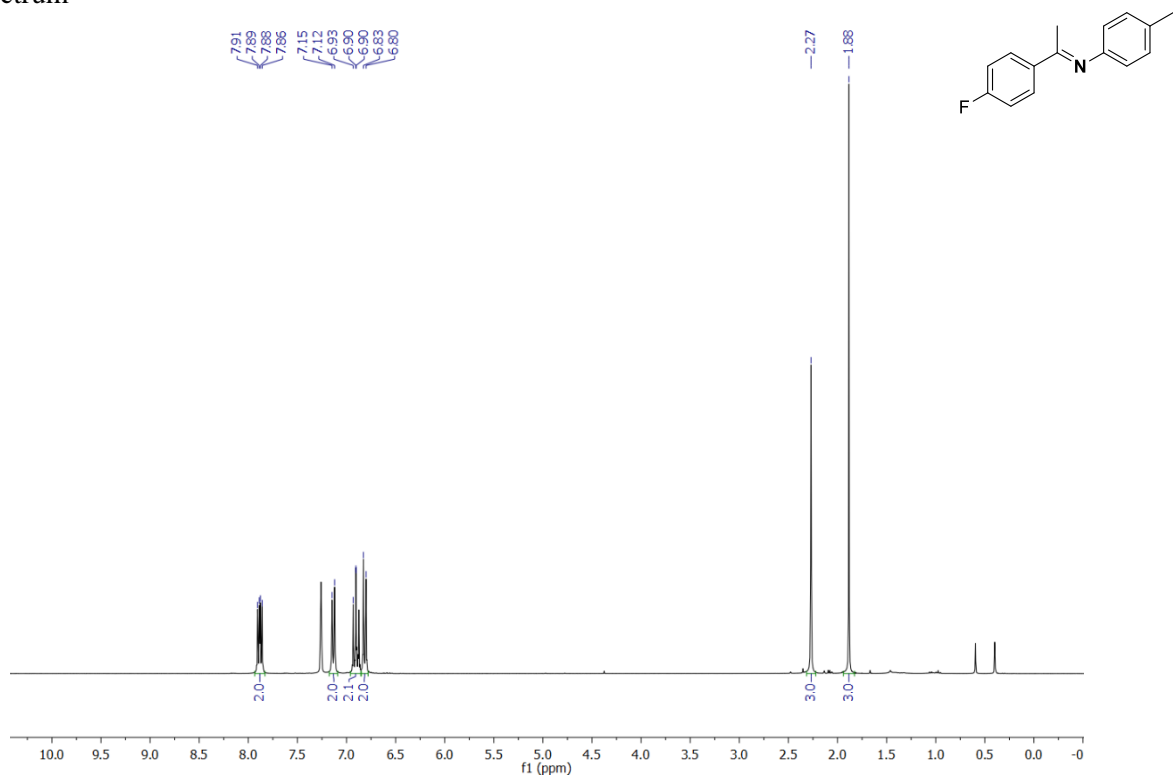


$^{13}\text{C}\{^1\text{H}\}$ spectrum

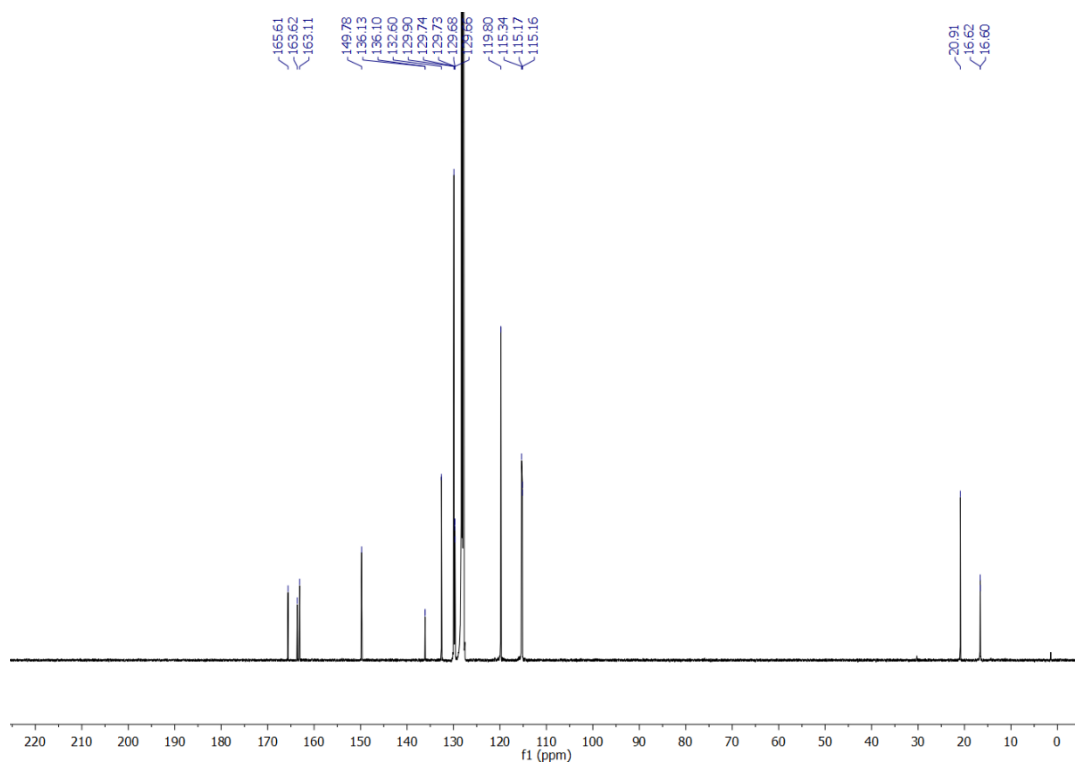


Compound **4.8e** was isolated in 90% yield (0.238 g) and agrees with a previous literature report.¹⁷³ ^1H NMR (300 MHz, C_6D_6) δ 7.88 (dd, $J = 9.0, 5.5$ Hz, 2H), 7.13 (d, $J = 7.9$ Hz, 2H), 6.94 – 6.87 (m, 2H), 6.81 (d, $J = 8.2$ Hz, 2H), 2.27 (s, 3H), 1.88 (s, 3H). $^{13}\text{C}\{^1\text{H}\}$ NMR (126 MHz, C_6D_6) δ 165.6, 163.6, 163.1, 149.8, 136.1 (d, $J = 3.1$ Hz), 132.6, 129.9, 129.7 (dd, $J = 8.3, 2.1$ Hz), 119.8, 115.5 – 115.1 (m), 20.9, 16.6 (d, $J = 2.6$ Hz). ^{19}F NMR (282 MHz, C_6D_6) δ -111.54 ppm.

^1H spectrum



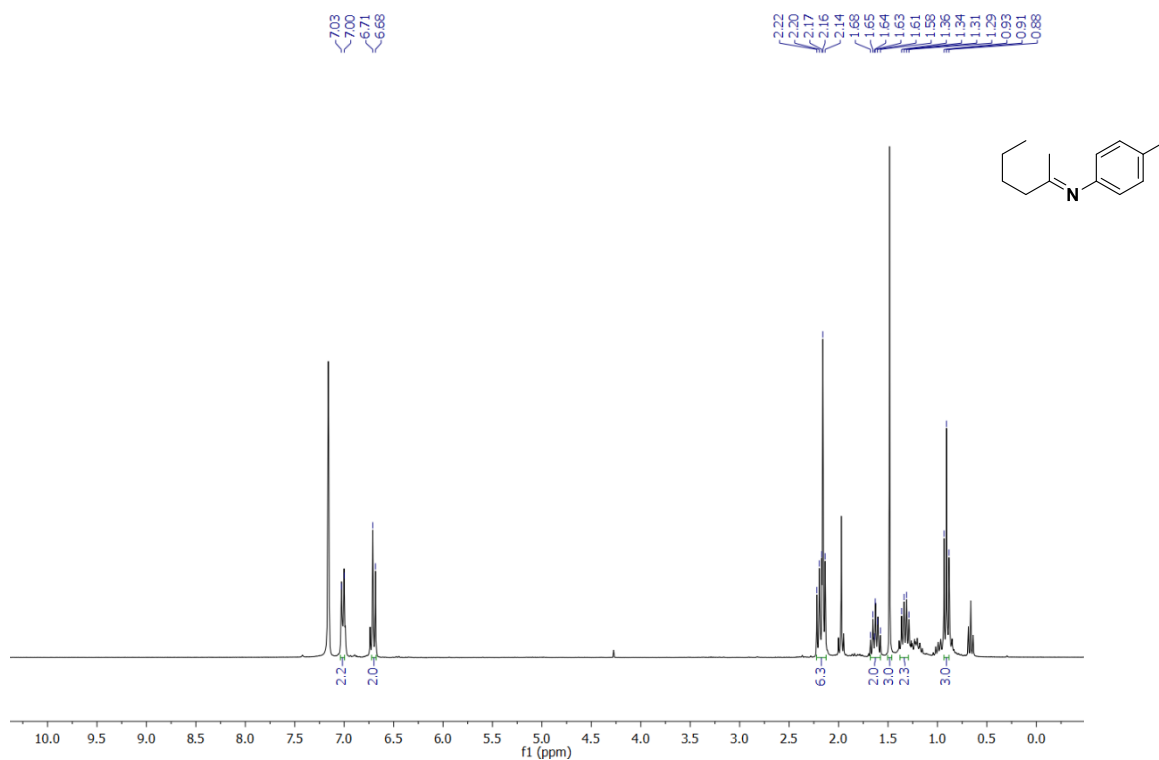
$^{13}\text{C}\{^1\text{H}\}$ spectrum



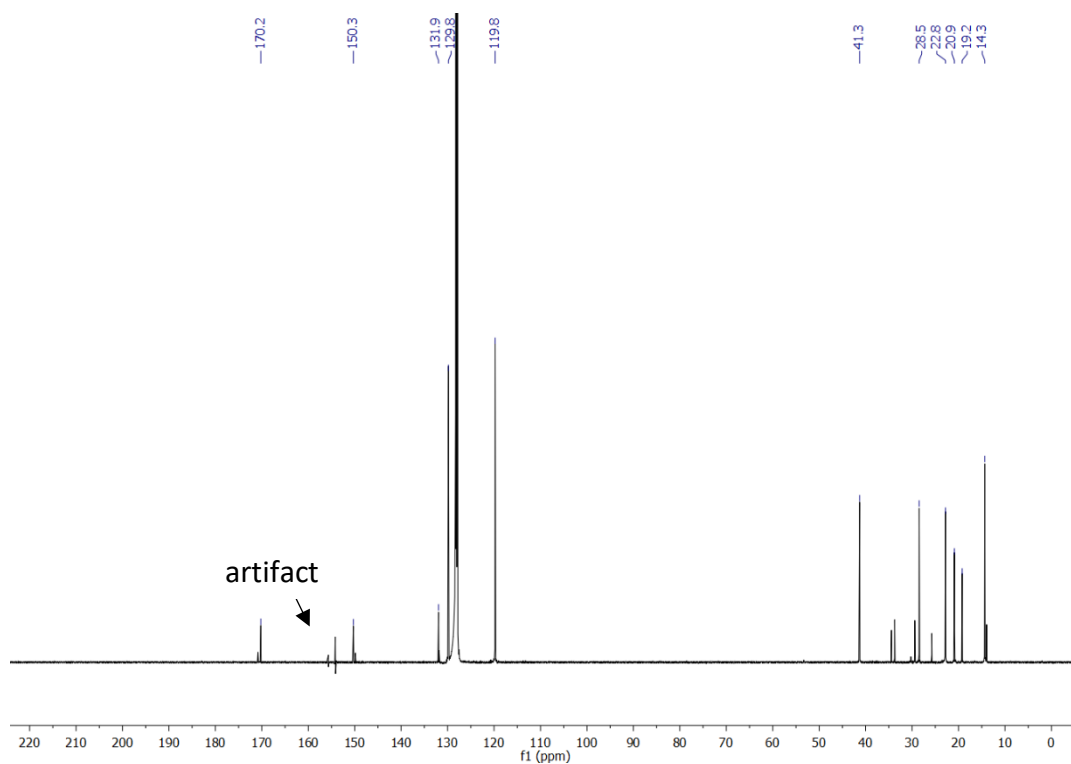
Compound **4.8f** was isolated in 92% yield (0.202 g) and agrees with a previous literature report.¹⁷⁴

¹H NMR (300 MHz, C₆D₆) 7.01 (d, *J* = 8.0 Hz, 2H), 6.70 (d, *J* = 8.2 Hz, 2H), 2.16 (s, 3H), 2.25 – 2.11 (m, 3H), 1.71 – 1.54 (m, 2H), 1.48 (s, 3H), 1.41 – 1.27 (m, 3H), 0.91 (t, *J* = 7.3 Hz, 3H). ¹³C{¹H} NMR (126 MHz, C₆D₆) δ 170.2, 150.3, 131.95, 129.8, 119.8, 41.3, 28.5, 22.8, 20.9, 19.2, 14.3 ppm.

¹H spectrum



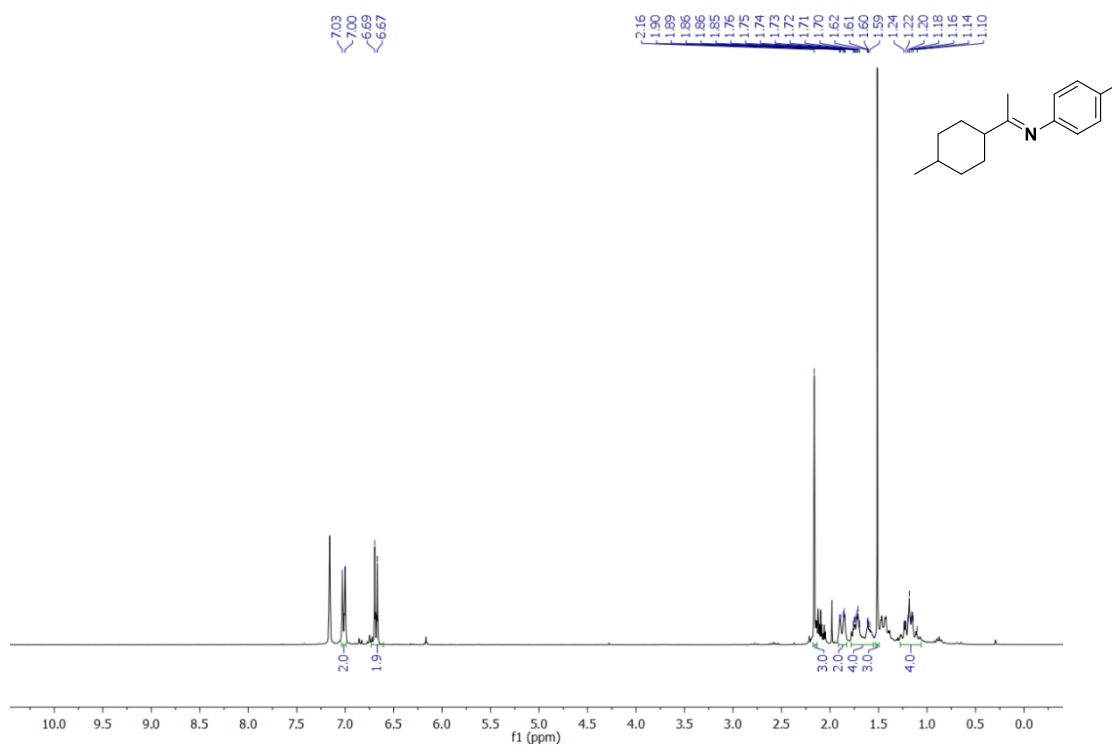
$^{13}\text{C}\{^1\text{H}\}$ spectrum



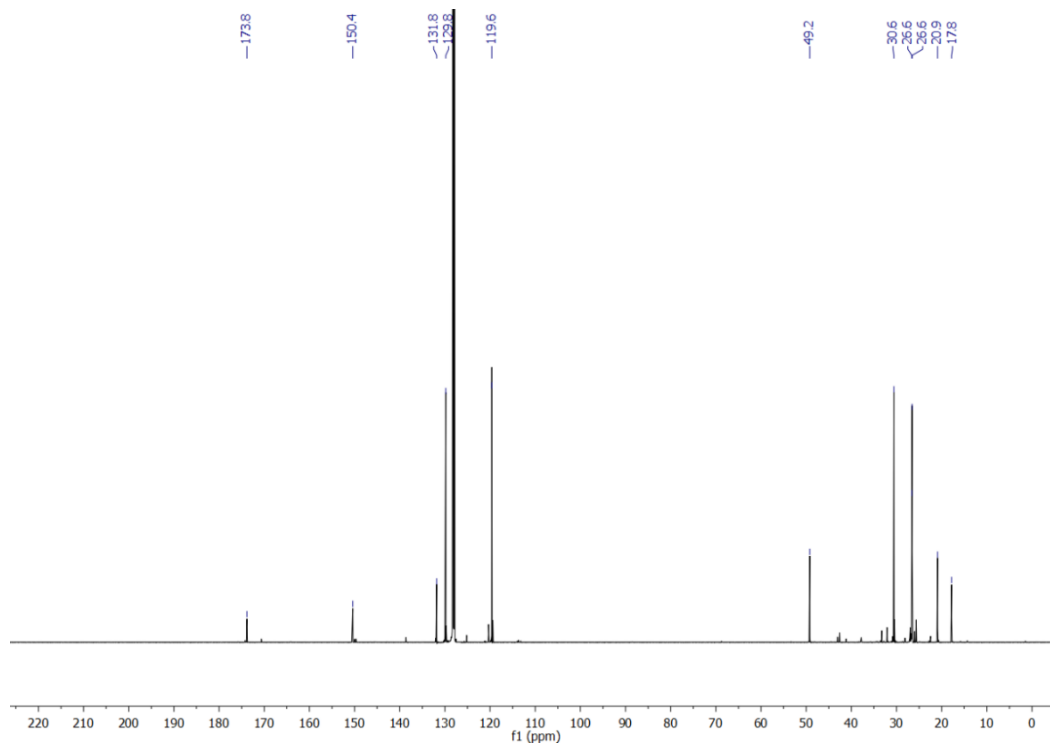
Compound **4.8g** was isolated in 93% yield (0.248 g) and agrees with a previous literature report.¹⁷²

^1H NMR (300 MHz, C_6D_6) δ 7.01 (d, $J = 8.1$ Hz, 2H), 6.68 (d, $J = 8.2$ Hz, 2H), 2.16 (s, 3H), 1.88 (dd, $J = 11.2, 2.9$ Hz, 2H), 1.79 – 1.56 (m, 4H), 1.51 (s, 3H), 1.27 – 1.07 (m, 5H). $^{13}\text{C}\{^1\text{H}\}$ NMR (126 MHz, C_6D_6) δ 173.8, 150.4, 131.8, 129.8, 119.6, 49.2, 30.6, 26.6, 26.6, 20.9, 17.8.

^1H spectrum

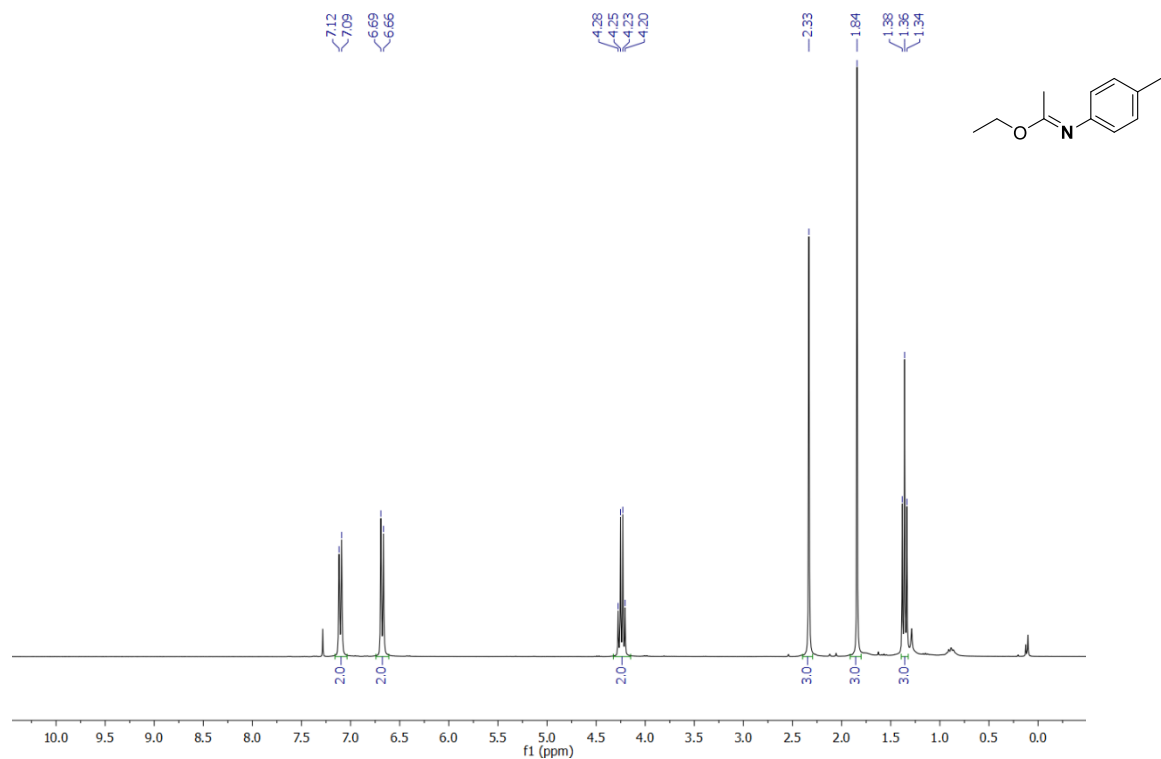


$^{13}\text{C}\{^1\text{H}\}$ spectrum

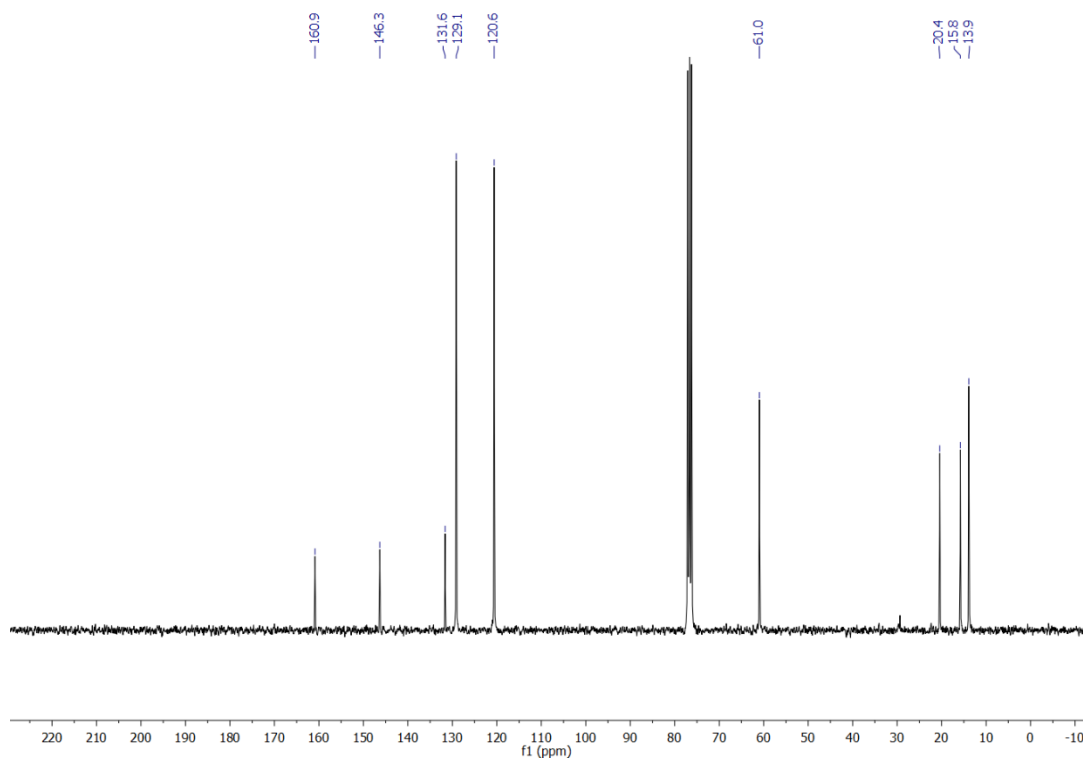


Compound **4.8h** was isolated in 97% yield (0.200 g). ^1H NMR (300 MHz, CDCl_3) δ 7.10 (d, $J = 7.9$ Hz, 2H), 6.68 (d, $J = 8.2$ Hz, 2H), 4.24 (q, $J = 7.1$ Hz, 2H), 2.33 (s, 3H), 1.84 (s, 3H), 1.36 (t, $J = 7.1$ Hz, 3H). $^{13}\text{C}\{^1\text{H}\}$ NMR (75 MHz, CDCl_3) δ 160.9, 146.3, 131.6, 129.1, 120.6, 61.0, 20.4, 15.8, 13.9.

^1H spectrum

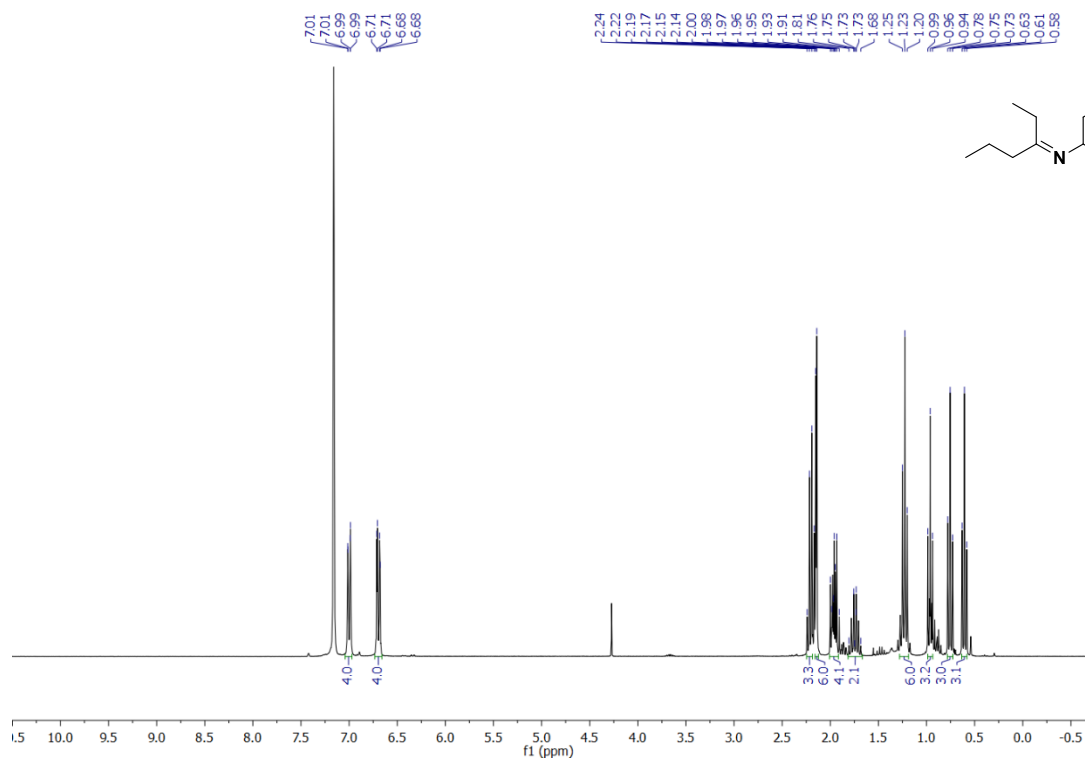


$^{13}\text{C}\{^1\text{H}\}$ spectrum

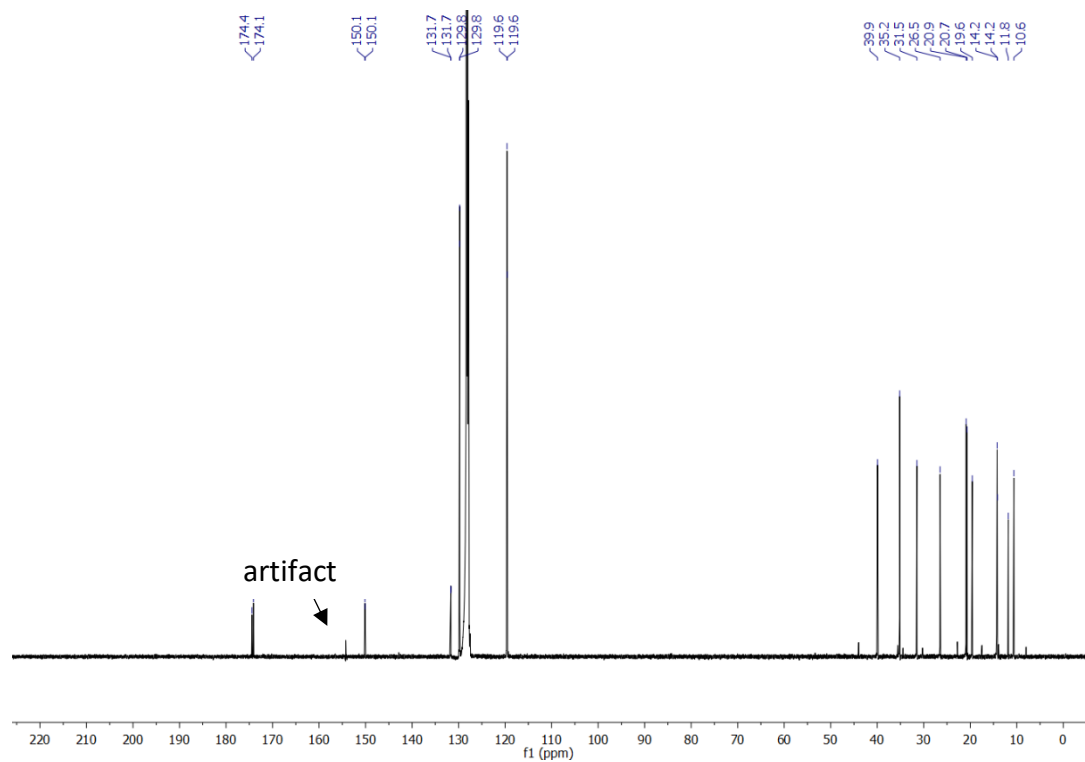


Compound **4.8i** was isolated in 50% yield (0.110 g). ^1H NMR (300 MHz, C_6D_6) δ 6.99 (dd, $J = 8.2$, 2.0 Hz, 4H), 6.69 (dd, $J = 8.2$, 2.0 Hz, 4H), 2.20 (q, $J = 7.4$ Hz, 3H), 2.15 (d, $J = 3.3$ Hz, 6H), 2.03 – 1.87 (m, 4H), 1.84 – 1.65 (m, 2H), 1.23 (t, $J = 7.3$ Hz, 6H), 0.96 (t, $J = 7.3$ Hz, 3H), 0.75 (t, $J = 7.7$ Hz, 3H), 0.61 (t, $J = 7.3$ Hz, 3H). $^{13}\text{C}\{^1\text{H}\}$ NMR (126 MHz, C_6D_6) δ 174.3 (d, $J = 41.5$ Hz), 150.1 (d, $J = 3.7$ Hz), 131.7 (d, $J = 2.5$ Hz), 129.8 (d, $J = 4.3$ Hz), 119.6 (d, $J = 5.4$ Hz), 39.9, 35.2, 31.5, 26.5, 20.9, 20.7, 19.6, 14.2, 14.2, 11.8, 10.6.

^1H spectrum



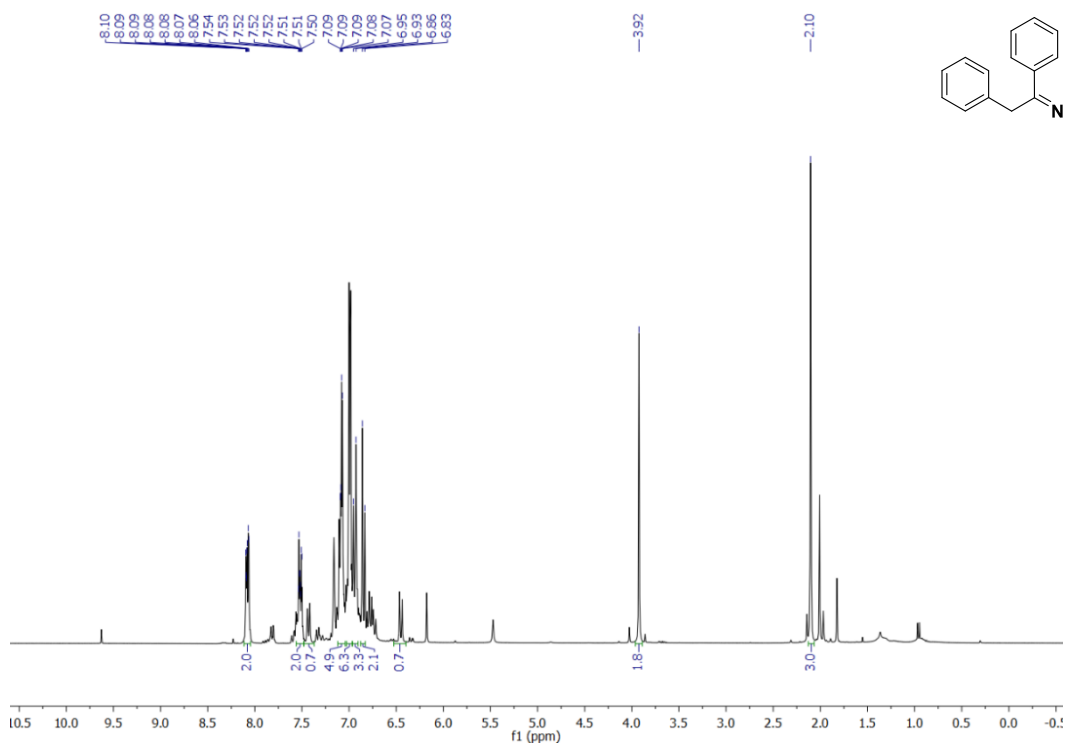
$^{13}\text{C}\{^1\text{H}\}$ spectrum



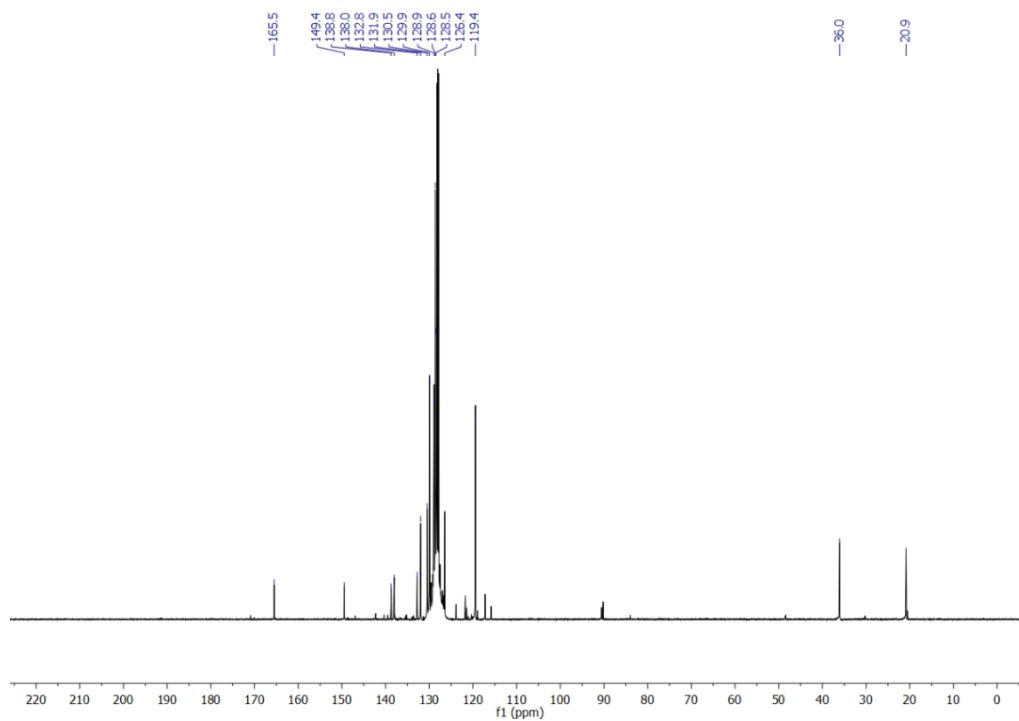
Compound **4.8j** was isolated in 76% yield (0.252 g) and agrees with a previous literature report.¹⁷⁵

¹H NMR (300 MHz, C₆D₆) δ 8.11 – 8.04 (m, 2H), 7.56 – 7.48 (m, 2H), 7.08 (dd, *J* = 4.8, 2.1 Hz, 4H), 6.94 (d, *J* = 8.2 Hz, 1H), 6.85 (d, *J* = 8.2 Hz, 1H), 3.92 (s, 2H), 2.10 (s, 3H). ¹³C{¹H} NMR (126 MHz, C₆D₆) δ 165.5, 149.4, 138.75, 138.0, 132.8, 131.95, 130.5, 129.9, 128.9, 128.6, 128.5, 126.45, 119.4, 36.0, 20.9.

¹H spectrum

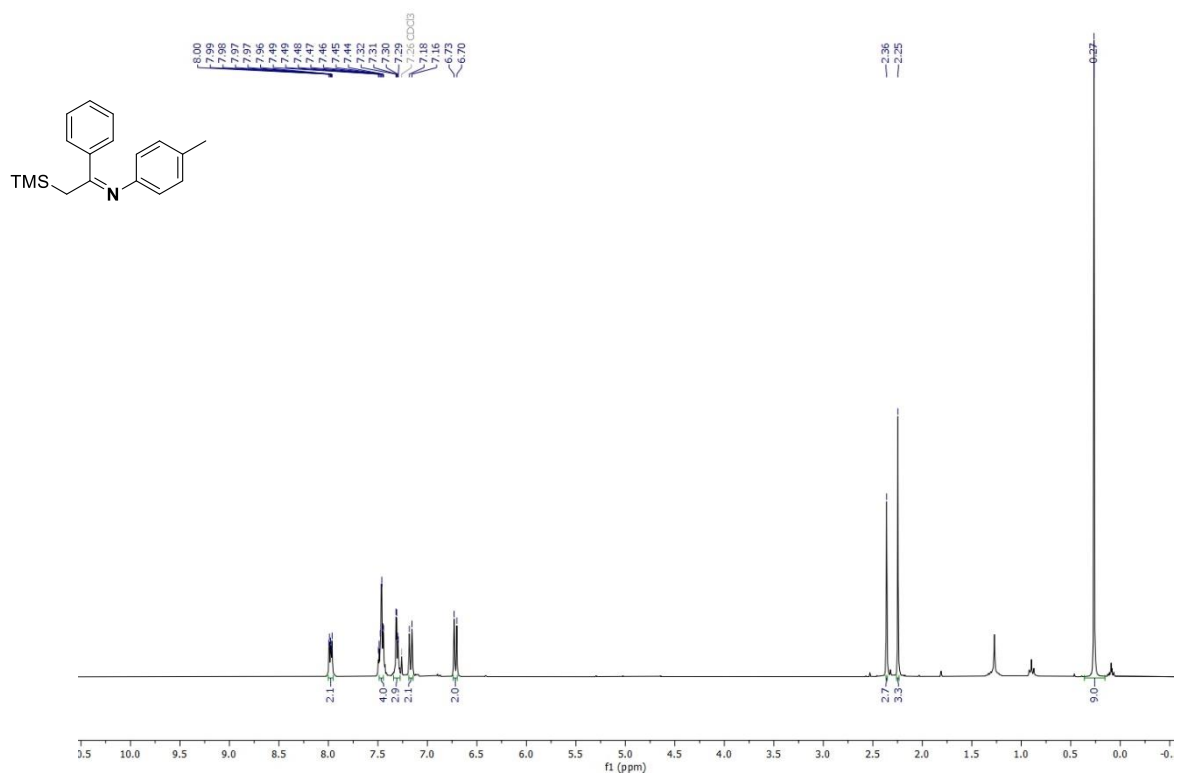


$^{13}\text{C}\{^1\text{H}\}$ spectrum

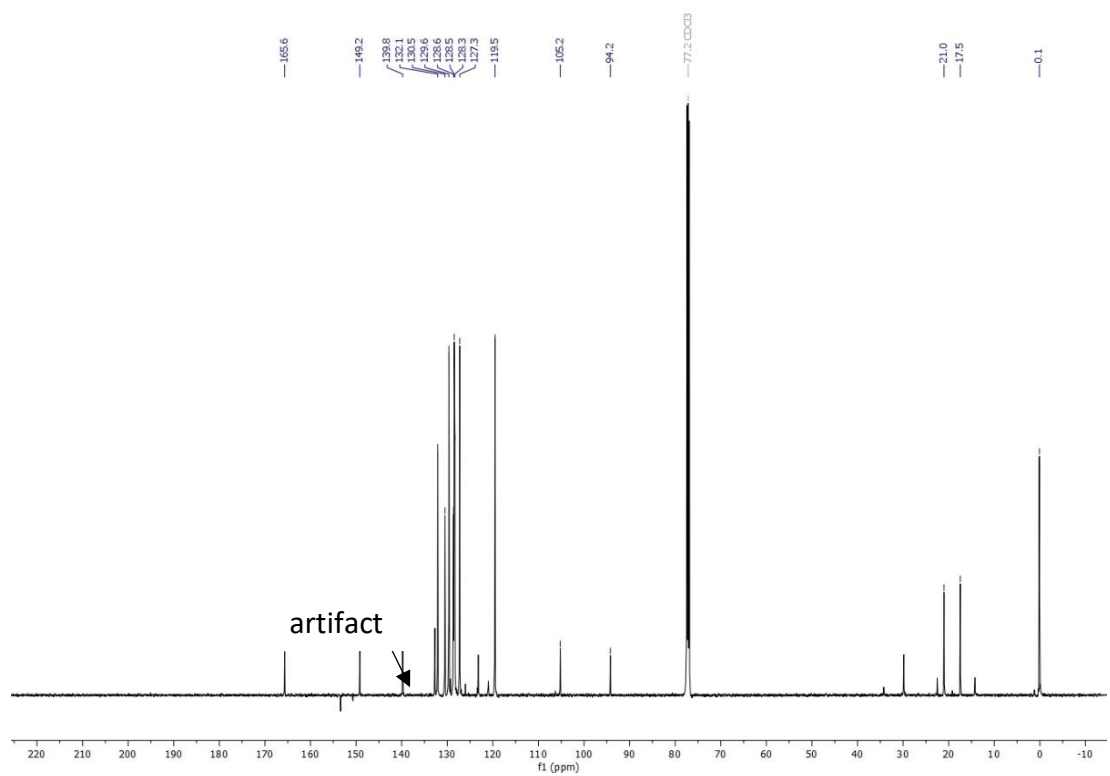


4.8k ^1H NMR (300 MHz, CDCl_3) δ 8.03 – 7.91 (m, 2H), 7.46 (td, $J = 5.6, 5.1, 2.7$ Hz, 3H), 7.30 (dd, $J = 5.1, 2.0$ Hz, 2H), 7.17 (d, $J = 8.0$ Hz, 2H), 6.72 (d, $J = 8.2$ Hz, 2H), 2.36 (s, 2H), 2.25 (s, 3H), 0.27 (s, 9H). $^{13}\text{C}\{^1\text{H}\}$ NMR (126 MHz, CDCl_3) δ 165.6, 149.2, 139.8, 132.1, 130.5, 129.6, 128.5 (t, $J = 18.7$ Hz), 127.3, 119.5, 105.2, 94.2, 19.2 (d, $J = 446.9$ Hz), 0.1.

¹H spectrum



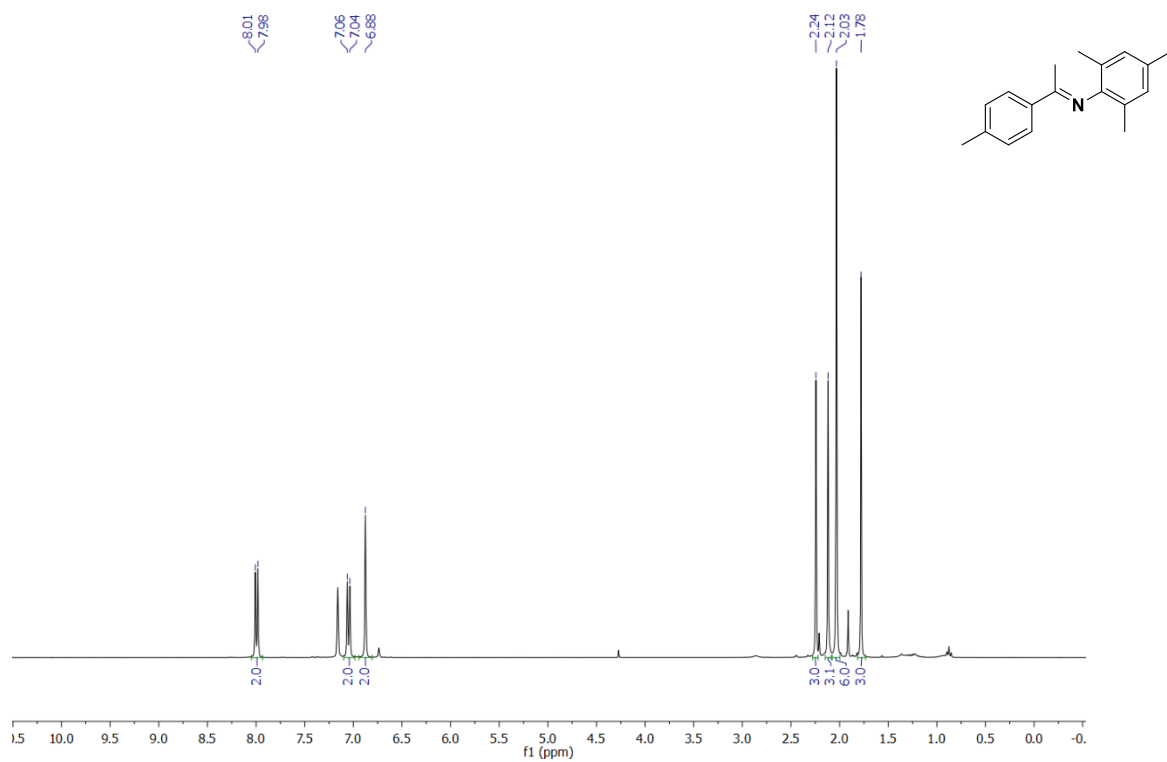
¹³C{¹H} spectrum



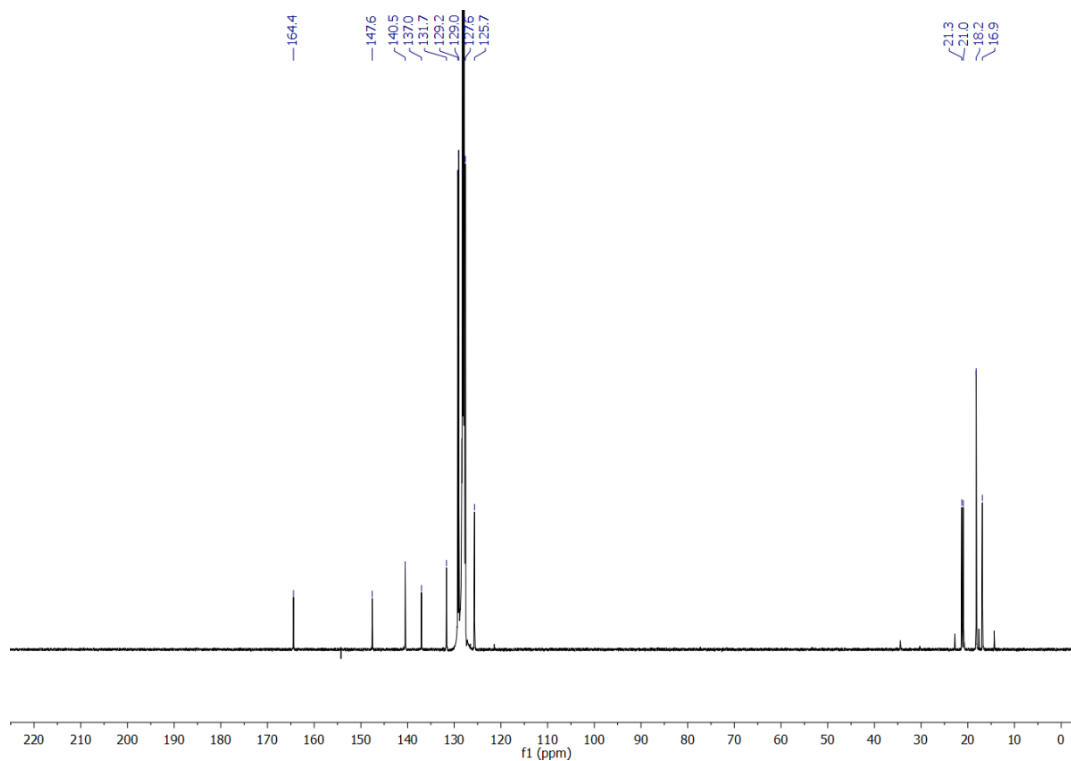
Compound **4.8I** was isolated in 95% yield (0.278 g) and agrees with a previous literature report.¹⁷⁶

¹H NMR (300 MHz, C₆D₆) δ 7.99 (d, *J* = 8.2 Hz, 2H), 7.05 (d, *J* = 8.0 Hz, 2H), 6.88 (s, 2H), 2.24 (s, 3H), 2.12 (s, 3H), 2.03 (s, 6H), 1.78 (s, 3H). ¹³C{¹H} NMR (126 MHz, C₆D₆) δ 164.4, 147.6, 140.5, 137.0, 131.7, 129.2, 129.0, 127.6, 125.65, 21.3, 20.95, 18.2, 16.9.

¹H spectrum

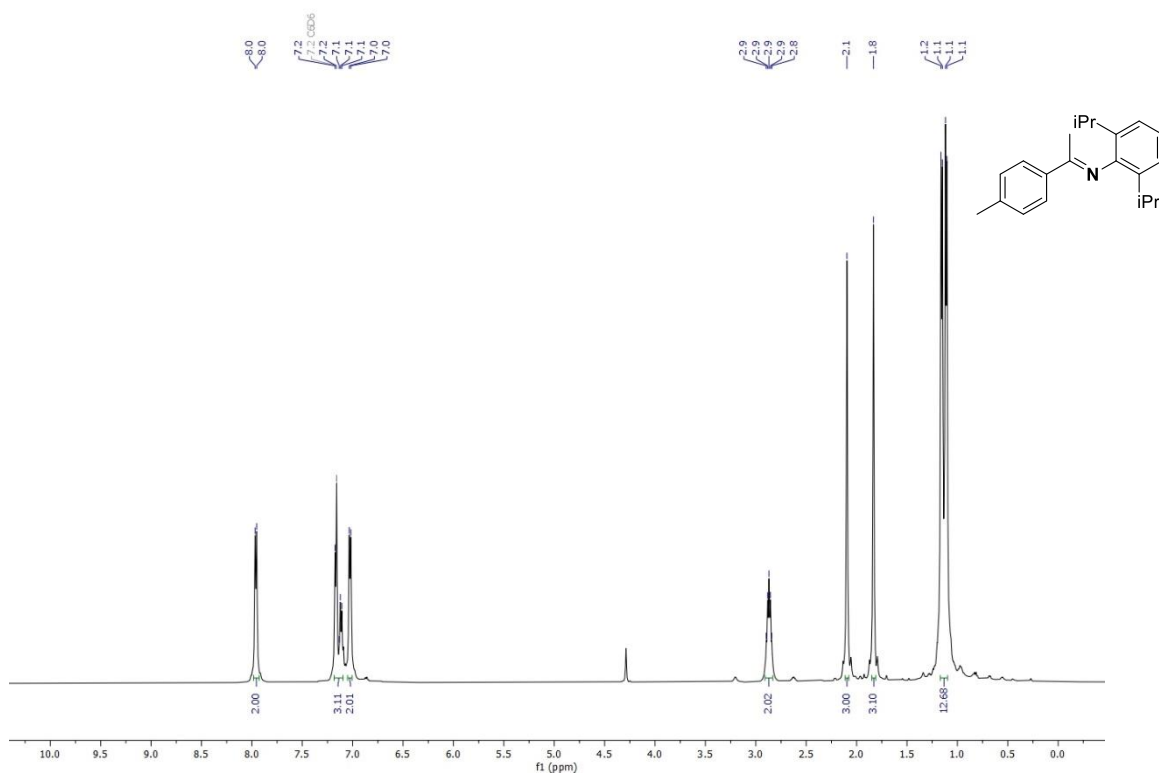


$^{13}\text{C}\{^1\text{H}\}$ spectrum

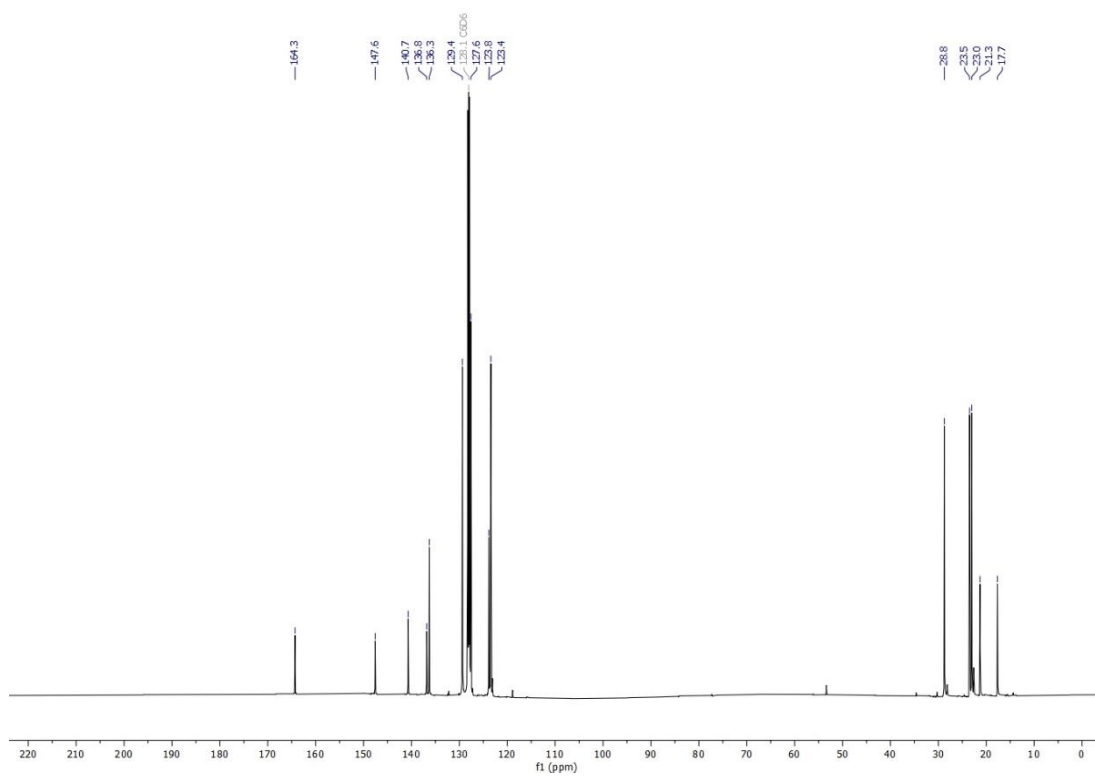


Compound **4.8m** was isolated in 99% yield (0.338 g). ^1H NMR (500 MHz, C_6D_6) δ 7.96 (d, $J = 7.9$ Hz, 2H), 7.20 – 7.07 (m, 3H), 7.03 (d, $J = 7.9$ Hz, 2H), 2.87 (p, $J = 6.8$ Hz, 2H), 2.10 (s, 3H), 1.83 (s, 3H), 1.18 (d, $J = 7.1$ Hz, 6H), 1.12 (d, $J = 7.1$ Hz, 6H). ^{13}C NMR (126 MHz, C_6D_6) δ 164.3, 147.6, 140.7, 136.8, 136.3, 129.4, 127.6, 123.8, 123.4, 28.8, 23.5, 23.0, 21.3, 17.7.

^1H spectrum

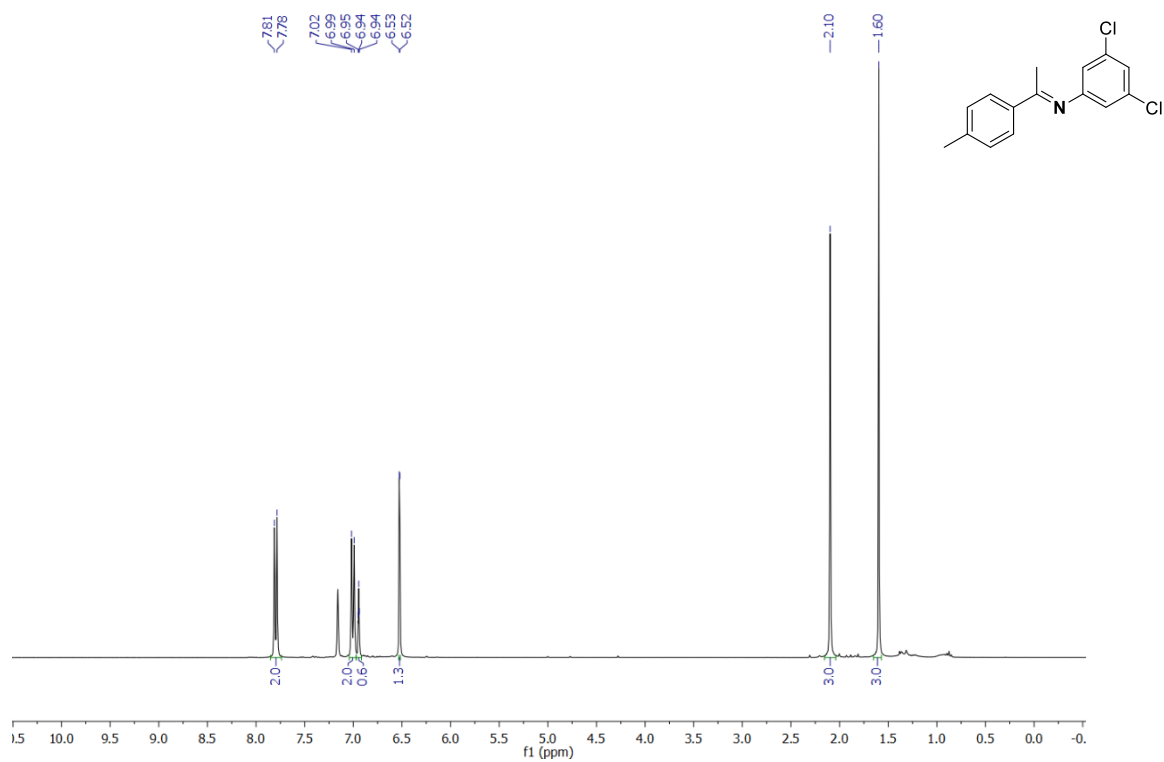


$^{13}\text{C}\{^1\text{H}\}$ spectrum

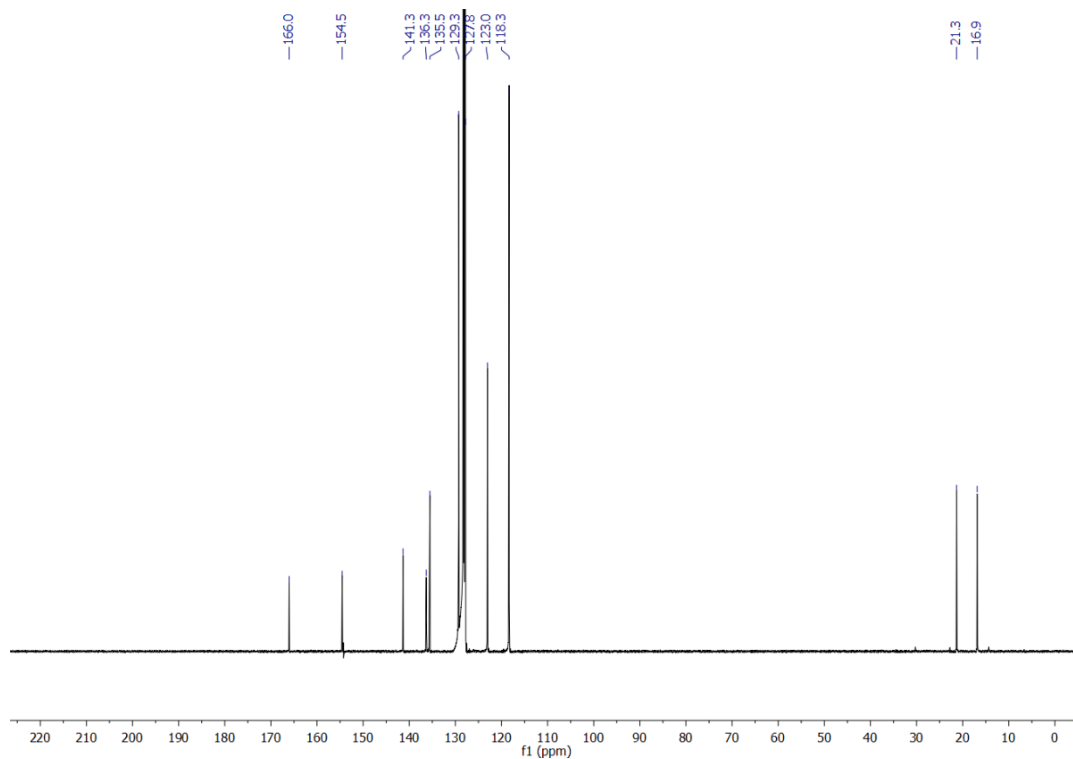


Compound **4.8n** was isolated in 94% yield (0.304 g). ^1H NMR (300 MHz, C_6D_6) δ 7.80 (d, $J = 8.3$ Hz, 2H), 7.00 (d, $J = 8.0$ Hz, 2H), 6.94 (t, $J = 1.9$ Hz, 1H), 6.52 (d, $J = 1.9$ Hz, 1H), 2.10 (s, 3H), 1.60 (s, 3H). $^{13}\text{C}\{^1\text{H}\}$ NMR (126 MHz, C_6D_6) δ 166.0, 154.5, 141.4, 136.3, 135.5, 129.3, 127.8, 123.1, 118.4, 21.4, 16.9.

^1H spectrum

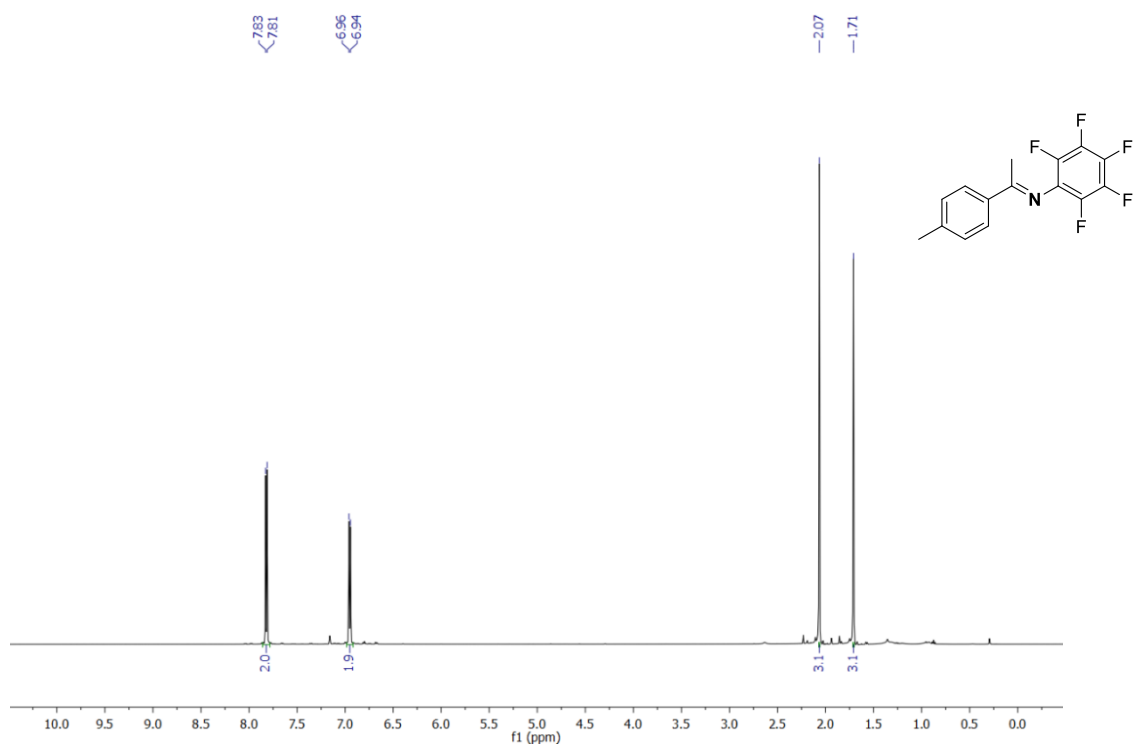


$^{13}\text{C}\{^1\text{H}\}$ spectrum

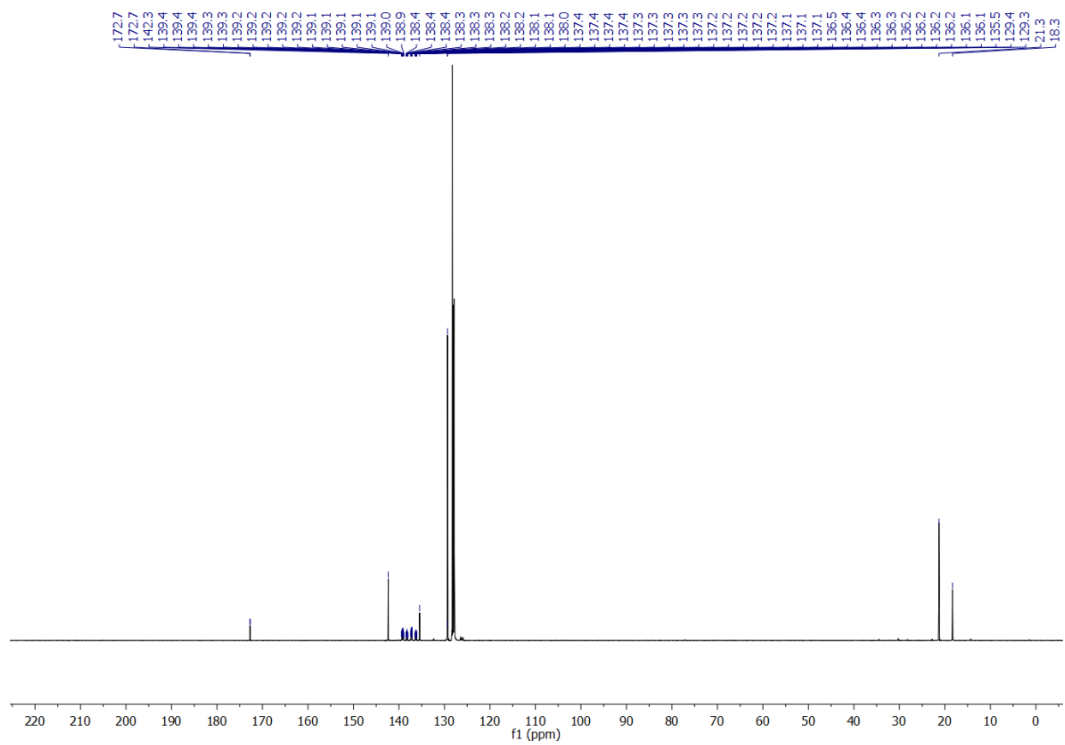


Compound **4.8o** was isolated in 96% yield (0.334 g). ^1H NMR (500 MHz, C_6D_6) δ 7.82 (d, $J = 8.3$ Hz, 2H), 6.95 (d, $J = 8.0$ Hz, 2H), 2.07 (s, 3H), 1.71 (s, 3H). $^{13}\text{C}\{^1\text{H}\}$ NMR (126 MHz, C_6D_6) δ 172.7 (d, $J = 1.3$ Hz), 142.3, 139.6–138.8(m), 138.5–137.9(m), 137.6–136.9 (m), 136.6–136.0(m), 135.5, 129.3, 21.3, 18.3. ^{19}F NMR (282 MHz, C_6D_6) δ -153.7, -164.7.

^1H spectrum



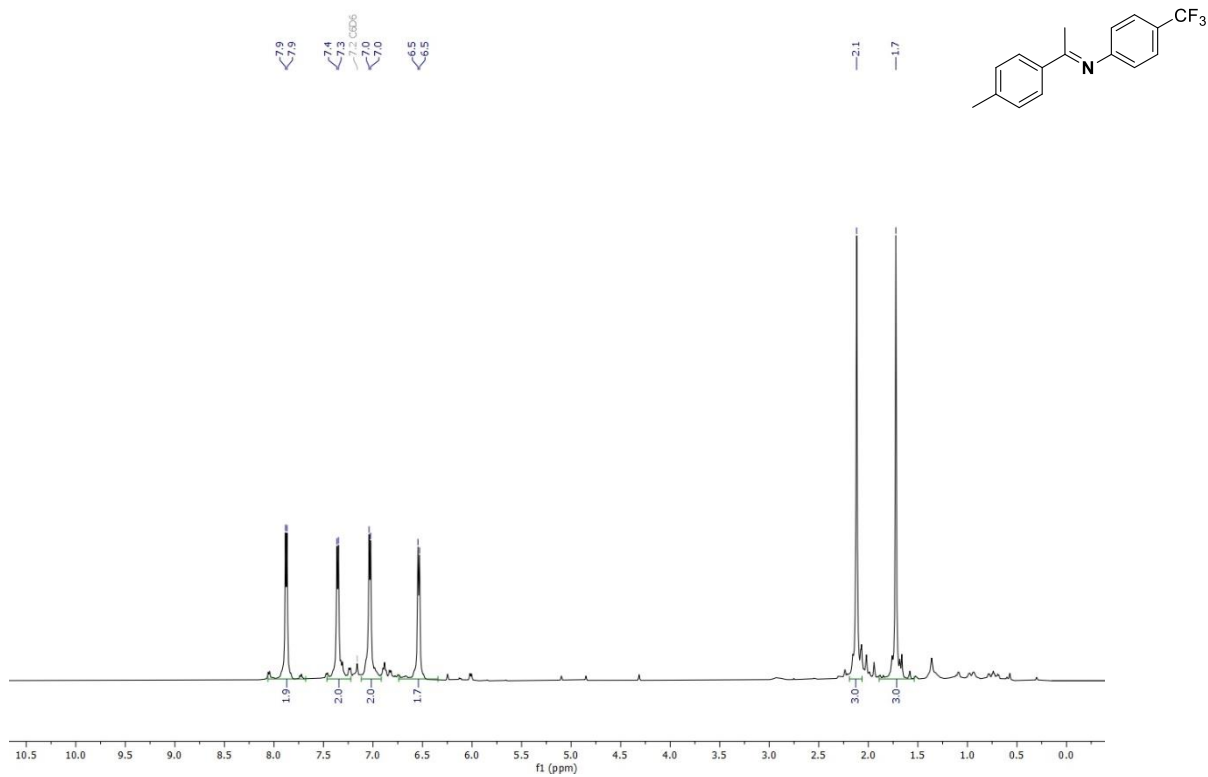
$^{13}\text{C}\{^1\text{H}\}$ spectrum



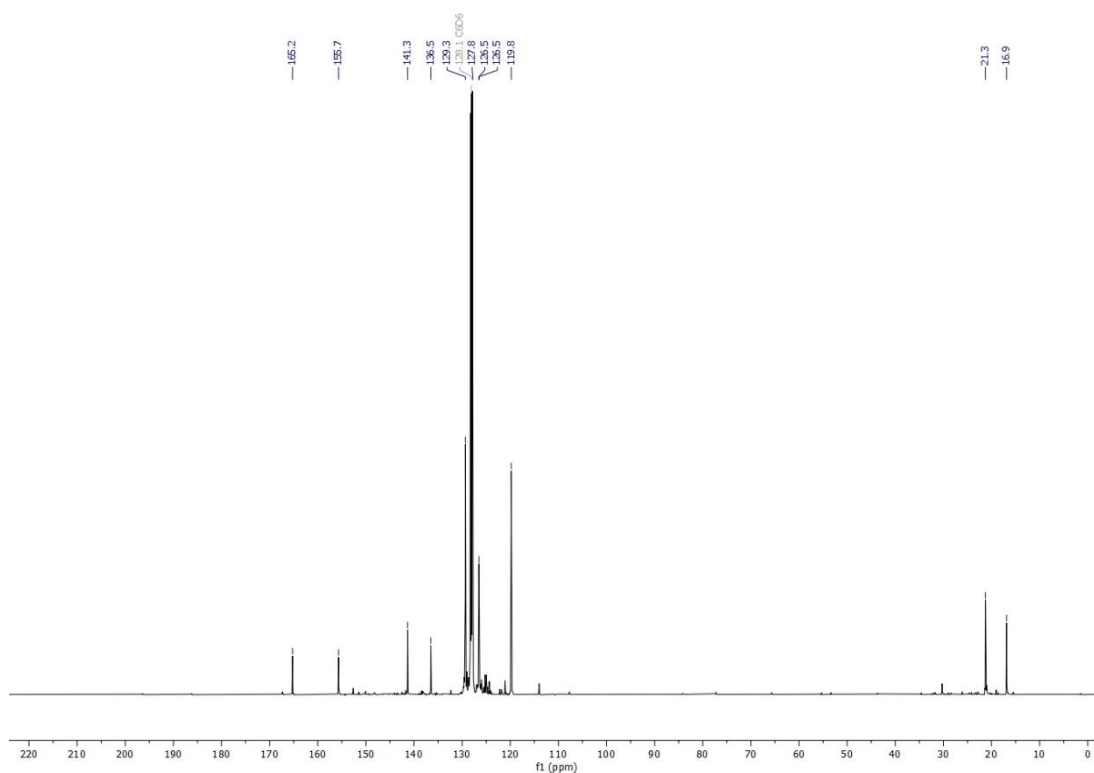
Compound **4.8p** was isolated in 42% yield (0.135 g) and agrees with a previous literature report.¹⁷³

¹H NMR (500 MHz, C₆D₆) δ 7.88 (d, *J* = 7.9 Hz, 2H), 7.36 (d, *J* = 8.1 Hz, 2H), 7.03 (d, *J* = 7.9 Hz, 2H), 6.54 (d, *J* = 8.1 Hz, 1H), 2.12 (s, 3H), 1.72 (s, 3H). ¹³C{¹H} NMR (126 MHz, C₆D₆) δ 165.2, 155.7, 141.3, 136.5, 129.3, 127.8, 126.5 (d, *J* = 3.8 Hz), 119.8, 21.3, 16.9. ¹⁹F NMR (282 MHz, C₆D₆) δ -62.09.

¹H spectrum

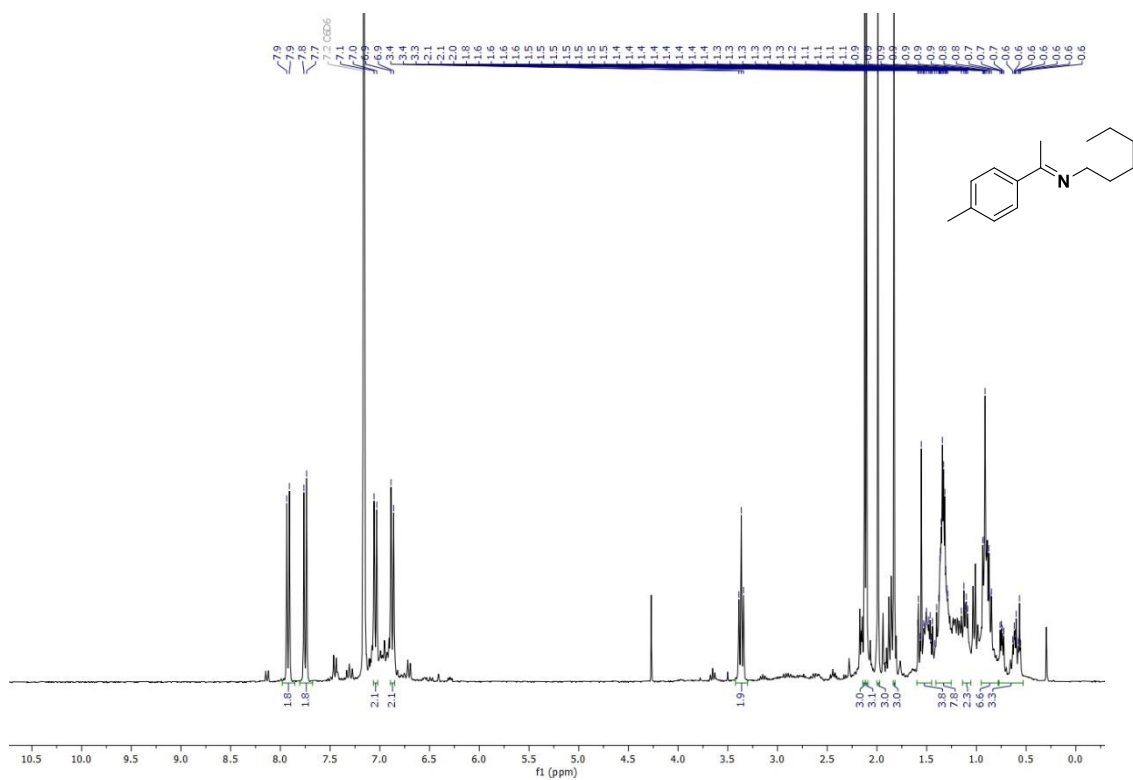


$^{13}\text{C}\{^1\text{H}\}$ spectrum

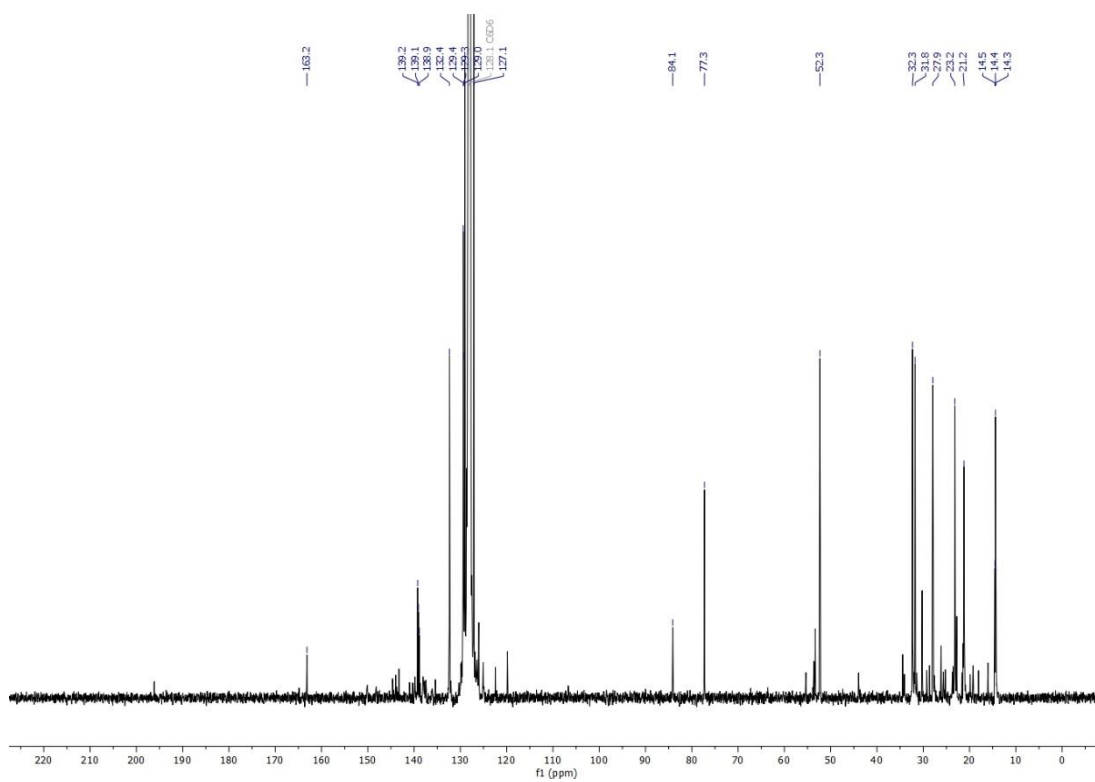


Compound **4.8q** was isolated under anhydrous conditions in 87% yield (0.220 g). ^1H NMR (500 MHz, C_6D_6) ^1H NMR (300 MHz, C_6D_6) δ 7.92 (d, $J = 8.2$ Hz, 2H), 7.75 (d, $J = 8.2$ Hz, 2H), 7.04 (d, $J = 8.0$ Hz, 2H), 6.87 (d, $J = 8.0$ Hz, 2H), 3.37 (t, $J = 6.9$ Hz, 2H), 2.12 (s, 3H), 2.11 (s, 3H), 1.99 (s, 3H), 1.83 (s, 3H), 1.59 – 1.42 (m, 4H), 1.40 – 1.28 (m, 8H), 1.15 – 1.08 (m, 2H), 0.95 – 0.83 (m, 6H), 0.77 – 0.50 (m, 3H). $^{13}\text{C}\{^1\text{H}\}$ NMR (126 MHz, C_6D_6) δ 163.2, 139.3 – 138.2 (m), 132.4, 129.3 (d, $J = 6.0$ Hz), 129.0, 127.1, 84.1, 77.3, 52.3, 32.0 (d, $J = 70.6$ Hz), 27.9, 22.2 (d, $J = 249.9$ Hz), 15.3 – 11.8 (m).

^1H spectrum

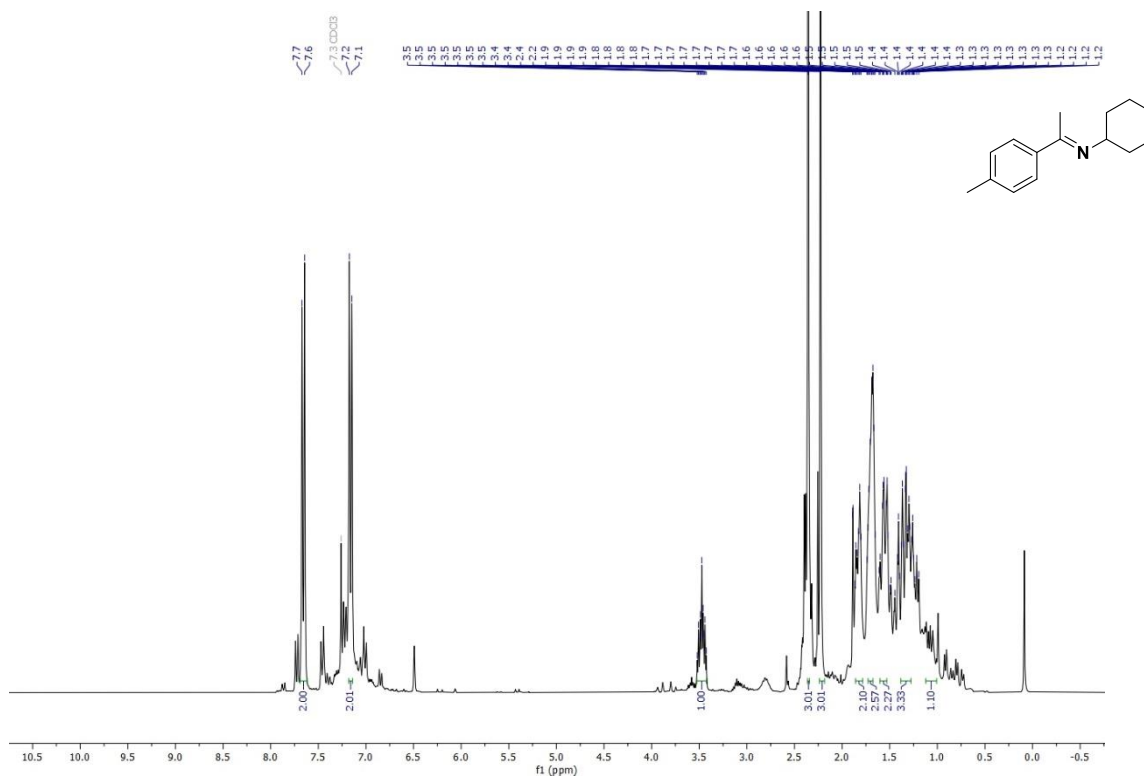


$^{13}\text{C}\{^1\text{H}\}$ spectrum

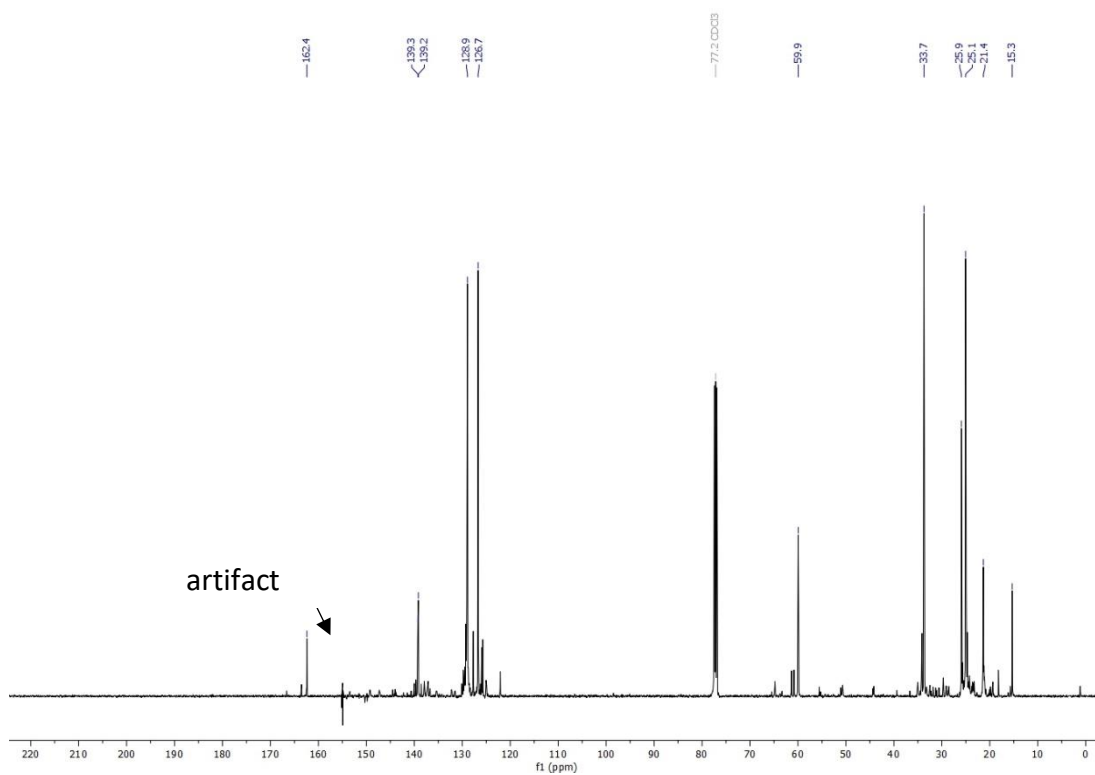


Compound **4.8r** was isolated in 67% yield (0.168 g). ^1H NMR (300 MHz, CDCl_3) δ 7.66 (d, $J = 8.2$ Hz, 2H), 7.16 (d, $J = 8.0$ Hz, 2H), 3.47 (tt, $J = 10.2, 4.1$ Hz, 1H), 2.36 (s, 3H), 2.23 (s, 3H), 1.93 – 1.10 (m, 10H). ^{13}C NMR (126 MHz, CDCl_3) δ 162.4, 139.3, 139.7, 128.9, 126.7, 59.9, 33.7, 25.9, 25.1, 21.4, 15.3.

^1H spectrum



$^{13}\text{C}\{^1\text{H}\}$ spectrum

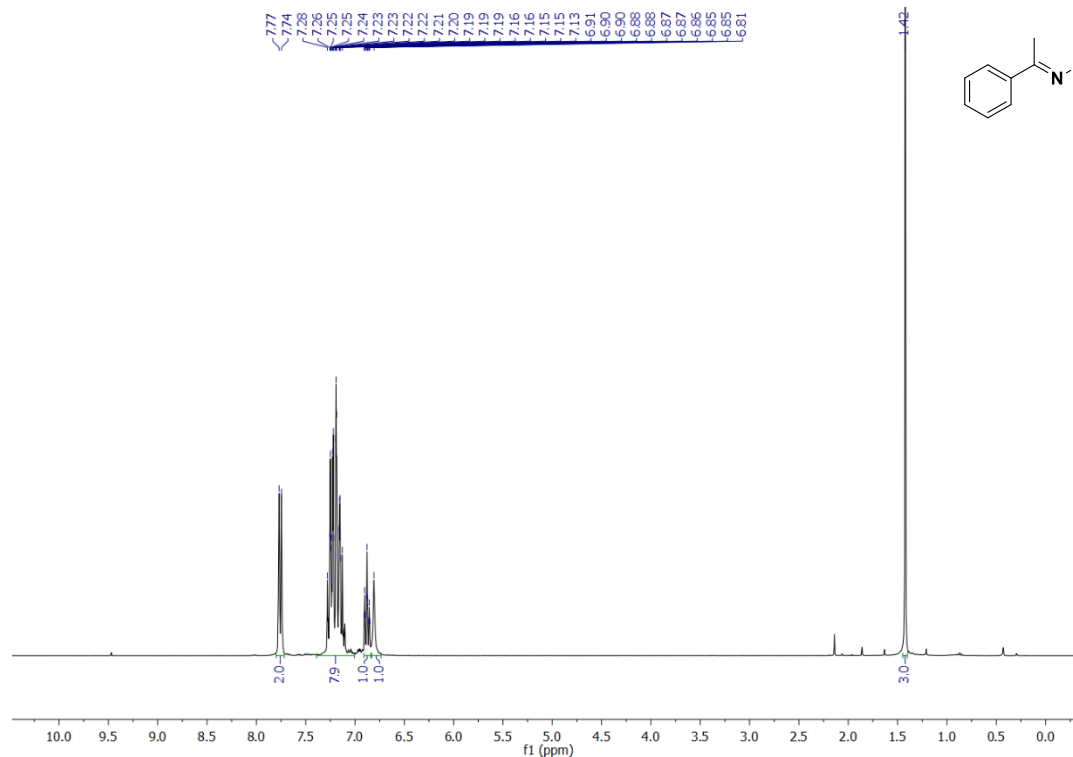


4.11. General method for the hydrohydrazination

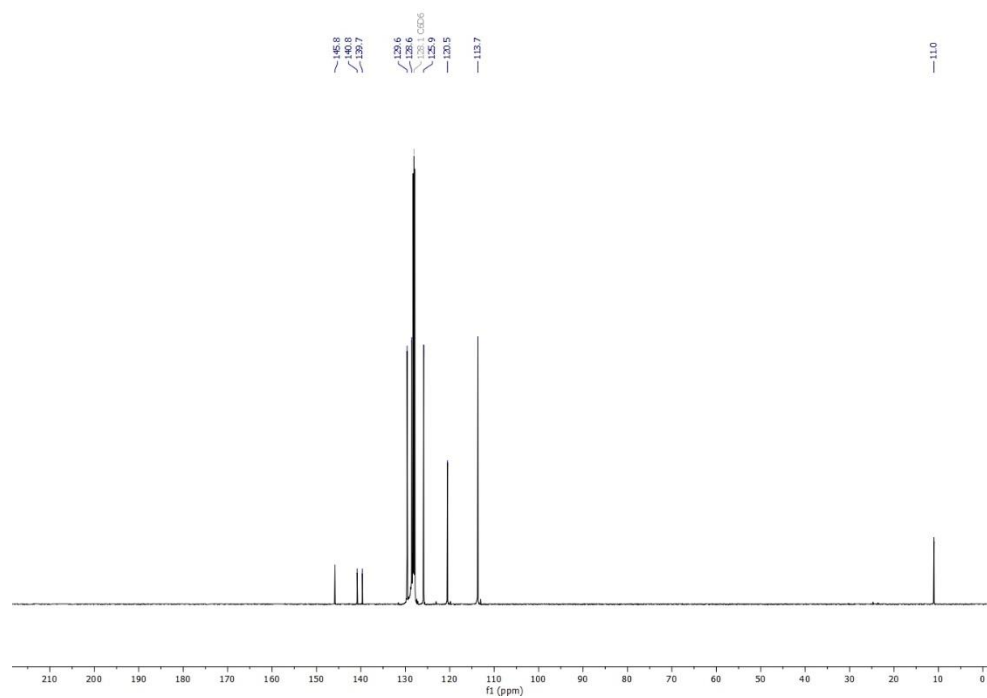
In air, a scintillation vial (3 mL) was charged with (**4.6.L**)AuCl (0.5 mol%, 0.001784 mmol), $\text{KB}(\text{C}_6\text{F}_5)_4$ (0.5 mol%, 0.001784 mmol), C_6H_6 (200 μL) and the alkyne (0.357 mmol, 1.0 eq.). After stirring for two minutes, the amine (0.357 mmol, 1.0 eq.) was added as a solution in C_6H_6 (200 μL). The mixture was then set stirring at the temperature shown in Figure 4.9. The products were purified by column chromatography using Florisil eluting with a gradient mixture of DCM/hexane. NB: Air sensitive products were purified under argon using dried Florisil.

For this reaction, 1.1 equivalents of hydrazine were added (0.043 g, 0.393 mmol). Compound **4.9a** was isolated in 100% yield (0.075 g) and agrees with a previous literature report.¹⁷⁷ δ 7.76 (d, $J = 7.4$ Hz, 2H), 7.28 – 7.13 (m, 8H), 6.88 (tt, $J = 6.9, 1.4$ Hz, 1H), 6.81 (s, 1H), 1.42 (s, 3H). $^{13}\text{C}\{^1\text{H}\}$ NMR (126 MHz, C_6D_6) δ 145.8, 140.8, 139.7, 129.6, 128.6, 125.9, 120.5, 113.7, 11.0.

^1H spectrum

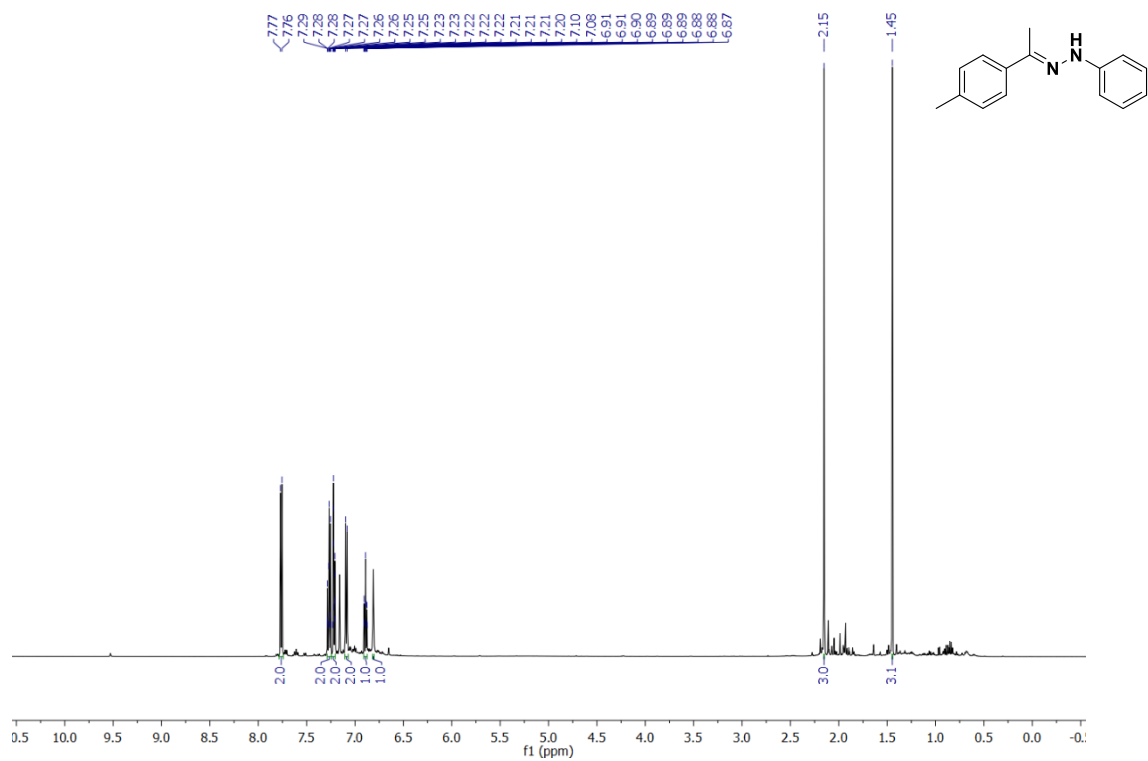


$^{13}\text{C}\{^1\text{H}\}$ spectrum

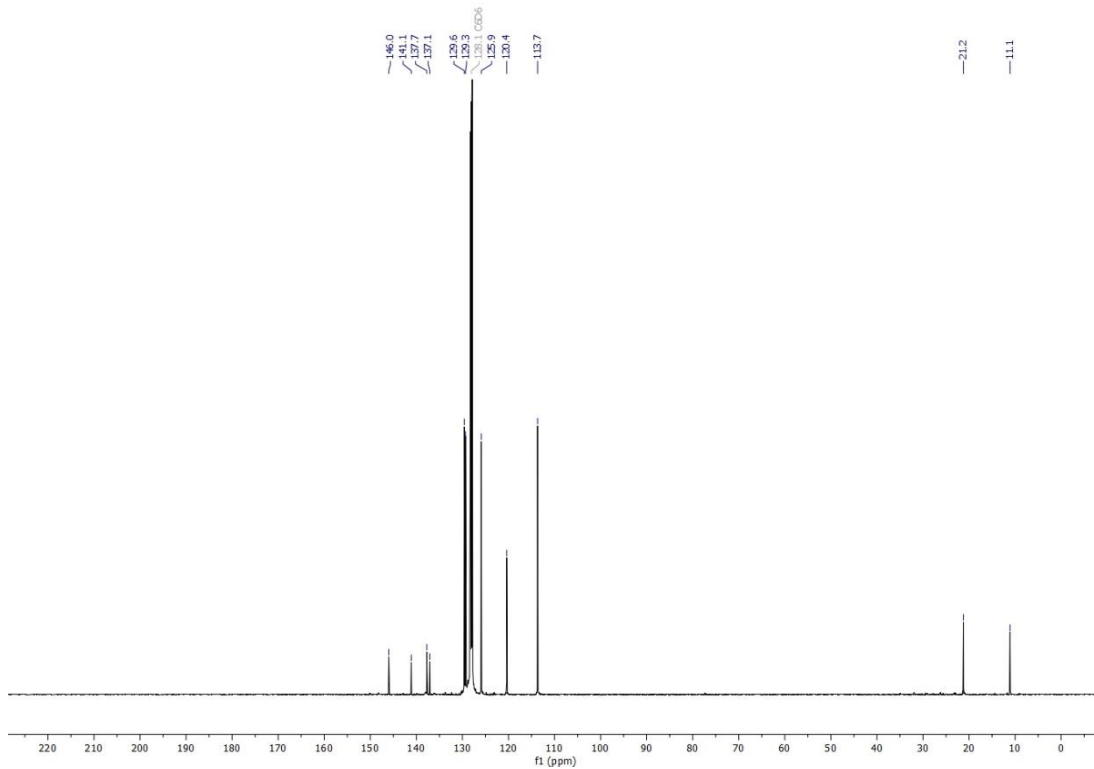


Compound **4.9b** was isolated in 95% yield (0.076 g) and agrees with a previous literature report.¹⁷⁷ ^1H NMR (500 MHz, C_6D_6) δ 7.76 (d, $J = 8.3$ Hz, 2H), 7.29 – 7.24 (m, 2H), 7.24 – 7.19 (m, 2H), 7.09 (d, $J = 7.9$ Hz, 2H), 6.89 (tt, $J = 7.2, 1.3$ Hz, 2H), 6.81 (s, 1H), 2.15 (s, 3H), 1.45 (s, 3H). $^{13}\text{C}\{^1\text{H}\}$ NMR (126 MHz, C_6D_6) δ 146.0, 141.1, 137.7, 137.1, 129.6, 129.3, 125.9, 120.4, 113.7, 21.2, 11.1.

^1H spectrum

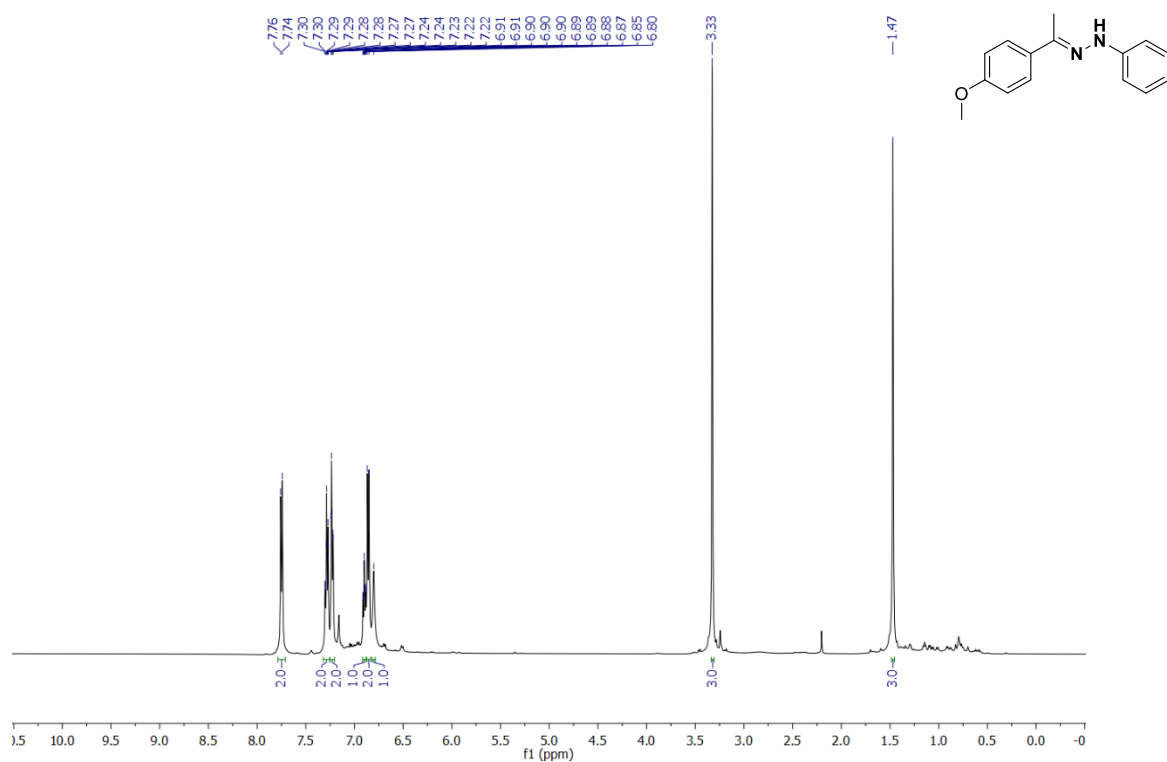


$^{13}\text{C}\{^1\text{H}\}$ spectrum

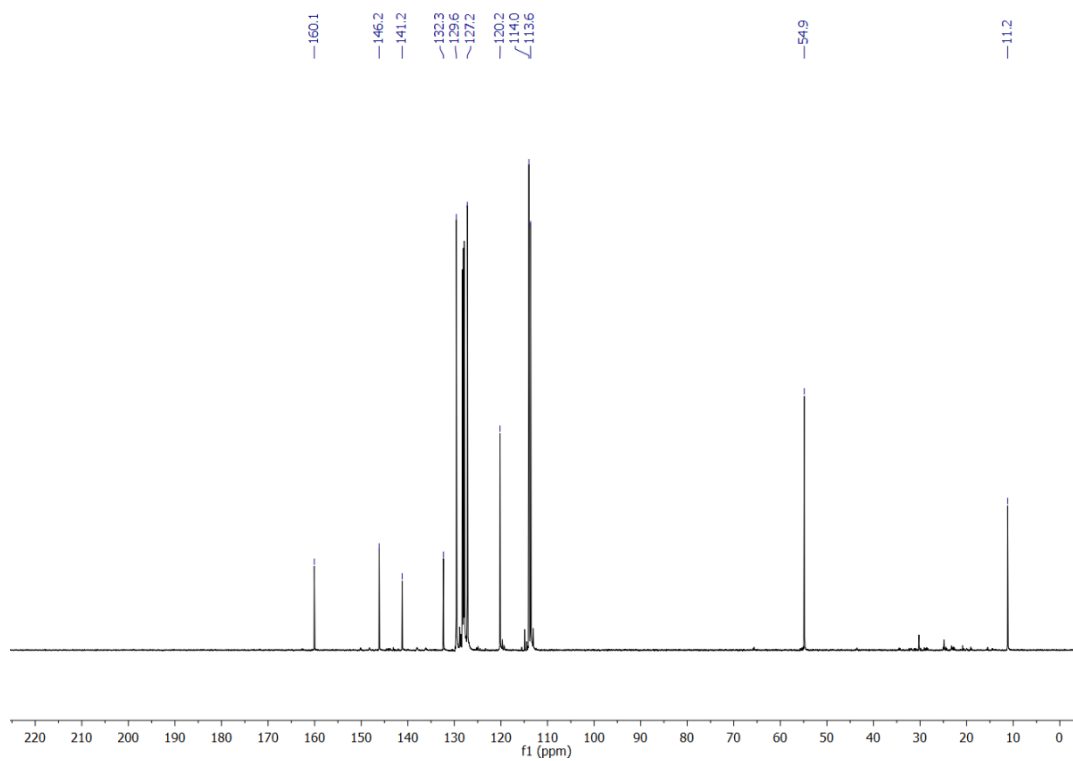


Compound **4.9c** was isolated in 99% yield (0.085 g). ^1H NMR (500 MHz, C_6D_6) δ 7.75 (d, $J = 8.9$ Hz, 2H), 7.29 (ddd, $J = 8.8, 6.9, 1.7$ Hz, 2H), 7.24 – 7.22 (m, 2H), 6.90 (td, $J = 7.1, 1.3$ Hz, 1H), 6.86 (d, $J = 9.1$ Hz, 2H), 6.80 (s, 1H), 3.33 (s, 3H), 1.47 (s, 3H). $^{13}\text{C}\{^1\text{H}\}$ NMR (126 MHz, C_6D_6) δ 160.1, 146.2, 141.2, 132.3, 129.6, 127.2, 120.2, 114.0, 113.6, 54.9, 11.2.

^1H spectrum

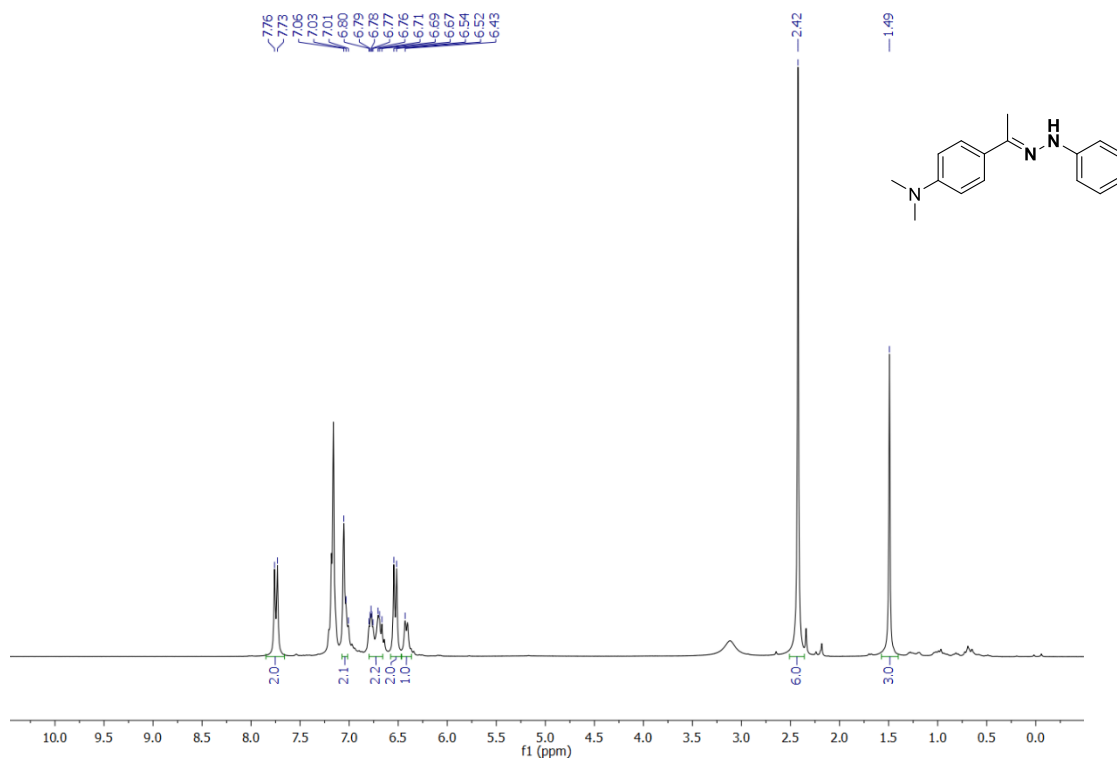


$^{13}\text{C}\{^1\text{H}\}$ spectrum

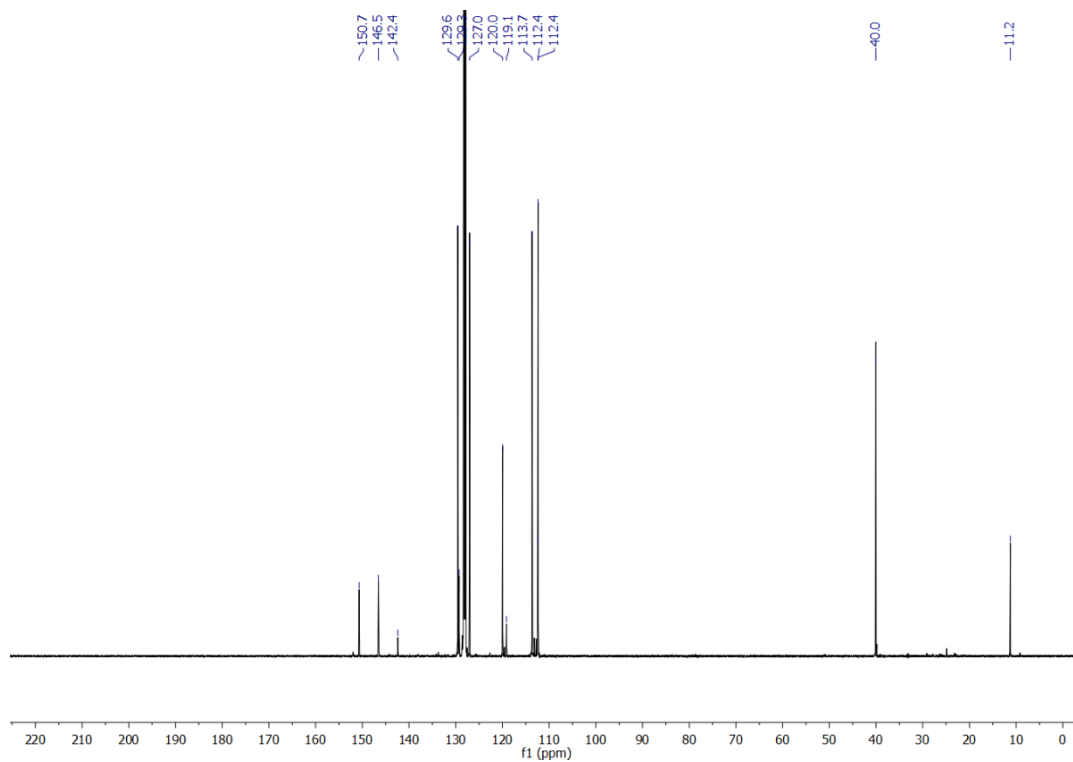


Compound **4.9d** was isolated in 95% yield (0.086 g). ^1H NMR (300 MHz, C_6D_6) δ 7.75 (d, $J = 8.4$ Hz, 2H), 7.04 (d, $J = 7.1$ Hz, 2H), 6.82 – 6.62 (m, 2H), 6.53 (d, $J = 8.5$ Hz, 2H), 6.43 (s, 1H), 2.42 (s, 6H), 1.49 (s, 3H). $^{13}\text{C}\{^1\text{H}\}$ NMR (126 MHz, C_6D_6) δ 150.7, 146.6, 142.4, 129.6, 129.3, 127.1, 120.0, 119.1, 113.7, 112.4, 112.4, 40.0, 11.2.

^1H spectrum

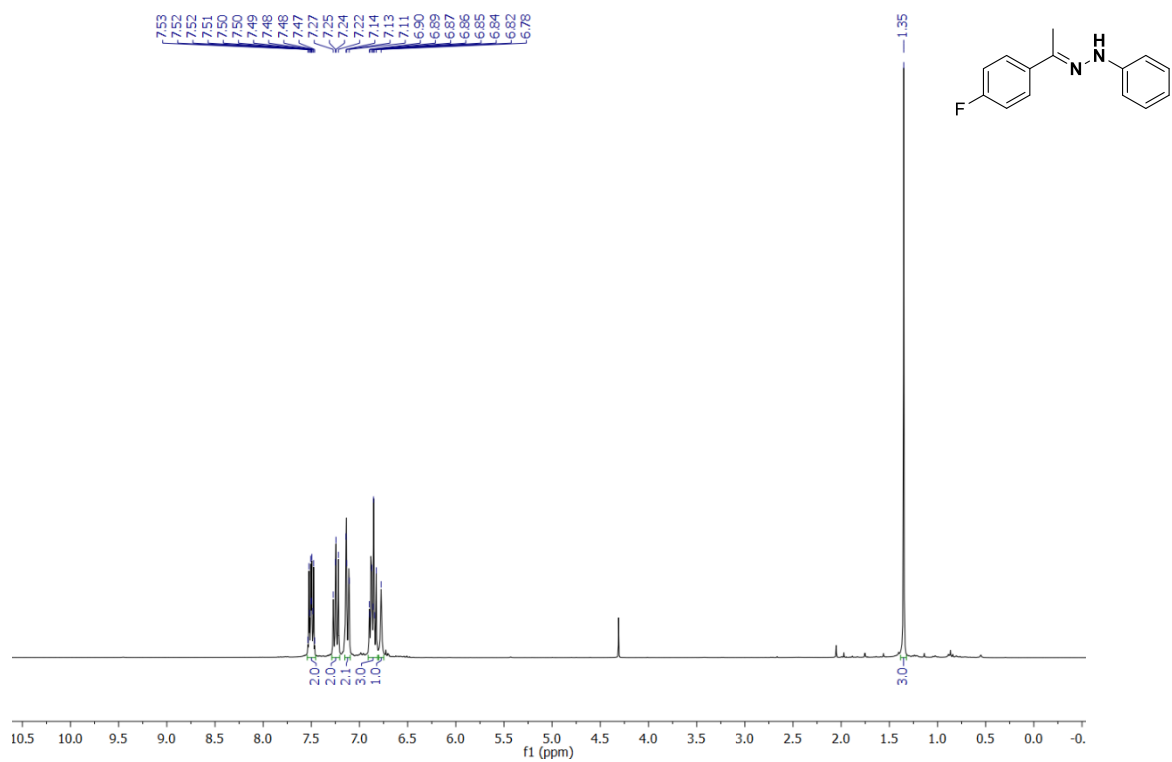


$^{13}\text{C}\{^1\text{H}\}$ spectrum

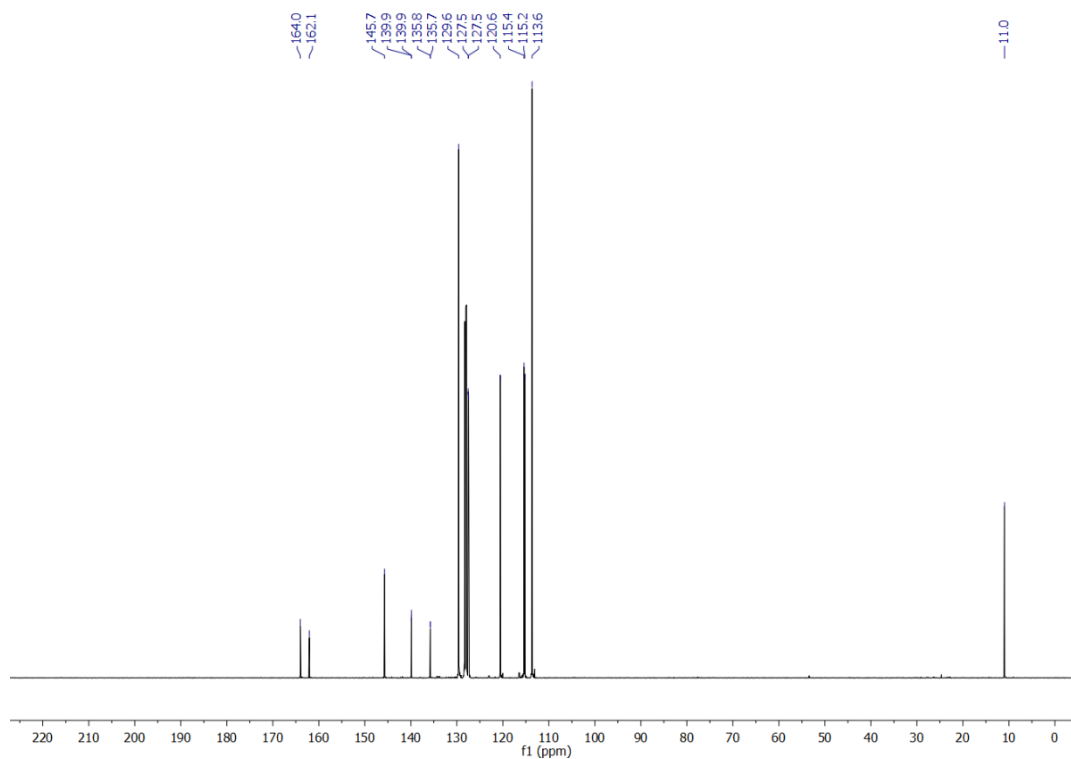


Compound **4.9e** was isolated in 95% yield (0.077 g). ^1H NMR (300 MHz, C_6D_6) δ 7.55 – 7.45 (m, 2H), 7.25 (dd, $J = 8.6, 7.2$ Hz, 2H), 7.17 – 7.07 (m, 2H), 6.93 – 6.79 (m, 3H), 6.78 (s, 1H), 1.35 (s, 3H). $^{13}\text{C}\{^1\text{H}\}$ NMR (126 MHz, C_6D_6) δ 164.0, 162.1, 145.7, 139.9, 139.9, 135.8, 135.7, 129.6, 127.5, 127.5, 120.6, 115.4, 115.2, 113.6, 10.9. ^{19}F NMR (282 MHz, C_6D_6) δ -115.13.

^1H spectrum

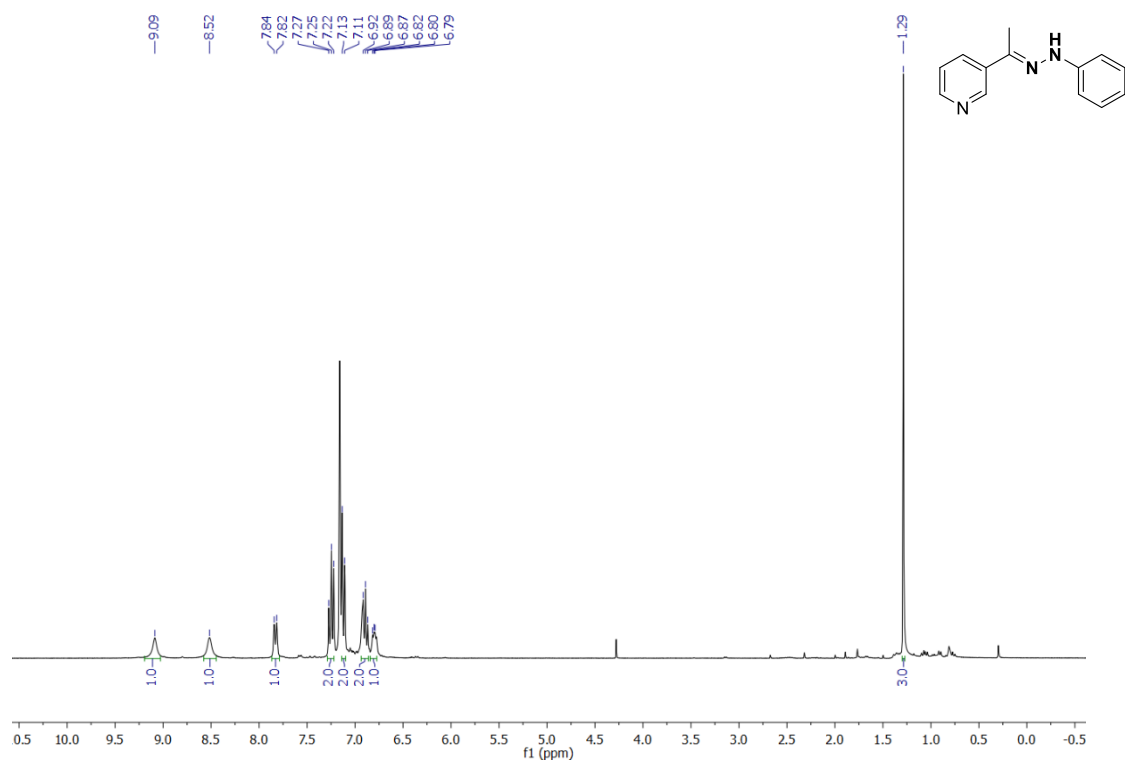


$^{13}\text{C}\{^1\text{H}\}$ spectrum

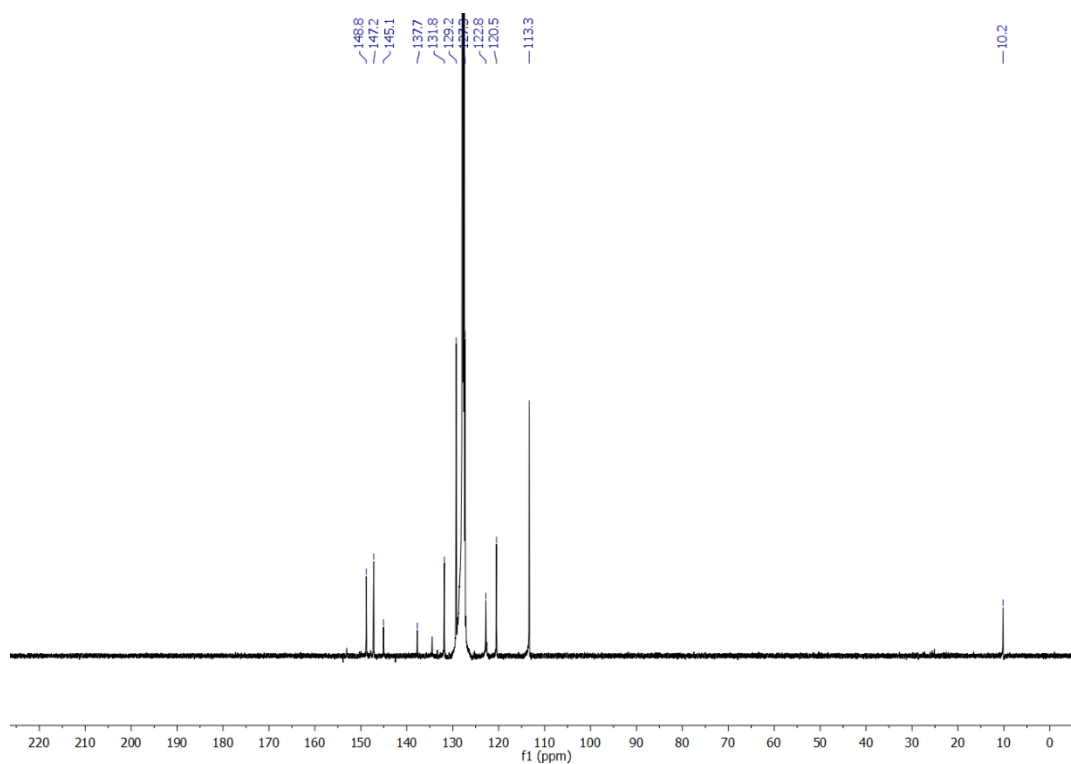


Compound **4.9f** was isolated in 93% yield (0.070 g). ^1H NMR (300 MHz, C_6D_6) δ 9.09 (br, 1H), 8.52 (s, 1H), 7.83 (d, $J = 8.1$ Hz, 1H), 7.25 (dd, $J = 8.6, 7.2$ Hz, 2H), 7.14 – 7.10 (m, 2H), 6.93 – 6.86 (m, 2H), 6.82 – 6.76 (m, 1H), 1.29 (s, 3H). $^{13}\text{C}\{^1\text{H}\}$ NMR (126 MHz, C_6D_6) δ 148.8, 147.2, 145.1, 137.7, 131.8, 129.2, 127.3, 122.8, 120.5, 113.3, 10.2.

^1H spectrum

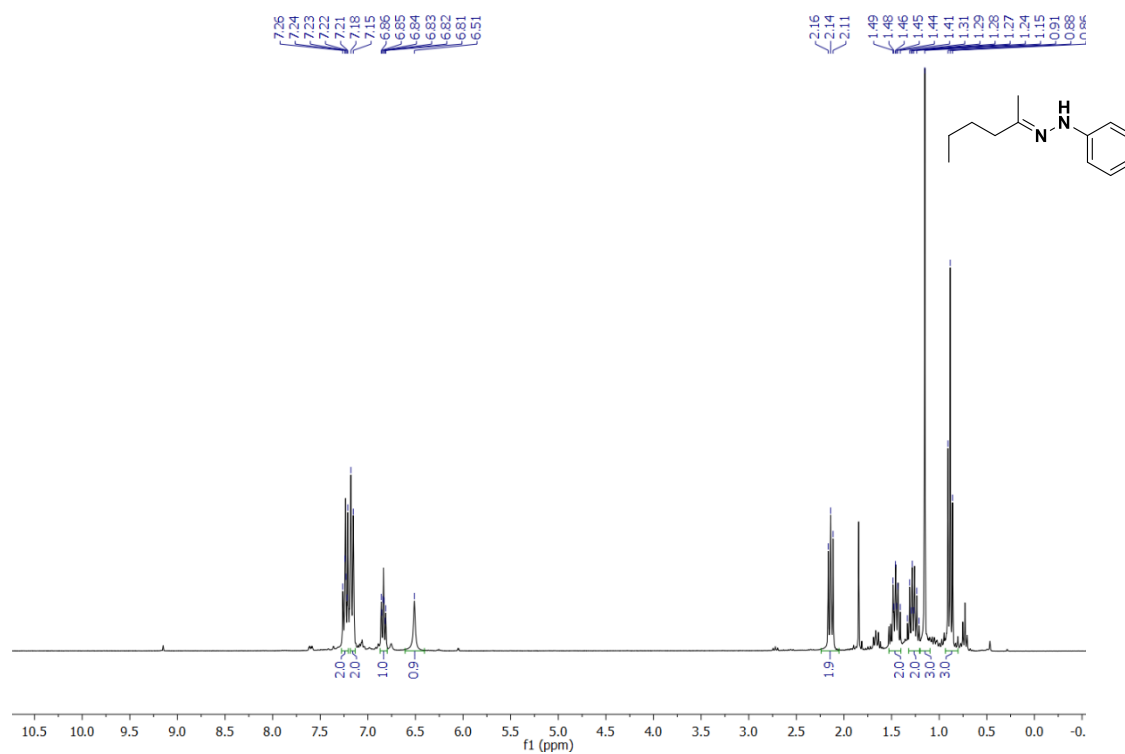


$^{13}\text{C}\{^1\text{H}\}$ spectrum

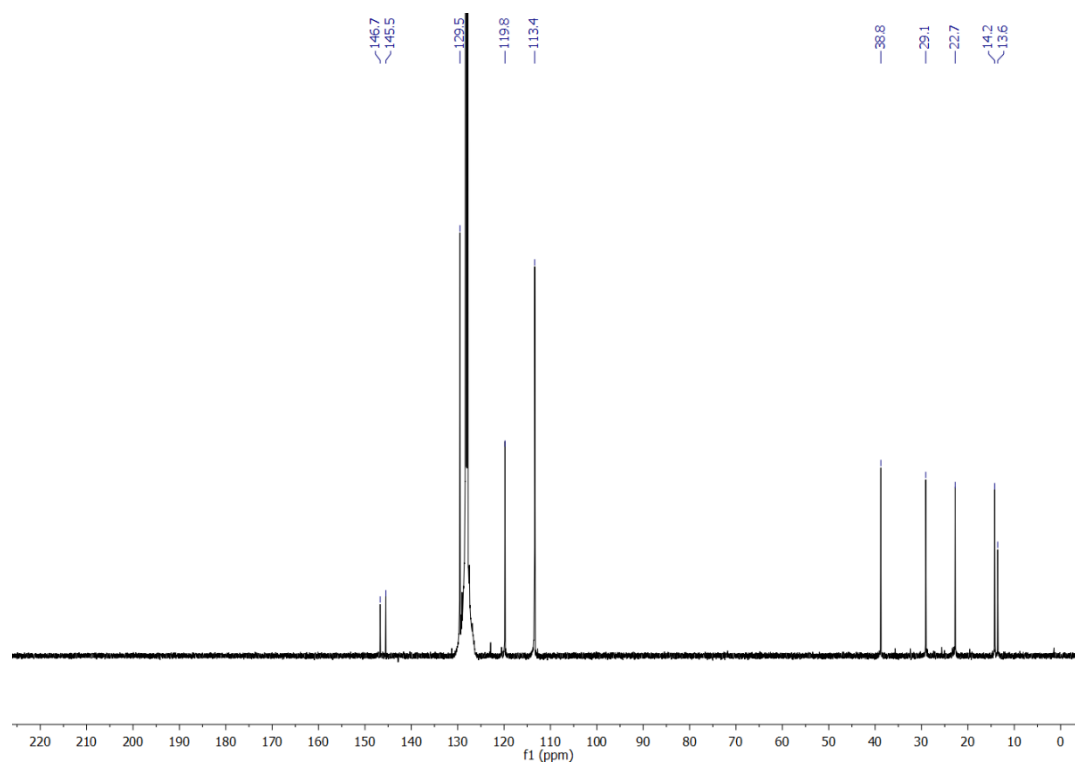


For this substrates, 1.1 equivalents of hydrazine were used (0.393 mmol). Compound **4.9g** was isolated in 91% yield (0.062 g) and agrees with a previous literature report.¹⁷⁷ ^1H NMR (300 MHz, C_6D_6) δ 7.27 – 7.20 (m, 2H), 7.17 (d, $J = 7.6$ Hz, 2H), 6.84 (tt, $J = 7.1, 1.4$ Hz, 1H), 6.51 (br, 1H), 2.18 – 2.10 (m, 2H), 1.51 – 1.39 (m, 2H), 1.35 – 1.19 (m, 2H), 1.15 (s, 3H), 0.88 (t, $J = 7.3$ Hz, 3H). $^{13}\text{C}\{^1\text{H}\}$ NMR (126 MHz, C_6D_6) δ 146.7, 145.5, 129.5, 119.8, 113.4, 38.8, 29.1, 22.7, 14.2, 13.6.

^1H spectrum

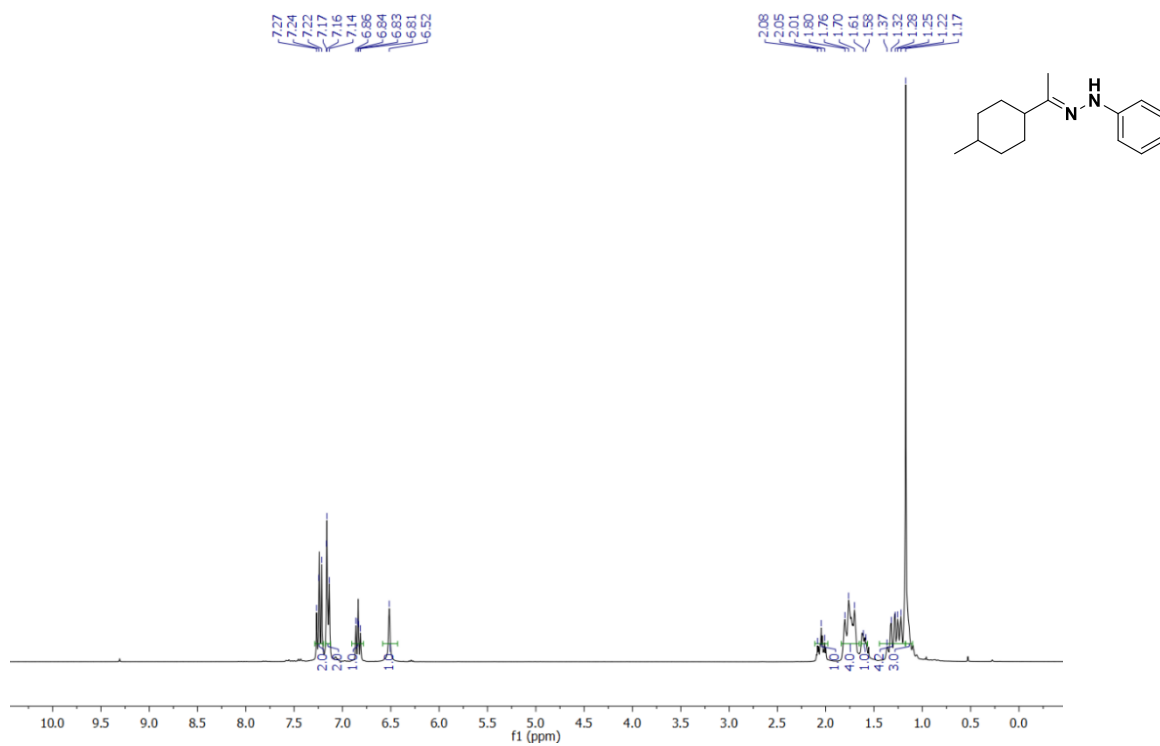


$^{13}\text{C}\{^1\text{H}\}$ spectrum

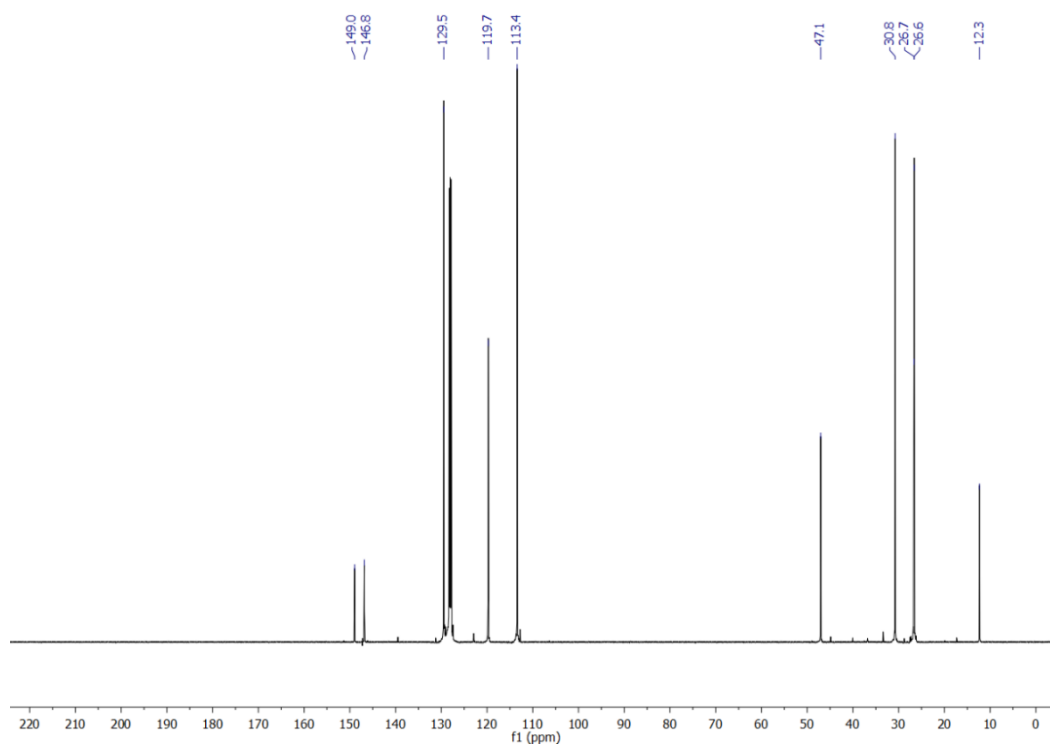


Compound **4.9h** was isolated in 99% yield (0.081 g). ^1H NMR (300 MHz, C_6D_6) δ 7.24 (dd, $J = 8.6, 7.1$ Hz, 2H), 7.17 – 7.13 (m, 2H), 6.87 – 6.80 (m, 1H), 6.52 (s, 1H), 2.04 (ddt, $J = 11.2, 6.8, 3.3$ Hz, 1H), 1.84 – 1.67 (m, 4H), 1.60 (ddt, $J = 8.1, 3.6, 1.5$ Hz, 1H), 1.40 – 1.22 (m, 4H), 1.17 (s, 3H). $^{13}\text{C}\{^1\text{H}\}$ NMR (126 MHz, C_6D_6) δ 148.95, 146.8, 129.5, 119.7, 113.4, 47.1, 30.8, 26.65, 26.6, 12.3.

^1H spectrum

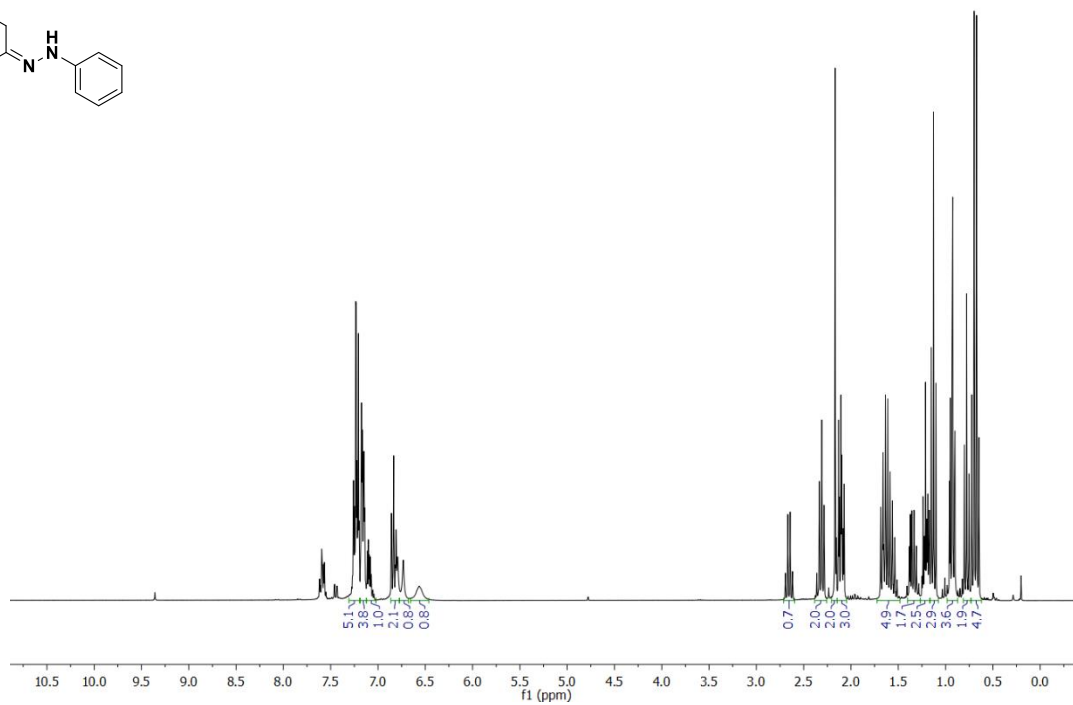
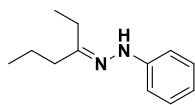


$^{13}\text{C}\{^1\text{H}\}$ spectrum

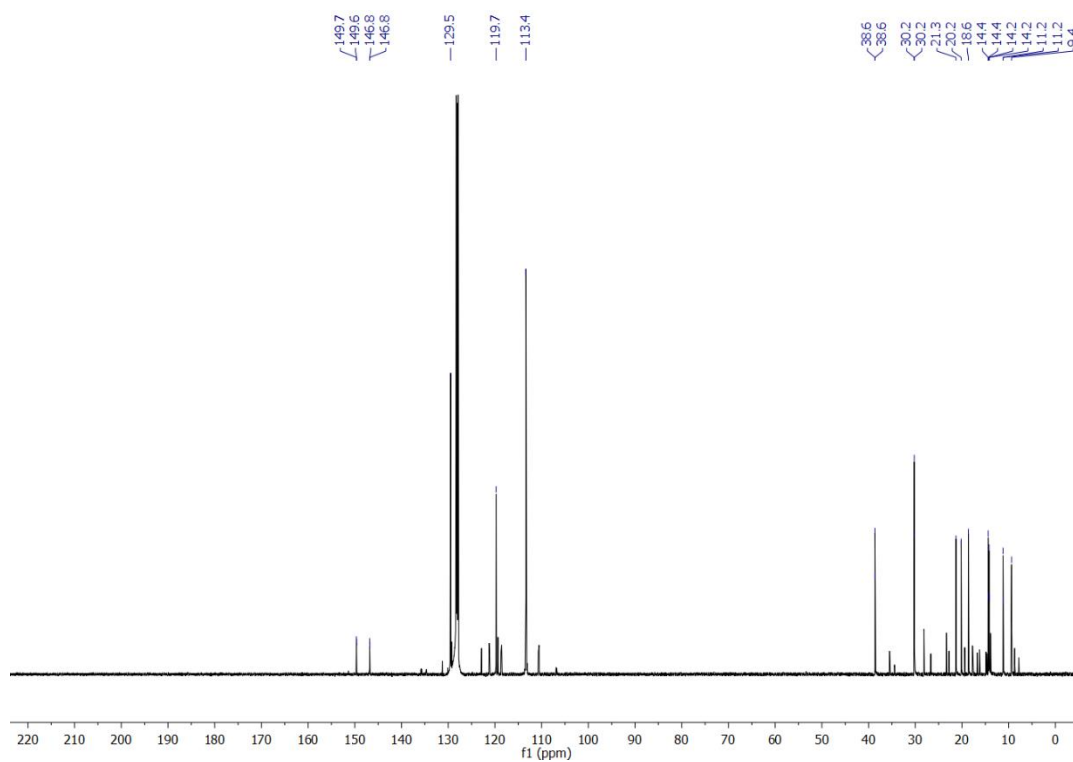


Compound **4.9i** was isolated in 99% yield (0.069 g). ^1H NMR (300 MHz, C_6D_6) δ 7.32 – 7.19 (m, 7H), 7.19 – 7.13 (m, 5H), 7.13 – 7.04 (m, 1H), 6.89 – 6.77 (m, 1H), 2.66 (q, $J = 7.5$ Hz, 2H), 2.38 – 2.25 (m, 2H), 2.17 (s, 2H), 2.14 – 2.05 (m, 3H), 1.71 – 1.49 (m, 5H), 1.41 – 1.27 (m, 2H), 1.26 – 1.16 (m, 3H), 1.13 (t, $J = 7.4$ Hz, 4H), 0.93 (td, $J = 7.4, 2.2$ Hz, 4H), 0.78 (t, $J = 7.3$ Hz, 2H), 0.69 (q, $J = 7.5$ Hz, 5H). $^{13}\text{C}\{^1\text{H}\}$ NMR (126 MHz, C_6D_6) δ 149.7, 149.6, 146.8, 146.8, 129.5, 119.7, 113.4, 38.6, 38.6, 30.2, 30.21, 21.3, 20.2, 18.6, 14.4, 14.4, 14.2, 14.9, 11.2, 11.2, 9.4.

^1H spectrum

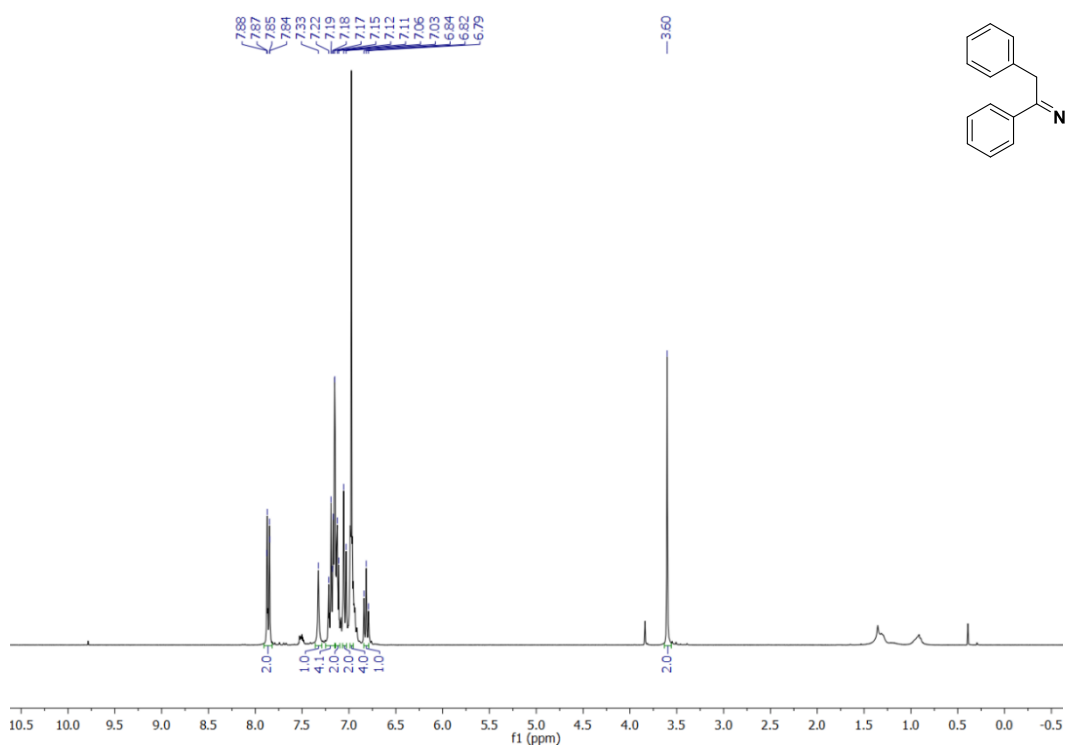


$^{13}\text{C}\{^1\text{H}\}$ spectrum

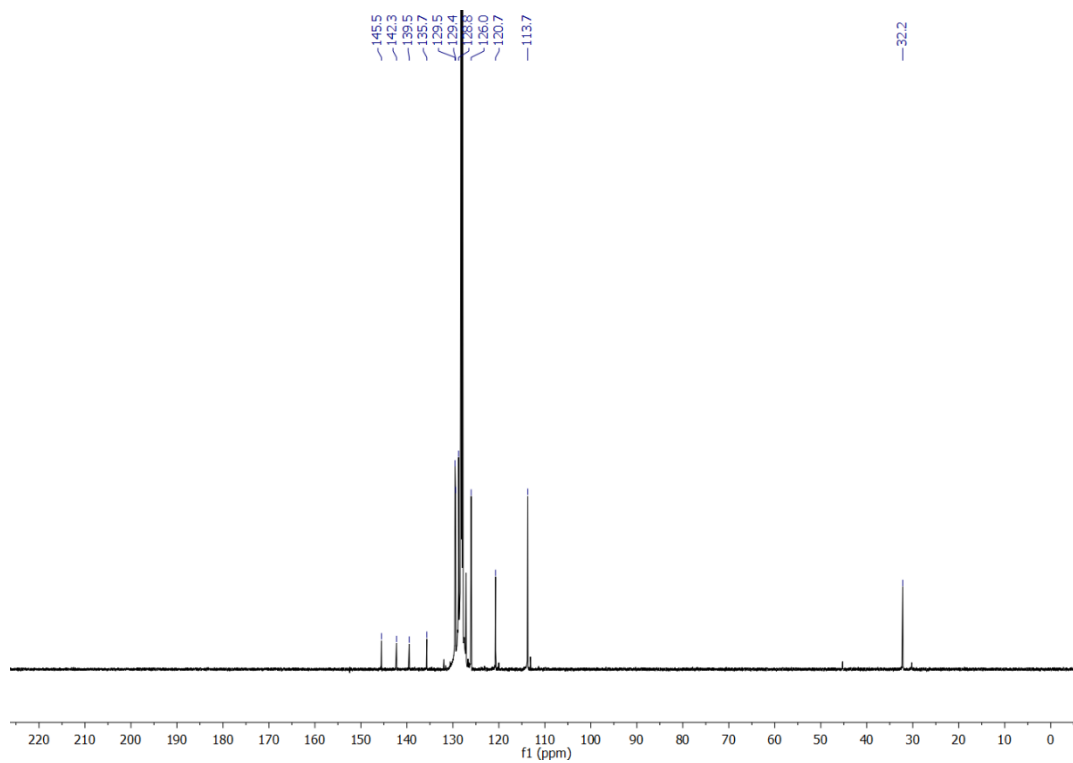


Compound **4.9j** was isolated in 86% yield (0.087 g). ^1H NMR (300 MHz, C_6D_6) δ 7.90 – 7.81 (m, 2H), 7.33 (br, 1H), 7.23 – 7.16 (m, 4H), 7.14 – 7.10 (m, 2H), 7.07 – 7.01 (m, 4H), 6.81 (ddt, $J = 7.2, 5.5, 1.3$ Hz, 1H), 3.60 (s, 3H). $^{13}\text{C}\{^1\text{H}\}$ NMR (126 MHz, C_6D_6) δ 145.5, 142.3, 139.5, 135.7, 129.5, 129.4, 128.8, 126.0, 120.7, 113.7, 32.2.

^1H spectrum

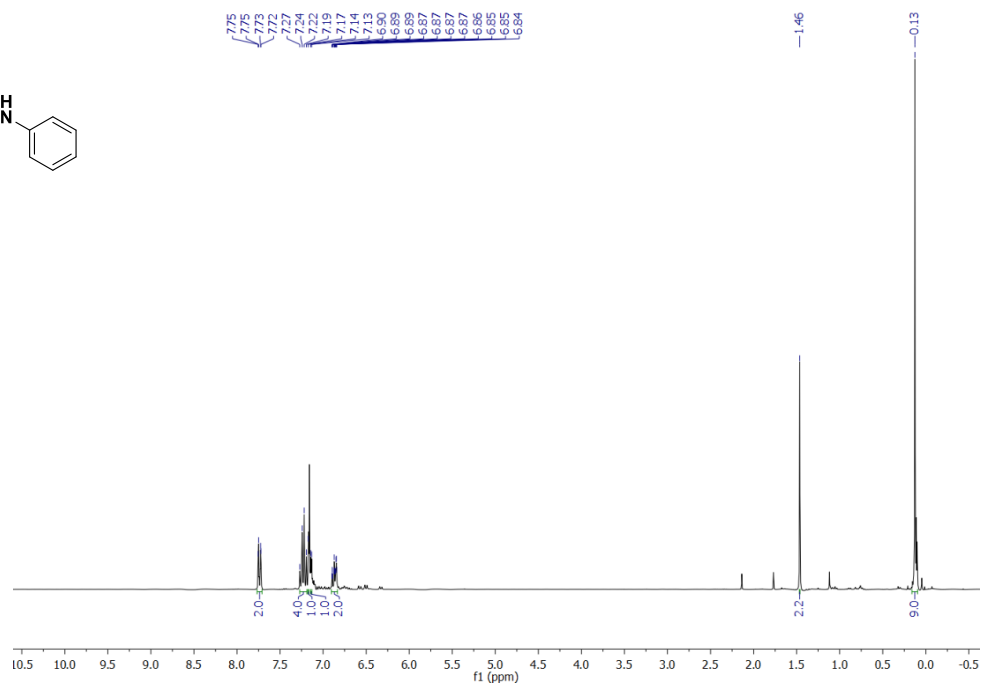
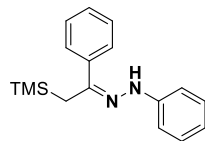


$^{13}\text{C}\{^1\text{H}\}$ spectrum

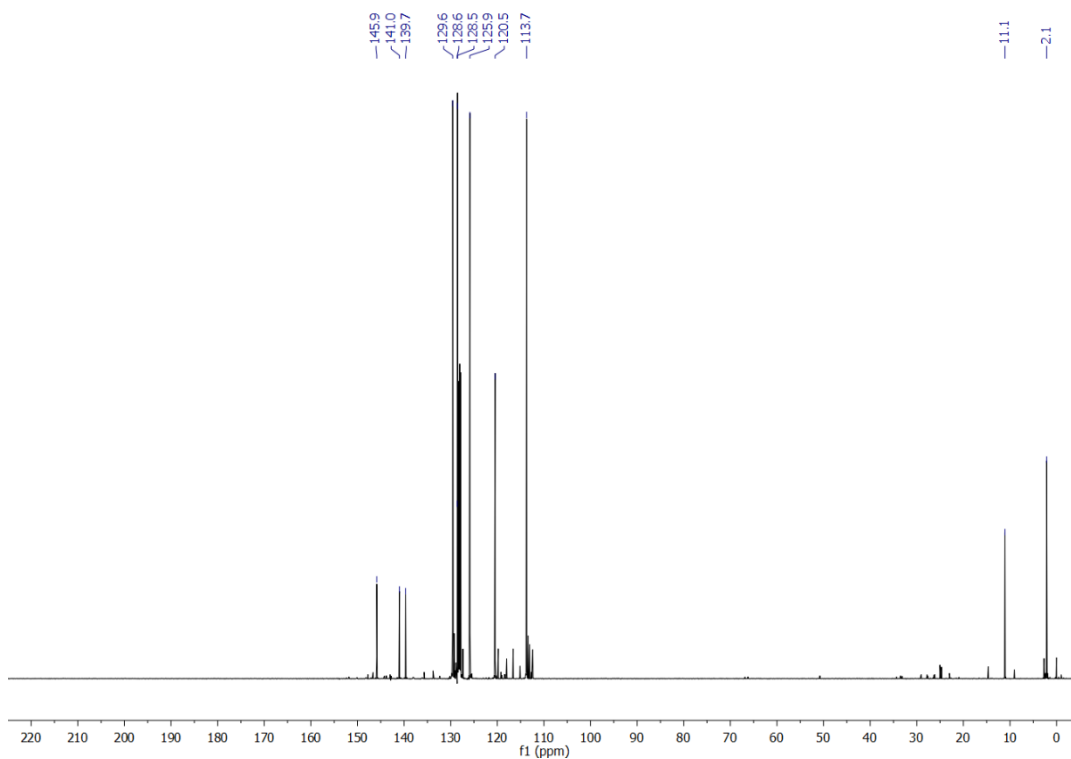


Compound **4.9k** was isolated in 76% yield (0.077 g). ^1H NMR (300 MHz, C_6D_6) δ 7.76 – 7.72 (m, 2H), 7.28 – 7.18 (m, 4H), 7.17 (t, $J = 1.1$ Hz, 1H), 7.15 – 7.13 (m, 1H), 6.91 – 6.82 (m, 2H), 1.46 (s, 2H)

^1H spectrum

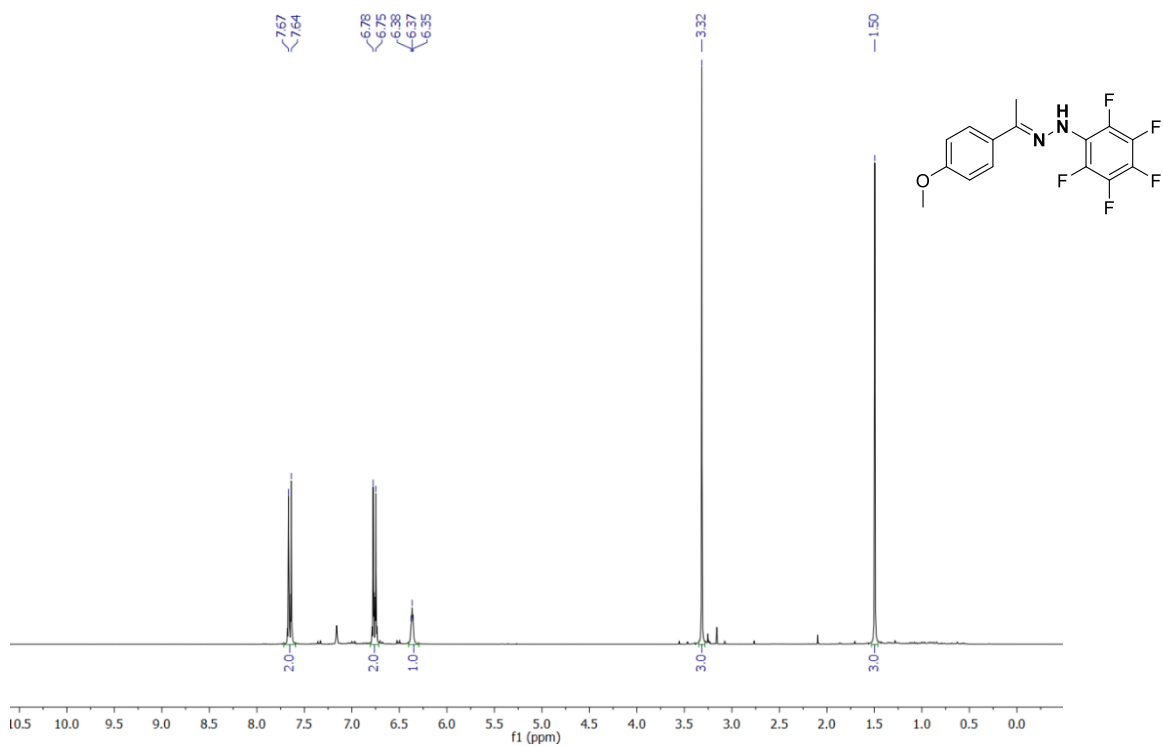


$^{13}\text{C}\{^1\text{H}\}$ spectrum

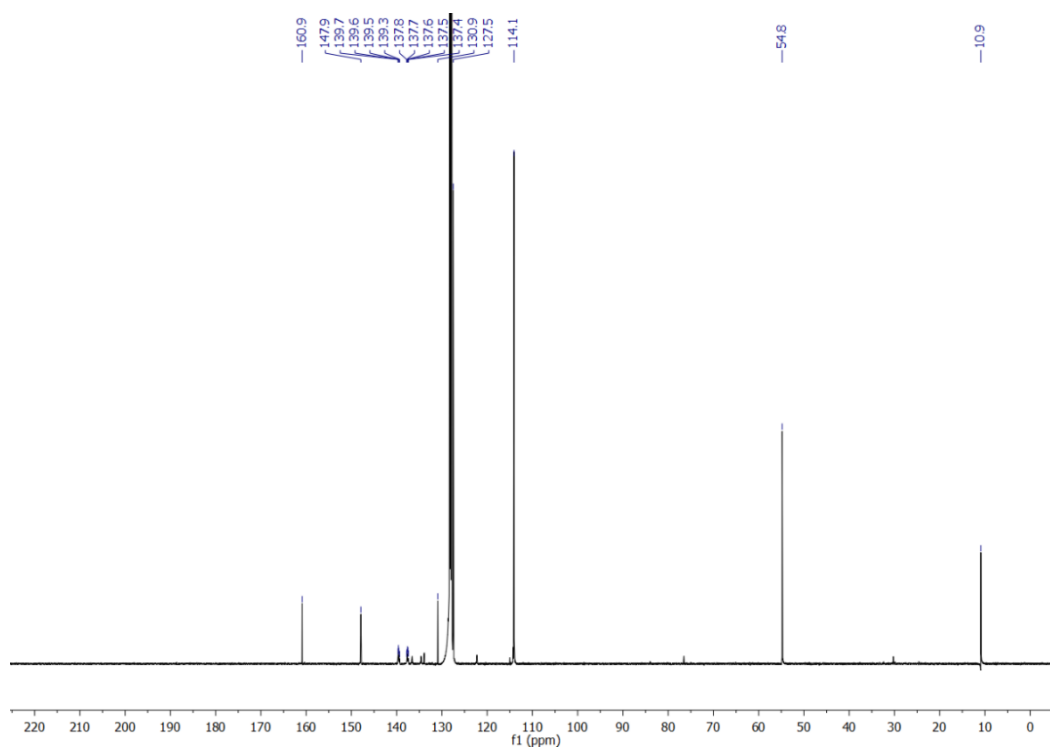


Compound **4.9l** was isolated in 99% yield (0.117 g). ^1H NMR (300 MHz, C_6D_6) δ 7.65 (d, $J = 8.9$ Hz, 2H), 6.76 (d, $J = 9.0$ Hz, 2H), 6.37 (t, $J = 3.4$ Hz, 1H), 3.32 (s, 3H), 1.50 (s, 3H). $^{13}\text{C}\{^1\text{H}\}$ NMR (126 MHz, C_6D_6) δ 160.9, 147.9, 139.5 (ddd, $J = 28.7, 12.3, 7.7$ Hz), 137.9–137.19 (m), 130.9, 127.5, 114.1, 54.8, 10.9. ^{19}F NMR (282 MHz, C_6D_6) δ -157.70 (dd, $J = 22.9, 5.0$ Hz), -164.88 – -165.31 (m), -168.85 – -169.31 (m). Crystals suitable for X-ray diffraction study were obtained from vapor diffusion from DCM solution with pentane.

^1H spectrum

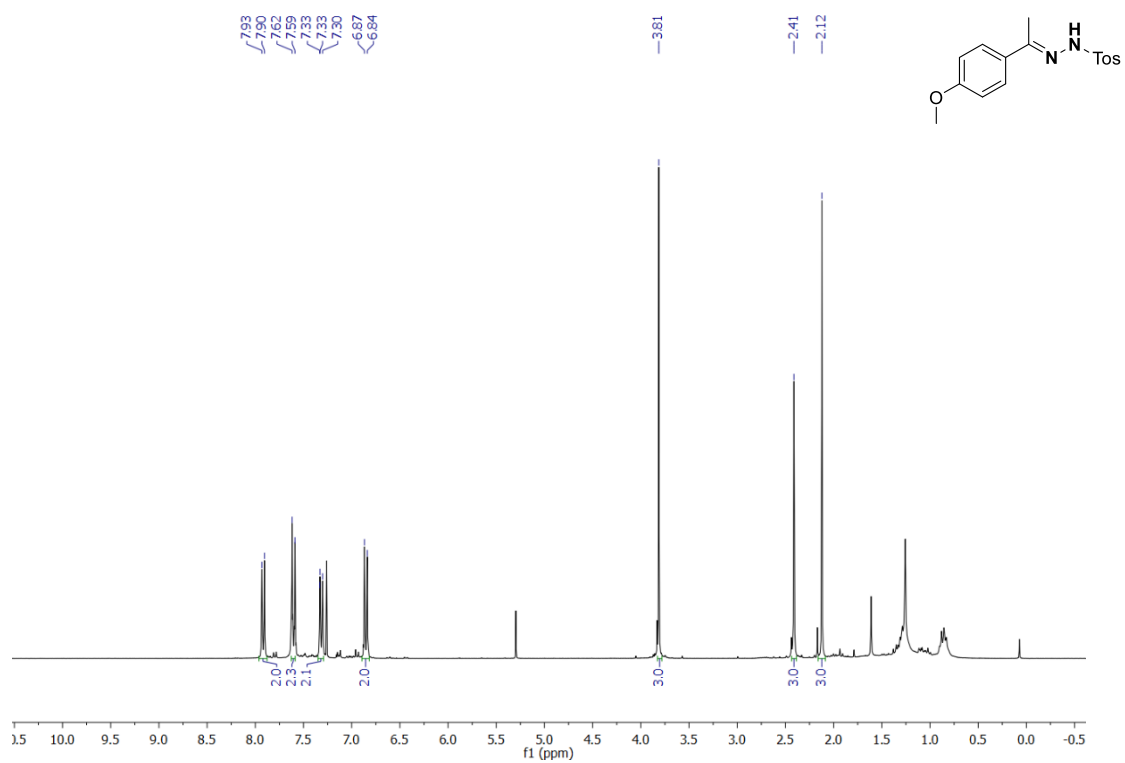


$^{13}\text{C}\{^1\text{H}\}$ spectrum

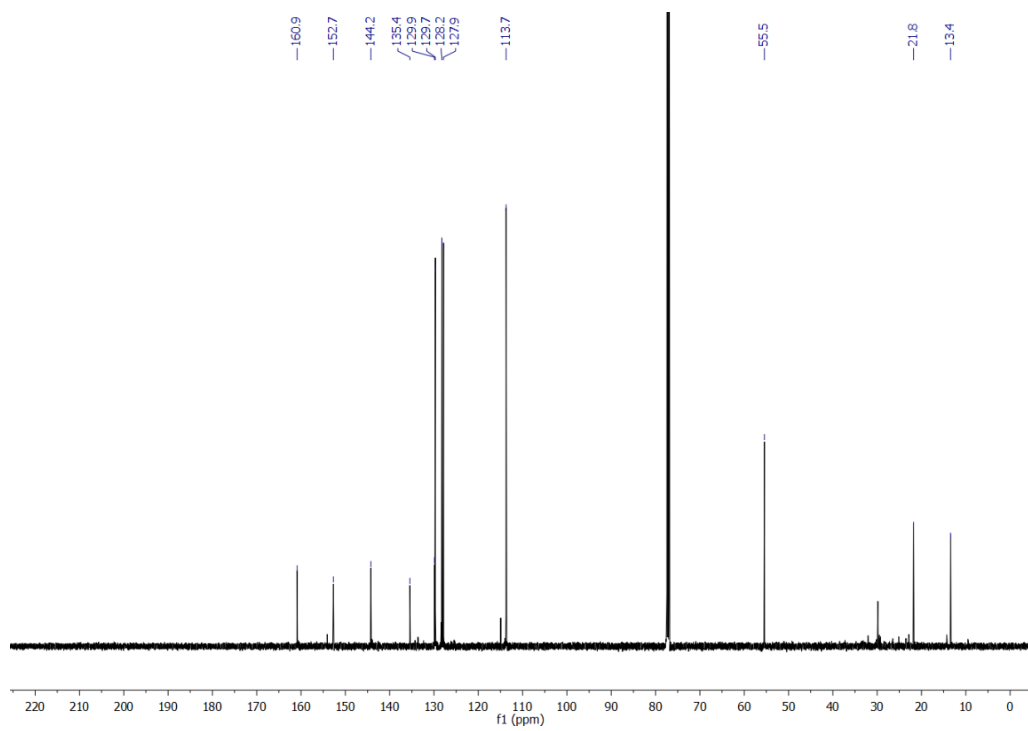


This reaction Compound **4.9m** was isolated in 56% yield (0.064 g) and agrees with a previous literature report.¹⁷⁸ ^1H NMR (300 MHz, CDCl_3) δ 7.92 (d, $J = 8.3$ Hz, 2H), 7.60 (d, $J = 8.9$ Hz, 2H), 7.34 – 7.29 (m, 2H), 6.85 (d, $J = 8.9$ Hz, 2H), 3.81 (s, 3H), 2.41 (s, 3H), 2.12 (s, 3H). $^{13}\text{C}\{^1\text{H}\}$ NMR (126 MHz, CDCl_3) δ 160.9, 152.7, 144.2, 135.4, 129.9, 129.7, 128.25, 127.9, 113.7, 55.45, 21.78, 13.4.

^1H spectrum

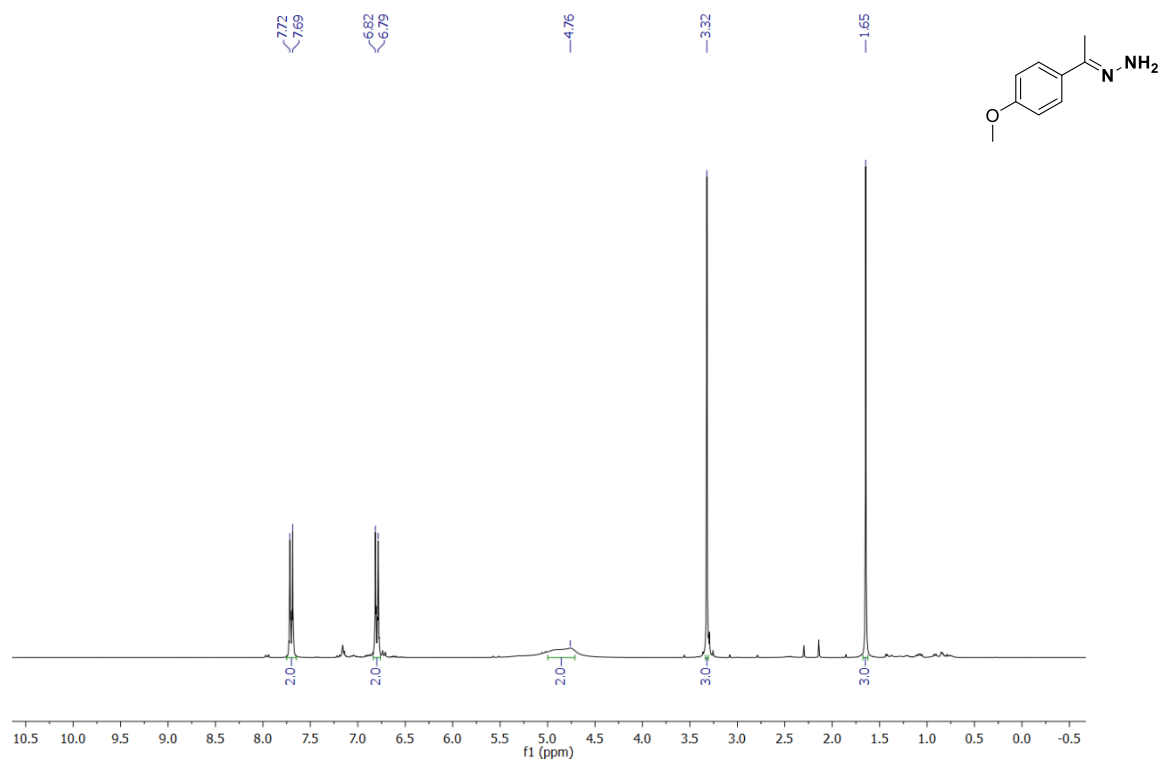


$^{13}\text{C}\{^1\text{H}\}$ spectrum

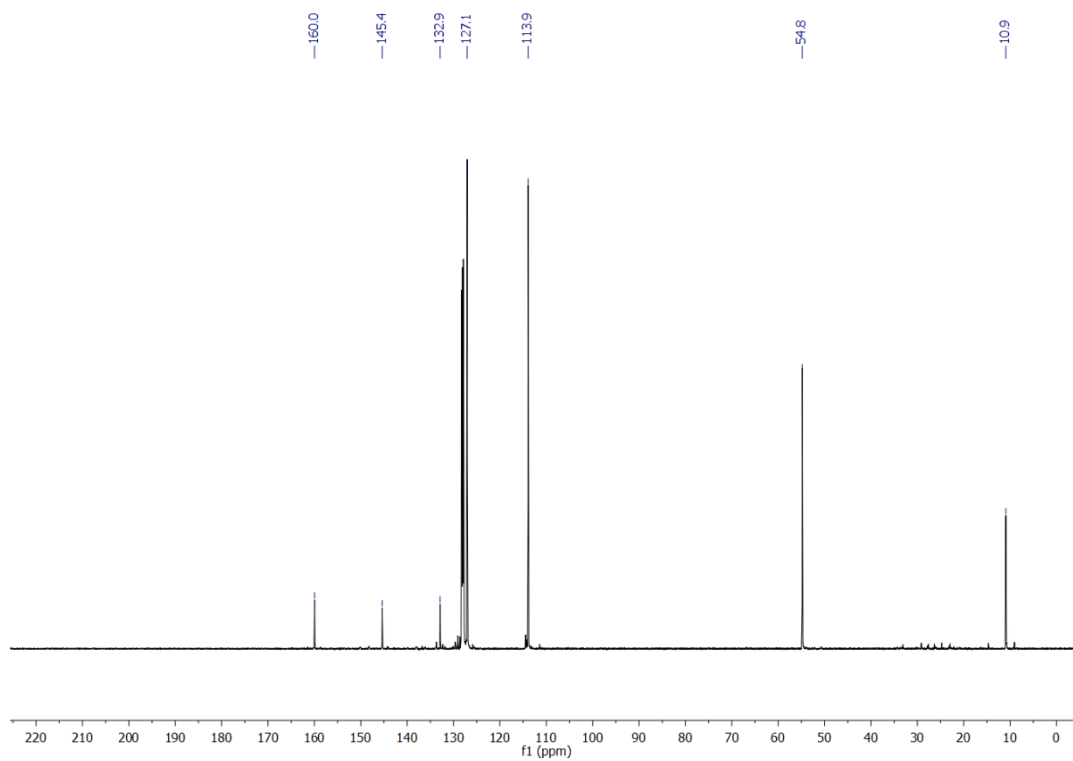


Hydrous hydrazine ($n\text{H}_2\text{O}\cdot\text{NH}_2\text{-NH}_2$, 50-60%) was used for this reaction. Compound **4.9n** was isolated in 73% yield (0.043 g) and agrees with a previous literature report.¹⁷⁹ ^1H NMR (300 MHz, C_6D_6) δ 7.70 (d, $J = 8.9$ Hz, 2H), 6.80 (d, $J = 8.9$ Hz, 2H), 4.76 (br, 2H), 3.32 (s, 3H), 1.65 (s, 3H). $^{13}\text{C}\{^1\text{H}\}$ NMR (126 MHz, C_6D_6) δ 160.0, 145.4, 132.9, 127.1, 113.9, 54.8, 10.9.

^1H spectrum

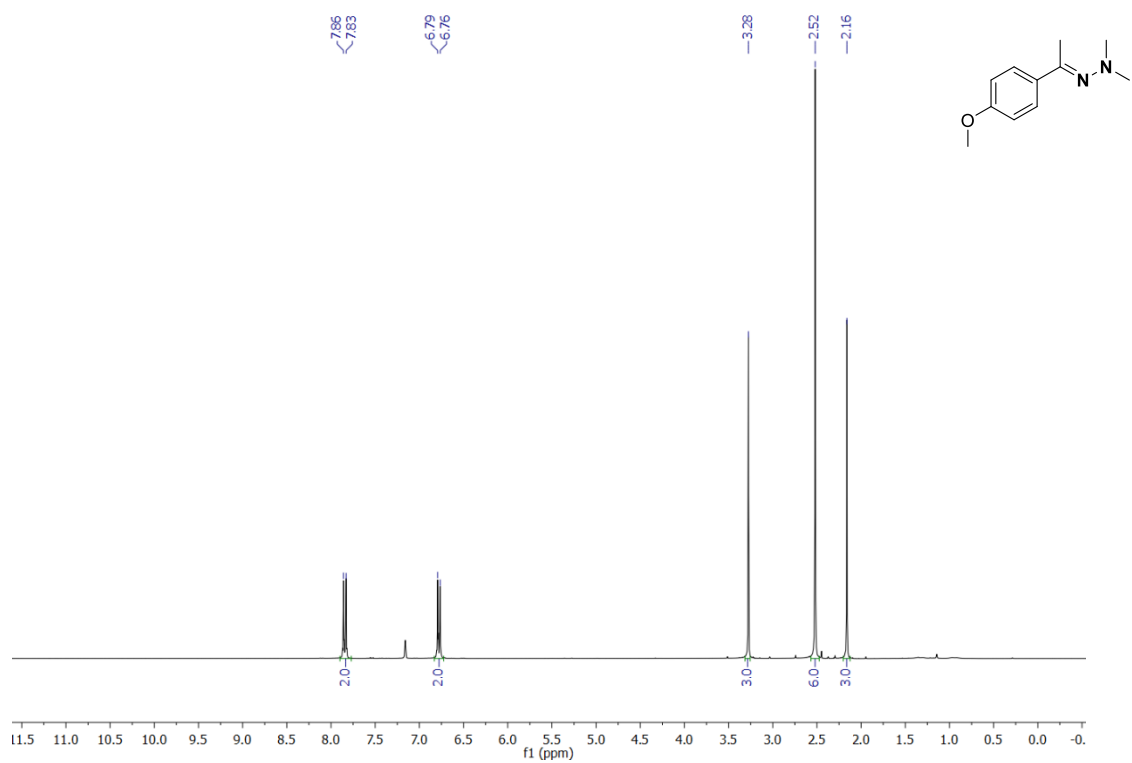


$^{13}\text{C}\{^1\text{H}\}$ spectrum

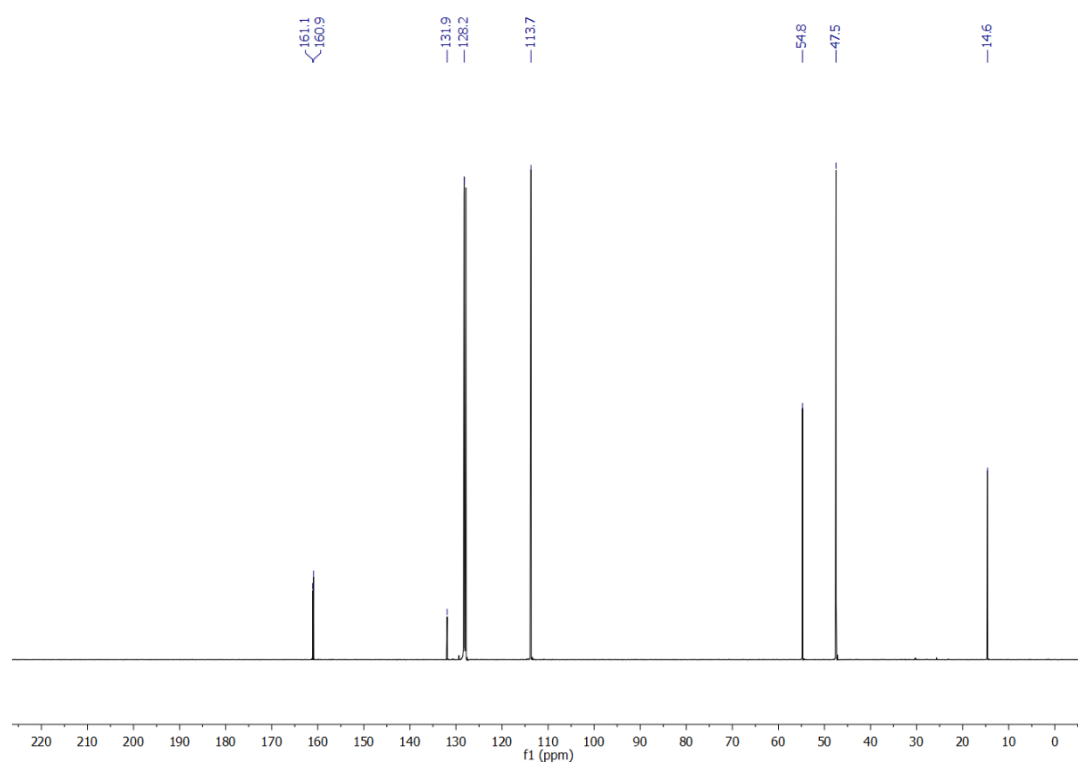


Compound **4.9o** was isolated in 81% yield (0.056 g) and agrees with a previous literature report.¹⁸⁰ ^1H NMR (300 MHz, C_6D_6) δ 7.84 (d, $J = 8.9$ Hz, 2H), 6.78 (d, $J = 8.9$ Hz, 2H), 3.28 (s, 3H), 2.52 (s, 6H), 2.16 (s, 3H). $^{13}\text{C}\{^1\text{H}\}$ NMR (126 MHz, C_6D_6) δ 161.1, 160.9, 131.9, 128.2, 113.7, 54.8, 47.5, 14.6.

^1H spectrum

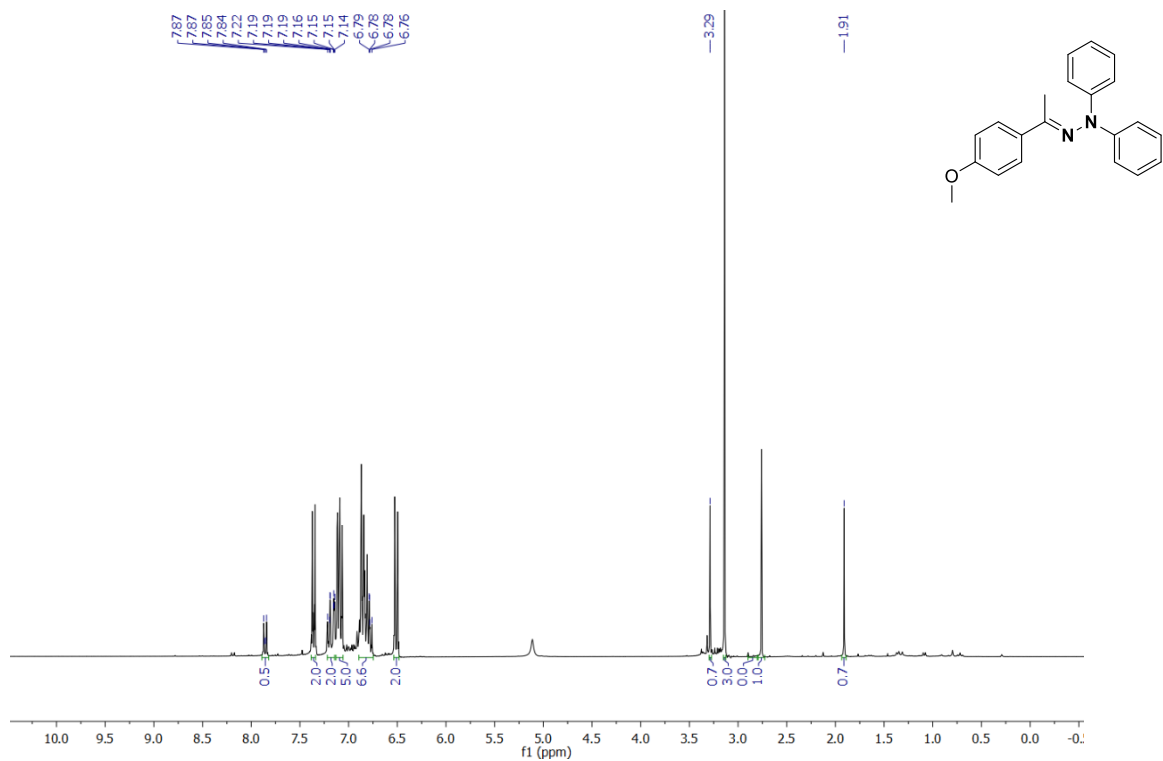


$^{13}\text{C}\{^1\text{H}\}$ spectrum

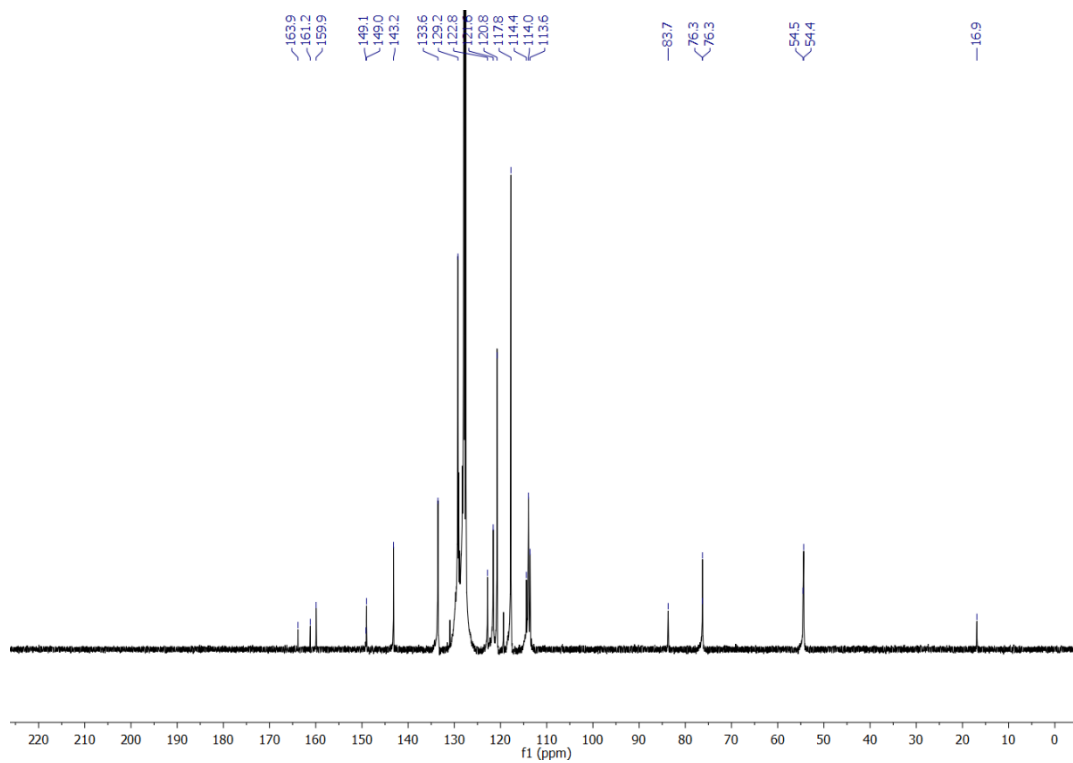


Despite several attempts **4.9k** was found to be too sensitive to purify by standard chromatographic methods even under anhydrous conditions. Consequently, the yield was determined by NMR (19%) as presented in the NMR spectrum of the crude reaction mixture.

¹H spectrum



$^{13}\text{C}\{^1\text{H}\}$ spectrum



4.12. Reaction optimization using ^1H NMR spectroscopic studies to determine kinetics (Figure 4.4 and 4.8).

All the kinetic measurements were performed in an NMR tube at room temperature on a Bruker 300 MHz NMR machine using the multi_zgvd command. In a typical experiment, the NMR tube was charged with the Au catalyst and $\text{KB}(\text{C}_6\text{F}_5)_4$ (1:1 ratio), 4-ethynylanisole (0.047 g, 0.356 mmol, 1.0 eq.) and the corresponding amount of deuterated solvent. The tube was locked and shimmed (T0) before starting the kinetic measurement. Following the addition of toluidine (0.356 mmol, 1.0 eq. - Figure 4.4) or phenylhydrazine (0.356 mmol, 1.0 eq. - Figure 4.8), the reaction was monitored as a function of the time at a constant temperature of 20 °C. Conversions were quantified by tracking the change in characteristic signals for the starting material and the product (imine). In all cases, and as highlighted below, the kinetic measurements were repeated 3-4 times to confirm the reproducibility of our results.

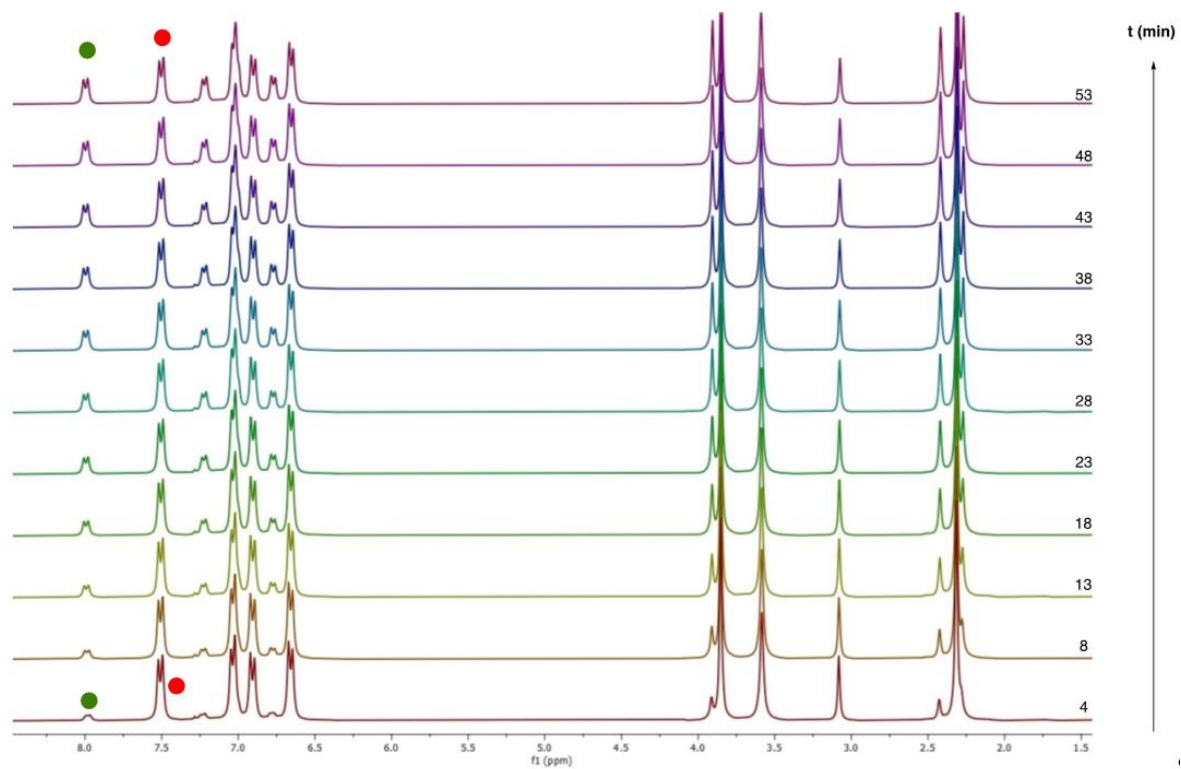
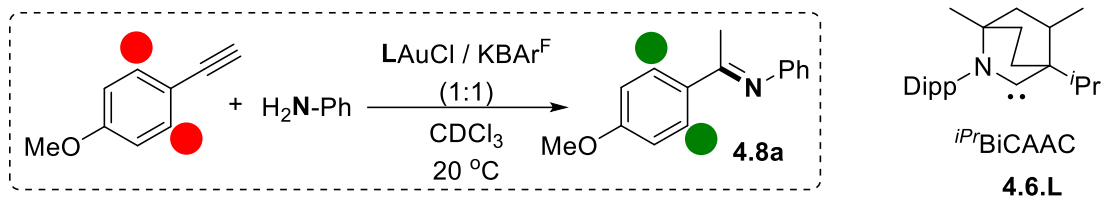


Figure 4.19. Figure illustrating the kinetics of the hydroamination reaction by ^1H NMR (CDCl_3)

References

- ¹ Duan, L.; Bozoglian, F.; Mandal, S.; Stewart, B.; Privalov, T.; Llobet, A.; Sun, L. A Molecular Ruthenium Catalyst with Water-Oxidation Activity Comparable to That of Photosystem II. *Nat. Chem.* **2012**, *4*, 418.
- ² Matheu, R.; Ertem, M. Z.; Benet-Buchholz, J.; Coronado, E.; Batista, V. S.; Sala, X.; Llobet, A. Intramolecular Proton Transfer Boosts Water Oxidation Catalyzed by a Ru Complex. *J. Am. Chem. Soc.* **2015**, *137*, 10786.
- ³ Wu, X.; Li, F.; Zhang, B.; Sun, L. Molecular Complexes in Water Oxidation: Pre-Catalysts or Real Catalysts. *Journal of Photochemistry and Photobiology C: Photochemistry Reviews* **2015**, *25*, 71.
- ⁴ Zhang, B.; Li, F.; Zhang, R.; Ma, C.; Chen, L.; Sun, L. Characterization of a Trinuclear Ruthenium Species in Catalytic Water Oxidation by Ru(Bda)(Pic)₂ in Neutral Media. *Chem. Commun.* **2016**, *52*, 8619.
- ⁵ Yazdani, S.; Silva, B. E.; Cao, T. C.; Rheingold, A. L.; Grotjahn, D. B. X-Ray Crystallography and Electrochemistry Reveal Electronic and Steric Effects of Phosphine and Phosphite Ligands in Complexes Ru^{II}(κ⁴-bda)(PR₃)₂ and Ru^{II}(κ³-bda)(PR₃)₃ (bda = 2,2'-Bipyridine-6,6'-Dicarboxylato). *Polyhedron* **2019**, *161*, 63.
- ⁶ Yazdani, S.; Junor, G. P.; Peltier, J. L.; Jazzar, R.; Grotjahn, D. B.; Bertrand, G. Influence of carbene and phosphine ligands on the catalytic activity of gold complexes in the hydroamination and hydrohydrazination of alkynes. *ACS Catalysis*, **2020**, *10*, 5190.
- ⁷ Broomell, S. B.; Winkles, J.-F.; Kane, P. B. The Perception of Daily Temperatures as Evidence of Global Warming. *Weather, Climate, and Society* **2017**, *9*, 563.
- ⁸ Shindell, D.; Smith, C. J. Climate and Air-Quality Benefits of a Realistic Phase-out of Fossil Fuels. *Nature* **2019**, *573*, 408.
- ⁹ Jin, M.; Dickinson, R. E. New Observational Evidence for Global Warming from Satellite. *Geophys. Res. Lett.* **2002**, *29*, 39-1-39.
- ¹⁰ Shindell, D.; Smith, C. J. Climate and Air-Quality Benefits of a Realistic Phase-out of Fossil Fuels. *Nature* **2019**, *573*, 408.
- ¹¹ Le Quéré, C.; Jackson, R. B.; Jones, M. W.; Smith, A. J. P.; Abernethy, S.; Andrew, R. M.; De-Gol, A. J.; Willis, D. R.; Shan, Y.; Canadell, J. G.; et al. Temporary Reduction in Daily Global CO₂ Emissions during the COVID-19 Forced Confinement. *Nat. Clim. Change* **2020**, *10*, 647.
- ¹² Gao, K.; Zhang, Y.; Häder, D. P. Individual and Interactive Effects of Ocean Acidification, Global Warming, and UV Radiation on Phytoplankton. *J. Appl. Phycol.* **2018**, *30*, 743.
- ¹³ Pelejero, C.; Calvo, E.; Hoegh-Guldberg, O. Paleo-Perspectives on Ocean Acidification. *Trends Ecol. Evol.* **2010**, *25*, 332.
- ¹⁴ Administration, U. S. E. I. International Energy Outlook 2019 with Projections to 2050. *Choice Reviews Online* **2019**, 85.

-
- ¹⁵ Yang, X.; Baik, M. H. The Mechanism of Water Oxidation Catalysis Promoted by [TpyRu^{IV}=O]₂L₃: A Computational Study. *J. Am. Chem. Soc.* **2008**, *130*, 16231.
- ¹⁶ BP Statistical Review of World Energy (2019) http://www.bp.com/content/dam/bp-country/de_de/PDFs/brochures/BP-statistical-review-of-world-energy-2019-full-report.pdf. 68th edition.
- ¹⁷ Rhodes, C. J. The Global Oil Supply – Prevailing Situation and Prognosis. *Sci. Prog.* **2017**, *100*, 231.
- ¹⁸ https://www.opec.org/opec_web/en/data_graphs/330.htm Macneill, M.; Quinn, M.; Bayer, C. OPEC Annual Statistical Bulletin. **2019**, *54*, 128pp.
- ¹⁹ US EIA. EIA: International Energy Outlook 2019 Presentation. *Eia* **2019**, *18*, accessed June 2021.
- ²⁰ <https://www.eia.gov/todayinenergy/detail.php?id=45516#>
- ²¹ Kärkäs, M. D.; Verho, O.; Johnston, E. V.; Åkermark, B. Artificial Photosynthesis: Molecular Systems for Catalytic Water Oxidation. *Chem. Rev.* **2014**, *114*, 11863.
- ²² Blakemore, J. D.; Crabtree, R. H.; Brudvig, G. W. Molecular Catalysts for Water Oxidation. *Chem. Rev.* **2015**, *115*, 12974.
- ²³ Pavlishchuk, V. V.; Addison, A. W. *Inorg. Chim. Acta* **2000**, *298*, 97. (b) Bard, A. J.; Faulkner, L. R. *Electrochemical Methods: Fundamentals and Applications*, 2nd ed.; John Wiley & Sons Inc.: New York, 2001.
- ²⁴ Shaffer, D. W.; Xie, Y.; Concepcion, J. J. O-O Bond Formation in Ruthenium-Catalyzed Water Oxidation: Single-Site Nucleophilic Attack: Vs. O-O Radical Coupling. *Chem. Soc. Rev.* **2017**, *46*, 6170.
- ²⁵ Roger, I.; Shipman, M. A.; Symes, M. D. Earth-Abundant Catalysts for Electrochemical and Photoelectrochemical Water Splitting. *Nat. Rev. Chem.* **2017**, *1*.
- ²⁶ Rand, D. A. J.; Dell, R. M.; *Hydrogen Energy-Challenges and Prospects*, RSC Publishing, Cambridge, UK, **2008**.
- ²⁷ Fillol, J. L.; Codolà, Z.; Garcia-Bosch, I.; Gómez, L.; Pla, J. J.; Costas, M. Efficient water oxidation catalysts based on readily available iron coordination complexes. *Nat. Chem.* **2011**, *3*, 807.
- ²⁸ Garrido-Barros, P.; Funes-Ardoiz, I.; Drouet, S.; Benet-Buchholz, J.; Maseras, F.; Llobet, A. Redox Non-innocent Ligand Controls Water Oxidation Overpotential in a New Family of Mononuclear Cu-Based Efficient Catalysts. *J. Am. Chem. Soc.* **2015**, *137*, 6758.
- ²⁹ Wang, L.; Duan, L.; Ambre, R. B.; Daniel, Q.; Chen, H.; Sun, J.; Das, B.; Thapper, A.; Uhlig, J.; Dinér, P.; et al. A Nickel (II) PY5 Complex as an Electrocatalyst for Water Oxidation. *J. Cat.* **2016**, *335*, 72.
- ³⁰ Asraf, M. A.; Younus, H. A.; Yusubov, M.; Verpoort, F. Earth-Abundant Metal Complexes as Catalysts for Water Oxidation; Is It Homogeneous or Heterogeneous? *Catal. Sci. Tech.* **2015**, *5*, 4901.
- ³¹ Wasylenko, D. J.; Ganesamoorthy, C.; Borau-Garcia, J.; Berlinguette, C. P. Electrochemical Evidence for Catalytic Water Oxidation Mediated by a High-Valent Cobalt Complex. *Chem. Comm.* **2011**, *47*, 4249.
- ³² Nieto, J.; Jiménez, M. V.; Álvarez, P.; Pérez-Mas, A. M.; González, Z.; Pereira, R.; Sánchez-Page, B.; Pérez-Torrente, J. J.; Blasco, J.; Subias, G.; et al. Enhanced Chemical and Electrochemical Water Oxidation

Catalytic Activity by Hybrid Carbon Nanotube-Based Iridium Catalysts Having Sulfonate-Functionalized NHC Ligands. *ACS Appl. Energy Mater.* **2019**, *2*, 3283.

³³ A. Llobet, *Molecular Water Oxidation Catalysis: A Key Topic for New Sustainable Energy Conversion Schemes*, Wiley-Interscience, New York, 2014.

³⁴ Corbucci, I.; Petronilho, A.; Müller-Bunz, H.; Rocchigiani, L.; Albrecht, M.; Macchioni, A. Substantial Improvement of Pyridine-Carbene Iridium Water Oxidation Catalysts by a Simple Methyl-to-Octyl Substitution. *ACS Catal.* **2015**, *5*, 2714.

³⁵ Zhang, B.; Sun, L. Ru-Bda: Unique Molecular Water-Oxidation Catalysts with Distortion Induced Open Site and Negatively Charged Ligands. *J. Am. Chem. Soc.* **2019**, *141*, 5565.

³⁶ Gersten, S. W.; Samuels, G. J.; Meyer, T. J. Catalytic Oxidation of Water by an Oxo-Bridged Ruthenium Dimer. *J. Am. Chem. Soc.* **1982**, *104*, 4029.

³⁷ Song, N.; Concepcion, J. J.; Binstead, R. A.; Rudd, J. A.; Vannucci, A. K.; Dares, C. J.; Coggins, M. K.; Meyer, T. J. Base-Enhanced Catalytic Water Oxidation by a Carboxylate-Bipyridine Ru(II) Complex. *Proc. Nat. Acad. Sci.* **2015**, *112*, 4935.

³⁸ Yamamoto, M.; Wang, L.; Li, F.; Fukushima, T.; Tanaka, K.; Sun, L.; Imahori, H. Visible Light-Driven Water Oxidation Using a Covalently-Linked Molecular Catalyst-Sensitizer Dyad Assembled on a TiO₂ Electrode. *Chem. Sci.* **2016**, *7*, 1430.

³⁹ Concepcion, J. J.; Tsai, M. K.; Muckerman, J. T.; Meyer, T. J. Mechanism of Water Oxidation by Single-Site Ruthenium Complex Catalysts. *J. Am. Chem. Soc.* **2010**, *132*, 1545.

⁴⁰ Oxidation López, I.; Ertem, M.Z.; Maji, S.; Benet-Buchholz, J.; Keidel, A.; Kuhlman, U.; Hildebrandt, P.; Cramer, C.J.; Batista, V.S.; Llobet, A. A Self-Improved Water-Oxidation Catalyst: Is One Site Really Enough? *Angew. Chem. Int. Ed.* **2014**, *53*, 205.

⁴¹ Sheehan, S. W.; Thomsen, J. M.; Hintermair, U.; Crabtree, R. H.; Brudvig, G. W.; Schmittenmaer, C. A. A Molecular Catalyst for Water Oxidation that Binds to Metal Oxide Surfaces and Exhibits High Activity without Ligand Degradation. *Nat. Commun.* **2015**, *6*, 6469.

⁴² Thomsen, J. M.; Sheehan, S. W.; Hashmi, S. M.; Campos, J.; Hintermair, U.; Crabtree, R. H.; Brudvig, G. W. Electrochemical Activation of Cp* Iridium Complexes for Electrode-Driven Water-Oxidation Catalysis. *J. Am. Chem. Soc.* **2014**, *136*, 13826.

⁴³ Kamdar, J. M.; Grotjahn, D. B. An Overview of Significant Achievements in Ruthenium-Based Molecular Water Oxidation Catalysis. *Molecules* **2019**, *24*, 13.

⁴⁴ Bozoglian, F.; Romain, S.; Ertem, M. Z.; Todorova, T. K.; Sens, C.; Mola, J.; Rodríguez, M.; Romero, I.; Benet-Buchholz, J.; Fontrodona, X.; et al. The Ru-Hbpp Water Oxidation Catalyst. *J. Am. Chem. Soc.* **2009**, *131*, 15176.

⁴⁵ Pramanik, N. C.; Bhattacharya, S. Chemical Oxidation of Water to Dioxygen. Homogeneous Catalysis by a Ruthenium Aquo-Complex. *Transit. Met. Chem.* **1997**, *22*, 524.

⁴⁶ Zong, R.; Thummel, R. P. A New Family of Ru Complexes for Water Oxidation. *J. Am. Chem. Soc.* **2005**, *127*, 12802.

-
- ⁴⁷ Duan, L.; Fischer, A.; Xu, Y.; Sun, L. Isolated Seven-Coordinate Ru(IV) Dimer Complex with [HOHOH]- Bridging Ligand as an Intermediate for Catalytic Water Oxidation. *J. Am. Chem. Soc.* **2009**, *131*, 10397.
- ⁴⁸ Koelewijn, J. M.; Lutz, M.; Dzik, W. I.; Detz, R. J.; Reek, J. N. H. Reaction Progress Kinetic Analysis as a Tool to Reveal Ligand Effects in Ce(IV)-Driven IrCp*-Catalyzed Water Oxidation. *ACS Catalysis* **2016**, *6*, 3418.
- ⁴⁹ Tolman, C. A. Steric Effects of Phosphorus Ligands in Organometallic Chemistry and Homogeneous Catalysis. *Chem. Rev.* **1977**, *77*, 313.
- ⁵⁰ Tolman, C. A. Electron Donor-Acceptor Properties of Phosphorus Ligands. Substituent Additivity. *J. Am. Chem. Soc.* **1970**, *92*, 2953.
- ⁵¹ Bravo, J.; Bolaño, S.; Gonsalvi, L.; Peruzzini, M. Coordination Chemistry of 1,3,5-Triaza-7-Phosphaadamantane (PTA) and Derivatives. Part II. The Quest for Tailored Ligands, Complexes and Related Applications. *Coordination Chemistry Rev.* **2010**, *254*, 555.
- ⁵² Phillips, A. D.; Gonsalvi, L.; Romerosa, A.; Vizza, F.; Peruzzini, M. Coordination Chemistry of 1,3,5-Triaza-7-Phosphaadamantane (PTA): Transition Metal Complexes and Related Catalytic, Medicinal and Photoluminescent Applications. *Coord. Chem. Reviews* **2004**, *248*, 955.
- ⁵³ DeLerno, J. R.; Trefonas, L. M.; Darensbourg, M. Y.; Majeste, R. J. Molecular Structure and Spectral Properties of Phosphotriazaadamantanemolybdenum Pentacarbonyl Complex. *Inorg. Chem.* **1976**, *15*, 816.
- ⁵⁴ Darensbourg, D. J.; Robertson, J. B.; Larkins, D. L.; Reibenspies, J. H. Water-Soluble Organometallic Compounds. 7. Further Studies of 1,3,5-Triaza-7-Phosphaadamantane Derivatives of Group 10 Metals, Including Metal Carbonyls and Hydrides. *Inorg. Chem.* **1999**, *38*, 2473.
- ⁵⁵ Huang, R.; Frost, B. J. Development of a Series of P(CH₂N=CHR)₃ and Trisubstituted 1,3,5-Triaza-7-Phosphaadamantane Ligands. *Inorg. Chem.* **2007**, *46*, 10962.
- ⁵⁶ Sears, J. M.; Lee, W. C.; Frost, B. J. Water Soluble Diphosphine Ligands Based on 1,3,5-Triaza-7-Phosphaadamantane (PTA-PR₂): Synthesis, Coordination Chemistry, and Ruthenium Catalyzed Nitrile Hydration. *Inorganica Chim. Acta* **2015**, *431*, 248.
- ⁵⁷ Battistin, F.; Balducci, G.; Iengo, E.; Demitri, N.; Alessio, E. Neutral 1,3,5-Triaza-7-Phosphaadamantane-Ruthenium(II) Complexes as Precursors for the Preparation of Highly Water-Soluble Derivatives. *Eur. J. Inorg. Chem.* **2016**, *2016*, 2850.
- ⁵⁸ Rossin, A.; Gonsalvi, L.; Phillips, A. D.; Maresca, O.; Lledós, A.; Peruzzini, M. Water-Assisted H - H Bond Splitting Mediated by [CpRu(PTA)₂Cl] (PTA=1,3,5-Triaza-7-Phosphaadamantane). A DFT Analysis. *Organometallics* **2007**, *26*, 3289.
- ⁵⁹ Wang, L.; Duan, L.; Stewart, B.; Pu, M.; Liu, J.; Privalov, T.; Sun, L. Toward Controlling Water Oxidation Catalysis: Tunable Activity of Ruthenium Complexes with Axial Imidazole/DMSO Ligands. *J. Am. Chem. Soc.* **2012**, *134*, 18868.
- ⁶⁰ Wu, X.; Li, F.; Zhang, B.; Sun, L. Molecular Complexes in Water Oxidation: Pre-Catalysts or Real Catalysts. *Journal of Photochemistry and Photobiology C: Photochemistry Reviews* **2015**, *25*, 71.

-
- 61 Duan, L.; Bozoglian, F.; Mandal, S.; Stewart, B.; Privalov, T.; Llobet, A.; Sun, L. A Molecular Ruthenium Catalyst with Water-Oxidation Activity Comparable to That of Photosystem II. *Nat. Chem.* **2012**, *4*, 418.
- 62 Mathew, J.; Thomas, T.; Suresh, C. H. Quantitative Assessment of the Stereoelectronic Profile of Phosphine Ligands. *Inorg. Chem.* **2007**, *46*, 10800.
- 63 Suresh, C. H.; Koga, N. Quantifying the Electronic Effect of Substituted Phosphine Ligands via Molecular Electrostatic Potential. *Inorg. Chem.* **2002**, *41*, 1573.
- 64 Kühn, O. Predicting the net donating ability of phosphines – do we need sophisticated theoretical methods? *Coord. Chem. Rev.* **2005**, *249*, 693.
- 65 Robert H. Crabtree. The organometallic chemistry of the transition metals. A Wiley-Interscience publication. **2005**, 4th Edition.
- 66 Chen, Z.; Concepcion, J.J.; Luo, H.; Hull, J.F.; Paul, A.; Meyer, T.J. Nonaqueous catalytic water oxidation, *J. Am. Chem. Soc.* **2010**, *132*, 17670.
- 67 Frisch, M.J.; Trucks, G.W.; Schlegel, H.B.; Scuseria, G.E.; Robb, M.A.; Cheeseman, J.R.; Scalmani, G.; Barone, V.; Petersson, G.A.; Nakatsuji, H.; Li, X.; Caricato, M. Marenich, A.V.; Bloino, J., Gaussian 16, Revision B.01, Gaussian Inc, Wallingford CT, **2016**.
- 68 Lee, C.; Yang, W.; Parr, R.G. Development of the Colle-Salvetti correlation-energy formula into a functional of the electron density. *Physical Review B* **1988**, *37*, 785.
- 69 Becke, A.D. Density-functional thermochemistry. III The role of exact exchange, *J. Chem. Phys.* **1993**, *98*, 5648.
- 70 Dunning, T.H. Gaussian basis sets for use in correlated molecular calculations. I. The atoms boron through neon and hydrogen, *J. Chem. Phys.* **1989**, *90*, 1007.
- 71 Andrae, D.; Häußermann, U.; Dolg, M.; Stoll, H.; Preuß, H.T. Energy-adjusted ab initio pseudopotentials for the second and third row transition elements, *Theor. Chim. Acta* **1990**, *77*, 123.
- 72 Fuentealba, P.; Preuss, H.; Stoll, H.; Von Szentpály, L. A proper account of corepolarization with pseudopotentials: single valence-electron alkali compounds, *Chem. Phys. Lett.* **1982**, *89*, 418.
- 73 Gil-Sepulcre, M.; Böhrer, M.; Schilling, M.; Bozoglian, F.; Bachmann, C.; Scherrer, D.; Fox, T.; Spingler, B.; Gimbert-Suriñach, C.; Alberto, R.; et al. Ruthenium Water Oxidation Catalysts Based on Pentapyridyl Ligands. *ChemSusChem* **2017**, *10*, 4517.
- 74 Matheu, R.; Ertem, M. Z.; Gimbert-Suriñach, C.; Benet-Buchholz, J.; Sala, X.; Llobet, A. Hydrogen Bonding Rescues Overpotential in Seven-Coordinated Ru Water Oxidation Catalysts. *ACS Catal.* **2017**, *7*, 6525.
- 75 Matheu, R.; Ertem, M. Z.; Pipelier, M.; Lebreton, J.; Dubreuil, D.; Benet-Buchholz, J.; Sala, X.; Tessier, A.; Llobet, A. The Role of Seven-Coordination in Ru-Catalyzed Water Oxidation. *ACS Catal.* **2018**, *8*, 2039.

-
- ⁷⁶ Matheu, R.; Garrido-Barros, P.; Gil-Sepulcre, M.; Ertem, M. Z.; Sala, X.; Gimbert-Suriñach, C.; Llobet, A. The Development of Molecular Water Oxidation Catalysts. *Nat. Rev. Chem.* **2019**, *3*, 331.
- ⁷⁷ Neudeck, S.; Maji, S.; López, I.; Meyer, S.; Meyer, F.; Llobet, A. New Powerful and Oxidatively Rugged Dinuclear Ru Water Oxidation Catalyst: Control of Mechanistic Pathways by Tailored Ligand Design. *J. Am. Chem. Soc.* **2014**, *136*, 24.
- ⁷⁸ Sato, Y.; Takizawa, S. Y.; Murata, S. Substituent Effects on Physical Properties and Catalytic Activities toward Water Oxidation in Mononuclear Ruthenium Complexes. *Eur. J. Inorg. Chem.* **2015**, *2015*, 5495.
- ⁷⁹ Xie, Y.; Shaffer, D. W.; Concepcion, J. J. O-O Radical Coupling: From Detailed Mechanistic Understanding to Enhanced Water Oxidation Catalysis. *Inorg. Chem.* **2018**, *57*, 10533.
- ⁸⁰ Staehle, R.; Tong, L.; Wang, L.; Duan, L.; Fischer, A.; Ahlquist, M. S.; Sun, L.; Rau, S. Water Oxidation Catalyzed by Mononuclear Ruthenium Complexes with a 2,2'-Bipyridine-6,6'-Dicarboxylate (Bda) Ligand: How Ligand Environment Influences the Catalytic Behavior. *Inorg. Chem.* **2014**, *53*, 1307.
- ⁸¹ Yazdani, S.; Colton, J. B.; Kumari, P.; Rheingold, A. L.; Jazzar, R.; Bertrand, G.; Grotjahn, D. B. Influence of Axial Phosphine Ligands in Six-coordinate Ruthenium Water Oxidation Catalysts. *In preparation*.
- ⁸² Andersen, N. G.; Keay, B. A. 2-Furyl Phosphines as Ligands for Transition-Metal-Mediated Organic Synthesis. *Chem. Rev.* **2001**, *101*, 997.
- ⁸³ Niemeyer, Z. L.; Milo, A.; Hickey, D. P.; Sigman, M. S. Parameterization of Phosphine Ligands Reveals Mechanistic Pathways and Predicts Reaction Outcomes. *Nature Chem.* **2016**, *8*, 610.
- ⁸⁴ Bilbrey, J. A.; Kazez, A. H.; Locklin, J.; Allen, W. D. Exact Ligand Cone Angles. *Comput. Chem.* **2013**, 1189.
- ⁸⁵ Roodt, A.; Otto, S.; Steyl, G. Structure and Solution Behaviour of Rhodium(I) Vaska-type Complexes for Correlation of Steric and Electronic Properties of Tertiary Phosphine Ligands. *Coord. Chem. Rev.* **2003**, *245*, 121.
- ⁸⁶ Kamdar, J. M.; Marelius, D. C.; Moore, C. E.; Rheingold, A. L.; Smith, D. K.; Grotjahn, D. B. Ruthenium Complexes of 2,2'-Bipyridine-6,6'-Diphosphonate Ligands for Water Oxidation. *ChemCatChem* **2016**, *8*, 3045.
- ⁸⁷ Matheu, R.; Benet-Buchholz, J.; Sala, X.; Llobet, A. Synthesis, Structure, and Redox Properties of a Trans-Diaqua Ru Complex That Reaches Seven-Coordination at High Oxidation States. *Inorg. Chem.* **2018**, *57*, 1757.
- ⁸⁸ Hurst, J. K.; Cape, J. L.; Clark, A. E.; Das, S.; Qin, C., Mechanisms of Water Oxidation Catalyzed by Ruthenium Diimine Complexes, *Inorg. Chem.* **2008**, *47*, 1753.
- ⁸⁹ Betley, T. A.; Wu, Q.; Van Voorhis, T.; Nocera, D. G. Electronic Design Criteria for O-O Bond Formation via Metal-Oxo Complexes. *Inorg. Chem.* **2008**, *47*, 1849.
- ⁹⁰ Roeser, S.; Farras, P.; Bozoglian, F.; Martinez-Belmonte, M.; Benet-Buchholz, J.; Llobet, A. Chemical, electrochemical, and photochemical catalytic oxidation of water to dioxygen with mononuclear ruthenium complexes. *ChemSusChem* **2011**, *4*, 197-207.

-
- ⁹¹ Romain, S.; Vigara, L.; Llobet, A. Oxygen–Oxygen Bond Formation Pathways Promoted by Ruthenium Complexes. *Acc. Chem. Res.* **2009**, *42*, 1944.
- ⁹² Oelkers, B. Na₂(Smbipy) - A Bipyridine-Derived Ligand with Chelating Sulfonate Tags and Its 3d Metal Complexes. *Eur. J. Inorg. Chem.* **2014**, *2014*, 5838.
- ⁹³ Hu, Y.; Chamchoumis, C.; Grebowicz, J. S.; Thummel, R. P. Unique 2 : 1 Complex with a Trans - Chelating Bis-Pyridine Ligand. *Inorg. Chem.* **2002**, *41*, 2296.
- ⁹⁴ Carlsson, A. C. C.; Mehmeti, K.; Uhrbom, M.; Karim, A.; Bedin, M.; Puttreddy, R.; Kleinmaier, R.; Neverov, A. A.; Nekoueishahraki, B.; Gräfenstein, J.; et al. Substituent Effects on the [N-I-N]⁺ Halogen Bond. *J. Am. Chem. Soc.* **2016**, *138*, 9853.
- ⁹⁵ Vanderkooy, A.; Gupta, A. K.; Földes, T.; Lindblad, S.; Orthaber, A.; Pápai, I.; Erdélyi, M. Halogen Bonding Helicates Encompassing Iodonium Cations. *Angew. Chem. Int. Ed.* **2019**, *58*, 9012.
- ⁹⁶ Reiersølmoen, A. C.; Csókás, D.; Øien-Ødegaard, S.; Vanderkooy, A.; Gupta, A. K.; Carlsson, A.-C. C.; Orthaber, A.; Fiksdahl, A.; Pápai, I.; Erdélyi, M. Catalytic Activity of Trans-Bis(Pyridine)Gold Complexes. *J. Am. Chem. Soc.* **2020**, *142*, 6439.
- ⁹⁷ Suzaki, Y.; Saito, T.; Osakada, K. Catalytic and Stoichiometric Reactions of Arylpalladium(II) Complexes Bearing a Trans-Chelating Dinitrogen Ligand with Arylboronic Acids. *J. Organomet. Chem.* **2020**, *910*, 121088.
- ⁹⁸ Schönfeld, S.; Lochenie, C.; Hörner, G.; Weber, B. Iron(II) Complexes with N₂O₂ Coordinating Schiff Base-like Equatorial Ligand and 1,2-Bis(Pyridin-2-Ylethynyl)Benzene as Axial Pincer Ligand. *J. Phys. Condens. Matter* **2019**, *31*.
- ⁹⁹ Pereira, F. A.; Fallows, T.; Frank, M.; Chen, A.; Clever, G. H. Stable and Metastable Self-Assembled Rings Based on Trans-Chelated Pd II. *Zeitschrift für Anorganische und Allgemeine Chemie* **2013**, *639*, 1598.
- ¹⁰⁰ Jiang, Y.; Li, F.; Zhang, B.; Li, X.; Wang, X.; Huang, F.; Sun, L. Promoting the Activity of Catalysts for the Oxidation of Water with Bridged Dinuclear Ruthenium Complexes. *Angew. Chem. Int. Ed.* **2013**, *52*, 3398.
- ¹⁰¹ Liu, Z.; Gao, Y.; Zhang, M.; Liu, J. Design of a Dinuclear Ruthenium Based Catalyst with a Rigid Xanthene Bridge for Catalytic Water Oxidation. *Inorg. Chem. Commun.* **2015**, *55*, 56.
- ¹⁰² Zhang, L. L.; Gao, Y.; Liu, Z.; Ding, X.; Yu, Z.; Sun, L. C. A Trinuclear Ruthenium Complex as a Highly Efficient Molecular Catalyst for Water Oxidation. *Dalton Trans.* **2016**, *45*, 3814.
- ¹⁰³ Kunz, V.; Schulze, M.; Schmidt, D.; Würthner, F. Trinuclear Ruthenium Macrocycles: Toward Supramolecular Water Oxidation Catalysis in Pure Water. *ACS Energy Lett.* **2017**, *2*, 288.
- ¹⁰⁴ M. Schulze, V. Kunz, P. D. Frischmann, F. Würthner, *Nat. Chem.* 2016, *8*, 576; b) V. Kunz, M. Schulze, D. Schmidt, F. Würthner, *ACS Energy Lett.* 2017, *2*, 288.
- ¹⁰⁵ Kunz, V.; Lindner, J. O.; Schulze, M.; Röhr, M. I. S.; Schmidt, D.; Mitrić, R.; Würthner, F. Cooperative Water Oxidation Catalysis in a Series of Trinuclear Metallosupramolecular Ruthenium Macrocycles. *Energy Environ. Sci.* **2017**, *10*, 2137.

-
- ¹⁰⁶ Kunz, V.; Schmidt, D.; Röhr, M. I. S.; Mitrić, R.; Würthner, F. Supramolecular Approaches to Improve the Performance of Ruthenium-Based Water Oxidation Catalysts. *Adv. Energy Mater.* **2017**, *7*, 1.
- ¹⁰⁷ Duan, L.; Wang, L.; Inge, A. K.; Fischer, A.; Zou, X.; Sun, L. Insights into Ru-Based Molecular Water Oxidation Catalysts: Electronic and Noncovalent-Interaction Effects on Their Catalytic Activities. *Inorg. Chem.* **2013**, *52*, 7844.
- ¹⁰⁸ Wang, L.; Duan, L.; Wang, Y.; Ahlquist, M. S. G.; Sun, L. Highly efficient and robust molecular water oxidation catalysts based on ruthenium complexes. *Chem. Commun.*, **2014**, *50*, 12947.
- ¹⁰⁹ Wang, L.; Duan, L.; Stewart, B.; Pu, M.; Liu, J. T. Privalov and L. Sun, Toward controlling water oxidation catalysis: tunable activity of ruthenium complexes with axial imidazole/DMSO ligands. *J. Am. Chem. Soc.*, **2012**, *134*, 18868.
- ¹¹⁰ Meyer, K.; Ranocchiari M.; Bokhoven J. A. van. Metal organic frameworks for photo-catalytic water splitting. *Energy Environ. Sci.*, **2015**, *8*, 1923.
- ¹¹¹ Hansen, R. E.; Das, S. Biomimetic di-manganese catalyst cage-isolated in a MOF: robust catalyst for water oxidation with Ce(IV), a non-O-donating oxidant. *Energy Environ. Sci.*, **2014**, *7*, 317.
- ¹¹² Wang, C.; Wang, J.-L.; Lin, W. Metal–Organic Frameworks for Light Harvesting and Photocatalysis. *J. Am. Chem. Soc.*, **2012**, *134*, 7211.
- ¹¹³ Richmond, C. J.; Llobet, A. Incorporation of a Ruthenium-Bis(Pyridine)Pyrazolate (Ru-Bpp) Water Oxidation Catalyst in a Hexametallc Macrocycle. *Catal. Sci. Technol.* **2016**, *6*, 6697.
- ¹¹⁴ Tong, L.; Duan, L.; Xu, Y.; Privalov, T.; Sun, L. Structural Modifications of Mononuclear Ruthenium Complexes: A Combined Experimental and Theoretical Study on the Kinetics of Ruthenium-Catalyzed Water Oxidation. *Angew. Chem., Int. Ed.* **2011**, *50*, 445.
- ¹¹⁵ Douglas Grotjahn, unpublished work.
- ¹¹⁶ Wang, L. P.; Wu, Q.; Van Voorhis, T. Acid-Base Mechanism for Ruthenium Water Oxidation Catalysts. *Inorganic Chemistry* **2010**, *49*, 4543.
- ¹¹⁷ Greco, N. J.; Hysell, M.; Goldenberg, J. R.; Rheingold, A. L.; Tor, Y. Alkyne-containing chelating ligands: synthesis, properties and metal coordination of 1,2-di(quinolin-8-yl)ethyne. *Dalton Trans.* **2006**, No. 19, 2288.
- ¹¹⁸ Minozzi, C.; Caron, A.; Grenier-Petel, J. C.; Santandrea, J.; Collins, S. K. Heteroleptic Copper(I)-Based Complexes for Photocatalysis: Combinatorial Assembly, Discovery, and Optimization. *Angew. Chem. Int. Ed.* **2018**, *57*, 5477.
- ¹¹⁹ Widner, D. L.; Knauf, Q. R.; Merucci, M. T.; Fritz, T. R.; Sauer, J. S.; Speetzen, E. D.; Bosch, E.; Bowling, N. P. Intramolecular Halogen Bonding Supported by an Aryldiyne Linker. *J. Org. Chem.* **2014**, *79*, 6269.
- ¹²⁰ Molander, G. A.; Brown, A. R. Suzuki-Miyaura Cross-Coupling Reactions of Potassium Vinyltrifluoroborate with Aryl and Heteroaryl Electrophiles. *J. Org. Chem.* **2006**, *71*, 9681.

-
- ¹²¹ Sakamoto, Y.; Suzuki, T. Tetrabenz[8]Circulene: Aromatic Saddles from Negatively Curved Graphene. *J. Am. Chem. Soc.* **2013**, *135*, 14074.
- ¹²² Igau, A.; Grutzmacher, H.; Baceiredo, A.; Bertrand, G. Analogous .alpha.,.alpha.'-bis-carbenoid, triply bonded species: synthesis of a stable .lambda.3-phosphino carbene-.lambda.5-phosphaacetylene *J. Am. Chem. Soc.* **1988**, *110*, 6463.
- ¹²³ Arduengo, A. J.; Harlow, R. L.; Kline, M. A stable crystalline carbene. *J. Am. Chem. Soc.* **1991**, *113*, 361.
- ¹²⁴ Aldrecht, M. Carbenes in action. *Science*, **2009**, *326*, 532.
- ¹²⁵ Melaimi, M.; Jazzar, R.; Soleilhavoup, M.; Bertrand, G. Cyclic(Alkyl)(amino)carbenes (CAACs): Recent Developments. *Angew. Chem. Int. Ed.*, **2017**, *56*, 10056.
- ¹²⁶ Lavallo, V.; Canac, Y.; Präsang, C.; Donnadiou, B.; Bertrand, G. Stable Cyclic (Alkyl)(Amino)Carbenes as Rigid or Flexible, Bulky, Electron-Rich Ligands for Transition-Metal Catalysts: A Quaternary Carbon Atom Makes the Difference. *Angewandte Chemie - International Edition* **2005**, *44*, 5705.
- ¹²⁷ Melaimi, M.; Jazzar, R.; Soleilhavoup, M.; Bertrand, G. Cyclic (Alkyl)(Amino)Carbenes (CAACs): Recent Developments. *Angewandte Chemie - International Edition* **2017**, *56*, 10046.
- ¹²⁸ Tomàs-Mendevíl, E. Hansmann, M. M., Weinstein, C., Jazzar, R., Melaimi, M., Bertrand, G. Bicyclic (Alkyl)(amino)carbenes (BICAACs): Stable Carbenes More Ambiphilic than CAACs. *J. Am. Chem. Soc.* **2017**, *139*, 7753.
- ¹²⁹ Weinstein, C. M., Junor, G. P. Tolentino, D. Jazzar, R., Melaimi, M. Bertrand, G. Highly Ambiphilic Room Temperature Stable Six-Membered Cyclic (Alkyl)(amino)carbenes. *J. Am. Chem. Soc.* **2018**, *140*, 9255.
- ¹³⁰ Wu, C.; Horibe, T.; Jacobsen, C. B.; Toste, F. D. Stable gold(III) catalysts by oxidative addition of a carbon-carbon bond. *Nat.* **2014**, *517*, 449.
- ¹³¹ (a) Martin, D.; Marx, V. M.; Grubbs, R. H.; Bertrand, G. A ruthenium catalysis for olefin metathesis featuring an anti-Bredt N-heterocyclic carbene ligand. *Adv. Synth. Catal.*, **2016**, *358*, 965; (b) Marx, V. M.; Sullivan, A. H.; Melaimi, M.; Virgil, S. C.; Keitz, B. K.; Weinberger, D. S.; Bertrand, G.; Grubbs, R. H. Cyclic Alkyl Amino Carbene (CAAC) ruthenium complexes as remarkably active catalysts for ethenolysis. *Angew. Chem. Int. Ed.* **2014**, *54*, 1919.
- ¹³² Wiesenfeldt, M. P.; Nairoukh, Z.; Li, W.; Glorius, F. Hydrogenation of fluoroarenes: Direct access to all-*cis*-(multi)fluorinated cycloalkanes. *Science* **2017**, *357*, 908.
- ¹³³ Babbini, D. C.; Iluc, V. M. Synthesis and reactivity of a nucleophilic palladium(II) carbene. *Organometallics* **2015**, *34*, 3141.
- ¹³⁴ Hopkinson, M. N.; Richter, C.; Schedler, M.; Glorius, F. An overview of N-heterocyclic carbenes. *Nat.* **2014**, *510*, 485.
- ¹³⁵ Melaimi, M., Jazzar, R., Soleilhavoup, M., Bertrand, G. Cyclic(Alkyl)(amino)carbenes (CAACs): Recent Developments. *Angew. Chem. Int. Ed.* **2017**, *56*, 10056.

-
- ¹³⁶ Kinjo, R.; Donnadiou, B.; Bertrand, G. Gold-Catalyzed Hydroamination of Alkynes and Allenes with Parent Hydrazine. *Angew. Chem. Int. Ed.* **2011**, *50*, 5560.
- ¹³⁷ (a) Zeng, X.; Frey, G. D.; Kinjo, R.; Donnadiou, B.; Bertrand, G. Synthesis of a Simplified Version of Stable Bulky and Rigid Cyclic (Alkyl)(amino)carbenes, and Catalytic Activity of the Ensuing Gold(I) Complex in the Three-Component Preparation of 1,2-Dihydroquinoline Derivatives. *J. Am. Chem. Soc.* **2009**, *131*, 8690. (b) Zeng, X.; Soleilhavoup, M.; Bertrand, G. Gold-Catalyzed Intermolecular Markovnikov Hydroamination of Allenes with Secondary Amines. *Org. Lett.* **2009**, *11*, 3166.
- ¹³⁸ Zeng, X.; Kinjo, R.; Donnadiou, B.; Bertrand, G. Serendipitous Discovery of the Catalytic Hydroammoniumation and Methylation of Alkynes. *Angew. Chem. Int. Ed.* **2010**, *49*, 942.
- ¹³⁹ Lavallo, V.; Frey, G. D.; Donnadiou, B.; Soleilhavoup, M.; Bertrand, G. Homogeneous Catalytic Hydroamination of Alkynes and Allenes with Ammonia. *Angew. Chem. Int. Ed.* **2008**, *47*, 5224.
- ¹⁴⁰ Müller, T. E.; Hultsch, K. C.; Yus, M.; Foubelo, F.; Tada, M. Hydroamination: Direct Addition of Amines to Alkenes and Alkynes. *Chem. Rev.* **2008**, *108*, 3795.
- ¹⁴¹ Takabe, K.; Katagiri, T.; Tanaka, J.; Fujita, T.; Watanabe, S.; Suga, K. Addition Of Dialkylamines To Myrcene: N,N-diethylgeranylamine. *Org. Synth.* **1989**, *67*, 44.
- ¹⁴² (a) Widenhofer, R. A.; Xiaoqing, H. Gold-catalyzed hydroamination of C-C multiple bonds. *Eur. J. Org. Chem.* **2006**, *20*, 4555. (b) Dorel, R.; Echavarren, A. M. Gold(I)-catalyzed activation of alkynes for the construction of molecular complexity. *Chem. Rev.* **2015**, *115*, 9028. (c) Alyabyev, S. B.; Beletskaya, I. P. Gold as a catalyst. Part I. Nucleophilic addition to the triple bond *Russ. Chem. Rev.*, **2017**, *86*, 689.
- ¹⁴³ (a) Gorin, D. J.; Toste, F. D. Relativistic effects in homogeneous gold catalysis. *Nature*, **2007**, *446*, 395-403. (b) Gorin, D. J.; Sherry, B. D.; Toste, F. D. Ligand Effects in Homogeneous Au Catalysis. *Chem. Rev.* **2008**, *108*, 3351.
- ¹⁴⁴ Wang, W.; Hammond, G. B.; Xu, B. Ligand Effects and Ligand Design in Homogeneous Gold(I) Catalysis. *J. Am. Chem. Soc.* **2012**, *134*, 5697.
- ¹⁴⁵ (a) Cheng, X.; Wang, Z.; Quintanilla, C. D.; Zhang, L. Chiral Bifunctional Phosphine Ligand Enabling Gold-Catalyzed Asymmetric Isomerization of Alkyne to Allene and Asymmetric Synthesis of 2,5-Dihydrofuran. *J. Am. Chem. Soc.* **2019**, *141*, 3787. (b) Liao, S.; Porta, A.; Cheng, X.; Ma, X.; Zononi, G.; Zhang, L. Bifunctional Ligand Enables Efficient Gold-Catalyzed Hydroalkenylation of Propargylic Alcohol. *Angew. Chem., Int. Ed.* **2018**, *57*, 8250. (c) Li, T.; Zhang, L. Bifunctional Biphenyl-2-Ylphosphine Ligand Enables Tandem Gold-Catalyzed Propargylation of Aldehyde and Unexpected Cycloisomerization. *J. Am. Chem. Soc.* **2018**, *140*, 17439. (d) Wang, Z.; Ying, A.; Fan, Z.; Hervieu, C.; Zhang, L. Tertiary Amino Group in Cationic Gold Catalyst: Tethered Frustrated Lewis Pairs That Enable Ligand-Controlled Regiodivergent and Stereoselective Isomerizations of Propargylic Esters. *ACS Catal.* **2017**, *7*, 3676. (e) Wang, Z.; Nicolini, C.; Hervieu, C.; Wong, Y.-F.; Zononi, G.; Zhang, L. Remote Cooperative Group Strategy Enables Ligands for Accelerative Asymmetric Gold Catalysis. *J. Am. Chem. Soc.* **2017**, *139*, 16064. (f) Li, X.; Wang, Z.; Ma, X.; Liu, P. -N.; Zhang, L. Designed Bifunctional Phosphine Ligand-Enabled Gold-Catalyzed Isomerizations of Ynamides and Allenamides: Stereoselective and Regioselective Formation of 1-Amido-1,3-Dienes. *Org. Lett.* **2017**, *19*, 5744. (g) Li, X.; Liao, S.; Wang, Z.; Zhang, L. Ligand-Accelerated Gold-Catalyzed Addition of in Situ Generated Hydrazoic Acid to Alkynes under Neat Conditions. *Org. Lett.* **2017**, *19*, 3687. (h) Wang, Z.; Wang, Y.; Zhang, L. Soft Propargylic Deprotonation: Designed Ligand Enables Au-Catalyzed Isomerization of Alkynes to 1,3-Dienes. *J. Am. Chem. Soc.* **2014**, *136*, 8887.

¹⁴⁶ (a) Carreras, J.; Pereira, A.; Zanini, M.; Echavarren, A. M. Variations on the Theme of JohnPhos Gold(I) Catalysts: Arsine and Carbene Complexes with Similar Architectures. *Organometallics*, **2018**, *37*, 3588-3597. (b) Zhang, J.Q.; Liu, Y.; Wang, X. -W.; Zhang, L. Synthesis of Chiral Bifunctional NHC Ligands and Survey of Their Utilities in Asymmetric Gold Catalysis. *Organometallics*, **2019**, *38*, 3931.

¹⁴⁷ Wang, Y.; Wand, Z.; Li, Y.; Wu, G.; Gao, Z.; Zhang, L. A general ligand design for gold catalysis allowing ligand-directed anti-nucleophilic attack of alkynes. *Nat. Comm.* **2014**, *5*, 3470.

¹⁴⁸ Tang, Y.; Benaissa, I.; Huynh, M.; Vendier, L.; Lugan, N.; Bastin, S.; Belmont, P.; César, V.; Michelet, V. An Original L-Shape, Tunable N-Heterocyclic Carbene Platform for Efficient Gold(I) Catalysis. *Angew. Chem., Int. Ed.* **2019**, *58*, 7977.

¹⁴⁹ Schießl, J.; Schulmeister, J.; Doppiu, A.; Wörner, E.; Rudolph, M.; Karch, R.; Hashmi, A. S. K., An Industrial Perspective on Counter Anions in Gold Catalysis: Underestimated with Respect to “Ligand Effects”. *Adv. Synth. Cat.* **2018**, *360*, 2493.

¹⁵⁰ Couce-Rios, A.; Kovács, G.; Ujaque, g.; Lledós, A. Hydroamination of C–C Multiple Bonds with Hydrazine Catalyzed by N-Heterocyclic Carbene–Gold(I) Complexes: Substrate and Ligand Effects. *ACS Catal.* **2015**, *5*, 815.

¹⁵¹ Blackmond, D. G.; Kinetic Profiling of Catalytic Organic Reactions as a Mechanistic Tool. *J. Am. Chem. Soc.* **2015**, *137*, 10852.

¹⁵² Clavier, H.; Nolan, S. P. Percent Buried Volume for Phosphine and N-Heterocyclic Carbene Ligands: Steric Properties in Organometallic Chemistry. *Chem. Commun.* **2010**, *46*, 841.

¹⁵³ Poater, A.; Cosenza, B.; Correa, A.; Giudice, S.; Ragone, F.; Scarano, V.; Cavallo, L. SambVca: A Web Application for the Calculation of the Buried Volume of N-Heterocyclic Carbene Ligands. *Eur. J. Inorg. Chem.* **2009**, *13*, 1759.

¹⁵⁴ Dash, C.; Shaikh, M. M.; Butcher, R. J.; Ghosh, P. Highly Convenient Regioselective Intermolecular Hydroamination of Alkynes Yielding Ketimines Catalyzed by Gold(I) Complexes of 1,2,4-triazole Based N-heterocyclic Carbenes. *Inorg. Chem.* **2010**, *49*, 4972.

¹⁵⁵ (a) Sergievskaya, A. P.; Tatarchuk, V. V.; Makotchenko, E. V.; Mironov, I. V. Formation of Gold Nanoparticles During the Reduction of H₂AuBr₄ In Reverse Micelles Of Oxyethylated Surfactant: Influence of Gold Precursor on the Growth Kinetics and Properties of the Particles. *J. Mater. Res.* **2015**, *30*, 1925. (b) Yang, X.-F.; Wang, A.-Q.; Wang, Y.-L.; Zhang, T.; Li, J. Unusual Selectivity of Gold Catalysts for Hydrogenation of 1,3-Butadiene toward *cis*-2-Butene: A Joint Experimental and Theoretical Investigation. *J. Phys. Chem.* **2010**, *114*, 3131.

¹⁵⁶ Klinkenberg, J. L.; Hartwig, J. F. catalytic Organometallic Reactions of Ammonia. *Angew. Chem., Int. Ed.* **2011**, *50*, 86.

¹⁵⁷ (a) Heaton, B. T.; Jacob, C.; Page, P. Transition Metal Complexes Containing Hydrazine and Substituted Hydrazines *Coord. Chem. Rev.* **1996**, *154*, 193; (b) Van der Vlugt, J. I. Advances in selective activation and application of ammonia in homogeneous catalysis. *Chem. Soc. Rev.* **2010**, *39*, 2302; (c) Young, P. C.; Green, S. L. J.; Rosair, G.; Lee, A.-L. Deactivation of gold (I) catalysts in the presence of thiols and amines characterization and catalysis. *Dalton Trans.* **2013**, *42*, 9645; (d) Kim, J.; Kim, H. J.; Chang, S. Synthetic uses of ammonia in transition-metal catalysis. *Eur. J. Org. Chem.* **2013**, 3201.

¹⁵⁸ Manzano, R.; Wurm, T.; Rominger, F.; Hashmi, A. S. K. Room-Temperature Hydrohydrazination of Terminal Alkynes Catalyzed by Saturated Abnormal N-Heterocyclic Carbene–Gold(I) Complexes. *Chem. Eur. J.* **2014**, *20*, 6844.

¹⁵⁹ Martin, D.; Lassauque, N.; Donnadieu, B.; Bertrand, G. Cyclic Diaminocarbene with a Pyramidalized Nitrogen Atom: A Stable N-Heterocyclic Carbene with Enhanced Electrophilicity, *Angew. Chem. Int. Ed.* **2012**, *51*, 6172.

¹⁶⁰ López-Gómez, M. J.; Martin, D.; Bertrand, G. Anti-Bredt N-Heterocyclic Carbene: an Efficient Ligand for the Gold(I)-Catalyzed Hydroamination of Terminal Alkynes with Parent Hydrazine. *Chem. Commun.* **2013**, *49*, 4483.

¹⁶¹ (a) Frey, G. D.; Dewhurst, R. D.; Kousar, S.; Donnadieu, B.; Bertrand, G., Cyclic (Alkyl)(amino)carbene Gold(I) Complexes: A Synthetic and Structural Investigation. *J. Organomet. Chem.* **2008**, *693*, 1674. (b) Hamze, R.; Jazzar, R.; Soleilhavoup, M.; Djurovich, P. I.; Bertrand, G.; Thompson, M. E. Phosphorescent 2-, 3- and 4-Coordinate Cyclic (Alkyl)(amino)carbene (CAAC) Cu(I) Complexes. *Chem. Comm.* **2017**, *53*, 9008.

¹⁶² Couce-Rios, A.; Kovács, G.; Ujaque, G.; Lledós, A. Hydroamination of C-C Multiple Bonds with Hydrazine Catalyzed by N-Heterocyclic Carbene-Gold(I) Complexes: Substrate and Ligand Effects. *ACS Catalysis* **2015**, *5*, 815.

¹⁶³ (a) Herrero-Gómez, E.; Nieto-Oberhuber, C.; López, S.; Benet-Buchholz, J.; Echavarren, A. M. Cationic η^1/η^2 -Gold(I) Complexes of Simple Arenes. *Angew. Chem., Int. Ed.* **2006**, *45*, 5455. (b) Li, Q.-S.; Wan, C.-Q.; Zou, R.-Y.; Xu, F.-B.; Song, H.-B.; Wan, X.-J.; Zhang, Z.-Z. Gold(I) η^2 -Arene Complexes. *Inorg. Chem.* **2006**, *45*, 1888.

¹⁶⁴ Gaussian 09, Revision D.01, M. J. Frisch, G. W. Trucks, H. B. Schlegel, G. E. Scuseria, M. A. Robb, J. R. Cheeseman, G. Scalmani, V. Barone, B. Mennucci, G. A. Petersson, H. Nakatsuji, M. Caricato, X. Li, H. P. Hratchian, A. F. Izmaylov, J. Bloino, G. Zheng, J. L. Sonnenberg, M. Hada, M. Ehara, K. Toyota, R. Fukuda, J. Hasegawa, M. Ishida, T. Nakajima, Y. Honda, O. Kitao, H. Nakai, T. Vreven, J. A. Montgomery, Jr., J. E. Peralta, F. Ogliaro, M. Bearpark, J. J. Heyd, E. Brothers, K. N. Kudin, V. N. Staroverov, T. Keith, R. Kobayashi, J. Normand, K. Raghavachari, A. Rendell, J. C. Burant, S. S. Iyengar, J. Tomasi, M. Cossi, N. Rega, J. M. Millam, M. Klene, J. E. Knox, J. B. Cross, V. Bakken, C. Adamo, J. Jaramillo, R. Gomperts, R. E. Stratmann, O. Yazyev, A. J. Austin, R. Cammi, C. Pomelli, J. W. Ochterski, R. L. Martin, K. Morokuma, V. G. Zakrzewski, G. A. Voth, P. Salvador, J. J. Dannenberg, S. Dapprich, A. D. Daniels, O. Farkas, J. B. Foresman, J. V. Ortiz, J. Cioslowski, and D. J. Fox, Gaussian, Inc., Wallingford CT, 2013.

¹⁶⁵ All computational results are available for download free of charge from UCSD Library Digital Collections. Yazdani, S.; Junor, Glen P.; Pelier, J. L.; Jazzar, R.; Grotjahn, D. B.; Bertrand, G. (2020). Hydroamination Au. UC San Diego Library Digital Collections. Dataset. <https://doi.org/10.6075/J0GB22FN>

¹⁶⁶ For review on dispersion corrections: Grimme, S. *Wiley Interdisciplinary Reviews: Computational Molecular Science* **2011**, *1*, 211.

¹⁶⁷ Tomasi, J.; Mennucci, B.; Cammi, R. Quantum Mechanical Continuum Solvation Models. *Chem. Rev.*, **2005**, *105*, 2999.

-
- ¹⁶⁸ (a) Hashmi, A. S. K. Homogeneous Gold Catalysis Beyond Assumptions and Proposals-Characterized Intermediates. *Angew. Chem. Int. Ed.* **2010**, *49*, 5232-5241. (b) Ranieri, B.; Escofet, I.; Echavarren, A. M. Anatomy of gold catalysts: facts and myths. *Org. Biomol. Chem.* **2015**, *13*, 7103.
- ¹⁶⁹ Lavallo, V.; Wright, J. H., II; Tham, F. S.; Quinlivan, S. Perhalogenated Carba-closo-dodecaborate Anions as Ligand Substituents: Applications in Gold Catalysis. *Angew. Chem. Int. Ed.* **2013**, *52*, 3172.
- ¹⁷⁰ Dolomanov, O. V.; Bourhis, L. J.; Gildea, R. J.; Howard, J. A. K.; Puschmann, H. OLEX2: a complete structure solution, refinement and analysis program. *J. Appl. Cryst.* **2009**, *42*, 339.
- ¹⁷¹ Li, B.; Bheeter, C. B.; Darcel, C.; Dixneuf, P. H. Sequential Catalysis for the Production of Sterically Hindered Amines: Ru(II)-Catalyzed C-H Bond Activation and Hydrosilylation of Imines. *ACS Catalysis* **2011**, *1*, 1221.
- ¹⁷² Ueno, A.; Watanabe, K.; Daniliuc, C. G.; Kehr, G.; Erker, G. Unsaturated Vicinal Frustrated Phosphane/Borane Lewis Pairs as Ligands in Gold(i) Chemistry. *Chem. Comm.* **2019**, *55*, 4367.
- ¹⁷³ Cao, Z.; Cao, C.; Cao, C. Comparison of the ¹³C (C=N) Chemical Shifts of Substituted N-(Phenyl-Ethylene)-Anilines and Substituted N-(Benzylidene)-Anilines. *J. Phys. Org. Chem.* **2015**, *28*, 564.
- ¹⁷⁴ Yang, H.; Gabbal, F. P. Activation of a Hydroamination Gold Catalyst by Oxidation of a Redox-Noninnocent Chlorostibine Z-Ligand. *J. Am. Chem. Soc.* **2015**, *137*, 13425.
- ¹⁷⁵ Anderson, L. L.; Arnold, J.; Bergman, R. G. Catalytic Hydroamination of Alkynes and Norbornene with Neutral and Cationic Tantalum Imido Complexes. *Org. Lett.* **2004**, *6*, 2519.
- ¹⁷⁶ Katam, S.; Ganesan, P. Large CuI₈ Chalcogenone Cubic Cages with Non-Interacting Counter Ions. *Dalton Trans.* **2017**, *46*, 16615.
- ¹⁷⁷ Dabb, S. L.; Messerle, B. A. Rh(I) and Ir(I) Catalysed Intermolecular Hydroamination with Substituted Hydrazines. *Dalton Trans.* **2008**, *45*, 6368.
- ¹⁷⁸ Chen, Z. S.; Duan, X. H.; Wu, L. Y.; Ali, S.; Ji, K. G.; Zhou, P. X.; Liu, X. Y.; Liang, Y. M. Palladium-Catalyzed Coupling of Propargylic Carbonates with N-Tosylhydrazones: Highly Selective Synthesis of Substituted Propargylic N-Sulfonylhydrazones and Vinylallenes. *Chem. Eur. J.* **2011**, *17*, 6918.
- ¹⁷⁹ Kinjo, R.; Donnadiou, B.; Bertrand, G. Gold-catalyzed hydroamination of alkynes and allenes with parent hydrazine. *Angew. Chem. Int. Ed.* **2011**, *50*, 5560.
- ¹⁸⁰ Weitershaus, K.; Wadepohl, H.; Gade, L. H. Erratum: Titanium Hydrazinediido Half-Sandwich Complexes: Highly Active Catalysts for the Hydrohydrazination of Terminal Alkynes at Ambient Temperature. *Organometallics* **2009**, *28*, 4898.